Trapping and Diffusion of Helium in Lunar Materials

Kimberly R. Harris-Kuhlman

December 1998

UWFDM-1095

Ph.D. thesis.

FUSION TECHNOLOGY INSTITUTE

UNIVERSITY OF WISCONSIN

MADISON WISCONSIN

Trapping and Diffusion of Helium in Lunar Materials

Kimberly R. Harris-Kuhlman

Fusion Technology Institute
University of Wisconsin
1500 Engineering Drive
Madison, WI 53706

http://fti.neep.wisc.edu

December 1998

UWFDM-1095

Ph.D. thesis.

TRAPPING AND DIFFUSION OF HELIUM IN LUNAR MINERALS

by

Kimberly R. Harris-Kuhlman

A dissertation submitted in partial fulfillment

of the requirements for the degree of

Doctor of Philosophy

(Nuclear Engineering and Engineering Physics)

at the

UNIVERSITY OF WISCONSIN - MADISON

1998

Abstract

The goal of the research performed in this dissertation is to improve the understanding of the trapping and diffusion of helium in lunar minerals, especially ilmenite. The Moon is the most promising source of large amounts of ^{3}He needed for future fusion fuel, and ^{3}He seems to be preferentially trapped in lunar ilmenite. The parabolic differential equation for diffusion was combined with solar wind data from Pioneer 10 and a description of the lunar environment to create a computational model of helium implantation and diffusion in the lunar regolith. This computational approach established an upper bound of 3×10^{-25} cm^2/s for the diffusivity of He in the lunar regolith at 400K, the maximum lunar temperature. The diffusivity of He isotopes in ilmenite, a mineral known for its helium retention capability, was measured experimentally. Samples of several terrestrial ilmenites were analyzed using electron probe microanalysis to determine the closest analog of lunar ilmenite. The most suitable simulants were ilmenite from Quebec and New York. These samples were implanted with ^{4}He to 10^{16} ions/cm^2, ^{3}He to 10^{13} ions/cm^2 and H from 10^{14} ions/cm^2 to 10^{17} ions/cm^2 at solar-wind energies using Plasma Source Ion Implantation (PSII). Isochronal annealing with mass spectroscopy of the evolved ^{4}He demonstrated release behavior similar to that of the Apollo 11 regoliths. Moderate fluences of H were seen to retard ^{3}He release, while a high fluence of H had little effect. A three-dimensional computational code, ANNEAL, was developed for calculating diffusivity from the results of these annealing experiments. The helium (both ^{3}He and ^{4}He) diffusion in these samples is characterized by four distinct activation energies, E_1=0.26 eV, $E_2 \cong$0.5 eV, $E_3 \cong$1.4 eV and E_4>2.2 eV. These energies are characteristic of diffusion through two amorphous layers and detrapping from oxygen vacancies and constitutional vacancies, respectively. The diffusivity of ^{3}He was seen to be at least a factor of 10 higher than the diffusivity of ^{4}He. A diffusivity of 9×10^{-24} cm^2/s at 400K was determined for diffusion of helium with activation energy of 1.5 eV. This behavior is consistent with helium trapping in oxygen vacancies.

Used by permission of the artist, 1998.

Acknowledgements

"He gives power to the faint; and to them that have no might, he increases strength. Even the youths shall faint and be weary, and the young men shall utterly fall. But they that wait upon the Lord shall renew their strength, they shall mount up with wings as eagles, they shall run and not be weary, they shall run and not faint." Isaiah 40:29-31.

I would like to express my appreciation to my thesis advisor, Professor Gerald L. Kulcinski for presenting me with a challenge and encouraging me in traveling the many paths required to get to the end of this thesis. I would also like to thank Professor Harrison H. Schmitt for encouraging this research and for many insightful suggestions. Perhaps, one day, I will be allowed to follow in his footsteps.

Many people have been instrumental to various parts of this research. I want to thank the staff of the Fusion Technology Institute at the University of Wisconsin for all of their support, moral and financial. Special thanks go to Dr. Hesham Khater for his work on the computations involved in the study of the remote detection of lunar ^{3}He, and to Dr. John F. Santarius for many thoughtful discussions, moral support and extra time on the Cray. I also want to thank Mr. Igor Sviatslovsky and Dr. Layton Wittenberg for discussions on various aspects of this research. My thanks also go to Professor James P. Blanchard for his assistance and great patience concerning the numerical codes written for this thesis. Thanks also go to Dennis Bruggink, Elaine DuCharme, Linda Kraft and Sue Ann Hubanks for all their help. Special thanks goes to Scott White with whom I shared an office for 6 years.

I also want to thank the staff of the Wisconsin Space Grant Consortium for their generous support over the last three years. I am deeply appreciative of the support that allowed me to attend the International Space University in Stockholm, Sweden during the summer of 1995. Thanks also go to Dean John Bollinger for his financial support for that particular endeavor. This research has also been generously supported by NASA Johnson Space Center, by the Graduate School of the University of Wisconsin, and by the Grainger

Foundation. I also want to thank the Committee on Institutional Cooperation (CIC) Women in Science and Engineering (WISE) Initiative for partially funding my travel to the Space 98 conference in Albuquerque.

I want to extend my sincerest appreciation to Professors Donald H. Lindsley (SUNY - Stony Brook), Stephen E. Haggerty (University of Massachusetts), Lawrence A. Taylor (University of Tennessee), Eugene N. Cameron and John W. Valley (University of Wisconsin) for suggesting and providing samples of terrestrial ilmenites as well as much needed advice concerning the geological aspects of this thesis. Thanks also to Dr. William Barker and Dr. John Fournelle (University of Wisconsin) for performing the high resolution TEM work and assistance in performing the electron probe microanalysis, respectively. I am in your debt. Special thanks also goes to Marie Dvorzak of the UW Geology Library for her wonderful ability to track down obscure references.

My deep appreciation also goes to the members of the Materials Science Center (MSC) at the University of Wisconsin. Thank you to Professor Reid F. Cooper, Professor Thomas F. Kelly, Professor Susan E. Babcock, Professor Richard J. Matyi for our conversations and for generously allowing me to use your facilities and supplies. Thanks also to the staff and students of the MSC, in particular, Christopher Kailhoffer, Richard Noll, Richard Casper, Glenn Cook and Kathy Dunn.

My sincere thanks also go to the generous members of the Plasma Source Ion Implantation (PSII) group at the University of Wisconsin: Professor John R. Conrad, Dr. Robert Breun, Dr. Muhammad Shamim, Dr. Kumar Sridharan and Paul Fetherston. Thank you for performing the implantations, and for many conversations. Thanks, Paul, for helping me "make moon rocks."

I also want to thank Professor Robert O. Pepin, Dr. Richard H. Becker and Dr. Dennis J. Schlutter of the University of Minnesota for generously performing the isochronal and isothermal annealing with mass spectrometry in this thesis and for considerable feedback

concerning this thesis. Special thanks to Dr. Becker for the conversation which stimulated the development of the ANNEAL code.

My sincere thanks also go to Professor Kelvin G. Lynn and Dr. Marc Weber of Washington State Unversity for allowing me to conduct the positron annihilation spectroscopy for this thesis in their laboratory and for their assistance with the results.

I wish to extend my appreciation to Dr. John Nealy at the NASA Langley Research Center for providing access to the baryon transport code BRYNTRN and to Dr. Paul Gazis of NASA Ames Research Center for providing the Pioneer 10 data. My thanks also go to Professor R. K. Pandey of the University of Alabama for the sample of synthetic ilmenite and to Dr. Jeremy Mitchell and Dr. Kurt Sickafus of Los Alamos National Laboratory for discussions concerning the TRIM code, synthetic ilmenite and the amorphization of minerals by irradiation.

Finally, I want to express my sincere thanks to the people who have given me such incredible personal support. First and foremost, I want to thank my husband, Gregory M. Kuhlman, for all the sacrifices he has made in the last several years. Thanks to my parents, Allan and Elizabeth Harris for being tremendous role models and for all their encouragement in my continuing education. Thanks Mom and Dad for giving me the opportunities to follow my dreams. I also want to thank Michael and Marian Kuhlman for all of their support and for being my second parents. My deep appreciation also goes to my long-time mentor, Jonathan Alexander, his wife, Mary, and their children for taking me in as an undergraduate and for always being there with support and encouragement. Finally, I want to thank my long-time friends, Karen Schlangen and Kristine Klotzbach for all of their support and encouragement in spite of the miles between us.

Table of Contents

Table of Figures

Chapter 2

Chapter 3

Chapter 4

Chapter 5

Chapter 6

Chapter 7

Chapter 8

Chapter 9

Table of Tables

Chapter 2

Chapter 3

Chapter 5

Chapter 6

Chapter 7

Chapter 8

Chapter 9

Chapter 1 Introduction

Thesis Objectives

The goal of this research is to improve the understanding of the trapping and diffusion of helium in lunar minerals, especially ilmenite. This understanding will 1) allow more accurate estimates of lunar ^{3}He inventory using lunar samples and newly acquired elemental maps of the lunar surface, 2) assist the design of crewed or automated lunar miners and material processors, 3) help develop greater understanding of lunar regolith dynamics, and 4) provide greater understanding of the radiation history of the moon and evolution of the sun.

Why Lunar ^{3}Helium?

1.1 *The Need for ^{3}Helium*

In thermonuclear research, reactions involving deuterium and ^{3}He -- (D + ^{3}He) and (^{3}He + ^{3}He) -- are well-known to generate few or no neutrons. This property makes the use of these fuels desirable to greatly reduce radiation damage and improve safety-related design features of fusion reactors. These reactors will also reduce the amount of radioactive waste storage facilities needed [Kulcinski et al., 1991].

The lack of large sources of terrestrial ^{3}He has hindered the development of fusion reactors that utilize these reactions [Kulcinski et al., 1988]. Tens of tonnes of ^{3}He per year will be needed to provide a significant fraction of the world's energy needs. While several thousand tonnes of ^{3}He had been identified in terrestrial reserves, only about 25 kg/yr of ^{3}He can currently be recovered from these sources by the year 2000 [Wittenberg, 1989].

It has long been known that the solar wind implants helium isotopes in the lunar regolith and rocks [Eberhardt et al., 1970; Funkhouser, et. al.; 1970; Heymann, and Yaniv, 1970; Hintenberger et al., 1970; Hohenberg et al., 1970; Kirsten et al., 1970; Marti, et. al. 1970; Pepin et al., 1970]. Upon reanalyzing results of noble gas studies performed on the Apollo samples, scientists at the University of Wisconsin-Madison realized that there is a

large supply (~one million tonnes) of ^{3}He in the upper 3 meters of the lunar regolith [Wittenberg et al., 1986; Kulcinski and Schmitt, 1987]. They concluded that the Moon was the only reasonably accessible location to obtain the needed quantities of this valuable isotope.

1.2 Lunar Helium

Light elements and noble gases have been deposited in the lunar regolith by the solar wind since the beginning of the solar system 4.5 billion years ago. The reason for this implantation is the lack of a global lunar magnetic field and the lack of an atmosphere on the Moon. The solar wind contains about 5% helium with ^{4}He/^{3}He $\approx$ 2000 [Geiss, 1973]. The particles in the solar wind have energies that average about 1 keV/amu. Even particles in the high energy tail of the solar wind distribution do not penetrate beyond 0.5 μm into the lunar surface. "Gardening" of the lunar surface by meteorite impacts has resulted in large amounts of solar wind gases being trapped in the regolith to depths on the order of meters [Criswell, 1975; Bogard and Hirsch, 1976]. It has been estimated that over 250 million tonnes of ^{3}He have bombarded the Moon since its creation [Kulcinski et al., 1988].

Various processes have caused some of the incident solar wind gases to be lost from the lunar regolith. Analysis of the Apollo and Luna samples have shown that some lunar soils contain helium concentrations up to 50 wppm [Cameron, 1988]. The Moon's current ^{3}He inventory has been estimated at over 1,000,000 tonnes -- more than enough to supply the world's energy needs for centuries [Kulcinski et al., 1988].

Information concerning the diffusion and trapping of helium isotopes in the lunar regolith is desirable for several reasons:

1) A more accurate determination of the locations of high concentrations of He using elemental correlations and recently collected remote sensing data from the Moon can be made.
2) It will allow fine-tuning of He extraction processes to be utilized in lunar mining devices.

3) It will develop greater understanding of lunar regolith dynamics.

4) Greater understanding of the processes of the ancient sun can be obtained.

1.2.1 Location of He Resources

The most important piece of information needed to select an initial mining site is the location of the richest ore. For centuries, miners have sought the choicest "claims." Mining the Moon for ^{3}He will be no different. Ideally, a three-dimensional map of ^{3}He concentration as a function of longitude, lattitude and depth is required. This map is virtually impossible to generate using current technology. One possible method to directly measure the ^{3}He present has been described by Harris, et. al. [1994].

The Apollo and Luna samples have provided us with a very limited view of the ^{3}He resources of the Moon. Cameron [1988] emphasizes that only minute fractions of a few maria have been sampled. However, the samples returned and analyzed have shown an empirical trend indicating that high-titanium regoliths are also high in helium -- and thus, high in ^{3}He [Cameron, 1988; Fegley and Swindle, 1993]. Highly mature soils (those exposed to the solar wind on the lunar surface for a long time) are also shown to contain large amounts of helium [Taylor, 1990]. These trends can be general guides in the selection of favorable areas for mining. Understanding of the He diffusion and trapping properties of the minerals involved will help refine these guides. For instance, if magnesian ilmenite ($Mg_xFe_{1-x}TiO_3$) is found to retain He better than stoichiometric ilmenite ($FeTiO_3$), remote sensing data for Mg could be considered in addition to Ti and maturity data as has been the recent practice [Cameron, 1988; Swindle et al., 1990]. It appears that no relationships other than the Ti and maturity correlations have been found to date to locate high He concentration on the Moon. These trends will be discussed in more detail in Section 2.2.

In addition to the correlection of helium with high-titanium regoliths, the diffusion and trapping properties of these minerals will help to calculate estimates of helium inventory at the lunar poles. Research is currently underway at the Fusion Technology Institute at University

of Wisconsin to develop a new calculation of solar wind flux on all parts of the lunar surface based on the recent observations of spacecraft such as Ulyseses and SOHO.

1.2.2 Helium Extraction

Knowledge of the trapping mechanisms and diffusion characteristics of helium within the minerals of the lunar regolith will enable the optimization of the parameters used to extract solar wind gases from regolith particles. These parameters include the temperature and time of extraction, particle size, and gas yield [Kulcinski et al., 1988]. Such knowledge may increase the efficiency of the process and increase the profitability of a mining venture.

1.2.3 Regolith Dynamics

A large number of lunar samples have been studied with respect to the evolution of the regolith and the processes that affect its geologic, petrographic and chemical composition [Gault et al., 1974]. Regolith dynamics have been investigated using micrometeoroid fluxes, cosmic-ray track densities, noble gas concentrations and distributions, distributions of other volatile species, fraction of agglutinates produced by impacts and grain size of regolith particles. The system is so complex that most studies have focused only on a single aspect or mechanism related to the formation and mixing of the regolith. The diffusion characteristics of helium in the minerals involved will help reduce this complexity.

1.2.4 Astrophysics

The trapping and diffusion properties of helium in lunar minerals also has implications with respect to astrophysical observations. Changes in the physical mechanisms operating in the Sun during its lifetime have been extensively studied through long-term variations in elemental and isotopic ratios of solar wind gases trapped in the lunar regolith and gas-rich meteorites [Frick et al., 1988]. Knowledge of the trapping characteristics of the lunar minerals will enable a more accurate determination of the origin of gas particles embedded in the regolith -- such as solar wind, flare, cosmogenic, etc. -- which in turn, will enable a more accurate determination of the physical processes active in young stars.

Issues to Consider for Helium Trapping in Minerals

Previous studies concerning lunar helium have involved isochronal annealing [e.g. Pepin et al., 1970; Srinivassan et al., 1972; Futagami et al., 1993], stepwise etching [Signer et al., 1991] and the rare gas ion probe [Müller et al., 1976]. Each of these methods has produced useful information concerning the ratios of rare gas isotopes, gas release as a function of temperature and in the latter case, helium profiles as a function of depth. However, none of these studies have generated consistent values of the diffusivity or the activation energy of helium in ilmenite. Nor has the trapping mechanism been identified.

It has been postulated that either an amorphous coating, called a petina, or the radiation damage resistance of ilmenite is responsible for the relative enrichment of He in high-Ti regoliths. However, helium diffuses more quickly through an amorphous coating or damaged surface layer than through the crystal matrix [Frick et al., 1988]. Therefore, the diffusivity of He in crystalline ilmenite (volume diffusion) is thought to be the limiting factor.

The resistance of ilmenite to radiation damage has been investigated using 400 keV Xe^{2+} ions [Mitchell et al., 1996a,b]. Terrestrial ilmenite was shown to amorphize at temperatures between 173 and 473 K under relatively low ion fluences -- approximately $1x10^{15}$ ions/cm^2. Concurrent ion-electrons experiments demonstrated that electron bombardment significantly delayed amorphization.

The structure of a mineral may also contribute to its ability to retain noble gases. Ilmenite has the same crystal structure as hematite (Fe_2O_3), based on the hexagonal closest packing of the oxygen lattice with cations in octahedral positions between them. This configuration is less tightly packed than a face-centered cubic lattice such as that found in Fe-Ni alloys. Silicates, such as olivine, are significantly less tightly packed than ilmenite. The degree of packing may explain the observation of Wieler [1995] on helium retentivity: Fe-Ni > ilmenite > olivine-pyroxene > plagioclase. Further correlations between helium diffusion

and packing have been made by Boschmann-Käthler [1986] for U+Th/He dating of several minerals including hematite.

Two additional trapping mechanisms are explored in this dissertation. First, the concept that oxygen vacancies may be the majority point defect in ilmenite as they are in the end member, hematite (Fe_2O_3) [Dieckmann, 1993] is explained. These vacancies are the only type of defect large enough to contain helium atoms, and may provide the mechanism by which helium is trapped. Second, one-third of the cation sites in ilmenite are intrinsically vacant sites and may provide energetically favorable sites for helium as is shown for helium in corundum (Al_2O_3) which has the same crystal structure as ilmenite [Allen, 1991].

Approach Taken in this Research

3.1 Computational Approach

At first, a computational approach was taken to generating map of the spatial distribution of ^3He in the lunar regolith. Such a map is needed to locate the first cost-effective mining operations on the moon. The direct detection of prompt gamma-rays from ^3He in the lunar regolith was investigated computationally as precursor research to this dissertation [Harris et al., 1994]. Gamma-ray spectroscopy has been successfully used to map the abundances and distributions of major elements present in planetary regoliths. Preliminary research for this thesis also included the development of a computer model combining solar wind implantation with regolith dynamics and diffusion.

Since the computational approaches taken yielded less than satisfactory results, the three-dimensional ANNEAL code was developed for this research. This code calculates the diffusivity based on the fractional release of helium at each temperature step of isochronal annealing experiments and the depth profile of helium calculated using the program TRIM [Ziegler, 1996].

3.2 Experimental Approach

The early computational work showed that greater understanding of the trapping mechanisms of helium in minerals was needed. This experimental work for this thesis focuses on ilmenite ($FeTiO_3$) since lunar helium concentration has been empirically shown to be correlated with titanium content and ilmenite contains most of the lunar titanium [Cameron, 1988]. The first step in the research performed in this thesis was the identification of a suitable terrestrial analog of lunar ilmenite using electron probe microanalysis (EPMA). Solar wind exposed lunar ilmenite samples were then simulated using Plasma Source Ion Implantation (PSII) at the University of Wisconsin - Madison [Conrad et al., 1990]. The simulants were then studied using isochronal annealing in conjuction with mass spectroscopy, positron annihilation spectroscopy (PAS), transmission electron microscopy (TEM) and secondary electron microscopy (SEM).

Papers Published from this Dissertation

Harris-Kuhlman, K. R., and G. L. Kulcinski (1998) "Terrestrial Analogs for Lunar Ilmenite," *Proceedings of the Sixth International Conference on Engineering, Construction, and Operations in Space*, R. G. Galloway and S. Lokaj, eds., (American Society of Civil Engineers, Albuquerque, New Mexico, April 26-30), pp. 533-540.

Harris, K. R., H. Y. Khater, and G. L. Kulcinski (1994) "Remote Sensing of Astrofuel^{TM}," *Proceedings of the 4th International Conference on Engineering, Construction, and Operations in Space*, R.G. Galloway and S. Lokaj, eds., (American Society of Civil Engineers, Albuquerque, New Mexico) **1**, pp. 648-657.

Harris, K. R., H. Y. Khater, and G. L. Kulcinski (1993) "Remote Sensing of Lunar Helium-3," *Proceedings of the Second Wisconsin Symposium on Helium-3* J. F. Santarius, ed., (Fusion Technology Institute, University of Wisconsin, Madison, Wisconsin).

References

Allen, W. R. (1991) "Lattice Location of Ion Implanted ^{3}He in Sapphire," *Nuclear Instruments and Methods in Physics Research*, **B61**, pp. 325-336.

Bogard, D. D. and W. C. Hirsch (1976) "Noble Gases in 60009-60010 Drive Tube Samples: Trapped Gases and Irradiation History," *Seventh Lunar Science Conference, Houston*, (Texas, Pergamon Press) **1**, pp. 259-279.

Boschmann-Käthler, W. (1986) "Uranium and Helium in Ore Minerals and the Question of Their Dates," *Heidelberger Geowissenschaftliche Arbeiten* **4** (Ph.D. Thesis), 234 pages.

Cameron, E. N. (1988) "Helium Mining on the Moon: Site Selection and Evaluation." *The Second Conference on Lunar Bases and Space Activities of the 21st Century*, (Houston, Texas: Lunar and Planetary Institute), pp. 89-97.

Conrad, J. R., R. A. Dodd, S. Han, M. Madapura, J. Scheuer, K. Sridharan and F. J. Worzala (1990) *Journal of Vacuum Science Technology A*, **8**, p. 3146.

Criswell, D. R. (1975) "The Rosiwal Principle and the Regolithic Distributions of Solar-wind Elements," *Sixth Lunar Science Conference*, (Houston, Texas, Pergamnon Press) **2**, pp. 1967-1987.

Dieckmann, R. (1993) "Point Defects and Transport in Haematite ($Fe_2O_{3-\varepsilon}$)," *Philosophical Magazine, A* **68**(4), pp. 725-745.

Eberhardt, P., J. Geiss, H. Graf, N. Grogler, U. Krahenbuhl, H. Schwaller, J. Schwarzmuller and A. Stettler (1970) "Trapped Solar Wind Noble Gases, Exposure Age and K/Ar-age in Apollo 11 Lunar Fine Material," *Proceedings of the Apollo 11 Lunar Science Conference* **2**, pp. 1037-1070.

Fegley, B., Jr. and T. D. Swindle (1993) "Lunar Volatiles: Implications for Lunar Resource Utilization," *Resources of Near-Earth Space*, J. S. Lewis, M. S. Matthews, and M. L. Guerrieri, eds., (Tucson, Arizona: The University of Arizona Press) pp. 367-426.

Frick, U., R. H. Becker, and R. O. Pepin (1988) "Solar Wind Record in the Lunar Regolith: Nitrogen and Noble Gases," *Eighteenth Lunar and Planetary Science Conference*, G. Ryder, ed., (Cambridge: Cambridge University Press) pp. 87-120.

Funkhouser, J. G., O. A. Schaeffer, D. D. Bogard and J. Zahringer (1970) "Gas Analysis of the Lunar Surface," *Proceedings of the Apollo 11 Lunar Science Conference*, **2**, pp. 1111-1116.

Futagami, T., M. Ozima, S. Nagai, and Y. Aoki (1993) "Experiments on Thermal Release of Implanted Noble Gases in Lunar Soil Grains," *Geochimica et Cosmochimica Acta* **57**, pp. 3177-3194.

Gault, D. E., F. Horz, D. E. Brownlee, and J. B. Hartung (1974) "Mixing of the Lunar Regolith," Fifth Lunar Conference, Houston, Texas, Supplement 5, *Geochimica et Cosmochimica Acta*, pp. 2365-2386.

Geiss J. (1973) "Solar wind Composition and Implications about the History of the Solar System," *Papers Presented to the 13th International Cosmic Ray Conference*, (University of Denver, Denver, Colorado), 5, pp. 3375-3398.

Harris, K. R., H. Y. Khater, and G. L. Kulcinski (1994) "Remote Sensing of Astrofuel™," *Proceedings of the 4th International Conference on Engineering, Construction, and Operations in Space*, R.G. Galloway and S. Lokaj, eds., (American Society of Civil Engineers, Albuquerque, New Mexico) **1**, pp. 648-657.

Heymann, D. and A. Yaniv (1970) "Inert Gases in the Fines From the Sea of Tranquillity," *Proceedings of the Apollo 11 Lunar Science Conference*, **2**, pp. 1247-1259.

Hintenberger, H., H. W. Weber, H. Voshage, H. Wanke, F. Begemann and Wlotzka (1970) "Concentrations and Isotopic Abundances of the Rare Gases, Hydrogen and Nitrogen in Apollo 11 Lunar Matter," *Proceedings of the Apollo 11 Lunar Science Conference*, **2**, pp. 1269-1282.

Hohenberg, C. M., P. K. Davis, W. A. Kaiser, R. S. Lewis and J. H. Reynolds (1970) "Trapped and Cosmogenic Rare Gases From Stepwise Heating of Apollo 11 Samples," *Proceedings of the Apollo 11 Lunar Science Conference*, **2**, pp. 1283-1309.

Kirsten, T., O. Müller, F. Steinbrunn, and J. Zahringer (1970) "Study of Distribution and Variations of Rare Gases in Lunar Material by a Microprobe Technique," *Proceedings of the Apollo 11 Lunar Science Conference*, pp. 1331-1343.

Kulcinski, G. L. and H. H. Schmitt (1987) "The Moon: An Abundant Source of Clean and Safe Fusion Fuel for the 21st Century," *11th International Scientific Forum on Fueling the 21st Century*, (Moscow, USSR).

Kulcinski, G. L, E. N. Cameron, J. F. Santarius, I. N. Sviatoslavsky, L. J. Wittenberg, and H. H. Schmitt (1988) "Fusion Energy from the Moon for the 21st Century," *The Second Conference on Lunar Bases and Space Activities of the 21st Century*, (Houston, Texas: Lunar and Planetary Institute), pp. 459-74.

Kulcinski, G. L., G. A. Emmert, J. P. Blanchard, L. A. El-Guebaly, H. Y. Khater, C. W. Maynard, E. A. Mogahed, J. F. Santarius, M. E. Sawan, I. N. Sviatoslavsky (1991) "Apollo-L3, An Advanced Fuel Fusion Power Reactor Utilizing Direct and Thermal Energy Conversion," *Fusion Technology*, **19**, pp. 791-801.

Marti, K., G. W. Lugmair and H. C. Urey (1970) "Solar Wind Gases, Cosmic-ray Spallation Products and the Irradiation History of Apollo 11 Samples," *Proceedings of the Apollo 11 Lunar Science Conference* **2**, pp. 1357-1367.

Mitchell, J. N. (1996a) Personal communication, (July).

Mitchell, J. N., R. Devanathan, K. E. Sickafus, K. J. McClellan (1996b) "The Mineralogy of Radiation-resistant Ceramics and the Suitability fo Ilmenite-group Minearls for Fusion Reactor Applications," (abstract) Unpublished.

Müller, H. W., J. Jordan, S. Kalbitzer, J. Kiko and T. Kirsten (1976) "Rare Gas Ion Probe Analysis of Helium Profiles in Individual Lunar Soil Particles," *Seventh Lunar Science Conference*, (Houston, Texas), pp. 937-951.

Pepin, R. O., L. E. Nyquist, D. Phinney and D. C. Black (1970) "Rare Gases in Apollo 11 Lunar Material," *Proceedings of the Apollo 11 Lunar Science Conference*, **2**, pp. 1435-1454.

Signer, P., H. Baur, and R. Wieler (1991) "Closed System Stepped Etching; An Alternative to Stepped Heating." *Alfred O. Nier Symposium on Inorganic Mass Spectrometry*, (Durango, Colorado), D. J. Rokop, ed., pp. 181-202.

Srinivasan, B., E. W. Hennecke, D. E. Sinclair, and O. K. Manuel (1972) "A Comparison of Noble Gases Geleased From Lunar Fines (#15601,64) with Noble Gases in Meteorites and in the Earth," *Third Lunar Science Conference*, **2** (Houston, Texas), pp. 1927-1945.

Swindle, T. D., C. E. Glass, and M. M. Poulton (1990) *Mining lunar soils for ^3He*, Fusion Power Associates of Gaithersburg, Maryland and the Japanese Institute for Future Technology, TM-90/1.

Taylor, L. A. (1990) "Hydrogen, Helium and other Solar-Wind Components in Lunar Soil: Abundances and Predictions." *Proceedings of the 2rd International Conference on Engineering, Construction, and Operations in Space*, Albuquerque, New Mexico, S. W. Johnson and J. P. Wetzel, eds., (American Society of Civil Engineers), pp. 68-77.

Wieler, R. (1995) Personal communication.

Wittenberg, L. J., J. F. Santarius, and G. L. Kulcinski (1986) "Lunar source of ^3He for commercial fusion power," *Fusion Technology*, **10** (2, pt 1), pp. 167-78.

Wittenberg, L. J. (1989) "Terrestrial Sources of Helium-3 Fusion Fuel - A Trip to the Center of the Earth," *Fusion Technology*, **15**, pp. 1108-1113.

Ziegler, J. P.(1996) *SRIM Instruction Maual: The St opping and Range of Ions in Matter*, (Yorktown, New York: IBM - Research); based on Ziegler, J. P., J. P. Biersack and U. Littmark, *The Stopping and Range of Ions in Solids*, (New York: Pergamon Press, 1985).

Chapter 2 The Search for ^{3}Helium

2.1 Where Can ^{3}Helium be Found and How Did it Get There?

2.1.1 Terrestrial Sources of Helium

2.1.1.1 Natural ^{3}Helium

Helium, the second lightest element, easily escapes from the Earth's atmosphere due to its low mass. However, the terrestrial atmosphere currently contains 5.24 parts per million helium [Craig and Luption, 1981]. This helium concentration is a balance between the helium input from the Earth and the helium lost to space. Terrestrial helium comes from several sources: 1) primordial helium that has been trapped in the Earth's mantle, 2) helium produced by the decay of radioactive elements such as U and Th in the Earth's crust, 3) interplanetary dust particles that have been deposited in deep sea sediments [Takayanagi and Ozima, 1987] and 4) the decay of natural and man-made tritium. These helium reserves have various ratios of ^{3}He/^{4}He [Craig and Lupton, 1981]. Cosmic-ray bombardment of the Earth's atmosphere also produces ^{3}He and tritium in small, but equal proportions [Libby, 1946].

Primordial helium on the Earth has a ^{3}He/^{4}He ratio similar to that of chondritic meteorites, and its presence may be explained by the accretion of chondritic meteorites on the pre-formed core of the Earth which had already lost its own helium because of its high heat [Reynolds et al., 1978]. This mechanism can also explain the abundance of water on the Earth. The mass deposited by meteorites accounts for about 20-30% of the weight of the Earth and makes up the present crust and upper mantle [Dreibus and Wänke, 1984]. The primordial helium remains dissolved in the molten upper mantle and escapes by several mechanisms: 1) mid-ocean vents, 2) oceanic crust formation, and 3) "hot spots" and convergent plate boundaries such as Kilauea Volcano and Yellowstone Park [Craig and Lupton, 1981].

Radiogenic ^{4}He formed by the decay of U or Th ores serves to dilute the helium in the Earth's enviroment. However, the spontaneous decay of ^{235}U generates neutrons which react with ^{6}Li to produce tritium which decays to ^{3}He. This radiogenic helium from crustal minerals diffuses towards the surface until it either escapes or becomes trapped in cavities covered by dense rock. These gas reservoirs also trap methane (natural gas) and helium is a commercial by-product of natural gas wells.

Deep sea sediments are another source of ^{3}He believed to be of primordial origin. Interplanetary dust particles (IDPs) are constantly incident on the Earth's atmosphere and most are deposited in the oceans with only moderate heating. Flynn [1989] predicts that interplanetary dust particles of asteroidal origin are not heated above about 700°C. Experimentally, IDPs of asteroidal origin do not appear to be heated above about 600°C [Sanford and Bradley, 1989]. Consequently, these particles retain a substantial fraction of their original helium when they come to rest on the ocean floor. As the tectonic plate on which ocean floor resides recedes under an adjacent continental plate (the former plate is also known as a subduction plate) and into the mantle, the sediments are heated and the helium released. The helium must either escape through volcanoes along the subduction zone or diffuse upward through the crust until it either escapes to the atmosphere or is trapped in natural gas reservoirs. Wittenberg [1989] has calculated that IDPs have provided nearly 200 tonnes of ^{3}He to these sediments in the last 200 million years.

Wittenberg [1989, 1993] has estimated the total terrestrial inventory of natural ^{3}He, excluding sources such as diamonds and Li/U bearing rocks since the contributions from these sources are neglible. His results are shown in Table 2-1.

In addition, Wittenberg [1993] calculated the energy payback for recovering ^{3}He from terrestrial sources and subsequently burning it in a D-^{3}He fusion reactor. He found that the energy cost for the production of ^{3}He is 450 times greater than the energy produced in the

fusion reactor. This is obviously not economically feasible, so other sources of ^{3}He must be considered.

Table 2-1. Estimated Terrestrial Inventory of Natural ^{3}Helium [from Wittenberg, 1993].

	^{3}He (tonnes)			
	Proved	Probable	Possible	Speculative
Atmosphere	4000	---	---	---
Oceans	13	---	---	---
U.S. crustal natural gas	0.23	0.18	0.20	0.08
Subduction zone natural gas	0.03	---	1000	25,000
Mantle gas	---	---	---	10^6 to 10^7
Total	4×10^3	0.18	10^3	10^6 to 10^7

2.1.1.2 ^{3}Helium from Tritium

The decay of man-made tritium is another potential source of ^{3}He for fusion fuel. It has been estimated that in the year 2000 the United States Department of Energy inventory of ^{3}He will be 59 kg, and the ^{3}He inventory of the Former Soviet Union will be about 76 kg [Wilkes, 1993]. Tritium may also be recovered from the Canadian deuterium (CANDU) reactors. Wilkes [1993] has estimated that ^{3}He from the CANDU reactors will grow from 3.3 kg in the year 2000 to 39.4 kg in the year 2020. A single 1000 MW(e) fusion power plant will require 50 kg ^{3}He per year. This need would require ^{3}He to be continuously separated from 1 tonne of tritium [Wittenberg, 1993]. This mode of production is economically and environmentally unacceptable. The deuterium (D) - deuterium (D) fusion fuel cycle is another means by which ^{3}He can be produced [Chacon and Miley, 1996], but such a process brings us full-circle to the undesirable safety and environmental aspects of D-D and D-T fusion which is mitigated by D-^{3}He fusion.

2.1.2 The Sun: A ^{3}Helium Generator

The major source of helium in our solar system is the Sun. The Sun produces helium via the proton-proton fusion reaction chain (Figure 2-1) [e. g. Bonnet, 1981]. While ^{3}He is not the final product of this fusion process, it is present in all parts of the sun due to radiation pressure and convection. Helium produced in the core diffuses through the extremely hot interior, into the radiative zone where the gamma-rays produced in the proton-proton chain are moderated. The atoms then diffuse into the interface layer between the radiative zone and the convective zone. This layer where the fluid flow changes from diffusive to convective is now believed to be the source of a magnetic dynamo which generates the Sun's magnetic field. Once in the convective zone, the helium atoms rise to the surface in the fluid flow and become available to the Sun's corona. In the corona, the gases are superheated (a process which is not yet understood) and hydrogen and helium are completely ionized. The gasses become so hot that the Sun's gravity is not enough to retain them and they are blown off as the solar wind.

2.1.2.1 The Solar Wind

The solar wind results from the absence of a counterpressure on the solar corona which expands until its pressure matches that of the interstellar medium. As the gasses expand, they are accelerated by dynamic pressure. The properties of the solar wind -- as well as those of solar and galactic cosmic rays -- are briefly summarized in Table 2-2. The Solar Wind Composition experiment on the lunar surface showed that the solar ^{3}He/^{4}He ratio ranges from about 4.08 - 4.38 x 10^{-4} over a three-year period [Geiss, 1973].

2.1.2.2 Solar Flares

Solar flares are violent explosions which occur intermittently on the Sun in areas of high magnetic disturbance. Although the process by which they form can not yet be explained, they are thought to be manifestations of highly twisted magnetic field lines which suddenly become unstable, much like a disruption in a tokamak reactor. These flares are

extremely complex and unpredictable. Some flares release very high fluxes of energetic charged particles or solar cosmic rays (SCR) [Vaniman et al., 1991]. The properties of these SCR particles are summarized in Table 2-2. Large amounts of helium can be deposited in a very short amount of time, but since flares are infrequent events, the average total flux at the Earth's orbit is rather small.

Table 2-2. Properties of the major types of radiation incident on the Moon [After Vaniman et al., 1991]

Property	Solar Wind	Solar Cosmic Rays	Galactic Cosmic Rays
Energies	0.3- 3 keV/amu	~1 - >100 MeV/amu	~0.1 - >10 GeV/amu
Mean Energy	1 keV/nucleon	-	-
Flux (protons/cm^{2}sec)	3 x 10^8	0 - 10^6	2-4
H/He Ratio	~22	~60	~7

2.1.2.3 Galactic Cosmic Rays

Galactic cosmic rays (GCR) are yet another source of ^{3}He in the Solar System. These particles have a lower proton/alpha ratio and a much wider range of energies (Table 2-2). The flux of GCR's is very small compared to that of the solar wind.

2.1.3 The Moon: A ^{3}Helium Collector

Due to its lack of a global magnetic field and atmosphere, the Moon has served as a collector of the solar wind, SCRs and GCRs for 4.5 billion years. For this reason, the lunar regoliths returned by the Apollo missions were extensively studied for their concentrations of noble and other volatile elements [Haskin and Warren, 1991].

Regoliths from regions with high concentrations of TiO_2 were found to have enhanced concentrations of helium (Figure 2-2) [Cameron, 1988, Fegley and Swindle, 1993]. When these data are plotted as a function of TiO_2 contents multiplied by the maturity

factor, I_s/FeO, an even stronger correlation results (Figure 2-3). The factor, I_s/FeO, is determined from the intensity, I_s, of the ferromagnetic resonance (FMR) spectra of the samples due to fine-grained native-iron, Fe^o, normalized to the total iron content, (FeO) [Taylor, 1990]. McKay et. al. [1974] suggested that this factor might be a measure of the quantity of agglutinitic glass in the lunar regolith and of the maturity. Maturity and titanium content taken together appears to be a better indication of helium content than either measure taken alone.

Since grain size was found to be inversely proportional to helium content (Figure 2-4) [Kirsten et al., 1970], the source of the helium was determined to be the solar wind. This relationship shows that the surface area is the determining factor for helium content. This is reasonable since the mean energy of the solar wind is about 1 keV/nucleon. Solar wind particles only penetrate to depths on the order of 10's of nanometers. Helium components from SCRs and GCRs penetrate up to meters into the regolith and would not be correlated with surface area.

It must be remembered that in almost all cases, helium and titanium concentrations are measured independently from subsamples of the returned material [Swindle, 1996]. Neutron activation analysis is typically used to determine major elemental abundances while the noble gases are extracted using annealing or etching. Both methods can not be used on one sample. As long as one has large enough samples of fine-grained material, performing analyses on adjacent subsamples is not a problem.

Despite all that is known about helium in the lunar regolith, the reason why high TiO_2 regoliths retain more helium has yet to be understood. Knowledge of the trapping mechanism(s) will greatly help in locating reserves of ^3He on the Moon, as well as aid in refining the extraction process.

2.2 Early Considerations of Direct Detection of Lunar ^{3}Helium

A map of the spatial distribution of ^{3}He in the lunar regolith is needed to locate the first cost-effective mining operations on the moon. While the concentration of TiO_2 in the regolith is a good guide to helium distribution [Cameron, 1988], the amount of solar-wind deposited helium also depends upon the maturity of the regolith. Thus, a direct method of detecting ^{3}He from lunar orbit is desired. One such method involves the production and detection of prompt gamma-rays from the neutron capture reaction involving the ^{3}He(n, γ)^{4}He reaction. Due to the complicated nature of the problem, only the production of these prompt gamma-rays will be discussed here. The detection of these gamma-rays is a subject for future research.

2.2.1 Production of Prompt Gamma-Rays From ^{3}He in the Lunar Regolith

2.2.1.1 Helium-3 - Neutron Capture Reaction

The direct detection of ^{3}He depends on the neutron capture reaction (Equation 2-1).

$$^3\text{He(n, }\gamma)^4\text{He} \qquad (2\text{-}1)$$

The flux of prompt gamma-rays yielded by this reaction depends on three quantities: 1) the flux of neutrons present, $\phi_n(E)$; 2) the neutron capture cross section of ^{3}He, $\sigma_{n,\gamma}(E)$; and 3) the concentration of ^{3}He atoms in the regolith, $N_{^3He}$ (Equation 2-2).

$$\frac{\text{Gamma} - \text{rays}}{\text{cm}^3 - \text{s}} = \sum \phi_n(E)\sigma_{n,\gamma}(E)N_{^3He} \qquad (2\text{-}2)$$

The quantities in Equation 2-2 are quite small: ϕ_n = 10 - 20 neutrons/cm^2-s for galactic cosmic-ray (GCR) induced thermal neutrons [Vaniman et al., 1991], $\sigma_{n,\gamma}$ = 0.03 mb at thermal energies [National Nuclear Data Center, 1993] and $N_{^3He} = 10^{16}$ atoms of ^{3}He per cm^3 in the lunar regolith. Since all of these values are relatively small, we are essentially "looking for a needle in a haystack." Fortunately, it is a different colored needle. The Q-value of this reaction is 20.6 MeV [National Nuclear Data Center, 1993]. The only other

neutron capture reactions capable of producing gamma-rays in this energy range are isotopes of the other low-Z elements which are more diffuse than ^{3}He in the lunar regolith. There should be very little competition from gamma-rays produced by other (n, γ) reactions at energies greater than about 20 MeV. The cross sections for the ^{3}He(n, γ)^{4}He reaction as well as two other possible neutron reactions involving ^{3}He and a neutron are shown in Figure 2-5. These data show that the probability of a prompt gamma-ray being produced is extremely small. Thus, the number of prompt 20.6 MeV gamma-rays available for remote detection is dependent only upon the flux of neutrons in the lunar regolith to the depth of a few attenuation lengths for the gamma-rays in the lunar regolith. The attenuation length of 20.6 MeV gamma-rays in the lunar regolith is 30.2 cm.

2.2.2 Possible Sources of Neutrons in the Lunar Regolith

The flux of prompt gamma-rays from ^{3}He in the lunar regolith is directly dependent on the number of neutrons available for capture. We have examined several possible sources of neutrons in the lunar regolith to determine if any might provide enough neutrons to make ^{3}He detectable. These sources include natural radioactivity from primordial and cosmogenic radioactive species, the solar wind, galactic cosmic-rays, solar flares and neutrons produced from neutral particle beams. Most of the neutrons in the regolith are the products of (p, n) reactions between higher-Z nuclei and incident protons with energies above about 30 MeV/nucleon.

The flux of neutrons in the regolith due to natural radioactivity and solar wind particles is negligible ($<<$ 1 neutron/cm^2-s) while GCR's induce approximately 10-20 neutrons/cm^2-s [National Nuclear Data Center, 1993]. Using this flux in Equation (1) results in a prompt gamma-ray flux of about 1.1×10^{-3} gamma-rays/m^2-hr. This flux is far too small to make remote detection feasible. Thus, very large solar proton flares (VLSPF's) were considered due to the large numbers of particles incident on the lunar surface during such

events. An orbiting neutral particle beam (NPB) was also considered as a possible means of artificially inducing neutrons in the lunar regolith. Calculation of the neutron flux induced by a VLSPF and a NPB are discussed below.

2.2.3 Neutron Source Characteristics

2.2.3.1 Very Large Solar Proton Flares (VLSPF's)

The ideal means of remotely detecting ^{3}He from lunar orbit would use naturally present neutrons reacting with the ^{3}He as discussed above. Since the GCR-induced flux of neutrons is thought to be too small to make detection currently feasible, another naturally occuring source was sought. Solar flares present a danger to astronauts living and working on the moon due to the large doses of proton-induced radiation. If the peak neutron flux created by flare protons -- via (p, n) reactions -- is large enough to overcome the background continuum, then a satellite could be placed in lunar orbit to wait for a large solar proton event.

Very large solar proton flares are relatively short and unpredictable. Only six VLSPF's have been recorded in the last three decades; three of these events occurred in 1989 alone. These events are predictable only in the sense that they tend to occur during the period leading to the maximum of the sun's 11-year sunspot cycle. These cycles vary greatly in amount of activity, and VLSPF's have also been known to occur after the maximum in the solar cycle. Very large solar proton flares are generally characterized by three bursts of high proton fluxes (Figure 2-6). These peaks vary greatly in duration, which is generally on the order of one day. The short duration of the peak flux would limit the surface coverage attainable by an orbiting detector.

The spectral properties of these flares are also highly unpredictable (Figure 2-7). The October 1989 solar flare was taken to be a typical VLSPF. The peak proton flux of this flare was about 10^5 protons/cm^2-s about 30 hours into the flare [Simonsen et al., 1991]. The omnidirectional integral fluence of protons with energies above 30 MeV contained in this event was 4.24×10^9 protons/cm^2 [Sauer, 1993]. The flare of February 1956 generated a

proton spectrum much harder than any of the other VLSPF's on record and lasted for only about 2 hours [Simonsen et al., 1991]. Since this flare was expected to generate more neutrons than any of the other VLSPF's, it was included in the current study as an upper limit to the neutron spectrum that could be produced.

2.2.3.2 Characteristics of A Neutral Particle Beam

A neutral particle beam (NPB) device was considered as an artificial means of introducing protons or higher-Z particles into the lunar regolith for the purpose of inducing high neutron fluxes, and in turn, high fluxes of 20.6 MeV gamma-rays from the neutron capture reaction of these neutrons with ^{3}He. Neutral particle beam devices have been developed for use in space for the interrogation of nuclear warheads, and many of their properties remain classified. We have considered a 100 MeV, 30 mA beam of protons and assumed an beam area of 10 cm^2 in the calculations and results described below. The advantages of using a NPB for the remote detection of ^{3}He are the control of the device energies and beam direction. Instead of waiting for an unpredictable event on the Sun, the neutrons could be induced at any time. By rastering the beam over the lunar surface and detecting the resulting gamma-rays from a separate satellite, high-resolution maps of lunar ^{3}He could be obtained.

2.2.4 Particle Interaction and Transport Calculations

The objective of this research is to calculate the flux of prompt gamma-rays coming from ^{3}He in the lunar regolith during a VLSPF or due to a NPB. A computational procedure that could model the production of neutrons via the interaction of incident protons with the regolith, transport the neutrons, model the (n,γ) reaction with ^{3}He and finally transport the resulting gamma-rays to the lunar surface was needed. Since a single computational model was unavailable, BRYNTRN [Wilson et al., 1989] was used to perform the charged particle interactions and generate the neutrons within the regolith. The computer code, ONEDANT

[O'Dell et al., 1982], was used to transport the resulting neutrons and generate the prompt gamma-ray flux (Figure 2-8). These codes are summarized in the following.

2.2.4.1 Charge Particle Interactions and Neutron Production: BRYNTRN

In order to utilize the neutron fluxes generated by the protons incident on the Moon during a solar flare, a numerical model capable of performing the interaction calculations is needed. Preferably, this model would include a data base of VLSPF events. The NASA-Langley Research Center has been heavily involved in developing numerical tools for the transport of baryons through shield materials based on a straight ahead approximation of the time-independent Boltzmann equation [Wilson et al., 1989]. The BRYNTRN code is self-contained, computationally efficient and requires only a fraction of the computer resources needed by a typical Monte Carlo code. The code also contains an input data base consisting of solar flare data taken by the GOES-7 satellite and obtained from the National Oceanic and Atmospheric Administration (NOAA). In the current study, BRYNTRN is also used to calculate the neutron flux induced in the lunar regolith by the February 1956 and October 1989 VLSPF's and by a 100 MeV, 3 mA/cm^2 neutral proton beam.

2.2.4.2 Neutron and Gamma-Ray Transport: ONEDANT

Once a neutron production spectrum has been calculated for a particular event using BRYNTRN, the neutrons must be transported through the lunar regolith, the local gamma-ray yield calculated and the gamma-rays transported to the surface of the regolith. The neutron and gamma-ray transport calculations are performed using the one-dimensional discrete ordinates neutral-particle transport code ONEDANT together with the Los Alamos National Laboratory (LANL) MATXS5 cross section data library processed from the ENDF/B-V evaluated files. The standard LANL 30 neutron, 12 gamma-ray energy group structure are used and the calculations are performed using the P_3-S_8 approximation. Since cross section data does not exist for neutrons above 20 MeV, all neutrons with higher energies were included in the highest energy group available. This approximation will result in an

underestimation of the gamma-ray flux since approximately 20% of the VLSPF-induced neutrons have energies higher than 20 MeV.

The gamma-ray flux was calculated for the top three meters of the lunar regolith using the peak neutron flux which occurs at 6.7 cm. This gamma-ray flux for VLSPF's can then be multiplied by the area of a detector in orbit around the moon to yield the number of counts per second that could be detected from a theoretical semi-infinte plane. Since the NPB is essentially a point source, the flux generated at the lunar surface must be divided by $4\pi r^2$ (where r is the detector's orbital distance from the lunar surface) before it is multiplied by the detector area.

2.2.5 Results

2.2.5.1 Neutrons Induced in the Lunar Regolith by Various Proton Sources

The total GCR-induced neutron production rate used was 16±5 neutrons/cm^2-s [Lingenfelter et al., 1972]. The neutron flux was calculated using BRYNTRN for each of the cases described above. This flux was then used as input for ONEDANT. At a depth of 6.7 cm (10 g/cm^2), the total neutron flux for the October 1989 flare was determined to be 2485 neutrons/cm^2-s. Figure 2-9 shows that the neutron flux (< 10 MeV) as a function of depth for the October 1989 flare is several orders of magnitude greater than the thermal neutron flux induced by galactic cosmic rays calculated by Lingenfelter et al., 1972. The local neutron flux induced by the NPB was calculated to be approximately 10^{16} neutrons/cm^2-s at a depth of 6.7 cm for a 100 MeV, 3 mA/cm^2 proton beam.

2.2.5.2 Gamma-Ray Fluxes from ^{3}He Resulting from Various Proton Sources

The GCR-induced gamma-ray flux was calculated using 16 neutrons/cm^2-s to be $4.2\text{x}10^{-3}$ gamma-rays/m^2-hr. The gamma-ray fluxes from ^{3}He were obtained by using the neutron fluxes calculated by BRYNTRN for the two VLSPF's and the NPB as input for ONEDANT. The VLSPF's of October 1989 and February 1956 yielded values of 0.85 and 8.8 gamma-rays/m^2-hr, respectively. The NPB yielded a flux of $5.5\text{x}10^9$ gamma-rays/m^2-hr

at the lunar surface. The increased gamma-ray flux due to VLSPF's and NPB's is seen to be significant compared to the background levels provided by GCR-induced reactions (Figure 2-10).

2.2.6 Conclusions

Very large solar flares can increase the $^3He(n, \gamma)^4He$ reaction rate by a factor of approximately 3000 over the background rate viewed from low lunar orbit generated by galactic cosmic-rays interacting with the lunar regolith via (p,n) reactions. This increased reaction rate will enhance the detectability of ^3He from low lunar orbit. A 100 MeV, 3 mA/cm^2 neutral particle beam has been shown to increase the local $^3He(n, \gamma)^4He$ reaction rate in the beam spot by a factor of approximately 10^{12} over the background rate due to incident GCR particles. The potential exists for high-resolution measurements of the spatial distribution of ^3He from lunar orbit using VLSPF's or optimized NPB's.

2.3 References

Bonnet, R.-M. (1981) "The Sun," *Larousse Astronomy*, M. R. Morris, ed. (Facts on File Publications, New York) pp. 81-112.

Cameron, E. N. (1988) "Helium Mining on the Moon: Site Selection and Evaluation," *The Second Conference on Lunar Bases and Space Activities of the 21st Century*, (Lunar and Planetary Institute, Houston, Texas) pp. 89-97.

Chacon, L. and G. H. Miley (1996) "IEC Breeder for D-3He Satellite Systems," *Fusion Technology*, **30**(3), pp. 1320-1325.

Craig, H. and J. E. Lupton (1981) "Helium-3 and Mantle Volatiles in the Ocean and the Oceanic Crust," *The Sea*, C. Emiliani, ed. (John Wiley & Sons, Inc, New York) **7**, pp. 391-428.

Dreibus, G. and H. Wänke (1984) "Accretion of the Earth and Inner Planets," in Proceedings of the 27th International Geological Congress, *Geochemistry and Cosmochemistry*, **11**, p. 1.

Eberhardt, P., J. Geiss, H. Graf, N. Grogler, U. Krahenbuhl, H. Schwaller, J. Schwarzmuller and A. Stettler (1970) "Trapped Solar Wind Noble Gases, Exposure Age and K/Ar-age in Apollo 11 Lunar Fine Material," *Proceedings of the Apollo 11 Lunar Science Conference*, **2**, pp. 1037-1070.

Fegley, B., Jr. and T. D. Swindle (1993) "Lunar Volatiles: Implications for Lunar Resource Utilization," *Resources of Near-Earth Space*, J. S. Lewis, M. S. Matthews, and M. L. Guerrieri, eds., (Tucson, Arizona: The University of Arizona Press) pp. 367-426.

Flynn, G. J. (1989) "Atmospheric Entry Heating: A Criterion to Distinguish Between Asteroidal and Cometary Sources of Interplanetary Dust," *Icarus*, **77**, pp. 287-310.

Funkhouser, J. G., O. A. Schaeffer, D. D. Bogard and J. Zahringer (1970) "Gas Analysis of the Lunar Surface," *Proceedings of the Apollo 11 Lunar Science Conference* **2**, pp. 1111-1116.

Geiss, J. (1973) "Solar Wind Composition and Implications About the History of the Solar System," *Thirteenth International Cosmic Ray Conference*, **5**, pp. 3375-3398.

Haskin, L. and P. Warren (1991) "Lunar Chemistry," *Lunar Sourcebook.*, G. Heiken, D. Vaniman and B. M. French, eds. (Cambridge, Cambridge University Press) pp. 357-476.

Heiken, G. H., D. T. Vaniman, and B. M. French, eds. (1991) *Lunar Sourcebook: A User's Guide to the Moon*, (Cambridge University Press, Cambridge).

Heymann, D. and A. Yaniv (1970) "Inert Gases in the Fines From the Sea of Tranquillity," *Proceedings of the Apollo 11 Lunar Science Conference*, **2**, pp. 1247-1259.

Hintenberger, H., H. W. Weber, H. Voshage, H. Wanke, F. Begemann and Wlotzka (1970) "Concentrations and Isotopic Abundances of the Rare Gases, Hydrogen and Nitrogen in Apollo 11 Lunar Matter," *Proceedings of the Apollo 11 Lunar Science Conference*, **2**, pp. 1269-1282.

Hohenberg, C. M., P. K. Davis, W. A. Kaiser, R. S. Lewis and J. H. Reynolds (1970) "Trapped and Cosmogenic Rare Gases From Stepwise Heating of Apollo 11 Samples," *Proceedings of the Apollo 11 Lunar Science Conference*, **2**, pp. 1283-1309.

Kirsten, T., O. Müller, F. Steinbrunn, and J. Zahringer (1970) "Study of Distribution and Variations of Rare Gases in Lunar Material by a Microprobe Technique," *Proceedings of the Apollo 11 Lunar Science Conference*, pp. 1331-1343.

Kulcinski, G. L. and H. H. Schmitt (1987) "The Moon: An Abundant Source of Clean and Safe Fusion Fuel for the 21st Century," *11th International Scientific Forum on Fueling the 21st Century*, (Moscow, USSR).

Kulcinski, G. L, E. N. Cameron, J. F. Santarius, I. N. Sviatoslavsky, L. J. Wittenberg, and H. H. Schmitt (1988) "Fusion Energy from the Moon for the 21st Century," *The Second Conference on Lunar Bases and Space Activities of the 21st Century*, (Houston, Texas: Lunar and Planetary Institute) pp. 459-74.

Kulcinski, G. L., G. A. Emmert, J. P. Blanchard, L. A. El-Guebaly, H. Y. Khater, C. W. Maynard, E. A. Mogahed, J. F. Santarius, M. E. Sawan, I. N. Sviatoslavsky (1991) "Apollo-L3, An Advanced Fuel Fusion Power Reactor Utilizing Direct and Thermal Energy Conversion," *Fusion Technology*, **19**, pp. 791-801.

Lingenfelter, R. E., E. H. Canfield, and V. E. Hampel (1972) "The Lunar Neutron Flux Revisited," Earth and Planetary Science Letters, Vol. 16, pp. 355-369.

McKay, D. S., R. M. Fruland, and G. T. Heiken (1974) "Grain Size and the Evolution of Lunar Soils," *Fifth Lunar Science Conference*, (Houston, Texas: Pergamon Press) pp. 887-906.

Marti, K., G. W. Lugmair and H. C. Urey (1970) "Solar Wind Gases, Cosmic-ray Spallation Products and the Irradiation History of Apollo 11 Samples," *Proceedings of the Apollo 11 Lunar Science Conference*, **2**, pp. 1357-1367.

O'Dell, R., et. al. (1982) "User's Manual for ONEDANT: A Code Package for One-Dimensional, Diffusion-Accelerated, Neutral Particle Transport," Los Alamos National Laboratory Report, LA-9184-M.

National Nuclear Data Center (1993) ENDF/B-VI Data Base.

Nealy, J. E., S. A. Striepe, and L. C. Simonsen (1992) "MIRACAL: A Mission Radiation Calculation Program for Analysis of Lunar and Interplanetary Missions," NASA TP-3211, p. 5.

Pepin, R. O., L. E. Nyquist, D. Phinney and D. C. Black (1970) "Rare Gases in Apollo 11 Lunar Material," *Proceedings of the Apollo 11 Lunar Science Conference*, **2**, pp. 1435-1454.

Reynolds, J. H., U. Frick, J. M. Neil and D. L. Phinney (1978) "Rare-gas-rich Separates from Carbonaceous Chondrites," *Geochimica et Cosmochimica Acta*, **42**, pp. 1775.

Sanford, S. A. and J. P. Bradley (1989) "Interplanetary Dust Particles Collected in the Stratosphere: Observations of Atmospheric Heating and Constraints on Their Interrelationships and Sources," *Icarus*, **82**, pp. 146-166.

Sauer, H. H. (1993) Personal communication, NOAA Space Environment Laboratory, (February 12).

Simonsen, L. C., J. E. Nealy, H. H. Sauer, and L. W. Townsend (1991) "Solar Flare Protection for Manned Lunar Missions: Analysis of the October 1989 Proton Flare Event," SAE Paper No. 911351, 21st International Conference on Environmental Systems, San Francisco, CA, 1991.

Swindle, T. (1996) Personal communication, (January 10).

Taylor, L. A. (1990) "Hydrogen, Helium and other Solar-Wind Components in Lunar Soil: Abundances and Predictions," *Proceedings of the 2rd International Conference on Engineering, Construction, and Operations in Space*, Albuquerque, New Mexico, S. W. Johnson and J. P. Wetzel, eds., (American Society of Civil Engineers) pp. 68-77.

Vaniman, D., R. Reedy, G. Heiken, G. Olhoeft and W. Mendell (1991) "The Lunar Environment," *Lunar Sourcebook.*, G. Heiken, D. Vaniman and B. M. French, eds. (Cambridge, Cambridge University Press) pp. 27-60.

Wilkes, W. R. (1993) "Potential ^{3}He Resources for D-^{3}He Fusion Development," *Second Wisconsin Symposium on 3He and Fusion Power*, (Wisconsin Center for Space Automation and Robotics, Madison, Wisconsin), pp. 179.

Wilson, J. W., L. W. Townsend, J. N. Nealy, S. Y. Chun, B. S. Hong, W. W. Buck, S. L. Lamkin, B. D. Ganapol, F. Khan, and F. A. Cucinotta (1989) "BRYNTRN: A Baryon Transport Model," NASA TP-2887.

Wittenberg, L. J., J. F. Santarius, and G. L. Kulcinski (1986) "Lunar source of ^{3}He for commercial fusion power." *Fusion Technology* **10** (2, pt 1), pp. 167-78.

Wittenberg, L. J. (1989) "Terrestrial Sources of Helium-3 Fusion Fuel - A Trip to the Center of the Earth," *Fusion Technology*, **15**, pp. 1108-1113.

Wittenberg, L. J. (1993) "Non-Lunar ^{3}He Resources," *Second Wisconsin Symposium on ^{3}He and Fusion Power*, (Wisconsin Center for Space Automation and Robotics, Madison, Wisconsin), pp. 179-191.

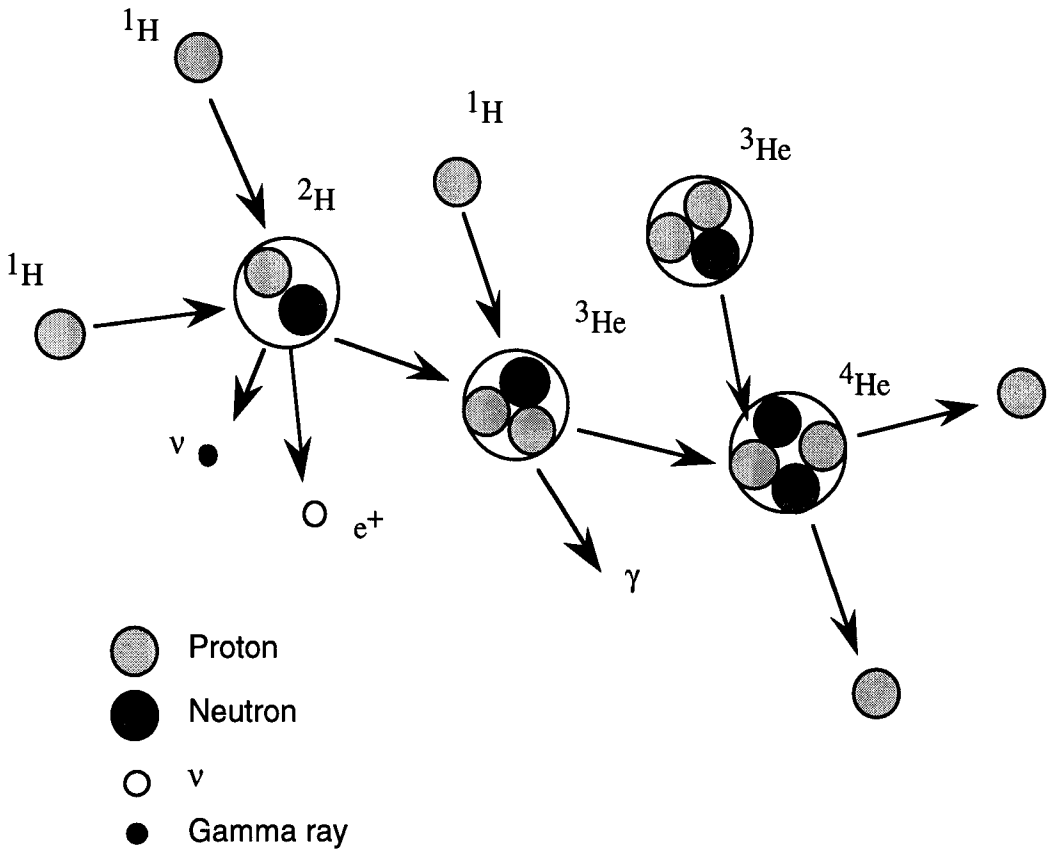

Figure 2-1. Solar ^{3}He production via the proton-proton fusion chain reaction.

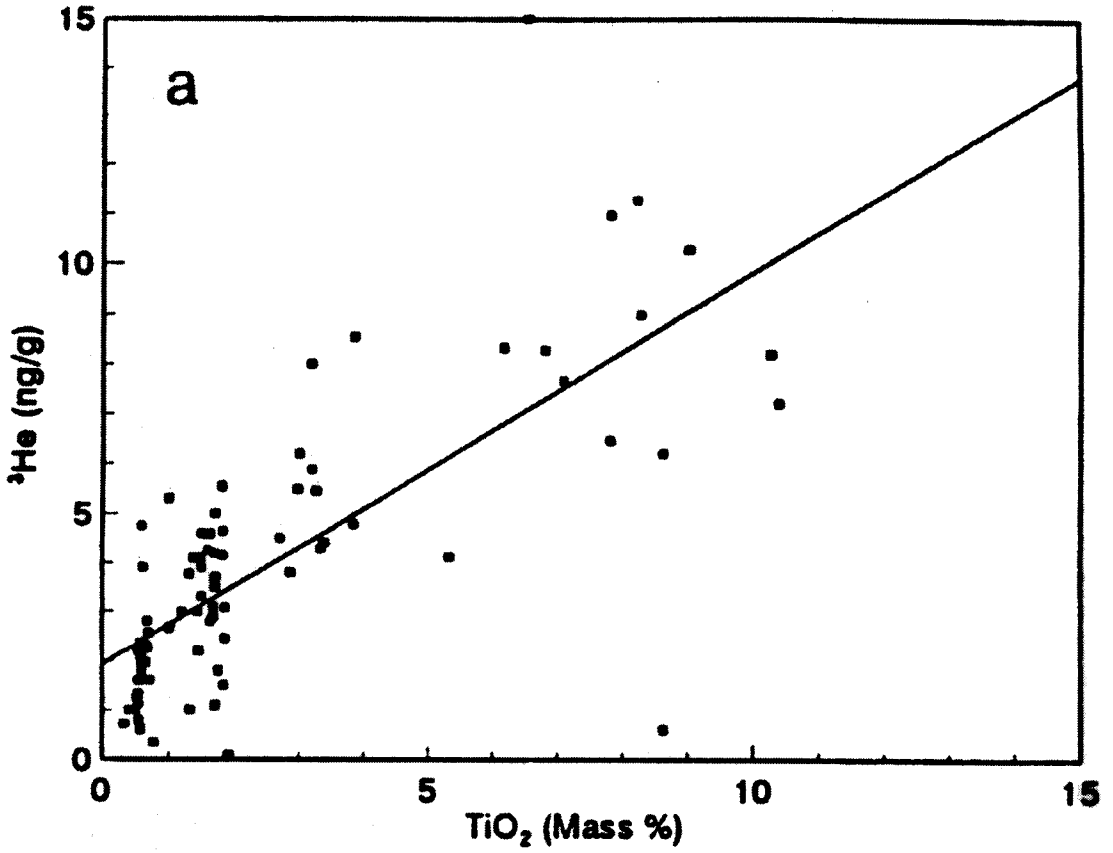

Figure 2-2. Relation between ^{3}He contents and TiO_2 contents of lunar regolith samples [From Fegley and Swindle, 1993].

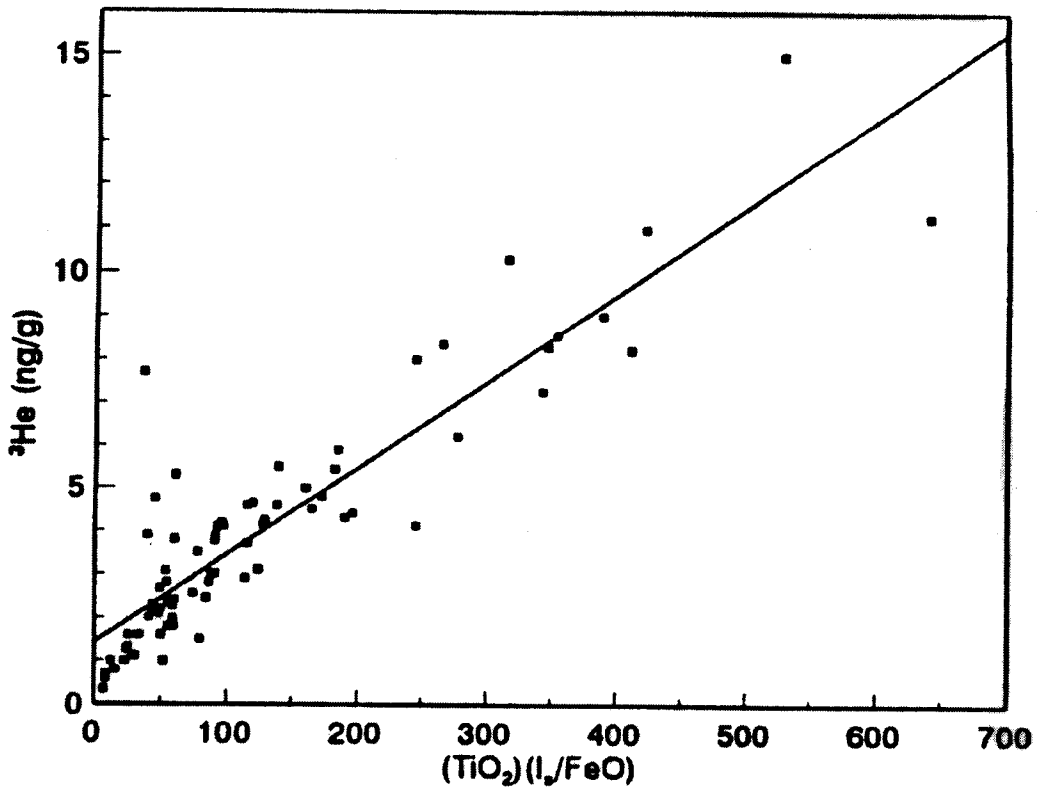

Figure 2-3. Relation between ^{3}He contents and TiO_2 contents of lunar regolith samples combined with maturity index, I_s/FeO [From Fegley and Swindle, 1993].

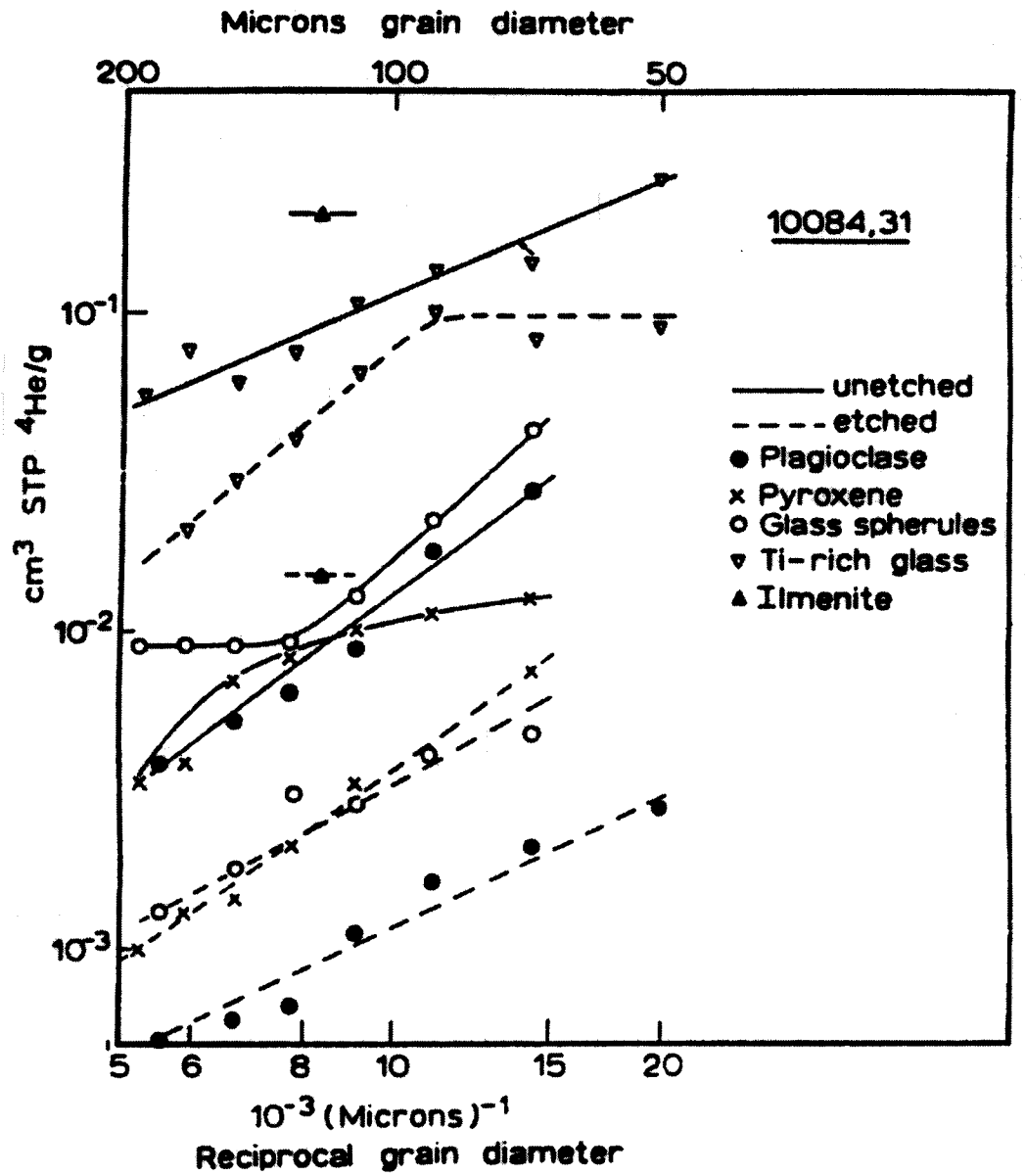

Figure 2-4. ^{3}He content of lunar soil sample 10084 as a function of grain-size [From Kirsten et al., 1970].

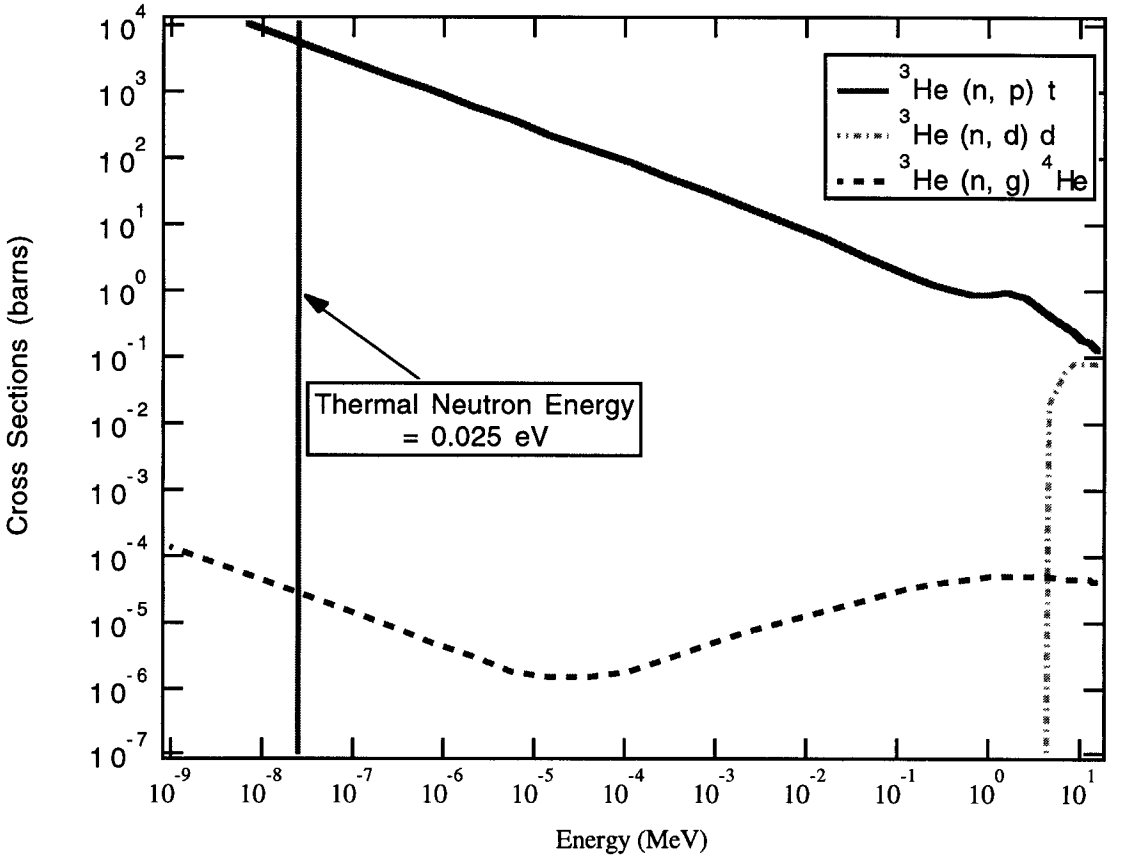

Figure 2-5. Possible ^{3}He - neutron interaction cross sections (National Nuclear Data Center, BROND-2 data base).

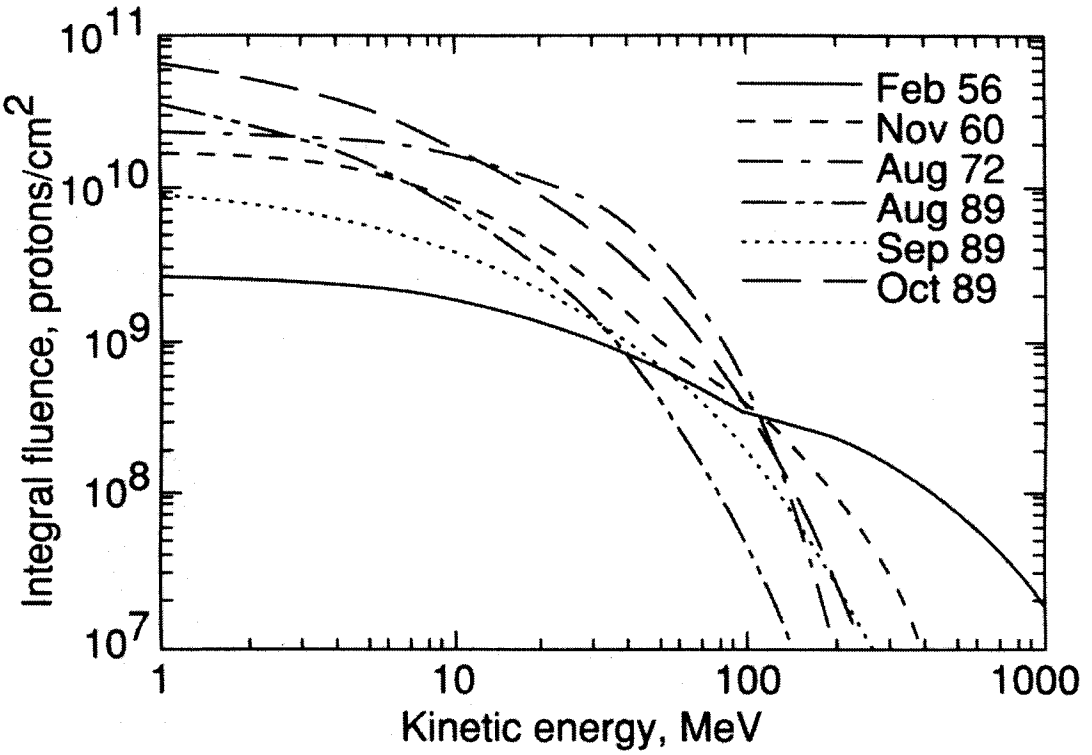

Figure 2-6. Integral fluence energy specta for six very large solar proton flares [Nealy et al., 1992].

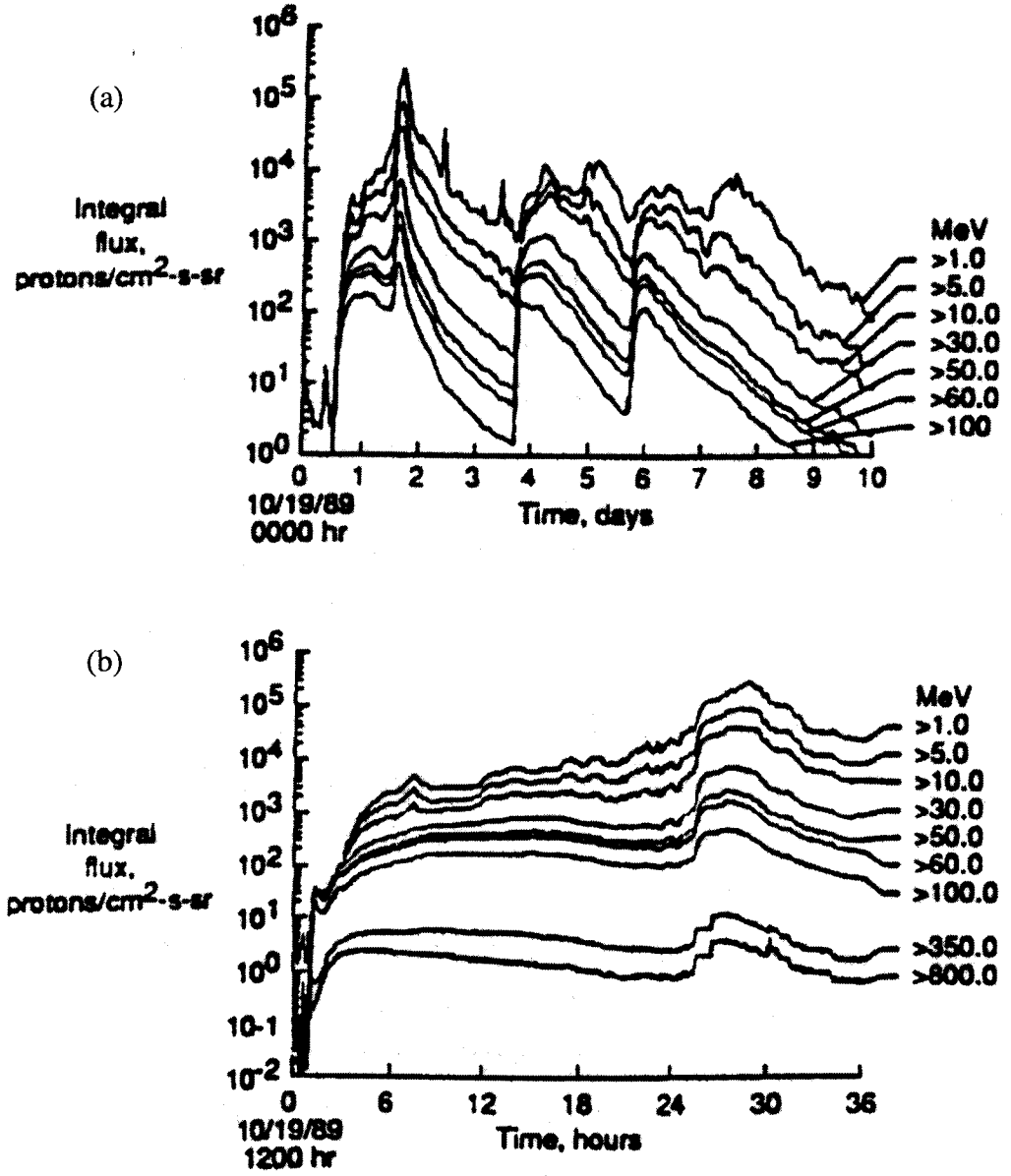

Figure 2-7. October 1989 VLSPF: (a) GOES-7 hourly average integral flux history and (b) GOES-7 five minute average integral flux history (GOES-7 data from NOAA Space Environment Laboratory) [Simonsen et al., 1991].

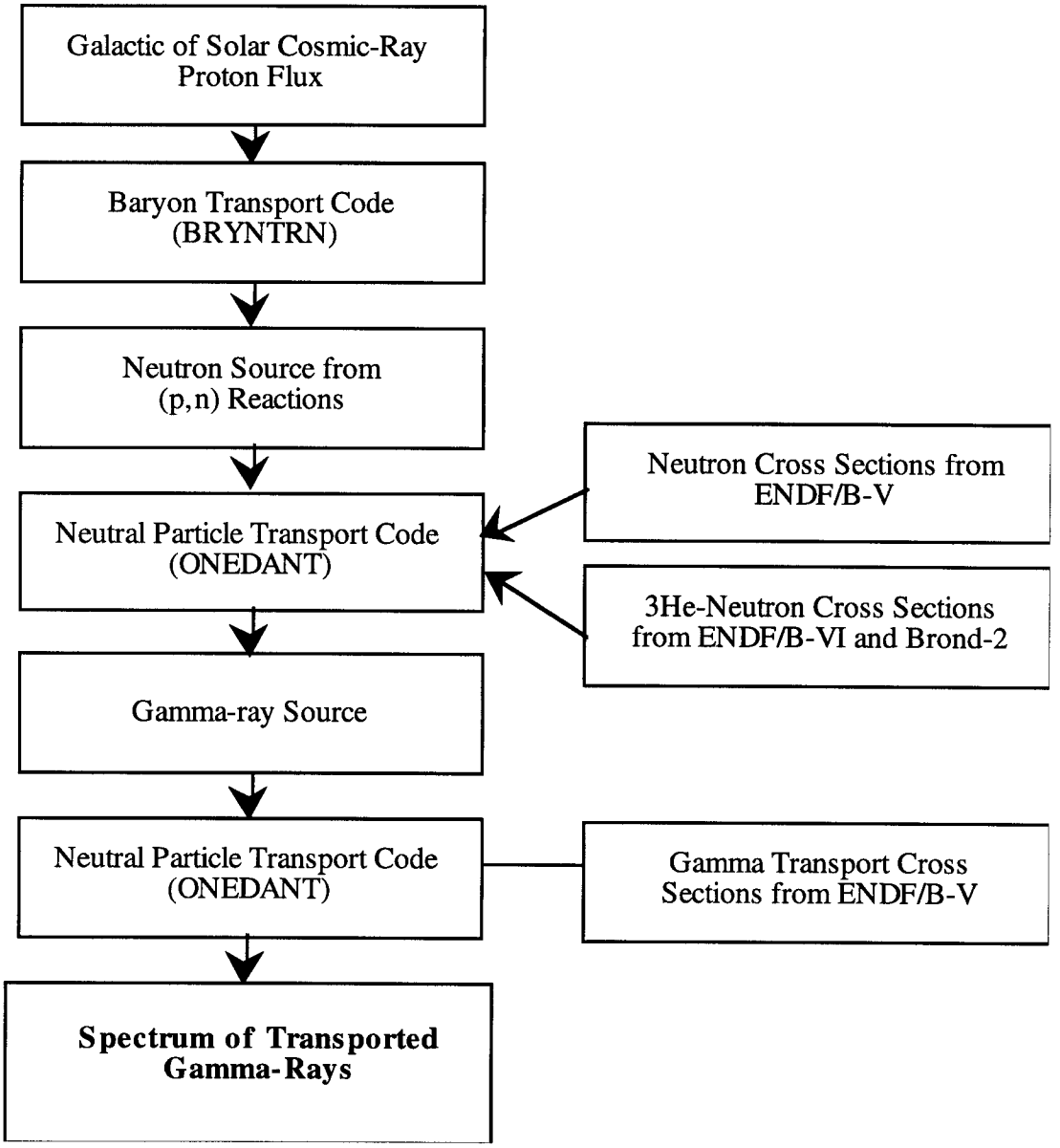

Figure 2-8. Flow chart of the computational method used in calculating the gamma-ray flux from ^{3}He due to an incident proton flux.

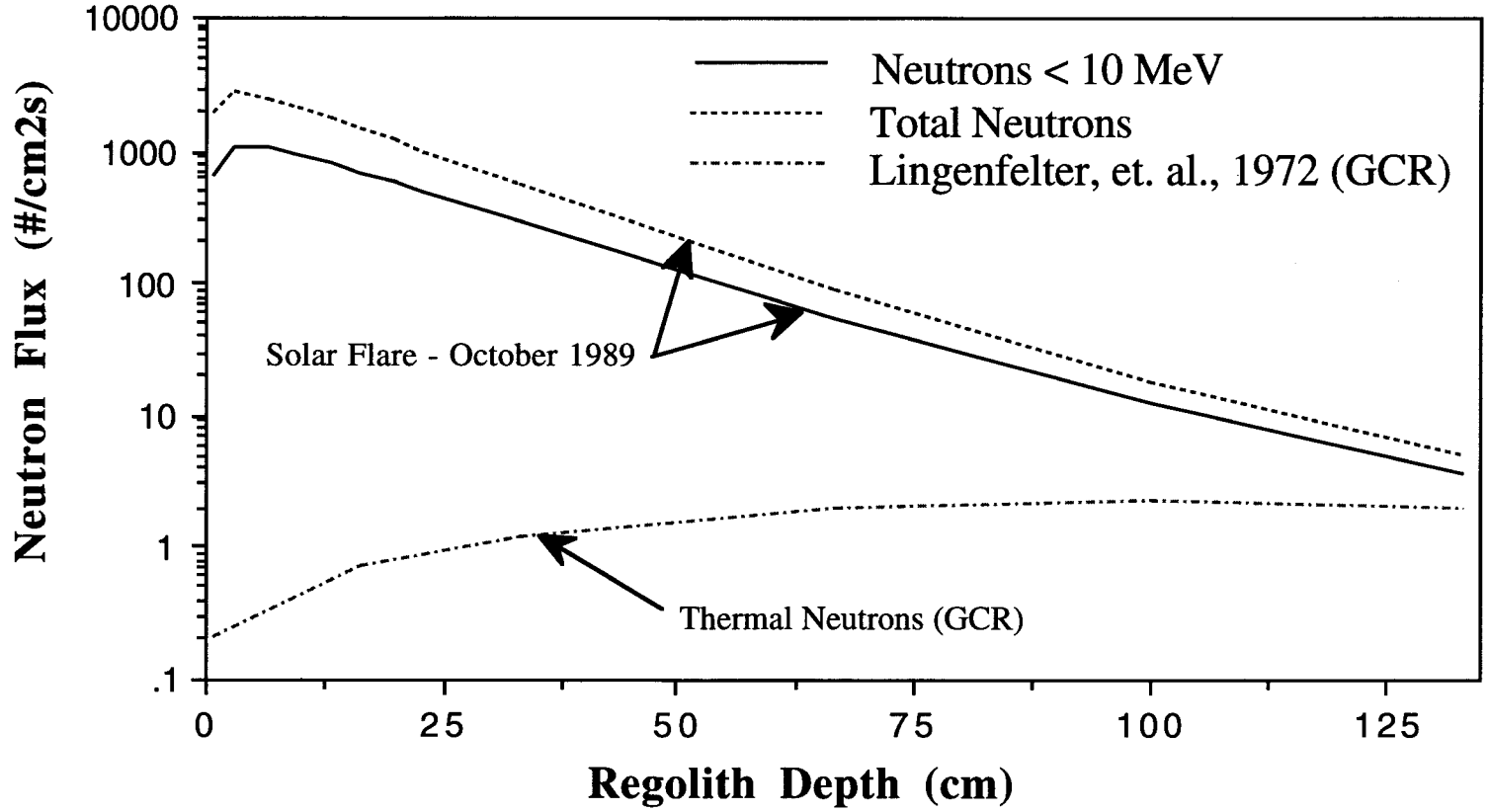

Figure 2-9. Neutron flux as a function of depth for the October 1989 VLSPF as calculated using BRYNTRN. The thermal neutron flux is that calculated by Lingenfelter et al. [1972].

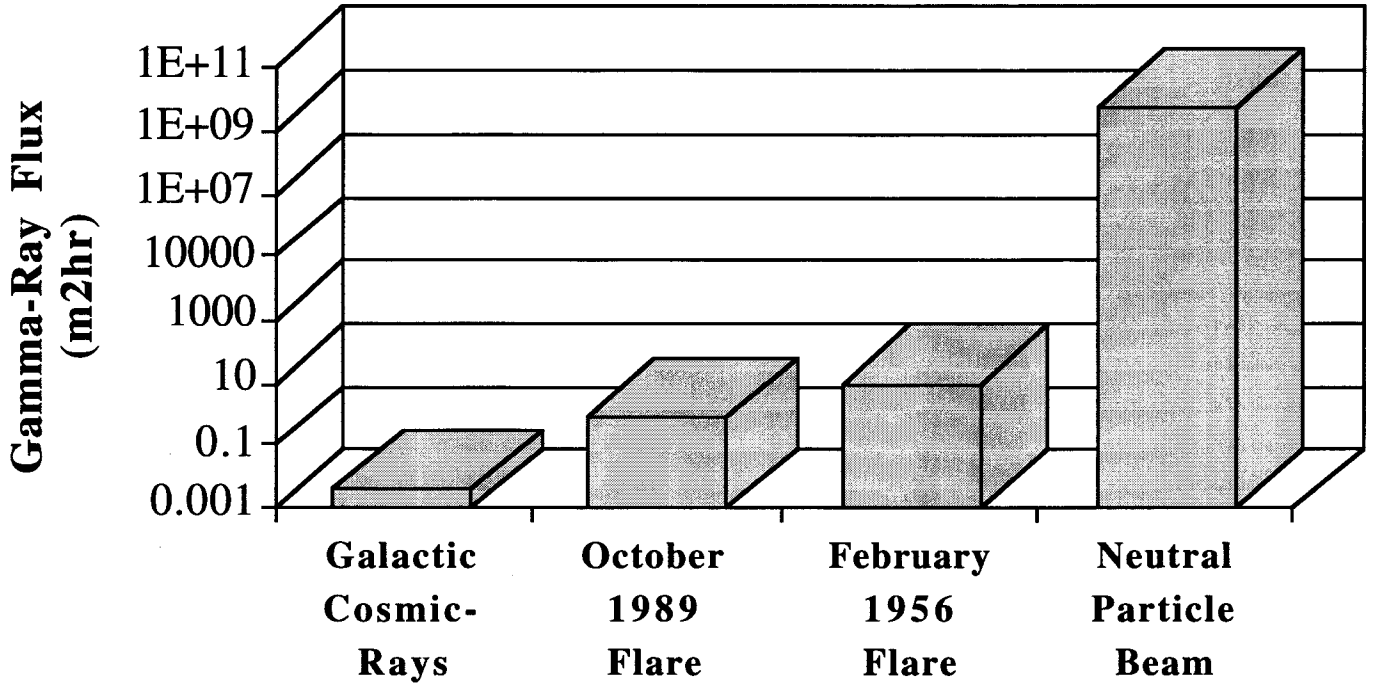

Figure 2-10. The 20.6 MeV gamma-ray flux at the Moon's surface from lunar ^{3}He calculated from various neutron sources. Note that the gamma-ray source from the NPB is a point source at the lunar surface.

Chapter 3 Retention and Release of Helium in Materials

3.1 Review of Diffusion and Annealing Equations

This section is devoted to a review of the diffusion equations and equations pertaining to first order annealing effects. This discussion will be followed by a review of the literature pertaining to the many issues that needed to be addressed in this doctoral research.

3.1.1 Diffusion Equations

Many studies of the diffusion of noble gases have been attempted using analytical solutions to Fick's second law of diffusion (Equation 3-1) [Crank, 1956]

$$\frac{\partial C}{\partial t} = D\nabla^2 C \qquad (3\text{-}1)$$

where C is the concentration (number/cm^3) and D is the diffusivity (cm^2/s) which is independent of the spatial variables. Some of these studies will be discussed later in this chapter.

The diffusivity exhibits Arrhenius behavior (Equation 3-2) with temperature where D_0 is the diffusion constant or coefficient, E_a is the activation energy of the defect, k_b is the Boltzmann constant and T is the temperature.

$$D = D_0 \exp\left[-\frac{E_a}{k_b T}\right] \qquad (3\text{-}2)$$

The diffusivity is seen to be very sensitive to both temperature and activation energy.

The diffusion of different isotopes of the same elements is also of importance in this research since we are interested in the diffusion of ^{3}He and ^{4}He. This isotope effect was defined by Schoen [1958] as Equation (3-3) where D_b/D_a is the ratio of the diffusion coefficients, m_a/m_b is the ratio of the atomic masses of the isotopes and E is a dimensionless proportionality constant.

$$E = \frac{\left[1 - \frac{D_b}{D_a}\right]}{\left[1 - \left(\frac{m_a}{m_b}\right)^{\frac{1}{2}}\right]} \tag{3-3}$$

3.1.2 Annealing of Irradiation Effects

Since lunar regolith and rocks are exposed to the solar wind, solar cosmic rays and galactic cosmic rays, it is useful to consider how lunar minerals respond to irradiation. The annealing of irradiation effects is also a means of analyzing these minerals. Annealing is defined as the "general processes of decay of property changes due to defects induced by temperature" [Kelly, 1966]. The description of annealing is similar to that of chemical kinetics and can be described by Equation 3-4 where P(t) is the property change remaining after time t at temperature T.

$$\frac{dP(t)}{dt} = -A[P(t)]^n \exp\left[-\frac{E}{k_b T}\right] \tag{3-4}$$

In Equation 3-4, k_b is Boltzmann's constant, A is a constant (for n = 1, A is a "frequency factor" with units of Hz), n is the "order of reaction," and E is the activation energy.

In the case of linear heating of the sample, the maximum annealing rate is given by

$$\frac{d^2P(t)}{dT^2} = 0 \tag{3-5}$$

Taking the derivative of Equation 3-4 and setting it equal to zero yields

$$n\left(\frac{dP}{dT}\right)_{\max} = -\frac{P_m E}{k_b T_m^2} \tag{3-6}$$

where the subscript, m, denotes the value at the point of maximum release per unit temperature (Figure 3-1) [Kelly, 1966]. This equation can then be solved for E, the activation energy of the defect.

3.1.3 What Diffusion Means for Lunar Helium

Since both diffusion and annealing processes are extremely sensitive to temperature variations, the ambient temperature becomes very important. The mean values of the extreme temperatures in the lunar regolith are 120 K (-153°C) at night and 380 K (107°C) during the day [Vaniman et al., 1991]. Temperature variations with depth have also been measured and depend greatly on the changing thermal conductivity and density of the regolith with depth [Langseth and Keihm, 1977]. At a depth of about 80 cm, temperature probes did not detect any perceptible variation during the monthly temperature cycle. At this depth, the temperature remains constant at about 252K ± 4 K.

These ambient lunar temperatures are quite low compared to the temperatures at which diffusion and annealing are normally studied, so extrapolation of "high" temperature results to low temperature environments is required. It is very desirable to make diffusivity measurements at the lowest temperatures feasible. The maximum temperature of the lunar regolith requires that one also consider the possibility of *in-situ* annealing of radiation damage during geologic timescales.

3.2 Ilmenite Mineralogy

3.2.1 Crystal Structure

The close-packed rhombohedral structure of ilmenite is less conducive to diffusion than a less tightly-packed structure such as that of olivine. Ilmenite is an "ordered version of hematite" where the alternating cation planes are occupied by Fe^{2+} and Ti^{4+} rather than Fe^{3+} (Figure 3-2) [Waychnuas, 1991]. In the *c* direction [0001], the cation stacking follows the pattern, $(\text{-Fe-Ti- -Fe-Ti- -})_n$ with a complete cell having six layers. The ordering of the

cation layers results in an adjustment of the oxygen lattice. The anions move away from the layers containing larger cations and towards the layers containing smaller cations.

Any mechanism that can change the degree of packing within the lattice can affect the diffusivity of helium through the lattice. Most lunar ilmenite contains some Mg substituting for Fe via the solid solution of ilmenite ($FeTiO_3$) with *geikeilite* ($MgTiO_3$) [Papike et al., 1991] Other elements are present in ilmenite only in trace amounts. The MgO content of ilmenite varies between 0.3 wt.% and 6.0 wt.%. The deviation from $FeTiO_3$ expressed in terms of weight percent MgO is shown in (Figure 3-3) [Papike et al., 1991]. The variation in Mg content of ilmenites may allow for volume changes within the lattice similar to that shown for olivine. Differing lattice volumes may in turn result in changes in the diffusion coefficients of light gas isotopes. Such dependences appear lacking in the literature [Frick et al., 1988]. In fact, few studies have been found concerning the diffusion of helium in minerals or oxides [Ducati et al., 1973; Hart, 1984; Jung, 1992; Jambon and Shelby, 1980; Trull et al., 1991]

Lunar chemistry is a significant factor in determining the amount of light solar gases present in the lunar regolith. The correlation between helium and titanium has been well documented, albeit not well understood (Chapter 2). Cameron [1988] plotted the titanium contents of regolith samples against the helium concentration in the lunar samples (Figure 3-4). The graph shows three clusters corresponding to the three principle groups of regolith: 1) very-high-titanium basalts (VHT) (8 wt. % < $Ti0_2$ < 14 wt.%), 2) low-titanium basalts (LT) (1.5 wt. % < $Ti0_2$ < 5 wt.%) and 3) very-low-titanium basalts (VLT) ($Ti0_2$ < 1.5 wt.%). Highland regolith samples exclusively lie in the VLT range while mare regolith samples show two distinct groups, one in the VHT range and the other in the LT range.

Various explanations have been given for this correlation. The titanium content of VHT lunar regoliths is closely associated with the mineral, ilmenite ($FeTiO_3$). Ilmenite is known to have a very tightly packed, rhombohedral lattice structure (Figure 3-5) [Papike et

al., 1991]. One method of determining the extent of packing within close-packed structures containing tetrahedrally and/or octahedrally coordinated cations is the symmetrical packing index (SPI) (Equation 3-7) [Zoltai and Stout, 1984].

$$SPI = \frac{\frac{4}{3}\pi R_a{}^3}{\frac{V}{ZA} - \left(\sqrt{\frac{1}{2}}\right)\left\{W^3 - 8R_a{}^3\right\}} \tag{3-7}$$

where

$$W = \frac{T\sqrt{\frac{8}{3}}\left(R_t + R_a\right) + M\sqrt{2}\left(R_m + R_a\right)}{T + M}. \tag{3-8}$$

In Equations 3-7 and 3-8, A is the number of anions per unit cell, T is the number of tetrahedral cations per unit cell times 4, M is the number of filled octahedra per unit cell times 6, Z is the number of chemical formula per unit cell, V is the volume of the unit cell, R_a is the anion radius, R_t and R_m are the ionic radii of the two cations. With these definitions, W is an effective radius and has the units of length. The values of SPI for the minerals in question are summarized in Table 3-1. The SPI for ilmenite is 78 [Zoltai and Stout, 1984]. The lattice structures of other lunar minerals such as olivine and pyroxene are not as tightly packed (Figure 3-6 and Figure 3-7). The SPI values for members of the olivine group range from 63 to 65 while the values for members of the pyroxene group vary from 66 to 74 [Zoltai and Stout, 1984]. One would expect that helium would diffuse more slowly through a tightly packed lattice than a loosely packed structure.

Another measure of the degree of packing of a mineral is its average specific gravity. The specific gravity is defined as "the ratio between the weight of a substance and the weight of an equal volume of water at 4°C." [Klein and Hurlbut, 1977]. As such, it is dimensionless. Density and average specific gravity are often used interchangably, but

density requires the citation of units, e.g. g/cm^3. The specific gravity of the minerals cited by Wieler [1995] are listed may explain his observation on helium retentivity (from highest to lowest): Fe-Ni > ilmenite > olivine-pyroxene > plagioclase.

Table 3-1. Summary of the symmetrical packing index (SPI) [Zoltai and Stout, 1984] and specific gravity of minerals under consideration [Klein and Hurlbut, 1977].

Mineral	Symmetrical Packing Index (dimensionless)	Specific Gravity (dimensionless)
Native (low) Iron (Fe)	68	7.3-7.9
Native Nickel (Ni)	N/A	8.9
Ilmenite ($FeTiO_3$)	78	4.7
Olivine ($(Mg,Fe)_2SiO_4$)	63 to 65	3.27-4.37
Pyroxene ($(Mg,Fe)SiO_3$)	66 to 74	3.2-3.6
Plagioclase ($NaAlSi_3O_8$ - $CaAl_2Si_2O_8$)	45 to 48	2.62-2.76
Corundum (Al_2O_3)	70	4.02

Both of these measures of packing within a lattice show that native Fe is the most tightly packed overall while ilmenite is the most tightly packed oxide. Gerling [1939] performed some of the earliest investigations of helium diffusion in minerals, and related his results to the packing fraction of the mineral. Some of his results are listed in Table 3-5.

3.2.2 Atomic Radii in Condensed Phases

The atomic volume of the atoms in the oxide lattice are an approximation to the volume of vacant lattice sites. The comparison of the atomic radii of the atoms in the lattice with the radius of a helium atom allows the elimination of open volume defects which are smaller than the implanted helium atoms from the list of possible trapping mechanisms. The effective ionic radii of the consituent atoms are dependent upon the chemical environment and

the coordination of the atoms [Shannon and Prewitt, 1969]. They are also dependent on the effect of covalence in specific metal-oxygen bonds [Shannon and Prewitt, 1969]. The effective ionic radius of an element in octahedral coordination in an oxide is shown in Table 3-2 for the cations in ilmenite [Shannon and Prewitt, 1969]. The effective ionic radius of an oxygen anion in a lattice is given in Table 3-3 along with the corresponding coordination number. It is easily seen that the radius of a bound oxygen atom only varies between 1.35 Å and 1.42 Å over the range of coordination numbers. An average value of 1.38 Å for the anion radius is generally used to calculate radius ratios often given in the literature [Shannon and Prewitt, 1969].

Table 3-2. Effective atomic radii in oxides for the cations in ilmenite [Shannon and Prewitt, 1969]. These values are calculated using an average oxygen anion radius of 1.38 Å and the "crystal radii" value for each cation reported by Shannon and Prewitt [1969].

Cation	Coordination Number	Effective Ionic Radii (Å)
Ti^{3+}	VI	0.92
Ti^{4+}	VI	0.83
Fe^{2+}	VI	1.01
Fe^{3+}	VI	0.87

The atomic radius of neutral helium dissolved in a condensed phase (silicate crystals/melts/glasses) has been calculated by Zhang and Xu [1994]. This data is "consistent with the ionic radii and hence should be useful in comparing the size of a noble gas atom and the size of a hole and of an ion in a crystal structure." The values of Zhang and Xu [1994] for the radius of a neutral helium atom in a condensed phase are given in Table 3-4. From the

atomic radii above, it is easily seen that neutral He atoms within the lattice will only fit into oxygen vaccancies.

Table 3-3. Anion radii of O^{2-} in oxides for different coordination numbers [Shannon and Prewitt, 1969].

CN	Anion Radius (Å)
II	1.35
III	1.36
IV	1.38
VI	1.40
VIII	1.42

Table 3-4. Atomic radii of He and Ne in condensed phases [Zhang and Xu, 1994].

	Atomic Radius (Å)	
CN	He	Ne
IV	0.91	1.18
VI	1.08	1.21
VIII	Not Given	1.32

3.2.3 Stoichiometry

The stoichiometry of lunar minerals may have a marked effect on their ability to retain light solar gases. For instance, Mokeyeva, et al. [1976] showed that volume changes in olivines take place exclusively as a result of changes in the interatomic distances M1-O and M2-O, while the Si-O distance remains virtually constant (Figure 3-6) [Mokeyeva et al., 1976]. This study used x-ray diffraction to accurately determine the Mg and Fe contents of

Table 3-5. Variation of activation energy for helium diffusion with packing fraction of several ore minerals considered by Käthler [1986] in the context of U+Th/He dating (After Gerling, 1939).

Mineral	Packing Fraction	Activation Energy (eV)
Magnetite (Fe_3O_4)	0.49	0.71
Sphalerite (ZnS)	0.56	0.81
Galena (PbS)	0.58	1.03
Pyrrhotite (Fe_7S_8 - FeS (troilite))	0.66	0.97
Hematite (Fe_2O_3)	0.70	1.25

both terrestrial and lunar olivines as well as their distribution between positions in the crystal structure. They concluded that these metal-oxygen distances increase as the iron content of the olivine increases. In another study on olivine, Buening and Buseck [1973] showed that changing the ambient oxygen fugacity from 10^{-14} atm to 10^{-12} atm at 1000°C resulted in an increase in the diffusivity of Mg and Fe in the c-direction by a factor of about 2.5. Similar lattice expansion may occur in ilmenite as iron or magnesium substitutes for titanium.

The Fe-Ti-O system is very complicated [D. H. Lindsley, 1991; R. W. Taylor, 1964]. This complexity is mainly due to the possible charge states for iron: 0, +2 and +3. As a result, the stability of these minerals is quite dependent on oxygen fugacity (f_{O_2}). The stability relations for several of the minerals in the Fe-Ti-O system have been well studied [Papike et al., 1991; L. A. Taylor et al., 1972]. Rutile and iron exsolve from ilmenite at room temperature and atmospheric pressure ($\log f_{O_2} = -0.68$). However, in experiments with pseudobrookite and ferropseudobrookite, Haggerty and Lindsley [1970] noted that even at 750°C they did not achieve equilibrium in three years. Lindsley states that the difficulty in characterizing the miscibility gap (necessary for intergrowths between hematite and ilmenite)

lies in the very slow reaction rates in the hematite-ilmenite system [Lindsley, 1991]. This observation has ramifications for the logistics of the current research as will be seen later.

3.2.4 Radiation Damage

Another explanation similar to the packing argument is that of radiation damage. Radiation damage causes the outer layers of the regolith particles to become amorphous. These amorphous layers lose the ability to retain gases [Cameron, 1988]. Due to its dense structure and relatively heavy atomic mass, ilmenite is more resistant to radiation damage than other lunar minerals [Ducati et al., 1973; Wieler, 1995]. Conversely, the resistance to radiation damage may allow correspondingly fewer trapping sites to develop.

Studies of hematite (Fe_2O_3) have shown that implanted Xe is released at lower temperatures for higher doses [Matzke, 1976]. Amorphization was seen to begin at fluences as low as $8x10^{10}$ Xe ions/cm^2. The resistance of ilmenite to radiation damage was investigated using 400 keV Xe^{2+} ions [Mitchell et al., 1996]. Ilmenite was shown to amorphize at temperatures between 173 and 473 K under ion fluxes of approximately $1x10^{15}$ ions/cm^2. Concurrent ion-electron experiments demonstrated that electron bombardment significantly delayed amorphization. Another study was conducted on ilmenite using 200 keV Ar^{2+} ions [Mitchell et al., 1997]. In this case, a fluence of $1x10^{15}$ ions/cm^2 produced an amorphous layer 150 nm thick. A comprehensive study of the rhombohedral oxides Al_2O_3, $FeTiO_3$, $MgTiO_3$ and $LiTO_3$ demonstrated that $MgTiO_3$ is consistently more radiation resistant than $FeTiO_3$ [Mitchell et al., 1998]. Since most lunar ilmenite has some Mg substituting for Fe as mentioned earlier, this result has implications for the siting of the first lunar mining operations. It may be possible to localize a mining site for helium by superimposing a map of lunar magnesium on a map of lunar titanium

It is also possible that the surfaces of lunar minerals are similar to naturally-occuring radioactive or "metamict" minerals. Metamict minerals are minerals that incorporated radioactive elements upon crystallization [Klein and Hurlbut, 1977]. As time goes on, the

radioactive elements decay, and the alpha and other particles emitted damage the crystalline structure. This is essentially the same process occuring on the lunar surface. Many metamict minerals such as zircon [Aines and Rossman, 1986] and titanite are known to have strong OH bands in the infrared spectum [Hawthorne et al., 1991] showing that $(OH)^-$ or H_2O has replaced O^{2-} in significant amounts. The hydrogen is assumed to diffuse into the damaged lattice. In the case of lunar minerals, the solar wind implants large amounts of hydrogen, creating more damage in the process. It has been postulated that this hydrogen could form $(OH)^-$ which could in turn stabilize the damage, reduce the cations and help to retain helium [Zeller et al., 1966]. No work has been done to test this thesis in ilmenite because ilmenite is an opaque mineral [Rossman, 1998]. The effect of hydrogen implantation on helium diffusivity will be discussed later in this thesis.

3.3 The Point Defect Structure of Hematite as an Analog to Ilmenite

Hematite can be considered a direct binary analog for the ternary mineral ilmenite since substitution of titanium atoms for one-half of the iron atoms in hematite results in ilmenite. Both of these minerals have rhombohedral structure with two-thirds occupation of the octahedral sites by metal cations within the main oxygen lattice. The lattice parameters of the two minerals are very similar with a = 5.04 Å and c = 13.76 Å in hematite [Klein and Hurlbut, 1977] and a = 5.08 Å and c = 14.09 Å in ilmenite [Pandey et al., 1996; Sunkara, 1995; Waychnuas, 1991]. The SPI of hematite is 71 versus 78 for ilmenite [Zoltai and Stout, 1984].

Iron oxides are well known to exhibit nonstoichiometry [Muan and Osborn, 1965]. As a result, these oxides show a variation of composition with oxygen partial pressure [Dieckmann, 1993]. Dieckmann [1993] has performed careful electrical conductivity and thermogravimetric measurements to determine the point defect structure and related transport

properties of the iron oxide, hematite (Fe_2O_3). Great care was taken to produce pure synthetic hematite.

The following point defect equilibria determine the formation of the different defect species possible in hematite [Dieckmann, 1983]:

(a) the formation of electronic point defects (where e' is a conduction electron and $h^{\bullet}$ is a hole):

$$0 \leftrightarrow e' + h^{\bullet}, \tag{3-9a}$$

(b) the formation of anion vaccancies (where $O^{2-}{}_{O2-}$ represents on oxygen atom on an oxygen lattice site, x stands for no charge, • stands for a positive charge, e' stands for a conduction electron, ' stands for a negative charge, and V_{O2-} is an oxygen vacancy):

$$\left(\begin{matrix} O^{2-} \\ O^{2-} \end{matrix}\right)^{x} \leftrightarrow 2e' + \left(V_{O^{2-}}\right)^{\bullet\bullet} + \frac{1}{2}O_2(gas), \tag{3-9b}$$

(c) the formation of oxygen interstitials (where V_I represents a vaccant interstitial position, and $O^{2-}{}_I$ is an oxygen atom in an interstitial position):

$$\frac{1}{2}O_2(gas) + \left(V_I\right)^{x} \leftrightarrow \left(O_I^{2-}\right)^{''} + 2h^{\bullet}, \tag{3-9c}$$

(d) the formation of cation vacancies (where V_{Fe3+} represents a vaccant cation position, and $Fe^{3+}{}_{Fe3+}$ is a cation in a cation position):

$$\left(\begin{matrix} Fe^{3+} \\ Fe^{3+} \end{matrix}\right)^{x} + \frac{3}{4}O_2(gas) \leftrightarrow 3h^{\bullet} + \left(V_{Fe^{3+}}\right)^{'''} + \frac{1}{2}Fe_2O_3, \tag{3-9d}$$

(e) the formation of iron interstitials (where $Fe^{3+}{}_I$ represents a cation in an interstital position):

$$\left(V_I\right)^{x} + \frac{1}{2}Fe_2O_3 \leftrightarrow \left(Fe_I^{3+}\right)^{\bullet\bullet\bullet} + 3e' + \frac{3}{4}O_2(gas). \tag{3-9e}$$

The electroneutrality condition given by Dieckmann [1993] is given in Equation 3-10.

$$[e'] + 2\left[\left(O_I^{2-}\right)''\right] + 3\left[\left(V_{Fe^{3+}}\right)'''\right] = \left[h^{\bullet}\right] + 2\left[\left(V_{O^{2-}}\right)^{\bullet\bullet}\right] + 3\left[\left(Fe_I^{3+}\right)^{\bullet\bullet\bullet}\right]. \quad (3\text{-}10)$$

Since he observed that the electrical conductivity of very pure $Fe_2O_{3-\varepsilon}$ is independent of oxygen activity, Dieckmann [1993] assumed the electroneutrality condition to be

$$[h\bullet] \approx [e']. \quad (3\text{-}11)$$

The oxygen activity is defined as $a_{O_2} = P_{O_2}/1$ bar. Dieckmann derived the following oxygen activity dependences based on the electroneutrality condition in Equation 3-11 (Equations 3-12):

$$\left[\left(V_{O^{2-}}\right)^{\bullet\bullet}\right] \propto a_{O_2}^{-1/2} \quad \text{(a)}$$

$$\left[\left(O_i^{2-}\right)''\right] \propto a_{O_2}^{1/2} \quad \text{(b)} \qquad (3\text{-}12)$$

$$\left[\left(V_{Fe^{3+}}\right)'''\right] \propto a_{O_2}^{3/4} \quad \text{(c)}$$

$$\left[\left(Fe_i^{3+}\right)^{\bullet\bullet\bullet}\right] \propto a_{O_2}^{-3/4} \quad \text{(d)}$$

If only one of these four possible kinds of defects is dominant, ε (the deviation from stoichiometry) will have an oxygen activity dependence characteristic of that particular defect. Since measured iron to oxygen ratios of hematite are always greater than 2/3, cation interstitials or oxygen vacancies are the best candidate for the dominant defect species. Upon fitting experimental data to the defect models discussed, Dieckmann [1993] observed an oxygen activity dependence of ε with a power of -1/2 (Figure 3-8). This value confirms that

oxygen vacancies are the dominant ionic defects between 1100°C and 1300°C since it has the dependence on oxygen activity of Equation 3-12a. The activity disorder for hematite can thus be described by Equation 3-13:

$$2Fe_{Fe}^{x} + O_{O}^{x} \leftrightarrow 2Fe_{Fe}^{'} + V_{O}^{\bullet\bullet} + \frac{1}{2}O_2(gas). \qquad (3\text{-}13)$$

An effective activation energy of 3.393 eV was derived for oxygen vacancy formation in hematite [Dieckmann, 1993]. Dieckmann [1996] has also observed that these oxygen vacancies store relatively large amounts of helium.

The observations of Dieckman [1993] can be extended to ilmenite which has the same crystal structure and similar composition. Under reducing conditions ($\log P_{O_2}$~-12 at)such as those found on the Moon [Taylor et al., 1972, Haggerty, 1978], the following reaction may occur by analogy [Cooper, 1998]:

$$2Ti_{Ti}^{x} + O_{O}^{x} \leftrightarrow 2Ti_{Ti}^{'} + V_{O}^{\bullet\bullet} + \frac{1}{2}O_2(gas), \qquad (3\text{-}13)$$

This mechanism could provide a large concentration of vacancies in lunar ilmenite in which helium could reside. Dieckmann [1996] has observed that the oxygen vacancies in hematite store relatively large amounts of helium.

3.4 Self-Diffusion in Related Ceramics and Minerals

The mobility of the atoms in the ilmenite lattice is of concern in the experiment described in this thesis since movement within the lattice could disguise the mechanism by which helium is trapped. The self-diffusion of iron, titanium and oxygen in ilmenite are not well known, but self-diffusivities have been measured for corundum (Al_2O_3), chromium (Cr_2O_3) and magnetite (Fe_3O_4). The values for the diffusivity of oxygen in these minerals are listed in Table 3-6 [Chiang et al., 1997; Giletti and Hess, 1988]. From this data, one can

see that oxygen is fairly immobile at 700°C in the corundum structure minerals, Al_2O_3 and Cr_2O_3, while it is diffuses somewhat more easily in Fe_3O_4.

Table 3-6. Diffusivity of oxygen in some oxide ceramics and minerals related to ilmenite by structure or composition [Chiang et al., 1997; Giletti and Hess, 1988].

Mineral or Ceramic	Diffusing Species	Diffusivity (cm^2/s) at 700 °C
Al_2O_3 (polycrystalline)	Al	$1x10^{-18}$
Al_2O_3 (polycrystalline)	O	$5x10^{-26}$
Cr_2O_3	Cr	$3x10^{-15}$
Cr_2O_3	O	$3x10^{-23}$
Fe_3O_4	O	$7x10^{-16}$

3.5 Helium Diffusion and Trapping

Isotopic ratios of helium ranging from $^4He/^3He \approx 1000$ to 3800 have been measured for lunar ilmenites [Becker and Pepin, 1989]. Comparison with the solar value of 480 mentioned earlier indicates the possibility of either a process operating which allows ^3He to diffuse more quickly than ^4He from the regolith or the ratio of these elements in the solar wind changing over time. Radioactive decay and spallation due to cosmic rays also contribute to the larger ratio of ^4He to ^3He in the lunar regolith. Studies concerning the isotopic fractionation of helium have been hindered by the low sensitivity of the methods used and the rapid rate at which helium diffuses. The matter is also complicated by the many factors affecting the ability of a material to retain implanted atoms.

Much of the data in the literature has been derived from isochronal annealing experiments and the subsequent analysis of the data using the methods of Fetzig and Kalbitzer [1966]. This method is valid for volume diffusion and assumes that the initial concentration is uniform throughout the specimen. However, it must be noted that this method is

inadaquate when considering diffusion in cases where the initial concentration is a strong function of depth as in the case of solar-wind implanted helium.

3.5.1 Helium Diffusion in Metals

Helium diffusion in metals has been studied for some time with respect to materials for nuclear applications. Stott [1978] suggests that small, light atoms like helium may have an affinity for low electron density regions of metals. He cites theoretical work done by Inglefield and Pendry [1976] which indicates that He in metals prefers to be located in vacancies or other low electron regions such as dislocations and voids. Their observations are supported by the experimental observation of He trapped in vacanies in W by Kornelson [1972].

In a discussion of point defect solute interactions, March [1976] cites additional theoretical work by Whitmore [1976] which indicates that He in Al and Mg will occupy a vacant octahedral site in these metals. Whitmore suggests that He diffusion in Mg is controlled by desorption of the He from a vaccancy followed by intersitial diffusion. The activation energy for diffusion is then the sum of the energy required for each process. Whitmore calculated this sum to be 1.65 eV for Mg and 5.56 eV for Al. Experimental measurements of He diffusion in these two metals yielded values of 1.57 ± 0.13 eV in Mg and 1.60 ± 0.07 eV in Al [Glyde and Mayne, 1965a; Glyde and Mayne, 1965b]. Since the calculated and measured activation energies for He diffusion in Al are so different, it appears that the vacancy desorption/interstitial diffusion mechanism does not operate in Al [Whitmore, 1976].

Self-diffusion in face-centered cubic (FCC) metals is of interest in the consideration of He diffusion in ilmenite and hematite. The latter two minerals are derivatives of the hexagonal close-packed (HCP) structure. Diffusion generally occurs by the same mechanism in HCP metals and FCC metals [Peterson, 1978]. Peterson [1978] also discusses self-diffusion in several FCC metals and concludes that the single vacancy mechanism dominates

with small contributions from the divacancy mechanism at temperatures near the melting point. He gives values of the activation energy for vacancy and divacancy diffusion in several FCC metals (Table 3-7). Heumann and Imm [1968] measured the activation energy for self-diffusion in γ-iron to be 2.95 eV between 1170°C and 1361°C. This measurement is consistent with vacancy diffusion, but allows for a significant divacancy contribution which is consistent with the temperatures used [Peterson, 1978].

Table 3-7. Activation energies of monovacanies and divacancies in some FCC metals [Peterson, 1978].

Metal	Activation Energy for Monovacancies (eV)	Activation Energy for Divacancies (eV)
Aluminum	1.28	1.59
Silver	1.76	2.19
Gold	1.76	2.37
Copper	2.07	2.59
Nickel	2.88	~3.7

Thermal desorption experiments were used by Sciani and Jung [1983] to measure the diffusion constants of helium in gold, silver and aluminum (Table 3-8). They also considered the activation energy of He in nickel measured by Philipps, et al. [1982]. These results were then compared to the values for vacancy diffusion in Table 3-7. This is justified by assuming the activation energy for a substitutional He atom behaving like a normal lattice atom is equal to the self-diffusion energy for the single vacancy mechanism [Peterson, 1978]. However, if the energy for vacancy formation is high, it may be more energetically favorable for the helium to jump out of a substitutional position (i.e. dissociate from the vacancy) and diffuse interstitially [Sciani and Jung, 1983]. The activation energies of helium in aluminum, silver

and gold agree with the values for self-diffusion indicating that the helium diffuses by the substitutional mechanism. Helium in nickel appears to diffuse interstitially [Sciani and Jung, 1983; Adams and Wolfer, 1988]. It should be noted that consistent values for aluminum and silver were only obtained at temperatures above $0.6T_m$, and the above statements rely heavily on the theoretical calculations used [Sciani and Jung, 1983].

Table 3-8. Activation energies and diffusion coefficients for He diffusion in some FCC metals [Sciani and Jung, 1983].

Metal	Diffusion Constant $\log_{10}D_0$ (cm^2/s))	Activation Energy (eV)
Aluminum	+0.1	1.35
Silver	-1.2	1.50
Gold	-1.0	1.70
Nickel	-2.2[a]	0.81[a]

[a]From Philipps et al., 1982.

Thomas et al., [1979] reported that in Ni and stainless steel only a small fraction of the total ^3He content was released at temperatures as high as 1000 K [Lässer, 1989]. This may indicate that He release is controlled by more than one mechanism which will result in a temperature dependence of the activation energy.

3.5.2 Helium Diffusion in Glasses

Helium diffusion in glass is of interest in the storage and measurement of tritium (through its decay to ^3He) in ocean water [Suckow et al., 1990], and in determining the inventory of He isotopes in the Earth's mantle [Kurz and Jenkins, 1981]. Suckow et al. [1990] measured the activation energies for diffusion of He in several glasses. The extremes of their data are summarized in Table 3-9 along with the measurement of Kurz and Jenkins

[1981] for oceanic basalt glasses and the measurement of Jambon and Shelby [1980] for obsidian. The values of activation energy for these glasses are significantly smaller than those obtained for metals (Table 3-8) and indicates that helium diffuses faster through amorphous materials than through crystalline materials.

Table 3-9. Results of He diffusion measurements on various types of glasses [Suckow et al., 1990; Kurz and Jenkins, 1981; Jambon and Shelby, 1980].

Material	Diffusion Constant $\log_{10}D_0$ (cm^2/s))	Activation Energy (eV)
Duran Glass	-3.15	0.29
Supremax	-2.74	0.59
Ocean Basalt Glass	-1.17	0.86
Obsidian	-5.87	0.37

3.5.3 Helium Diffusion in Ceramics and Minerals

3.5.3.1 Helium in Olivine

One of the first attempts to simulate the solar wind incident on lunar or meteoritic minerals was that of Lord [1968]. In his study, single crystals of naturally-occuring terrestrial olivine and samples of fine-grained terrestrial olivine were irradiated with H and He at solar wind energies and to fluences consistent with saturation. Irradiation of anisotropic minerals, with Xe from 0.5 to 40 keV, was found to cause metamictization (lattice disorder). Isotropic minerals generally appeared to be more resistant than anisotropic minerals to irradiation-induced disorder up to fluences of 2×10^{16} ions/cm^2. It was observed that the temperature at which helium is first released from olivine as well as the temperature of maximum release tended to increase with increasing helium dose [Lord, 1968]. Furthermore, hydrogen was released at a higher temperature than was helium. Lord points out the

suggestion of Brown and Davies [1963] that "the helium ions fill interstitial holes and that continued irradiation pushes the ions already in the lattice into deeper sites." Lord states that the bonding of hydrogen to oxygen ions in the lattice as suggested by Zeller, et al. [1966] may provide an effective barrier against ion penetration further into the lattice. Release of the hydrogen then requires enough energy to break the O-H bond as well as diffuse the atoms out [Lord, 1968]. Olivine was seen to reach saturation with He (1.8 keV) for fluences of about 6 x 10^{16} ions/cm^2 [Lord, 1968] The stoichiometry of olivine also seen to affect the retention of helium. The substitution of Fe for Mg noticeably reduced the helium retention of olivine [Lord, 1968].

A study of the diffusion of helium in olivine was performed by Hart [1984]. He obtained an activation energy of 5.21 eV and diffusion coefficient of 2.2 x 10^8 cm^2/s for naturally-occuring helium in a dunite xenolith (Table 3-10). An earlier review of cation diffusion in olivine had shown a large range of activation energies (1.26 eV to 5.69 eV) [Hart, 1981]. Hart suggests that the high activation energy of He in olivine may be due to a relationship between the He transport mechanism and vacancy diffusion. It should be noted that this work was performed in the temperature range 1180-1460°C -- temperatures characteristic of the Earth's mantle. Mechanisms of helium diffusion at low temperatures would not have been seen in this study.

Another study of helium in olivine -- and quartz -- was accomplished by Trull, et al. [1991]. This study was done on ^3He and at much lower temperatures (150 - 600°C) than that of Hart [1984]. Their results are summarized in Table 3-10. It appeared that cosmogenic ^3He (implanted or produced by a cosmic ray) and radiogenic ^4He diffused much faster than inherited ^3He (present upon mineral crystalization). It was thought that the diffusion of cosmogenic ^3He and radiogenic ^4He may be controlled by spallation-induced damage of the lattice [Trull, 1991].

Table 3-10. Results of cosmogenic ^3He diffusion measurements on olivine and quartz and radiogenic ^4He in quartz [Trull et al., 1991]. Also included is a diffusion measurement for inherited ^4He in olivine [Hart, 1984].

Mineral	Cation	Source	Diffusion Constant $\log_{10}D_0$ (cm^2/s))	Activation Energy (eV)
Olivine	^3He	Cosmogenic	-3.7	1.09
Quartz	^3He	Cosmogenic	0.2	1.09
Quartz	^4He	Radiogenic	-2.1	1.09
Olivine	^4He	Inherited	8.3	5.21

3.5.3.2 Helium in Corundum (α-Al_2O_3)

Corundum (α-Al_2O_3) has the same structure as hematite and ilmenite. Therefore, work done on the diffusion of helium in corundum has direct bearing on the current research. Theoretical calculations of helium migration and trapping have been reported by Welch, et al. [1976]. They have calculated the helium self-energy and migration energy using the polarizable point-ion shell model. The trapping energies of helium at oxygen and aluminum vacancies were also calculated. The results are given in Table 3-11. They report that all energies are relative to the value for the He self-energy, i.e. the energy needed to create a He interstitial [Welch et al., 1976]. The values given are only differences between the various states in which He can reside.

An experimental study of ion implanted ^3He in sapphire (corrundum) supports some of these calculations [Allen, 1991]. The structure of ilmenite, as we have seen earlier, is a hexagonal oxygen lattice with alternating layers of iron and titanium. Fully one-third of all the octahedral sites cation sites are intrinsically vacant (Figure 3-2). Allen [1991] and Allen and Zinkle [1992] implanted 200 keV ^3He into corrundum and used ion channeling angular

scans to identify the preferred locations of the ^{3}He atoms. Two mechanisms compete for trapping ^{3}He: 1) the vacant lattice sites (called holes, or constitutional vacancies in the literature) and 2) vacancies produced by the implantation process. The results of angular scans indicated that a typical ^{3}He atom prefers to be located in a position slightly displaced from the intrinsically vacant octahedral site. Axial channeling indicated that about 70% of the implanted ^{3}He occupied this type of site [Allen, 1991]. The capture of ^{3}He by a hole corresponds to the case of interstitial He migration which has an activation energy of 2.6 eV -- the most energetically favored situation [Allen, 1991]. Significant occupation of substitutional sites or tetrahedral interstices was not observed [Allen and Zinkle, 1992]. Bubbles were only observed at dislocation loops after implantation at 1073 K.

Table 3-11. Formation, trapping and migration energies for He in α-Al_2O_3 [From Welch et al., 1976].

Helium Defect	Energy (Relaxed Lattice Calculation) (eV)
(1) Formation energy of He interstitial	2.9
(2) Migration energy of He interstitial	2.6
(3) Trapping energy of He in oxygen vacancy relative to (1)	1.7
(4) Energy to move He from (3) to nearest interstitial position	1.7
(5) Trapping energy of He in interstitial position adjacent to Al vacancy relative to (1)	1.3
(6) Trapping energy of He in Al vacancy	1.1
(7) Energy barrier from (6) to (5)	0.3
(8) Trapping energy for second He at interstitial position, relative to (1) and (6)	1.1

Finally, the trapping of ^{3}He in titanium contaminated or implanted with oxygen has been investigated. Lewis [1987] implanted ^{3}He with an energy of 200 keV into heated titanium (up to 958 K) which contained oxygen in the surface layers or implanted oxygen. Peak ^{3}He concentrations reached a few tenths of an atomic percent. For temperatures well above 700 K, the He was seen to migrate to the oxygen rich layers and become trapped. The ^{3}He concentration profile was determined using nuclear reaction microanalysis. Lewis [1987] determined a consistent binding energy of 1.5 ± 0.2 eV relative to an effective bulk helium diffusion energy of 1.3 ± 0.2 eV using the concentration profile and a set of differential equations.

3.5.4 Study of Helium Diffusion in Minerals for U+Th/He Dating

The study of helium diffusion in minerals is important for the U+Th/He dating of crustal minerals containing radioactive isotopes [Boschmann-Käthler, 1986; Lippolt et al., 1994]. Boschmann-Käthler [1986] performed a series of helium retentivity experiments on ore minerals, including hematite. Some of his results are summarized in (Table 3-12). When these results are compared to the SPI and specific gravity of these minerals (Table 3-13), a correlation between helium retention and packing efficiency is not easily made.

3.5.5 Helium Diffusion in Lunar Materials

Many stepwise heating experiments were performed on the lunar samples returned by the Apollo missions [e.g. Hohenberg et al., 1970; Pepin et al., 1970; Srinivasan et al., 1972; Yaniv and Heymann, 1971; Frick et al., 1988]. These studies were instrumental in determining the qualitative helium retentivities of lunar minerals. Examples of the results of these studies for ^{4}He and ^{3}He are shown in Figure 3-9 and Figure 3-10.

Several diffusion studies were performed on lunar samples [e.g. Baur et al., 1972; Kirsten et al., 1972; Ducati et al., 1973; Frick et al., 1973]. These studies used analytical solutions of the diffusion equation (Equation 3-1) and made assumptions concerning the intial depth profile of the noble gases -- e.g. planar source, rectangular source, e^{-x}, etc [Frick et al.,

Table 3-12. Activation energies and diffusion coefficients for helium diffusion in some ore minerals as determined by Boschmann-Käthler [1986].

Mineral	Activation Energy (eV)	Diffusion Constant $\log_{10}D_0$ (cm^2/s)
Magnetite (Fe_3O_4)	0.61 - 0.82	-7.71 to -9.29
Pyrrhotite (Fe_7S_8 - FeS (troilite))	0.92 - 1.01	-2.56 to -3.15
Hematite (Fe_2O_3)	1.20 - 1.32	-4.74 to -5.71
Marcasite (FeS_2)	1.59	0.81
Apatite ($Ca_5(PO_4)_3$)	1.76†	4.22

†This value of the activation energy is in the upper range of average activation energies measured by Lippolt, et al. [1994] (0.67 eV to 2.03 eV) for apatite.

Table 3-13. Summary of the symmetrical packing index (SPI) [Zoltai and Stout, 1984] and specific gravity of minerals considered by Boschmann-Käthler [1986] [Klein and Hurlbut, 1977; Lippolt et al., 1994].

Mineral	Symmetrical Packing Index (dimensionless)	Specific Gravity (dimensionless)
Magnetite (Fe_3O_4)	73	5.18
Pyrrhotite (Fe_7S_8 - FeS (troilite))	N/A	4.58-4.65
Hematite (Fe_2O_3)	71	5.26
Marcasite (FeS_2)	N/A	4.89
Apatite ($Ca_5(PO_4)_3$)	50	3.15-3.20

N/A means the SPI is not applicable in these cases. The SPI is based on ionic radii and most sulfur-based minerals are largely covalent.

1973]. Several of the studies made use of the method of Fechtig and Kalbitzer [1966] which describes volume diffusion from a uniformly charged, spherical particle. These anlytical solutions also make the assumption of only one trapping mechanism with one corresponding activation energy. It is interesting to note that in few of these studies are the samples heated above 1000°C and none use temperatures above 1200°C. The results of these studies are summarized below.

3.5.5.1 Diffusion in Lunar Glasses

Ducati, et al. [1973] focused on lunar glass spherules in their study of rare gas diffusion in lunar soil particles. The following reasons were given for their focus:

1) Glass is a major constituent of the lunar regolith
2) The structure of glass is simple
3) Glasses were quantitatively outgassed in the process of their formation
4) The glass particles have a well-defined geometry (spherical).

The diffusion of implanted surface related gases was investigated for implanted glasses and for lunar samples using linear heating with mass spectroscopy. The activation energy for migration was then calculated using Equation 3-11 [Kelly and Matzke, 1966]

$$Q = \left[(70 \pm 4) + 4.6 \log_{10} T_{MDR} - 9.2 \log_{10} d\right] \frac{T_{MDR}}{1000} \qquad (3\text{-}11)$$

where Q = activation energy in kcal/mol, d = implantation depth in Angstroms, T_{MDR} = the temperature of maximum differential release in K. Calculations for implanted glasses were assumed an initial "plane" distribution at the theoretical implantation depth. The calculations for lunar samples used the assumption of an e^{-x} profile with x = d, where d is the depth above which 50% of the total gas was located. Migration energies of 1.04 eV and 1.74 eV were calculated for implanted He in synthetic glasses and lunar glasses, respectively. Ducati, et. al [1973] concludes that 1) the major part of the released gases is related to the solar wind, 2) lunar samples are heavily damage by solar wind irradiation in the outer ~50 nm and only

moderately damaged by solar flare ions to ~10 μm. They suggest that the high retentivity and low elemental fractionation of He in ilmenite is due to "its dense resistent lattice" and the consequent capture of He by high energy traps resulting from radiation damage [Ducati et al., 1973]. They also suggest that most of the He implanted in lunar materials by the solar wind is lost during the lunar day (T_{max} = ~400 K), and that the "major elemental fractionation occurs at the border between the amorphous layer and the weakly damaged interior" [Ducati et al., 1973].

3.5.5.2 Thermal Release Diffusion Studies of Helium from Lunar Fines

A study of He diffusion in the Apollo 14 fines was accomplished Baur, et al. [1972] using linear heating. The samples were held at each temperature for a long period of time and then the temperature was raised in less than a minute to the next temperature [Baur, 1996]. Baur described the method in the following:

> "During the step only a very small fraction of the gas contained in the sample was released and the partial pressure in the collection volume switched from an almost constant slope as a function of time, to a steeper slope. The ratio of these slopes or degassing rates was interpreted as being the ratio of diffusion coefficients for the temperatures before and after the step, assuming the concentration distribution in the sample did not change during the step. To calculate an activation energy, we had to assume a single diffusion mechanism with the diffusion coefficient obeying the Arrhenius's law:
>
> $$D = D_0 \exp\left[-\frac{Q}{kT}\right] \qquad (3\text{-}12)$$
>
> The activation energy Q could then be calculated from the ratio of slopes S1 and S2:
>
> $$\frac{S1}{S2} = \frac{D1}{D2} = \exp\left[-\frac{Q}{kT1}\right] \Big/ \exp\left[-\frac{Q}{kT2}\right] \qquad (3\text{-}13)$$
>
> $$Q = \ln\left(\frac{S1}{S2}\right) * \frac{k}{\left(\frac{1}{T2} - \frac{1}{T1}\right)} \qquad (3\text{-}14)$$
>
> This method is discussed in Huneke, J. C. et al., [1969]."

The activation energy for several sets of lunar fines was reported to increase as a function of temperature from 0.65 eV at about 150°C to 3.48 eV at 770 °C after which it decreased slightly [Baur et al., 1972]. These fines included the samples and grain size fractions found in Table 3-14.

Table 3-14. Samples included in measurements of the effective activation energy of He in lunar fines [Baur et al., 1972].

Sample	Grain Size Fractions Considered
10084 (Apollo 11)	< 25 μm, 25-42 μm and 64-100 μm
14163 (Apollo 14)	< 25 μm and 64-100 μm

Using the model of Fechtig and Kalbitzer [1966] and step-wise heating of one of the Apollo 14 grain size fractions (they do not report which), Baur, et al. reported an activation energy of 1.74 eV. This activation energy agrees with values of Kirsten, et al. [1972] and values calculated using the temperature of maximal gas release reported by Ducati, et al. [1973]. Baur, et al. [1972] compared the release from mineral separates (palgioclase, magnetic glass and pyroxene) to the release from the 30-48 μm grain size fraction of sample 14163 and noted that the release at low temperatures appears to be independent of mineral chemistry and structure. They do not, however, report activation energies for these samples.

3.6 Implantation Studies of Helium Diffusion in Terrestrial Minerals

The diffusion coefficients of He in ilmenite and olivine have been recently reported by Futagami, et al. [1993]. These measurements were performed on single crystal synthetic olivine (Mg_2SiO_4) and natural ilmenite ($Fe_{1.0}Ti_{1.1}Mn_{0.2}O_{3.4}$, as quoted by Futagami, et al. [1993]). Helium was implanted using an ion implanter at energies of 5-50 keV/amu along the (001) direction in olivine and the (113) direction in ilmenite. The only surface treatment prior to implantation involved polishing with 0.06 micron alumina powder. Thermal release

patterns were obtained, and depth profiles prior to heating were calculated using the TRIM code [Ziegler, 1996]. The diffusion coefficients of helium, neon and argon in ilmenite and olivine as a function of inverse temperature were obtained (Figure 3-11). They obtained activation energies of 0.48 eV and 1.34 eV for ilmenite and olivine, respectively.

While the study of Futagami, et al. [1993] is a well-detailed study, several questions remain. The fact that single crystal samples were implanted along known crystallographic directions may have made channeling a major problem. Great effort was made to study the formation of small bubbles of helium formed during thermal release. The mean maximum temperature of the Moon's surface is about 380 K [Vaniman et al., 1991]. Thus, diffusion of helium in the form of bubbles is irrelevant to the problem of helium diffusion from *in-situ* lunar soil grains except during meteorite impacts. This information does, however, have relevance to the design of the lunar miner. Differences between the diffusion of ^3He and ^4He were not addressed in the study of Futagami et al., [1993]. In addition, the samples were all observed to have melted at the last temperature step, about 1500°C.

Stoichiometric effects were also not considered in this study. The stoichiometry of lunar oxides -- ilmenite, spinels, armalcolite and rutile -- as well as silicates -- olivines, pyroxenes and plagioclase -- varies greatly [Agullo-Lopez et al., 1988; R. W. Taylor, 1964]. A key factor in this variability is the ease of substitution between iron and magnesium in many of these minerals. In oxides, MgO exhibits substantial solid solubility toward ideal FeO as a result of Mg^{2+}, Fe^{2+} substitution. The deviation from stoichiometry is very important in $Fe_{(1-x)}O$ where $0.05 < x < 0.16$ as mentioned earlier. However, even chemical stoichiometry is not equivalent to "perfect" structure. Such is the case for $Ti_{(1-x)}O_2$ where about 15% metal and oxygen vacancies are present for $x = 0$ [Agullo-Lopez et al., 1988]. Since the minerals we are concerned with are ternary oxides, several charge states are possible for the constituents and impurities. The low oxygen partial pressure on the Moon

also allows unusually low oxidation states in comparison to terrestrial minerals. As a result, the defect structures are complicated and strong interactions between defects can be present.

3.7 References

Adams, J. B. and W. G. Wolfer (1988) "On the Diffusion Mechanisms of Helium in Nickel," *Journal of Nuclear Materials*, **158**, pp. 25-29.

Agullo-Lopez, F., C. R. A. Catlow, and P. D. Townsend (1988) *Point Defects in Materials*, (London: Academic Press), pp. 152-153.

Aines, R. D. and G. R. Rossman (1986) "Relationships Between Radiation Damage and Trace Water in Zircon, Quartz and Topaz," *American Mineralogist*, **71**, pp. 1186-1193.

Allen, W. R. (1991) "Lattice Location of Ion Implanted ^{3}He in Sapphire," *Nuclear Instruments and Methods in Physics Research*, **B61**, pp. 325-336.

Allen, W. R. and S. J. Zinkle (1992) "Lattice Location and Clustering of Helium in Ceramic Oxides," *Journal of Nuclear Materials*, **191-194**, pp. 625-629.

Baur, H. (1996) Personal Communication, March 29.

Baur, H. U. Frick, H. Funk, L. Schultz and P. Signer (1972) "Thermal Release of Helium, Neon, and Argon from Lunar Fines and Minerals," Proceedings of the Third Lunar Science Conference, Supplement 3, *Geochimica et Cosmochimica Acta* , **2**, pp. 1947-1966.

Becker, R. H. and R. O. Pepin (1989) "Long-term Changes in Solar Wind Elemental and Isotopic Ratios: A Comparison of Two Lunar Ilmenites of Differenct Antiquities," *Geochimica et Cosmochimica Acta* , **53**, pp. 1135-1146.

Benkert, J-P., H. Baur, P. Signer, and R. Wieler (1993) "He, Ne, and Ar From the Solar Wind and Solar Energetic Particles in Lunar Ilmenites and Pyroxenes," *Journal of Geophysical Research* **98**(E7), pp. 13,147 - 13,162.

Boschmann Kathler, W. (1986) "Uran und Helium in Erzmineraliwn und die Frage ihrer Datierbarkeit," PhD Thesis, (Heidelberger Geowiss. Abh., Heidelberg).

Brown, F. and J. A. Davies (1963) "The Effect of Energy and Integrated Flux on the Retention and Range of Inert Gas Ions Injected at keV Energies in Metals," *Canadian Journal of Physics*, **41**, pp. 844-857.

Buening, D. K. and P. R. Buseck (1973) "Fe-Mg Latice Diffusion in Olivine," *Journal of Geophysical Research*, **78**, pp. 6852-6862.

Cameron, E. N. (1988) "Helium Mining on the Moon: Site Selection and Evaluation," *The Second Conference on Lunar Bases and Space Activities of the 21st Century*, (Houston, Texas: Lunar and Planetary Institute), pp. 89-97.

Chiang, Y.-M., P. B. Birnie III and W. D. Kingery (1997) *Physical Ceramics: Principles for Ceramic Science and Engineering*, (John Wiley & Sons, Inc., New York), p. 187.

Cooper, R. (1998) Personal communication.

Crank, J. (1956) *The Mathematics of Diffusion* (Oxford University Press, London) 347 pp.

Dieckmann, R. (1983) *Metallurgie, Teil: Eisenerzeugung*, (Verlag Stahleisen, Düsseldorf) **1**, p.1.

Dieckmann, R. (1993) "Point Defects and Transport in Haematite ($F_e2O_{3-\varepsilon}$)," *Philosophical Magazine, A* **68**(4), pp. 725-745.

Dieckmann, R. (1996) Personal communication.

Ducati, H., S. Kalbitzer, J. Kiko, T. Kirsten, and H. W. Müller (1973) "Rare Gas Diffusion Studies in Individual Lunar Soil Particles and in Artificially Implanted Glasses," *The Moon* **8**, pp. 210-227.

Fechtig, H and S. Kalbitzer (1966) "The Diffusion of Argon in Potassium-Bearing Solids," *Potassium Argon Dating*, O. A. Schaeffer and J Zahringer, eds., (Springer-Verlag, Berlin) pp. 68-107.

Frick, U., H. Baur, H. Funk, D. Phinney, Chr. Schafer, L. Schultz and P. Signer (1973) "Diffusion Properties of Light Noble Gases in Lunar Fines," Proceedings of the Fourth Lunar Science Conference, Supplement 4, *Geochimica et Cosmochimica Acta*, **2**, pp. 1987-2002.

Frick, U., R. H. Becker, and R. O. Pepin (1988) "Solar Wind Record in the Lunar Regolith: Nitrogen and Noble Gases," *Eighteenth Lunar and Planetary Science Conference*, G. Ryder, ed., (Cambridge: Cambridge University Press), pp. 87-120.

Futagami, T., M. Ozima, S. Nagai, and Y. Aoki (1993) "Experiments on Thermal Release of Implanted Noble Gases in Lunar Soil Grains," *Geochimica et Cosmochimica Acta* **57**, pp. 3177-3194.

Gerling, E. K. (1939) "Part taken by Close Packing of Crystals in the Diffusion of Helium," *Comp. Rend. de L'Acad. des Scien. de l'URSS*, **24**, pp. 274-277.

Giletti, B. J. and K. C. Hess (1988) "Oxygen Diffusion in Magnetite," *Earth and Planetary Science Letters*, **89**, pp. 115-122.

Glyde, H. R. and A. Mayne (1965a) *Philosophical Magazine*, **12**, p.919.

Glyde, H. R. and A. Mayne (1965b) *Philosophical Magazine*, **12**, p.997.

Haggerty, S. E. and D. H. Lindsley (1970) "Stability of the Pseudobrookite (Fe_2TiO_5)-Ferropseudobrookite ($FeTi_2O_5$) Series," *Carnegie Institution Washington Year Book*, **68**, pp. 247-249.

Haggerty, S. E. (1978) "The Redox State of Planetary Basalts," *Geophysical Research Letters*, **5**, pp. 443-446.

Hart, S. R. (1981) "Diffusion Compensation in Natural Silicates," *Geochimica et Cosmochimica Acta* , **45**, pp. 279-291.

Hart, S. R. (1984) "He Diffusion in Olivine," *Earth and Planetary Science Letters* **70** pp. 297-302.

Hawthorne, F. C., L. A. Groat, M. Raudsepp, N. A. Ball, M. Kimata, F. D. Spike, R. Gaba, N. M. Halden, G. R. Lumpkin, R. C. Ewing, R. B. Greegor, F. W. Lytle, T. S. Ercit, G. R. Rossman, F. J. Wicks, R. A. Ramik, B. L. Sherriff, M. E. Fleet and C. McCammon (1991) "Alpha-Decay Damage in Titanite," *American Minerologist*, **76**, pp. 370-396.

Heumann, Th. and R. Imm (1968) "Self-Diffusion and Isotope Effect in γ-Iron," *Journal of the Physics and Chemistry of Solids*, **29**, pp. 1613-1621.

Hohenberg, C. M., P. K. Davis, W. A. Kaiser, R. S. Lewis, and J. H. Reynolds (1970) "Trapped and Cosmogenic Rare Gases From Stepwise Heating of Apollo 11 Samples," *Proceedings of the Apollo 11 Lunar Science Conference*, Vol. 2, pp. 1283-1309.

Huneke, J. C., L. E. Nyquist, H. Funk, V. Köppel and P. Signer (1968) "The Thermal Release of Rare Gases from Separated Minerals of the Mócs Meteorite," *Meteorite Research*, P. Millman, ed. pp. 901-921.

Inglefield, J. E. and J. B. Pendry (1976) *Philisophical Magazine*, **34**, p. 590.

Jambon, A. and J. E. Shelby (1980) "Helium Diffusion and Solubility in Obsidians and Basaltic Glass in the Range 200-300°C," *Earth and Planetary Science Letters* **51**, pp. 206-214.

Jung, P. (1992) "Diffusion and Retention of Helium in Graphite and Silicon Carbide," *Journal of Nuclear Materials*, **191-194**, pp. 377-381.

Kelly, B. T. (1966) *Irradiation Damage to Solids* (Pergamon Press, Oxford).

Kelly, R. and Hj. Matzke (1966) *Journal of Nuclear Mathematics*, **20**, pp. 171-183.

Kirsten, T., J. Duebner, H. Ducati, W. Gentner, P. Horn, E. Jessgerger, S. Kalbitzer, I. Kaneoka, J. Kiko, W. Kraetschmer, H. W. Mueller, T. Plieninger and S. K. Thio (1972) "Rare Gases in Individual Components and Bulk Samples of Apollo 14 and 15 Fines and Fragmental Rocks" (abstract) *Lunar Science III*, C. Watkins, ed., pp. 452-454.

Klein, C. and C. S. Hurlbut, Jr. (1977) *Manual of Mineralogy*, Twenty-First Edition (John Wiley & Sons, Inc., New York).

Kornelson, E. V. (1972) *Radiation Effects*, **13**, p. 227.

Kulcinski, G. L, E. N. Cameron, J. F. Santarius, I. N. Sviatoslavsky, L. J. Wittenberg, and H. H. Schmitt (1988) "Fusion Energy from the Moon for the 21st Century," *The Second Conference on Lunar Bases and Space Activities of the 21st Century*, (Houston, Texas: Lunar and Planetary Institute), pp. 459-474.

Langseth, M. G. and S. J. Keihm (1977) "In-Situ Measurements of Lunar Heat Flow," Soviet-American Conference on Geochemistry of the Moon and Planets, NASA SP-370, pp. 283-293.

Lässer, R.(1989) Tritium and Helium-3 in Metals, (Springer-Verlag, Berlin), 159 pp.

Lewis, M. B. (1987) "Evidence for Helium Trapping to Oxygen Sites in Titanium," *Journal of Nuclear Instruments and Methods in Physics Research*, **B22**, pp. 499-503.

Lindsley, D. H. (1991) "Experimental Studies of Oxide Minerals," *Oxide Minerals: Petrologic and Magnetic Significance*, D. H. Lindsley, ed. Reviews in Mineralogy, Vol. 25, (Mineralogical Society of America: Washington, D. C.), pp. 69-106.

Lord, H. C. [1968] "Hydrogen and Helium Ion Implantation into Olivine and Enstatite: Retention Coefficients, Saturation Concentrations, and Temperature-Release Profiles," *Journal of Geophysical Research*, **73**(16), pp. 5271-5280.

March, N. H. (1978) "Point Defect-Solute Interactions in Metals," *Journal of Nuclear Materials*, **69&70**, pp. 490-520.

Matzke HJ. (1976) "Ion-Bombardment-Induced Structural Changes in Fe_2O_3, Cr_2O_3 and U_3O_8," *Radiation Effects*, **28**, pp. 249-251.

Mitchell, J. N., R. Devanathan, K. E. Sickafus, K. J. McClellan (1996) "The Mineralogy of Radiation-resistant Ceramics and the Suitability fo Ilmenite-group Minerals for Fusion Reactor Applications," (unpublished abstract).

Mokeyeva, V. I., M. A. Simonov, E. L. Belokoneva, E. S. Makarov, V. I. Ivanov, and N. V. Rannev (1976) "X-ray Study of Details of Atomic Structure and Distribution of Magnesium and Iron Atoms in Lunar and Terrestrial Olivines," *Geochemistry International*, **13**(1), pp. 50-57.

Muan, A. and E. F. Osborn (1965) *Phase Equilibria among Oxides in Steelmaking*, (Addison-Wesley Publishing Company, Inc., Reading, Mass.).

Müller, H. W., J. Jordan, S. Kalbitzer, J. Kiko and T. Kirsten (1976) "Rare Gas Ion Probe Analysis of Helium Profiles in Individual Lunar Soil Particles," *Seventh Lunar Science Conference*, (Houston, Texas), pp. 937-951.

Pandey, R. K., S. Sunkara and J. Muthusami (1996) "Crystal Growth and Characterization of an Oxide Semiconductor (Ilmenite) for Novel Electronic Devices," *Space Technology and Applications International Forum*, AIP Conference Proceedings 316, (Albuquerque, NM).

Papike, J., L. Taylor and S. Simon (1991) "Lunar Minerals," *Lunar Sourcebook.*, G. Heiken, D. Vaniman and B. M. French, eds. (Cambridge, Cambridge University Press) pp. 121-182.

Pepin, R. O., L. E. Nyquist, D. Phinney, and D. C. Black (1970) "Rare Gases in Apollo 11 Lunar Material," *Proceedings of the Apollo 11 Lunar Science Conference*, Vol. 2, pp. 1435-1454.

Peterson, N. L. (1978) "Self-Diffusion in Pure Metals," *Journal of Nuclear Materials*, **69&70**, pp. 3-37.

Philipps, V., K. Sonnenberg, and J. M. Williams (1982) *Journal of Nuclear Materials*, **107**, p. 271.

Schoen, A. H. (1958) *Physical Review Letters*, **1**, p. 138.

Sciani, V. and P. Jung (1983) "Diffusion of Helium in FCC Metals," *Radiation Effects*, **78**, pp. 87-99.

Shannon, R. D. and C. T. Prewitt (1969) "Effective Ionic Radii in Oxides and Fluorides," Acta Crystallographica, **B25**, pp. 925-946.

Signer, P., H. Baur, and R. Wieler (1991) "Closed System Stepped Etching; An Alternative to Stepped Heating," *Alfred O. Nier Symposium on Inorganic Mass Spectrometry*, (Durango, Colorado), D. J. Rokop, ed., pp. 181-202.

Srinivasan, B., E. W. Hennecke, D. E. Sinclair, and O. K. Manuel (1972) "A Comparison of Noble Gases Geleased From Lunar Fines (#15601,64) with Noble Gases in Meteorites and in the Earth," *Third Lunar Science Conference*, **2** (Houston, Texas) pp. 1927-1945.

Stott, M. J. (1978) "Electronic Structure of Vacancies and Interstitials in Metals," *Journal of Nuclear Materials*, **69 & 70**, pp. 157-175.

Sunkara, S. S. (1995) "Growth and Evaluation of Ilmenite Wide Bandgap Semiconductor for High Temperature Electronic Applications," Ph.D. Dissertation, (Texas A&M University, College Station, Texas).

Taylor, L. A., R. J. Williams and R. H. McCallister (1972) "Stability relations of ilmenite and ulvospinel in the Fe-Ti-O system and application of these data to lunar mineral assemblages," *Earth and Planetary Science Letters*, **16**, pp. 282-288.

Taylor, R. W. (1964) "Phase Equilibria in the System FeO-Fe_2O_3-TiO_2 at 1300°C," *American Mineralogist*, **49**, pp. 1016-1030.

Trull, T. W., M. D. Kurz, and W. J. Jenkins (1991) "Diffusion of cosmogenic ^3He in olivine and quartz: Implications for surface exposure dating," *Earth and Planetary Science Letters* **103**, pp. 241-256.

Vaniman, D., R. Reedy, G. Heiken, G. Olhoeft and W. Mendell (1991) "The Lunar Environment," *Lunar Sourcebook.*, G. Heiken, D. Vaniman and B. M. French, eds. (Cambridge, Cambridge University Press) pp. 27-60.

Warhaut, M., J. Kiko, and T. Kirsten (1979) "Microdistribution Patterns of Implanted Rare Gases in a Large Number of Individual Lunar Soil Particles," *Tenth Lunar and Planetary Science Conference*, Houston, Texas, Lunar and Planetary Institute, ed., (Pergamon Press) pp. 1531-1546.

Waychnuas, G. A. (1991) "Crystal Chemistry of Oxides and Oxyhydroxides," *Oxide Minerals: Petrologic and Magnetic* Significance, D. H. Lindsley, ed. Reviews in Mineralogy, Vol. 25, (Mineralogical Society of America, Washington, D. C.) pp. 11-68.

Welch, D. O., O. Lazareth, G. J. Dienes and R. D. Hatcher (1976) "Theory of Helium Migration and Trapping in α-Al_2O_3" *Radiation Effects*, **28**, pp. 195-198.

Whitmore, M. D. (1976) *Journal of Physics*, **F6**, p. 1259.

Wieler, R. (1995) Personal communication, (November 17).

Yaniv, A. and D. Heymann (1971) "Inert Gases from Apollo 11 and Apollo 12 Fines: Reversals in the Trends of Relative Element Abundances," *Earth and Planetary Science Letters*, **10**, pp. 387-391.

Zeller, E. J., L. B. Ronca and P. W. Levy (1966) "Proton Induced Hydroxyl Formation on the Lunar Surface," *Journal of Geophysical Research*, **71**, pp. 4855-4860.

Zhang, Y. and Z. Xu (1994) "Atomic Radii of Noble Gas Elements in Condensed Phases," *EOS Transactions of the American Geophysical Union*, **75**, 16 Suppl., p. 234

Ziegler, J. P. (1996) *SRIM Instruction Maual: The Stopping and Range of Ions in Matter*, (Yorktown, New York: IBM - Research); based on Ziegler, J. P., J. P. Biersack and U. Littmark, *The Stopping and Range of Ions in Solids*, (New York: Pergamon Press, 1985).

Zoltai, T. and J. H. Stout (1984) *Mineralogy: Concepts and Principles*, (Minneapolis, Minnesota: Burgess Publishing Company).

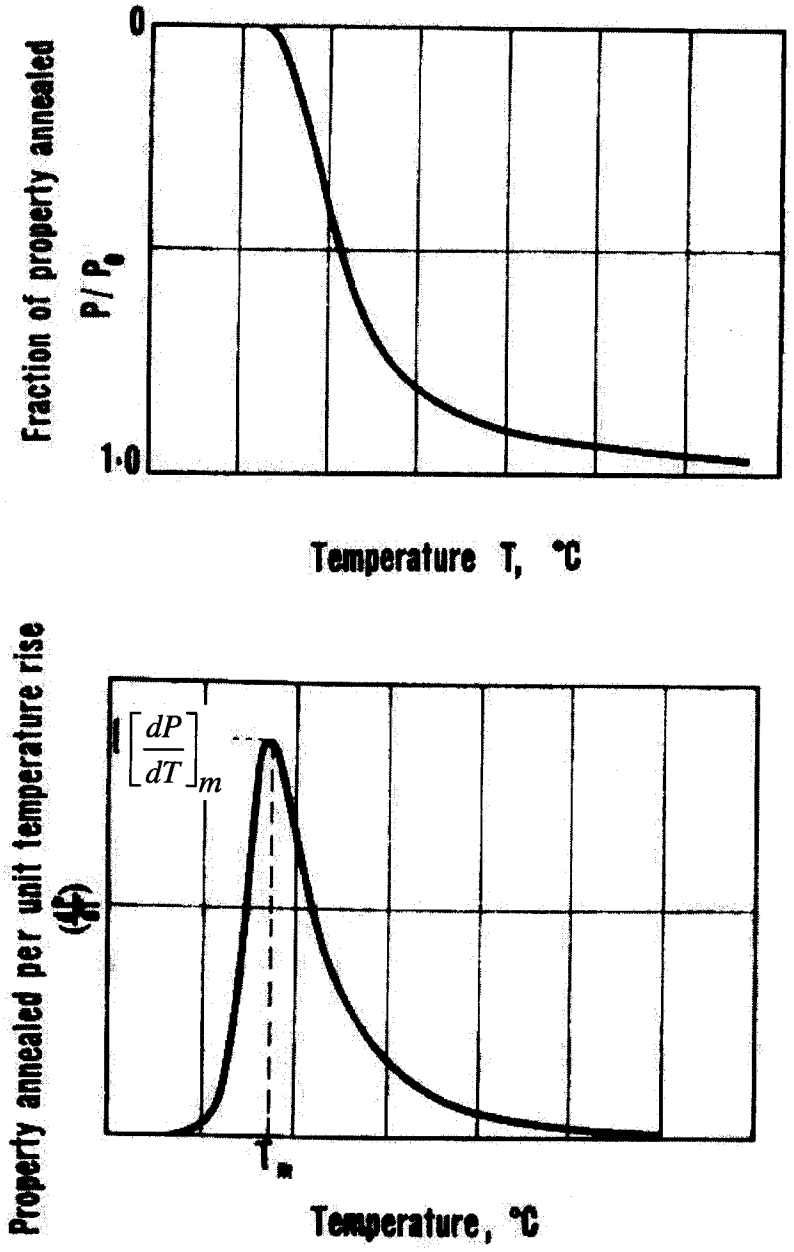

Figure 3-1. Annealing of irradiation induced defects according to Equation 3-4 using linear heating [From Kelly, 1966].

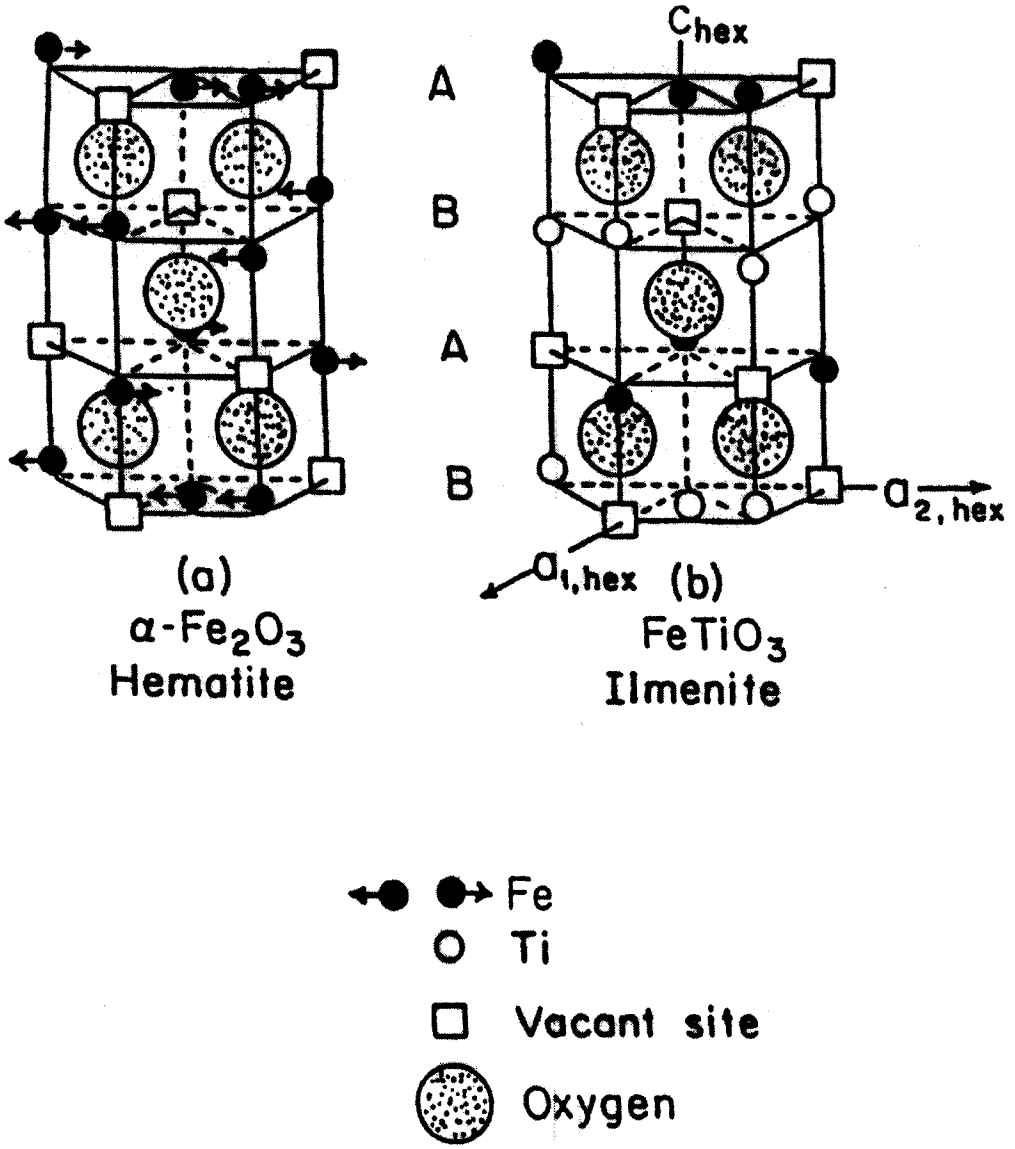

Figure 3-2. Schematics of the structures of (a) hematite, Fe_2O_3 and (b) ilmenite, $FeTiO_3$ [From Waychnuas, 1991].

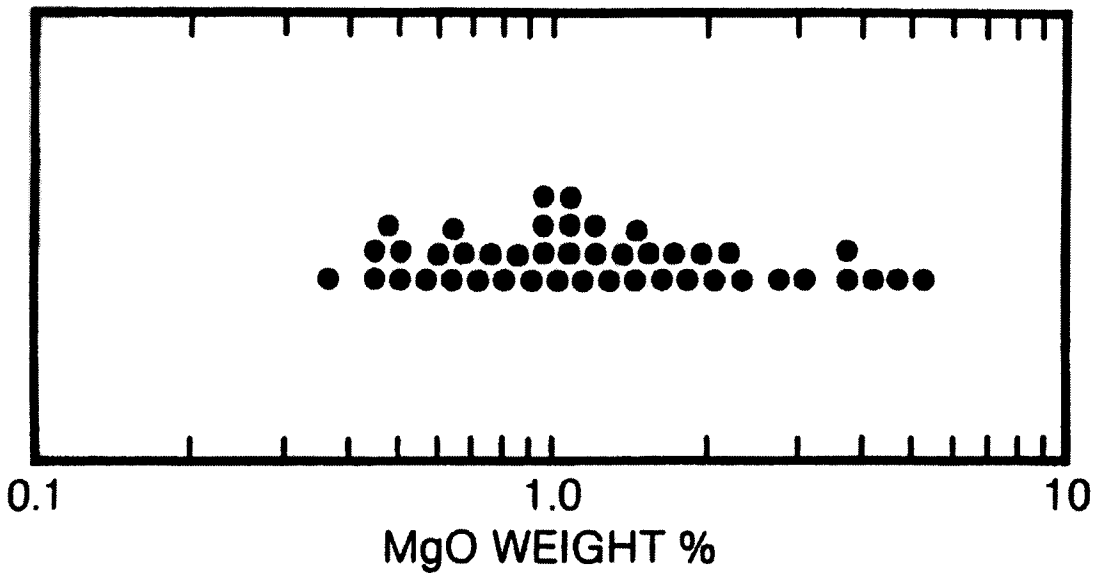

Figure 3-3. MgO contents (wt.%) of ilmenites in mare basalt samples from various lunar sites [From Papike et al., 1991]. Each dot represents a lunar sample.

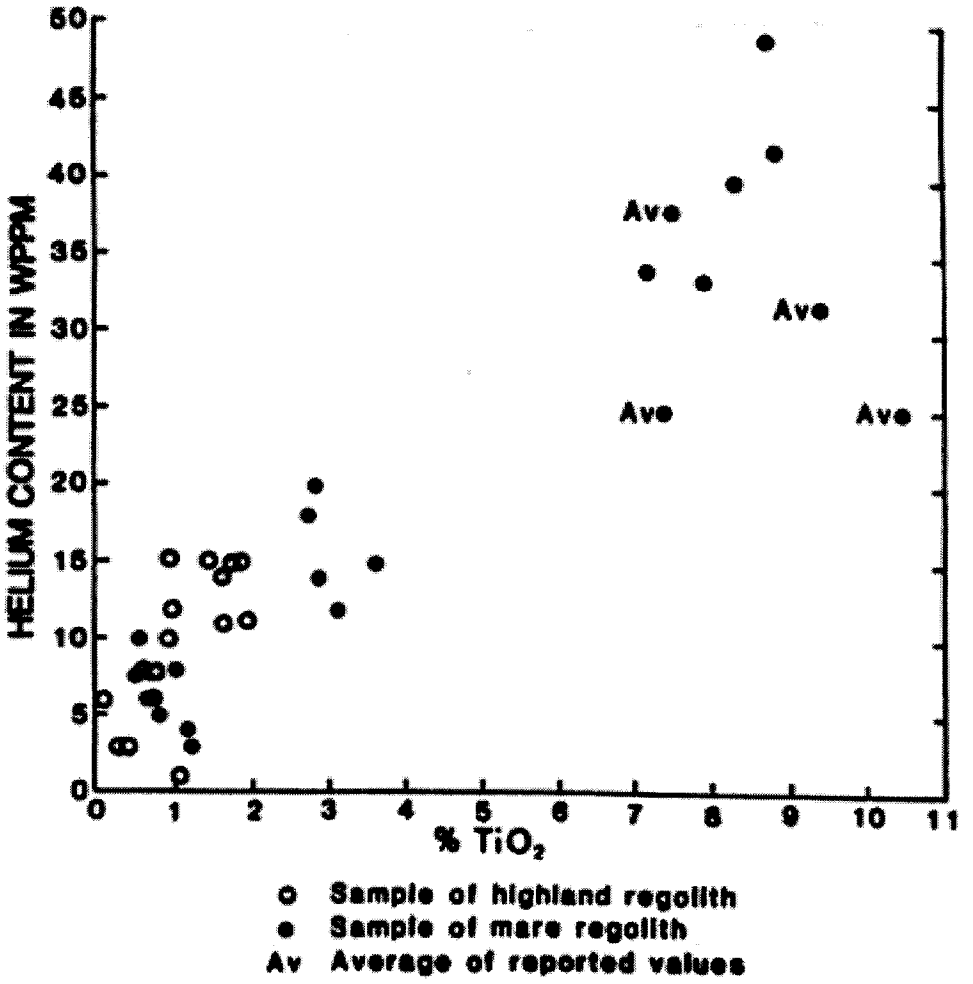

Figure 3-4. Relation between ^4He contents and TiO_2 contents of lunar regolith samples [From Cameron, 1988].

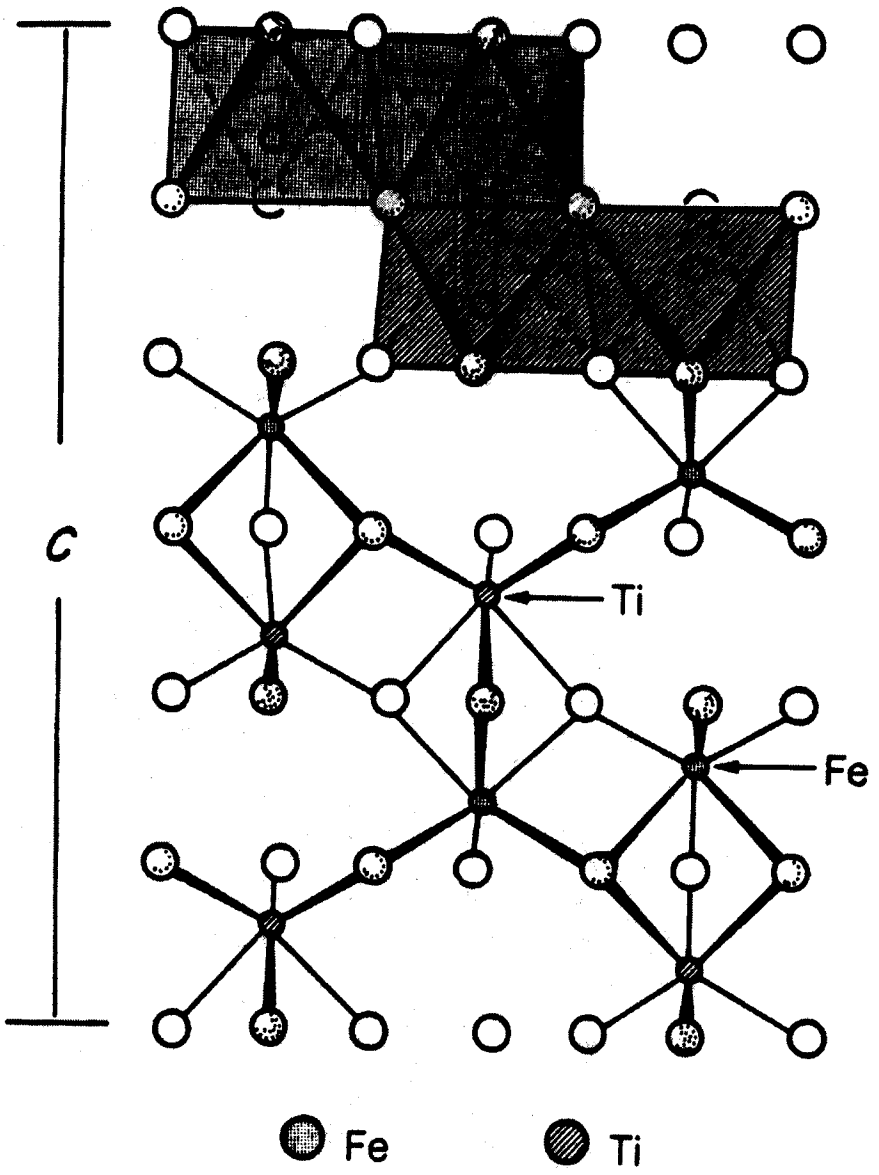

Figure 3-5. A unit cell of the crystal structure of ilmenite. Fe^{2+}, Ti^{4+} and other cations are contained within two-thirds of the octahedra defined by a hexagonal close-packed lattice of oxygen anions [From Papike et al., 1991]. The unit-cell dimension, *c*, is 14.09 Å [Pandey et al., 1996; Sunkara, 1995; Waychnuas, 1991].

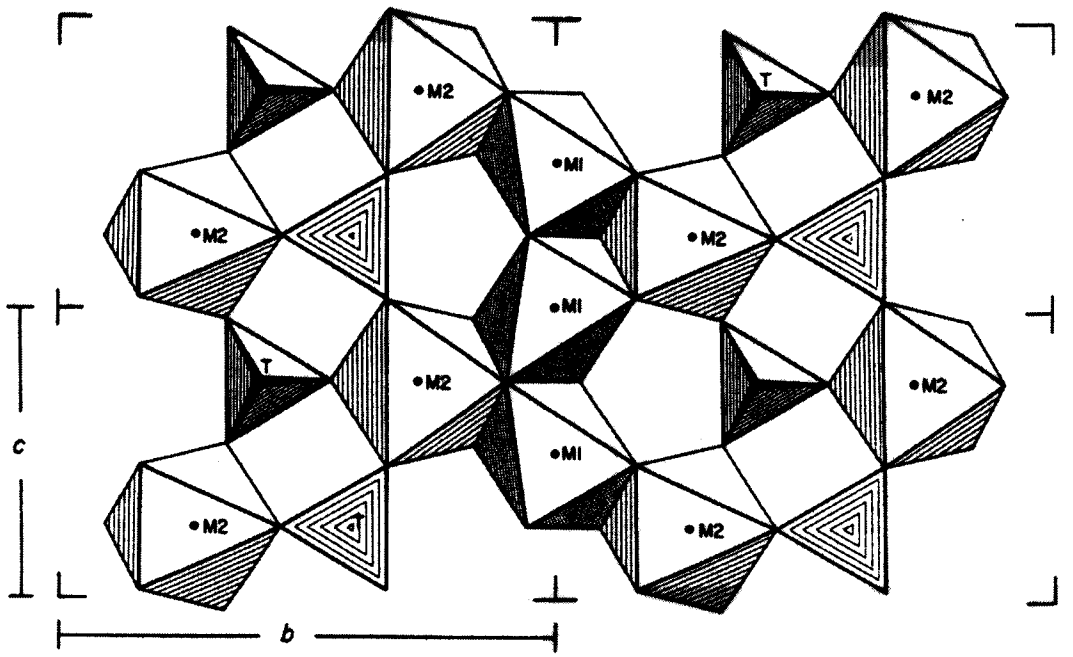

Figure 3-6. Crystal structure of olivine [From Papike et al., 1991]. Olivine is composed of tetrahedra (T) and octahedra (M1, M2) defined by oxygen atoms. The b and c axes of the forsterite form of olivine are 10.28 Å and 6.00 Å respectively.

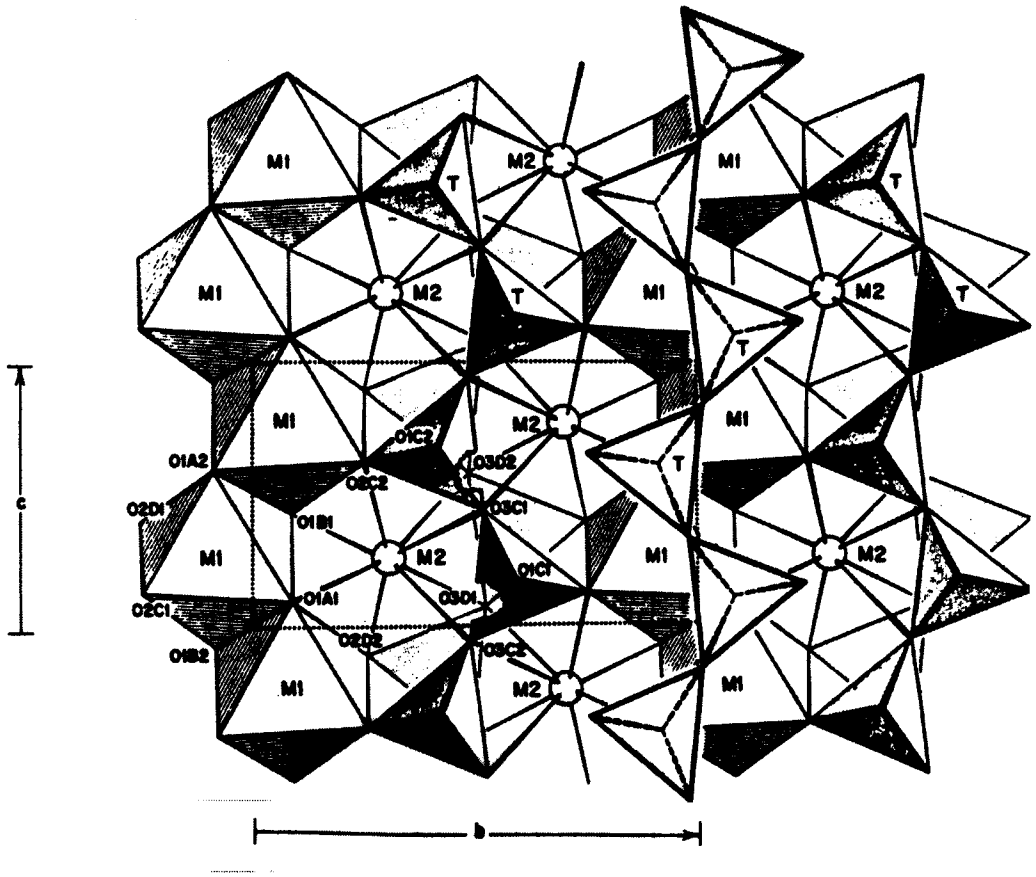

Figure 3-7. Crystal structure of pyroxene [From Papike et al., 1991]. Pyroxene is composed of polyhedra defined by oxygen atoms with tetrahdra (T), octahedra (M1) and distorted octahedra (M2). The b and c axes of the pigeonite form of pyroxene are 8.95 Å and 5.26 Å respectively.

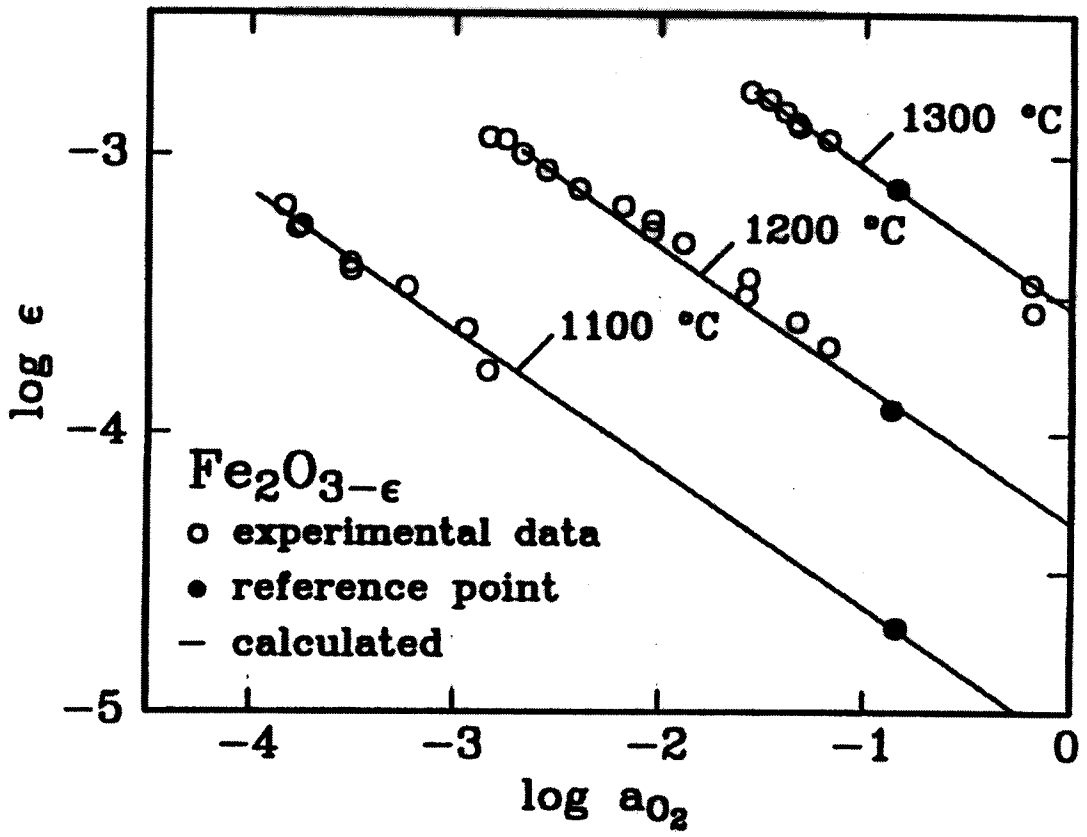

Figure 3-8. Results of fitting the non-stoichiometery changes determined by Dieckmann [1993] as a function of oxygen activity. The fit corresponds to the case where electronic defects are the majority defects and oxygen vacancies are the prevailing ionic defect [Dieckmann, 1993].

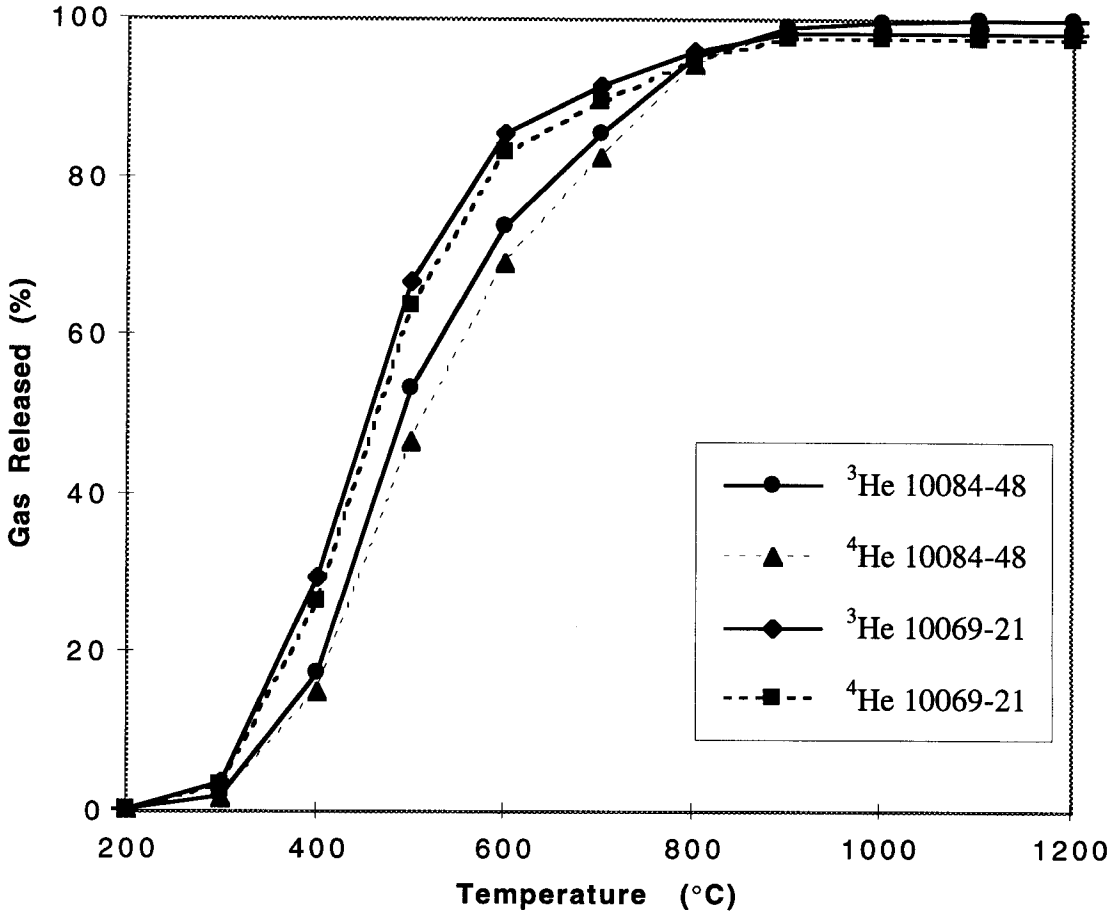

Figure 3-9. Helium release from Apollo 11 rock sample 10069 and regolith sample 10084 as a function of temperature during an isochronal anneal. Annealing temperature was increased 100 °C in time steps of 1 hour [Pepin et al., 1970].

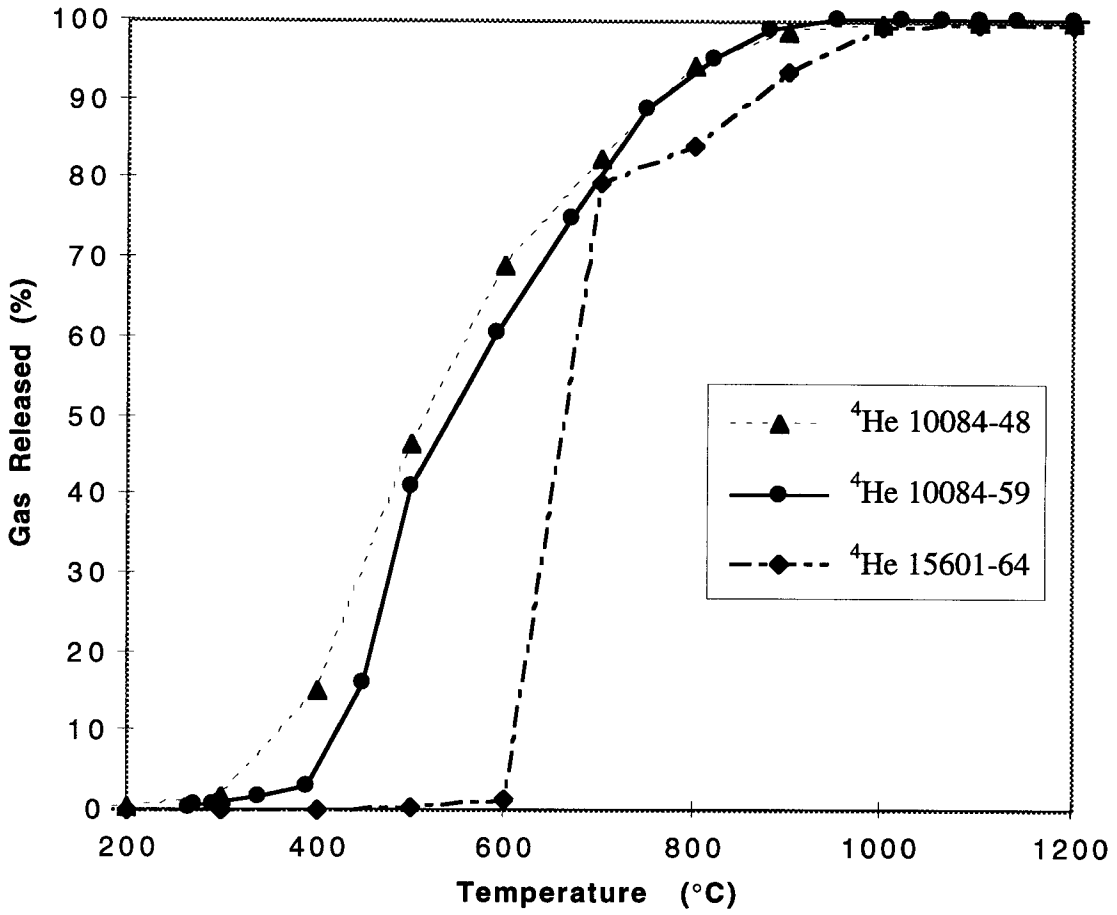

Figure 3-10. Results of three ^{4}He release data for Apollo 11 regolith sample 10084 and Apollo 15 fines sample 15601 as a function of temperature during isochronal anneals. The anneal of sample 10084-48 were done in 1 hour steps by Pepin et. al. [1970]. The anneal of 10084-59 was done in 1/2 hour steps by Hohenberg, et. al. [1970]. The anneal of 15601-64 was done by Srinivasan, et. al. [1972].

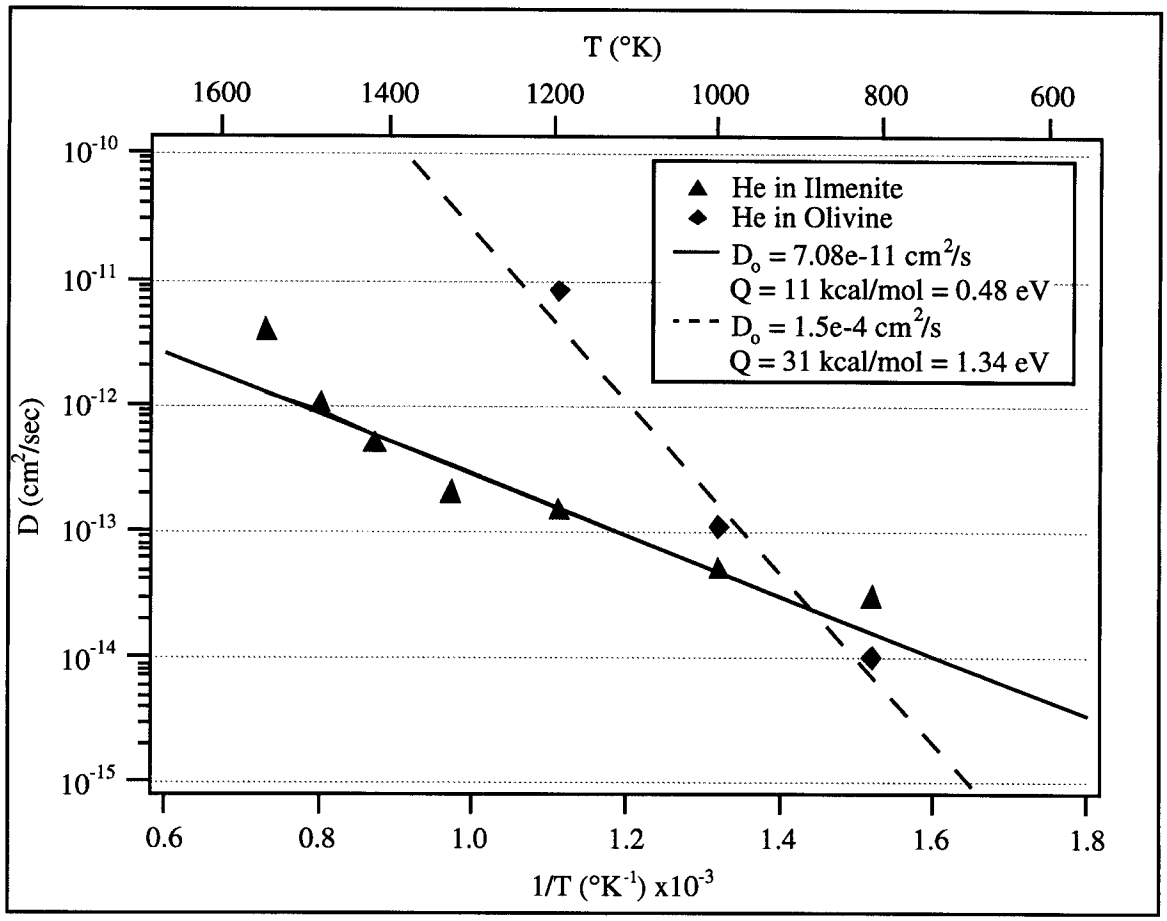

Figure 3-11. 1/T vs. diffusivity of 20 keV ^{4}He implanted in ilmenite and olivine [After Futagami et al., 1993].

Chapter 4 Research Approach

4.1 Computational Approach

Preliminary research for this thesis included the development of a computer model combining solar wind implantation with diffusion to show that an effective diffusivity could be obtained by fitting previously obtained profile and gas release data. The solar wind spectrum from Pioneer 10 [Gazis, 1996] was used to simulate the implantation of helium into ilmenite and subsequent diffusion under lunar conditions. The effect of sputtering by solar wind hydrogen and helium was also considered. It was shown that the diffusivity of helium in ilmenite must be lower than 2.9×10^{-25} cm^2/s in order to match the depth profile measured with a rare gas ion probe [Harris-Kuhlman, 1996].

4.2 Experimental Approach

The early computational work showed that greater understanding of the trapping mechanisms of helium in minerals was needed. This research involves several experimental and computational methods to determine the diffusivity and activation energy of helium in ilmenite ($FeTiO_3$), the major titanium-bearing lunar mineral. In addition, the mechanisms by which helium is trapped in ilmenite are discussed. The experimental approach is summarized in Figure 4-1.

4.2.1 Terrestrial Analogs of Lunar Ilmenite

The first step in the research performed in this thesis was the identification of a suitable terrestrial analog of lunar ilmenite. The identification of a terrestrial ilmenite analog to lunar ilmenite will be discussed, including verification that the material behaves like lunar ilmenite under the simulated irradiation of solar wind helium. It will be shown that the release of helium from the implanted terrestrial ilmenite chosen is quite similar to the helium release from the Apollo 11 samples.

4.2.2 Solar Wind Simulation

This research involves simulating lunar ilmenite samples using Plasma Source Ion Implantation (PSII) at the University of Wisconsin - Madison [Conrad, et. al., 1990] to generate a solar wind-like flux on samples of terrestrial ilmenite.. The samples were then subjected to isochronal and isothermal anneals and the gases evolved measured using a mass spectrometer [Frick, et. al., 1988; Nier and Schlutter, 1992]. Since depth profiles of helium are difficult to measure, profiles were calculated using TRIM [Zeigler, 1996]. The resulting data was used to calculate the diffusion coefficient and activation energy of helium within the ilmenite lattice using a numerical model of the diffusion process.

4.2.3 Analytical Tools

4.2.3.1 Annealing with Mass Spectometry

Isochronal and linear annealing experiments were performed in Professor R. O. Pepin's laboratories at the University of Minnesota. The profiles were then used as input to the ANNEAL code written for this research. The ANNEAL program performs a numerical simulation of the isochronal and linear annealing experiments. The fitting of the experimentally measured gas release data by ANNEAL allows the calculation of the diffusivity and activation energy of helium in ilmenite.

4.2.3.2 Positron Annihilation Spectroscopy

The trapping mechanism was explored further using positron annihilation spectroscopy (PAS). Positrons are very sensitive to the presence of open volume point defects. It is possible to distinguish between different types of defects due to the differences in the electron densities within the various defects. The electron density within a defect determines the lifetime of a positron trapped within the defect. This lifetime can be accurately measured and uniquely identifies the defect. A vacancy containing a helium atom will exhibit a shorter positron lifetime than an empty vacancy of the same type due to the additional electrons with which the positrons can annihilate. Positron annihilation spectroscopy may

also provide a means of measuring the helium profile with depth. Only preliminary studies were performed at Washington State University, but these studies helped refine the sample preparation process.

4.2.3.3 Transmission Electron Microscopy

Surface amorphization and structural changes in the bulk were monitored using the High-Resolution Transmission Electron Microscope (HRTEM) in the Department of Geology and Geophysics at the University of Wisconsin - Madison.

4.2.3.4 Electron Probe Microanalysis

The base composition of the samples were monitored using the Electron Microprobe (EM) at the University of Wisconsin - Madison [Harris-Kuhlman and Kulcinski, 1998] with the assistance of Dr. John Fournelle. Electron probe microanalysis (EPMA) is instrumental in selecting qualitatively pure terrestrial samples and monitoring the synthetic samples for exsolution of various end member phases.

4.2.4 Numerical Tools

The three-dimensional ANNEAL code was developed for this research for calculating diffusivity based on the fraction of solar-wind implanted gas released during each annealing step. It uses the alternating direction method to solve the parabolic differential equation that describes diffusion as well as heat transfer. This equation is of the general form (Equation 4-1) in three-dimensions:

$$\frac{\partial C}{\partial t} = D\nabla^2 C \qquad (4\text{-}1)$$

where D is the diffusivity (cm^2/s), C is the concentration ($atoms/cm^3$).

The diffusion coefficient and activation energies of helium are calculated by fitting the resulting diffusivities to Fick's Law (Equation 4-2), a well-known solution of Equation 4-1.

$$D = D_0 \exp\left(\frac{-Q}{K_b T}\right) \qquad (4\text{-}2)$$

where D is diffusivity (cm^2/s), D_0 is the diffusion constant (cm^3/s), K_b is Boltzman's constant (eV/K), T is the temperature, and Q is the activation energy (eV). The details of the calculations will be discussed in Chapter 8.

The two inputs to ANNEAL are the fractional release of helium at each temperature step and the depth profile of helium calculated using the program TRIM mentioned above. The results of fitting the data will be discussed in detail in Chapter 9.

4.3 References

Conrad, J. R., R. A. Dodd, S. Han, M. Madapura, J. Scheuer, K. Sridharan and F. J. Worzala (1990) *Journal of Vacuum Science Technology A*, **8**, p. 3146.

Frick, U., R. H. Becker, and R. O. Pepin (1988) "Solar Wind Record in the Lunar Regolith: Nitrogen and Noble Gases," *Eighteenth Lunar and Planetary Science Conference*, G. Ryder, ed., (Cambridge: Cambridge University Press), pp. 87-120.

Gazis, P. (1996) Personal communication, (May 8).

Harris, K. R., H. Y. Khater, and G. L. Kulcinski (1994) "Remote Sensing of Astrofuel™," *Proceedings of the 4th International Conference on Engineering, Construction, and Operations in Space*, R.G. Galloway and S. Lokaj, eds., (American Society of Civil Engineers, Albuquerque, New Mexico) **1**, pp. 648-657.

Harris-Kuhlman, K. R. (1996) Unpublished data.

Harris-Kuhlman, K. R., and G. L. Kulcinski (1998) "Terrestrial Analogs for Lunar Ilmenite," *Proceedings of the Sixth International Conference on Engineering, Construction, and Operations in Space*, R. G. Galloway and S. Lokaj, eds., (American Society of Civil Engineers, Albuquerque, New Mexico, April 26-30) , pp. 533-540.

Nier, A. O. and D. J. Schlutter (1992) "Extraction of Helium From Individual Interplanetary Dust Particles by Step-Heating," *Meteoritics*, **27** pp. 166-173.

Wieler, R. (1995) Personal communication.

Ziegler, J. P.(1996) *SRIM Instruction Maual: The Stopping and Range of Ions in Matter*, (Yorktown, New York: IBM - Research); based on Ziegler, J. P., J. P. Biersack and U. Littmark, *The Stopping and Range of Ions in Solids*, (New York: Pergamon Press, 1985).

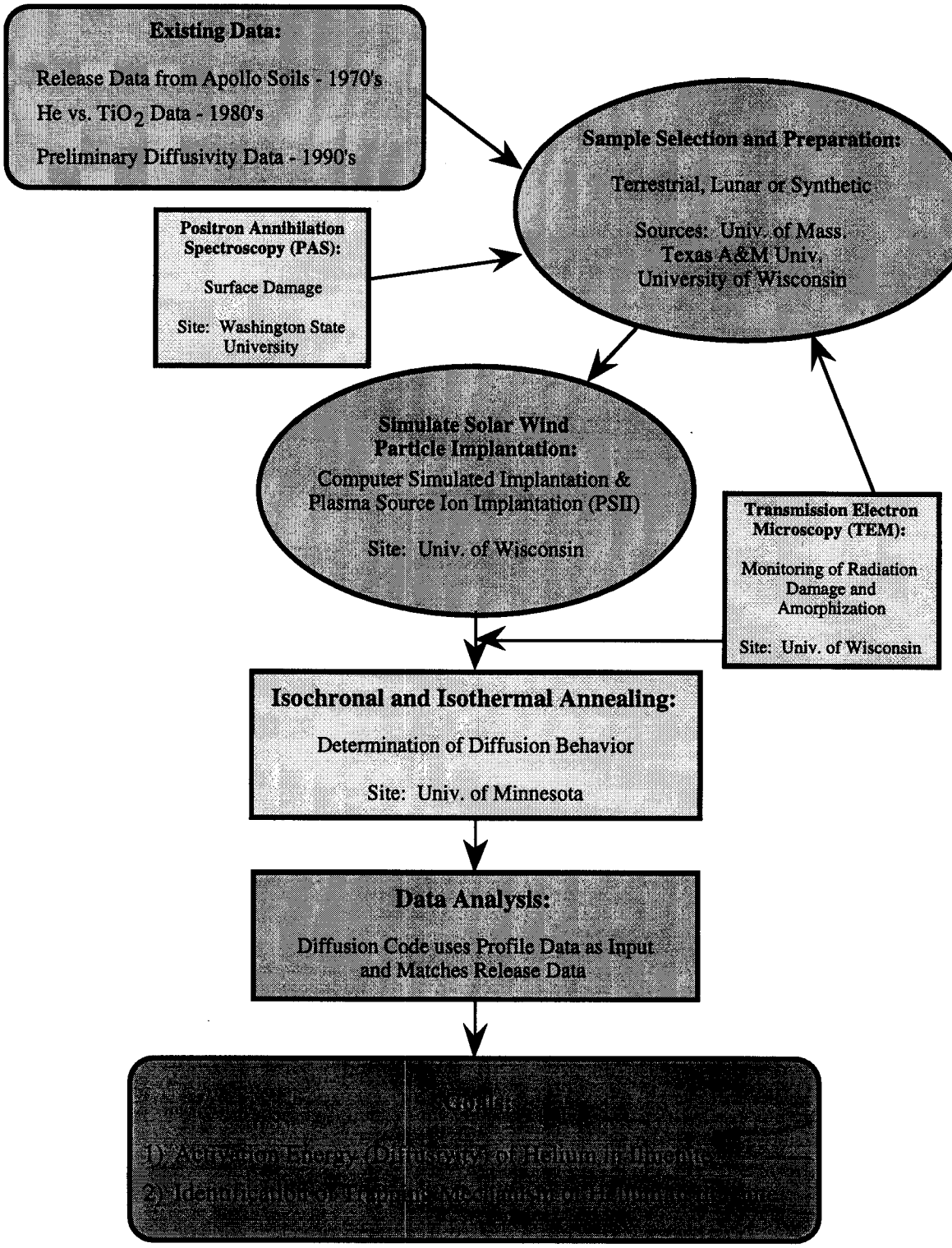

Figure 4-1. Flowchart of Doctoral Research.

Chapter 5 Computational Models Developed for or Used in This Research

5.1 TRIM - the Transport of Ions in Matter

The Monte Carlo electronic stopping code TRIM (the TRansport of Ions in Matter) [Ziegler, 1996] was used to generate range, sputtering and backscattering data for several different aspects of the research for this thesis. TRIM uses a full quantum mechanical treatment of ion-atom collisions (moving atoms = "ions", target atoms = "atoms") to calculate the stopping and range of ions from 10 eV - 2 GeV/amu. A full description of the calculation is given in The Stopping and Range of Ions in Solids [Ziegler et al., 1985].

TRIM calculations are quite sensitive to the parameters used to describe a compound such as ilmenite. The constituent atoms are identified and the stoichiometry is specified. The binding energy of a lattice atom to its site and the surface binding energy must be specified and are not well-known for oxides. The parameters used in this thesis were based on the experimental observations of Sickafus [1996] and are given in Table 5-1.

Table 5-1. Values of variable parameters used in TRIM calculations for solar wind ions incident on oxide minerals.

TRIM Parameter	Value
Incident Ion (mass)	^{4}He (4.0 amu) ^{3}He (3.0 amu) H (1.0 amu)
Incident Energy	0.5 keV - 15.0 keV for He 0.5 - 1.3 keV for H
Angle of Incidence (degrees)	90° (normal to surface)
Lattice Binding Energy [Sickafus, 1996]	
Oxygen	60 eV
All Cations (Fe, Ti, etc.)	30 eV
Surface Binding Energy	4 eV

5.2 LRDC - Lunar Regolith Dynamics Code

Since on-orbit gamma spectrometry was shown to not be feasible for the detection of ^{3}He due to its relatively small concentrations [Harris et al., 1994], the decision was made to reevaluate the literature pertaining to the correlation that *could* be measured remotely -- titanium content. The empirical relationship between helium concentrations and titanium dioxide concentrations is well-discussed in the literature [e.g. Wittenberg et al., 1986; Cameron, 1988; Fegley and Swindle, 1993; Swindle, et. al.; Frick et al., 1988; Papike, et. al. 1991]. However, the diffusivity of helium in lunar ilmenite has not been measured. Simulations have been performed on synthetic ilmenite [Futagami et al., 1993], but the resulting diffusivity values for olivine and ilmenite are counterintuitive to step-wise heating data, etching data, and rare gas ion probe profiles. The available experimental data indicates that ilmenite retains helium better than olivine and pyroxene.

Preliminary research was conducted for the purpose of better understanding the many processes involved in the implantation and diffusion of solar wind gases in the lunar regolith. A computer model combining solar wind implantation with diffusion was developed to show that an effective diffusivity could be obtained by fitting previously obtained profile and gas release data.

5.2.1 Solar Wind Fluence

Paul Gazis (NASA's Ames Laboratory) provided raw spectral data from Pioneer 10 for days 130-135 of 1972 [Gazis, 1996]. During this time, the Pioneer 10 spacecraft travelled between 1.38 and 1.43 AU. An energy spectrum was generated by processing the raw data. This spectrum is shown in Figure 5-1. The helium spectrum was obtained by simply dividing the total spectrum -- assumed to be mostly protons -- by 22, the approximate ratio of protons to helium nuclei in the solar wind [Vaniman et al., 1991]. The energies of the helium particles were obtained assuming that the energies of the ions were actually energy per atomic mass unit (amu). The total solar wind proton flux was calculated to be 2.7×10^8

protons/cm^2/s. This value agrees with the average value of 3x10^8 protons/cm^2/s at 1 A.U. given in the literature [Vaniman et al., 1991]. The average energy of a helium ion was found to be 2.5 keV, yielding an average energy per nucleon of 0.625 keV/amu. This is somewhat lower than values found in the literature which range from 0.82 keV/amu [Jull and Pillinger, 1977] to 1 keV/amu [Vaniman et al., 1991].

5.2.2 TRIM Calculation of Depth Profile and Sputtering Due to the Solar Wind

5.2.2.1 Depth Profile

The TRIM code [Ziegler, 1996] was used to generate range, sputtering and backscattering data for each of the 44 energy "bins" in the Pioneer 10 energy spectrum. These data sets were superimposed on each other using the fluences in the energy spectrum as a weighting factor to generate a data set consisting of "flux" as a function of depth. The final data set was then run through 10 binomial smoothing passes using the data analysis program IGOR [Wavemetrics, 1993], and is shown in Figure 5-2.

This profile has a spatial mesh of 4 Å in order to maintain as much resolution in the range data as possible. To this end, the TRIM runs were set up with sufficient thickness of material such that no transmission occured. As the energy of the incident particle increased, the depth of material needed to stop all of the ions also increased. The depths were incremented by 400 Å at a time to make superposition of the resulting ranges simple. Since TRIM generates a final mesh of 100 divisions of the input depth, the final spatial mesh is 4 Å.

5.2.2.2 Sputtering

Sputtering is important to the proposed study because it determines how much of the implanted gas is released through a non-diffusive mechanism. The magnitude of sputtering on the Moon has been the subject of great debate with values from 0.02 Å/year to 0.5 Å/year being reported [Jull and Pillinger, 1977].

The main contributions to solar wind sputtering of lunar materials are from the two major constituents of the solar wind, hydrogen and helium. Many studies have debated which of the two elements contributes the most to sputtering [Zinner et al., 1976]. An example of this is the value of 0.043 Å/year obtained by McDonnell and Flavill [1974]. Their study only measured erosion due to normally incident He and assumed 70% H erosion and 30% He erosion (i.e. H generates 70% of the total sputtering). The total sputtering for 80% He-erosion from this study was later reported as 0.016 Å/year by Zinner, et. al [1976].

Sputtering yields were calculated for helium and hydrogen using the Pioneer 10 solar wind energy spectrum and TRIM calculations. These sputtering yields for H and He are shown in Figure 5-3 along with the sputtering yields given for H and He on silicon in the literature [Jull and Pillinger, 1977; Roth et al., 1979]. Silicon is used since the average atomic weight of ilmenite is approximately that of silicon. The sputtering due to solar wind He ions was calculated to occur at the rate of 0.0254 Å/year while sputtering due to protons was calculated to be 0.0197 Å/year. Total sputtering due to light ions is thus 0.0451 Å/year. This is in good agreement with the value of 0.043 Å/year obtained by McDonnell and Flavill [1974] in sputtering experiments using 2.8 keV ^{4}He on a polished fragment of Apollo 14 breccia sample 14321. The fractions of sputtering due to hydrogen and helium calculated from the TRIM results are 44% and 56% respectively. This result is considerably different than those in the literature where one species is assumed to be much more dominant than the other [Zinner, 1976].

5.2.3 Numerical Model

The LRD code has been refined for use in fitting the helium profile in ilmenite obtained by Müller, et. al. [1976]. The available data results in concentrations several orders of magnitude larger than the measured concentrations of ^{4}He in the lunar regolith. The data used was not obtained for the conditions or minerals desired. The model combines simple diffusion with temperature variations as a function of time (night vs.day, surface vs. buried),

solar wind implantation of ^4He and constant sputtering. The equations of interest were solved using an implicit relaxation method with phantom zones on either side of the physical grid.

Fick's law with a term for solar wind implantation (Equation 5-1) is solved using a one-dimensional, implicit relaxation scheme (Equation 5-2). In Equation 5-2, I_0 is the solar wind helium flux, D_0 is the diffusion constant, n is the gas concentration in the solid, E_a is the activation energy of the defect, k_b is the Boltzmann constant and T is the temperature.

$$\frac{dn}{dt} = I_0 + D_0 \exp\left(-\frac{E_a}{k_b T}\right)\frac{d^2 n}{dt^2} \tag{5-1}$$

$$\frac{n_j^{i+1} - n_j^i}{\Delta t} = \frac{D_0}{(\Delta x)^2}\left(n_{j+1}^{i+1} - 2n_j^{i+1} + n_{j-1}^{i+1}\right) + I_0 \tag{5-2}$$

The model includes phantom zones on each side of the spatial mesh to measure the gas released by diffusion and provide the necessary boundary conditions where the gas released is eliminated from the system (see Appendix A for the source code).

The implicit solution of this equation results in a tridiagonal matrix which is solved using the subroutine TRIDAG [Press et al., 1986]. The factor of $Ddt/(dx)^2$ must be in the range 1-20 to produce reliable results [Blanchard, 1996]. The code calculates the time step based on the value of this factor.

5.2.4 Results

Results of the LRD code are shown in (Figure 5-4). These profiles were calculated using a gardening depth of 1 mm. The diffusion constant, $D_0 = 7.08 \times 10^{-11}$ cm^2/s, was calculated from the given activation energy of 11 kcal/mol for ^4He in ilmenite and values of D of Futagami, et. al. [1993]. Due to the long timescales considered (up to 4.5×10^9 years, the age of the solar system) and the small spatial scales necessitated by the range of solar wind particles, the implicit method has calculated the upper limit of the diffusivity, D, to be

2.87×10^{-25} cm^2/s using an effective activation energy of 25 kcal/mol = 1.08 eV. The activation energy reported by Futagami, et. al. [1993], 11 kcal/mol = 0.48 eV, is seen to be far too small for any significant ^4He accumulation. The exact solution may be found by extending the precision of the calculation to 64-bit precision now available on an HP workstation. The plot of maximum concentration at a point in the sample with respect to time (Figure 5-5) illustrates the limitation of the implicit solution of the differential equation (Equation 5-2).

5.3 ANNEAL - A 3-D Code for Analyzing Annealing Data

A numerical method, the ANNEAL code, has been developed for this thesis for calculating diffusivity based on the fraction of solar-wind implanted gas released during each annealing step. Analytical methods are typically based on uniform gas concentrations within the region of interest or within the entire particle although the implanted helium profile with depth resembles a gaussian distribution. Simple Fick's Law diffusion is assumed since the trapping mechanism is unknown. The resulting activation energies are characteristic of the trapping mechanism(s) and should aid in trap identification. A computational grid in the form of a rectangular prism has been constructed using the initial implantation profile as the initial condition and "phantom zones" on each surface to collect the gas released during each time step. The details of this construction are discuss in detail below (see Appendix B for the source code).

5.3.1 Geometry

A three-dimensional solution to the differential equation for diffusion was chosen to conform with the geometry of the current problem. While the samples were implanted in a slab geometry where the length and width are much greater than the slab height, the samples had to be crushed to get them into the small particle furnace at the University of Minnesota for annealing. Crushing resulted in irregularly shaped particles with all dimensions roughly

equal (Figure 5-6). In addition, the implanted helium distribution is very close to the polished surface -- for 4 keV ^{4}He, the average range $\approx$ 330 Angstroms and end of range $\approx$ 900 Angstroms (Figure 5-7). As the temperature increases, helium will not only diffuse out the polished surface, but also out the sides and further into the sample. The one-dimensional computational model artificially increases the diffusivity required to generate a given release fraction because it does not account for the release out the sides.

Since classical diffusion occurs "down" the concentration gradient, the diffusion in the z direction is critical in this model. The computational grid is constructed to have a higher mesh density in the z direction than in either the x or y directions. The physical model used is a rectangular prism 100 microns x 100 microns x 10 microns in the x, y, and z directions respectively. The three dimensional matrix that corresponds to the physical model is 10 or 20 zones in the x and y directions and 1000 zones in the z direction. Two phantom zones are added in each direction, one for each boundary.

5.3.2 Initial Conditions

Since distributions of helium with depth are difficult to measure experimentally due to its high ionization energy [Warhaut et al., 1979], a simulation of the depth profile was generated using TRIM '96, a Monte Carlo ion implantation modeling code developed at IBM [Zeigler, J. P., 1996] (Figure 5-7). The program IGOR from WaveMetrics was used to smooth this noisy profile. Twelve passes of binomial smoothing were performed, and the first four data points were replaced with the original TRIM data points to circumvent the discrepancy introduced by the zero boundary condition during the smoothing procedure. This profile is the initial condition input to the three-dimensional, Crank-Nicolson parabolic difference equation describing Fick's Law diffusion.

The concentrations calculated by TRIM are multiplied by the dose -- 10^{16} ions/cm^2 -- to get units of atoms/Angstrom/cm^2. The concentration is then recalculated in terms of atoms/micron^3 to minimize the affect of round-off error during the calculations.

5.3.3 Boundary Conditions

One set of boundary conditions are imposed on this computational system. "Phantom zones" are created along every surface, simulating the diffusion of atoms to a vacuum at the surface where they are lost. These zones behave as every other zone, except that after each time step their contents are summed and the fraction of the original total number of implanted atoms that have diffused out the surface is calculated. The fraction is stored in one of three variables -- *ntop, nsides, or nbottom* -- and the concentration of the phantom zones is set to zero. At the end of a temperature step, the total fraction of gas release during that step is calculated.

This fractional release is then compared to the a set of final conditions, the experimental fraction of gas released during the temperature step (e.g. Figure 5-8). The ratio of the two numbers is taken and must be closer to 1 than the tolerance parameter, *toler*, typically set equal to ±0.00001.

5.3.4 The Differencing Equations

An alternating direction method for three space variables formulated by Douglas [1962] was used to model the experimental data due to its compuational efficiency and accuracy. The parabolic differential equation that describes diffusion as well as heat transfer is of the general form (Equation 5-3) in three-dimensions.

$$\frac{\partial C}{\partial t} = D\nabla^2 C \qquad (5\text{-}3)$$

where D is the diffusivity (cm^2/s), C is the concentration ($atoms/cm^3$). For simplicity, the diffusivity, D, is assumed constant throughout this discussion. Equation 5-3 can be rewritten as

$$\omega_t = D\left(\omega_{xx} + \omega_{yy} + \omega_{zz}\right) \qquad (5\text{-}4)$$

where ω is now the concentration (atoms/cm^3) and ω_t and ω_{xx} are the first and second derivatives of the concentration with respect to t and x respectively. The method employed by Douglas [1962] is a modification of the Crank-Nicolson equation for three dimensions and is second order accurate in both time and space.

The general equation (5-3) can be written as (Douglas, 1962)

$$\left(\Delta_x^2 - \frac{2}{\Delta t}\right)\omega^*_{n+1} = -\left(\Delta_x^2 + 2\Delta_y^2 + 2\Delta_z^2 + \frac{2}{\Delta t}\right)\omega_n\,, \tag{5-5a}$$

$$\left(\Delta_y^2 - \frac{2}{\Delta t}\right)\omega^{**}_{n+1} = \Delta_y^2\omega_n + \frac{2}{\Delta t}\omega^*_{n+1}\,, \tag{5-5b}$$

$$\left(\Delta_z^2 - \frac{2}{\Delta t}\right)\omega_{n+1} = \Delta_z^2\omega_n + \frac{2}{\Delta t}\omega^{**}_{n+1}\,, \tag{5-5c}$$

where

$$x_i = i\Delta x,\quad y_j = j\Delta y,\quad z_k = k\Delta z,\quad t_n = n\Delta t \tag{5-6a}$$

$$\omega_{i,j,k,n} = \omega\left(x_i, y_j, z_k, t_n\right) \tag{5-6b}$$

$$\Delta_x^2\omega_{i,j,k,n} = D\frac{\left(\omega_{i+1,j,k,n} - 2\omega_{i,j,k,n} + \omega_{i-1,j,k,n}\right)}{(\Delta x)^2}. \tag{5-6c}$$

Substituting Equations 5-6 into Equations 5-5 results in three tridiagonal linear equations (Equations 7), one for each spatial variable. The evaluation of ω_{n+1} involves solving these equations in succession, hence the term, "alternating direction" iterative method. Equation 5-7a (x-direction) is solved for the array $\omega^*_{i,j,k,n+1}$ which is substituted into Equation 5-7b. Equation 5-7b (y direction) is solved for the array $\omega^{**}_{i,j,k,n+1}$ which is substituted into Equation 5-7c. Equation 5-7c (z direction) is solved for the array $\omega_{i,j,k,n+1}$ which is the solution for the time step, Δt. The process is then repeated for each Δt until the

annealing time is reached. The xy grid is symmetrical and much coarser than the z grid to keep within the computational resources available.

$$-\frac{\alpha}{2}\omega^{*}_{i+1,n+1}+(\alpha+1)\omega^{*}_{i,n+1}-\frac{\alpha}{2}\omega^{*}_{i-1,n+1}=\omega_{i,n}\left(1-3\alpha-2\alpha_1\right)+$$
$$\frac{\alpha}{2}\left(\omega_{i+1,n}+\omega_{i-1,n}+2\omega_{j+1,n}+2\omega_{j-1,n}\right)+\alpha_1\left(\omega_{k+1,n}+\omega_{k-1,n}\right), \tag{5-7a}$$

$$-\frac{\alpha}{2}\omega^{**}_{j+1,n+1}+(\alpha+1)\omega^{**}_{j,n+1}-\frac{\alpha}{2}\omega^{**}_{j-1,n+1}=$$
$$\frac{\alpha}{2}\left(\omega_{j+1,n}+\omega_{j-1,n}\right)+\alpha\omega_{i,j,k,n}+\omega^{*}_{i,j,k,n+1}, \tag{5-7b}$$

$$-\frac{\alpha_1}{2}\omega_{k+1,n+1}+\left(\alpha_1+1\right)\omega_{k,n+1}-\frac{\alpha_1}{2}\omega_{k-1,n+1}=$$
$$\frac{\alpha_1}{2}\left(\omega_{k+1,n}+\omega_{k-1,n}\right)+\alpha_1\omega_{i,j,k,n}+\omega^{**}_{i,j,k,n+1}, \tag{5-7c}$$

where

$$\alpha=D\frac{\Delta t}{(\Delta x)^2},\quad \alpha_1=D\frac{\Delta t}{(\Delta z)^2},\quad \Delta x=\Delta y\neq\Delta z. \tag{5-8}$$

In these equations, the indices of the directions not currently being considered have been omitted for readability (e.g. $\omega_{i,n+1}=\omega_{i,j,k,n+1}$ or $\omega_{j+1,n+1}=\omega_{i,j+1,k,n+1}$).

These tridiagonal linear systems are easily solved using one of a number of routines that are publicly available. The particular tridiagonal routine used here is the TRIDAG subroutine featured in Numerical Recipes, The Art of Scientific Computing (Press, W. H. et al., 1989).

It has been found for this scheme that $\alpha \leq 0.1$ to prevent instability as D increases throughout the simulation. This requirement is probably due to a combination of instability in the differencing scheme and roundoff error. At low temperatures where D is sufficiently low,

Δt is set to 1 second. When $\alpha > 0.1$, Δt is reset to a smaller value maintain $\alpha = 0.1$, and the number of time steps required for the heating interval is correspondingly increased.

An additional trick is used to analyze as many data points as possible before the number of time steps required gets too large to be practical. Once the number of times steps reaches a preset value (e.g. 100,000), the grid in the z direction is expanded by a preset factor (e.g. 2). This increase in Δx causes a decrease in α (Equation 5-8) allowing Δt to remain constant.

A limit of this method in its current form involves diffusion at high temperatures. Once the implanted species has diffused through the artificially thin computational slab, the release out the "bottom" can become significant. When this occurs, the diffusivity is kept artificially low to account for this release that is not physically occurring. Since we are mainly interested in the low temperature behavior of the implanted species -- the lunar surface temperature ranges between 100 K and 400 K -- the calculations are stopped at the point where this diffusion out the back side of the artifically thin computational grid becomes significant. The errors due to this code will be discussed in Chapter 8.

5.4 VEPFIT - Positron Diffusion Modeling Code

The computer code, VEPFIT (Variable Energy Positron FITting), developed at Delft University of Technology was used to attempt to characterize the positron annhilation spectroscopy studies attempted on ilmenite samples implanted using Plasma Source Ion Implantation (Chapter 6). The program performs a fast non-iterative calculation for the solution of the equation for the time-averaged positron density in any material [van Veen et al., 1990] using experimental data obtained with a variable energy positron beam. The main purpose of the program is to determine how positron diffusion after implantation affects the measurement of the S and F parameters (see Chapter 6 for discussion of experiment) and

calculate an effective diffusion length. The program was difficult to use and has historically had problems with its user interface [Lynn, 1997].

Several models are available within VEPFIT for describing the defect profile in the sample, including 1) a model of bulk sample and a single defect uniformly distributed within it and 2) a gaussian distribution of defects within the sample [van Veen et al., 1990]. The results of both models were approximately the same and will be discussed in Chapter 7.

5.5 References

Blanchard, J. P. (1996) Personal communication (August 12).

Cameron, E. N (1988) "Helium Mining on the Moon: Site Selection and Evaluation," *The Second Conference on Lunar Bases and Space Activities of the 21st Century*, (Houston, Texas: Lunar and Planetary Institute) pp. 89-97.

Fegley, B., Jr. and T. D. Swindle (1993) "Lunar Volatiles: Implications for Lunar Resource Utilization," *Resources of Near-Earth Space*, J. S. Lewis, M. S. Matthews, and M. L. Guerrieri, eds., (Tucson, Arizona: The University of Arizona Press) pp. 367-426.

Frick, U., R. H. Becker, and R. O. Pepin (1988) "Solar Wind Record in the Lunar Regolith: Nitrogen and Noble Gases," *Eighteenth Lunar and Planetary Science Conference*, G. Ryder, ed., (Cambridge: Cambridge University Press) pp. 87-120.

Gazis, P. (1996) Personal communication (July 16).

Harris, K. R., H. Y. Khater, and G. L. Kulcinski (1994) "Remote Sensing of Astrofuel™," *Proceedings of the 4th International Conference on Engineering, Construction, and Operations in Space*, R.G. Galloway and S. Lokaj, eds., (American Society of Civil Engineers, Albuquerque, New Mexico) **1**, pp. 648-657.

Jull, A. J. T. and C. T. Pillinger (1977) "Effects of Sputtering on Solar Wind Element Accumulation," *Eighth Lunar Science Conference*, Houston, Texas, Vol. 3, pp. 3817-3833.

Lynn, K. G. (1997) Personal communication.

McDonnell, J. A. M. and R. P. Flavill (1974) "Solar Wind Sputtering on the Lunar Surface: Equilibrium Crater Densities Related to Past and Present Microparticle Influx Rates," *Proceedings of the Fifth Lunar Science Conference*, pp. 2441-2449.

Müller, H. W., J. Jordan, S. Kalbitzer, J. Kiko and T. Kirsten (1976) "Rare Gas Ion Probe Analysis of Helium Profiles in Individual Lunar Soil Particles," Seventh Lunar Science Conference, (Houston, Texas) pp. 937-951.

National Nuclear Data Center (1993) ENDF/B-VI Data Base.

Papike, J., L. Taylor and S. Simon (1991) "Lunar Minerals," *Lunar Sourcebook: A User's Guide to the Moon*, G. Heiken, D. Vaniman and B. M. French, eds. (Cambridge, Cambridge University Press) pp. 121-182.

Press, W. H., B. P. Flannery, S. A. Teukolsky and W. T. Vetterling (1986) *Numerical Recipes: The Art of Scientific Computing* (Cambridge University Press, Cambridge).

Roth, J., J. Bohdansky and W. Ottenberger (1979) "Data on Low Energy Sputtering," (Max-Planck-Institut Fur Plasmaphysik, Garching Bei Munchen, May 1979) IPP 9/26.

Sickafus, K. (1996) Los Alamos National Laboratory, Personal communication, (May).

Swindle, T. D., C. E. Glass, and M. M. Poulton (1990) *Mining lunar soils for ^3He*, Fusion Power Associates of Gaithersburg, Maryland and the Japanese Institute for Future Technology, TM-90/1.

Vaniman, D., R. Reedy, G. Heiken, G. Olhoeft and W. Mendell (1991) "The Lunar Environment," *Lunar Sourcebook: A User's Guide to the Moon*, G. Heiken, D. Vaniman and B. M. French, eds. (Cambridge, Cambridge University Press) pp. 27-60.

van Veen, A., H. Schut, J. de Vries, R. A. Hakvoort and M. F. Ijpma (1990) "Analysis of Positron Profiling Data by Means of 'VEPFIT'," *Positron Beams for Solids and Surfaces*, American Institute of Physics, Conference Proceedings 218, (London, Ontario, Canada), pp. 171-192.

Warhaut, M., J. Kiko, and T. Kirsten (1979) "Microdistribution Patterns of Implanted Rare Gases in a Large Number of Individual Lunar Soil Particles." *Tenth Lunar and Planetary Science Conference*, Houston, Texas, Lunar and Planetary Institute, ed., pp. 1531-1546.

WaveMetrics (1993) *IGOR* data collection and analysis program.

Wittenberg, L. J., J. F. Santarius, and G. L. Kulcinski (1986) "Lunar source of ^3He for commercial fusion power." *Fusion Technology*, **10** (2, pt 1), pp. 167-178.

Ziegler, J. F., J. P. Biersack and U. Littmark (1985) *The Stopping and Range of Ions in Solids*, (Pergamon Press, New York).

Ziegler, J. P. (1996) *SRIM Instruction Manual: The Stopping and Range of Ions in Matter*, (Yorktown, New York: IBM - Research); based on Ziegler, J. P., J. P. Biersack and U. Littmark, *The Stopping and Range of Ions in Solids*, (New York: Pergamon Press, 1985).

Zinner, E., R.M. Walker, J. Chaumont, and J.C. Dran (1976) "Ion Probe Analysis of Artificially Implanted Ions in Terrestrial Samples and Surface Enhanced Ions in Lunar Sample 76215,77," *Seventh Lunar and Planetary Science Conference*, Houston, Texas, pp. 953-984.

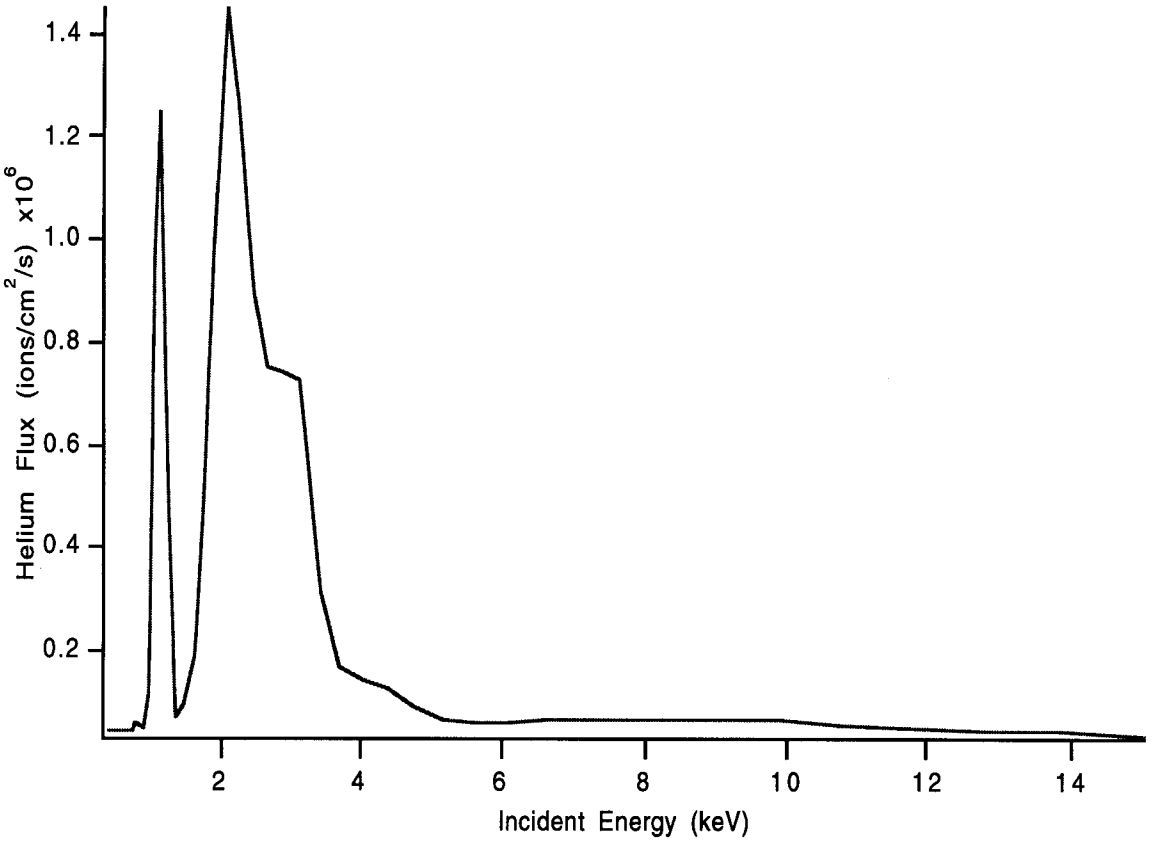

Figure 5-1. Energy spectrum of solar wind helium at 1 A.U. generated from data from Pioneer 10 data provided by Dr. Paul Gazis [1996].

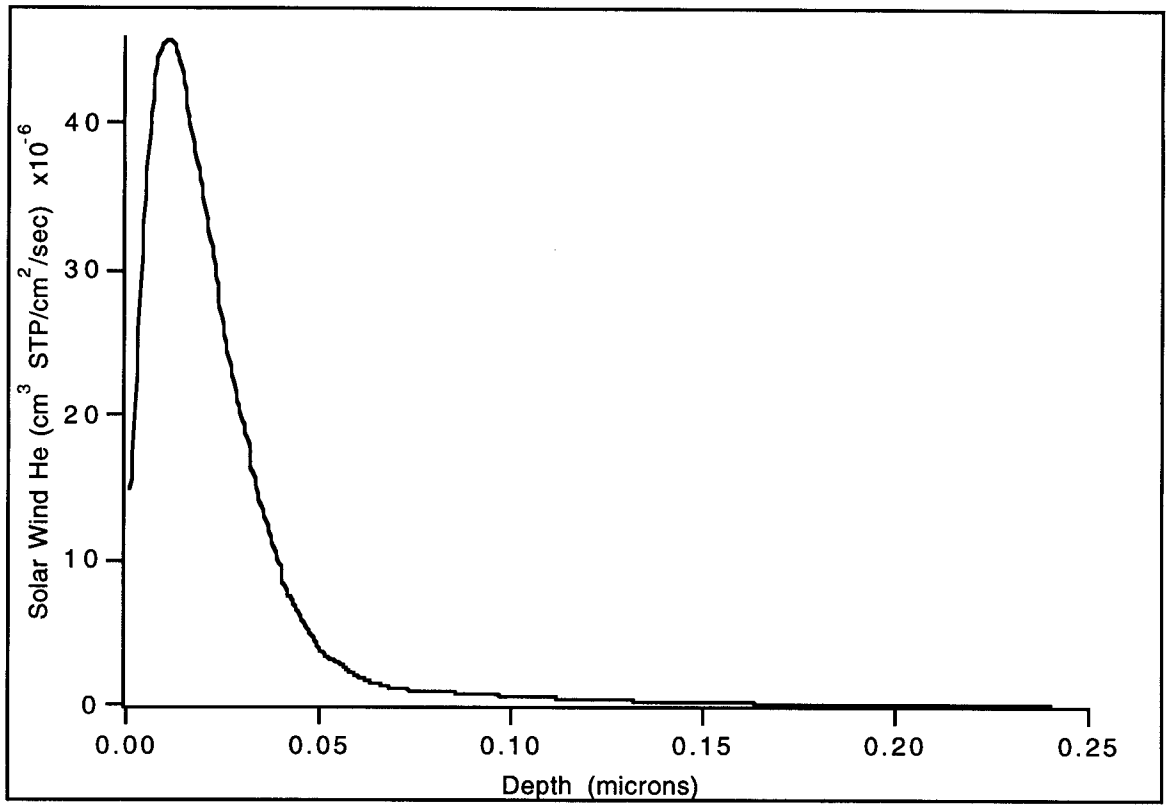

Figure 5-2. Smoothed solar wind helium flux as a function of depth calculated by superimposing results of TRIM calculations for the 44 energy bins in the energy spectrum from Pioneer 10.

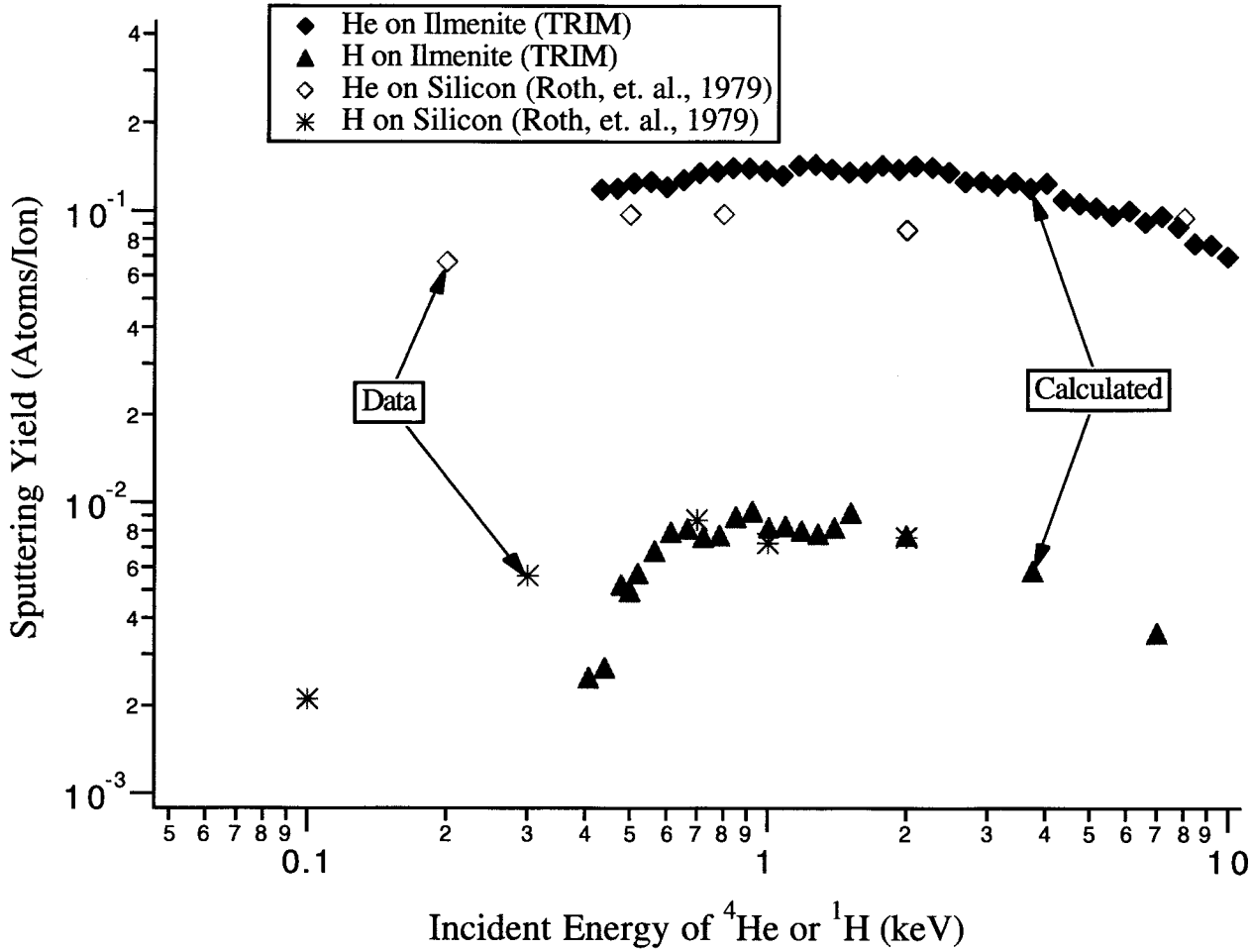

Figure 5-3. Sputtering yields for solar wind hydrogen and helium ions on ilmenite, as calculated using TRIM and the values in Table 5-1. Also shown are literature values for hydrogen and helium on silicon [Roth et al., 1979].

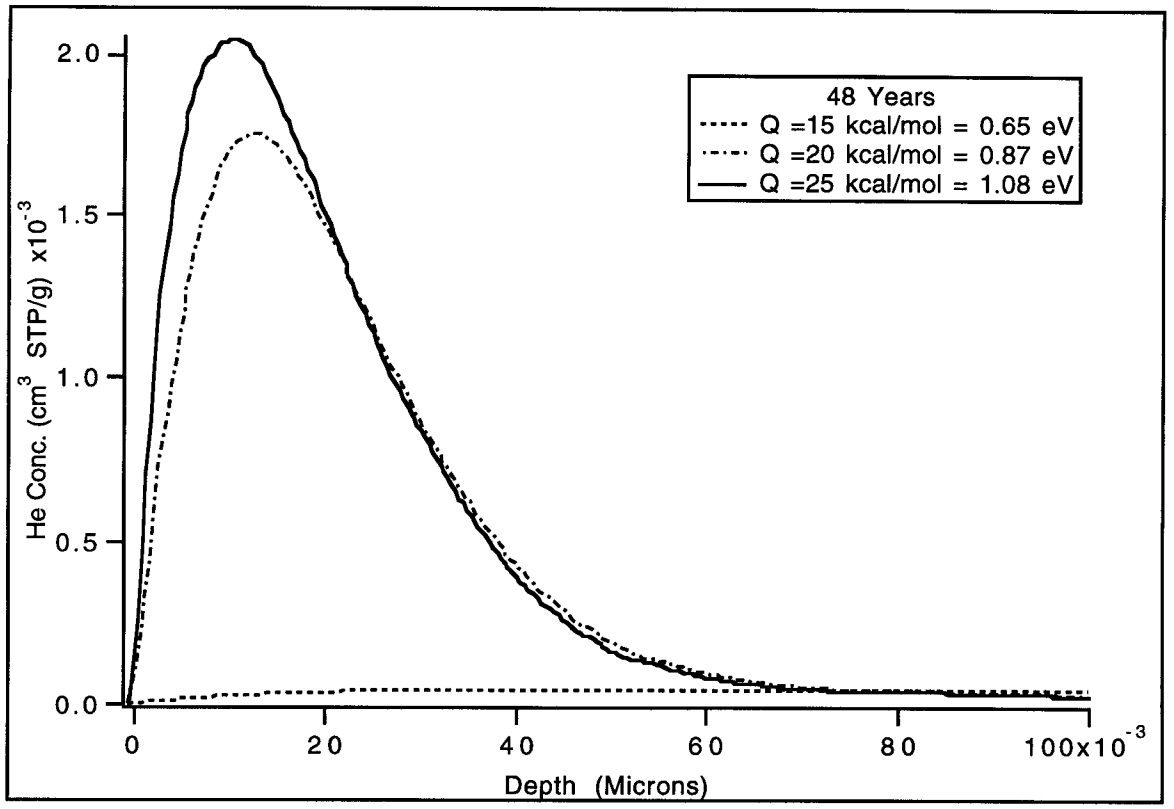

Figure 5-4. Plot of He concentration as a function of depth calculated by the LRD code for $D_0=7.08\times10^{-11}$ cm^2/s and three activation energies. Total time simulated by each run was 60 years.

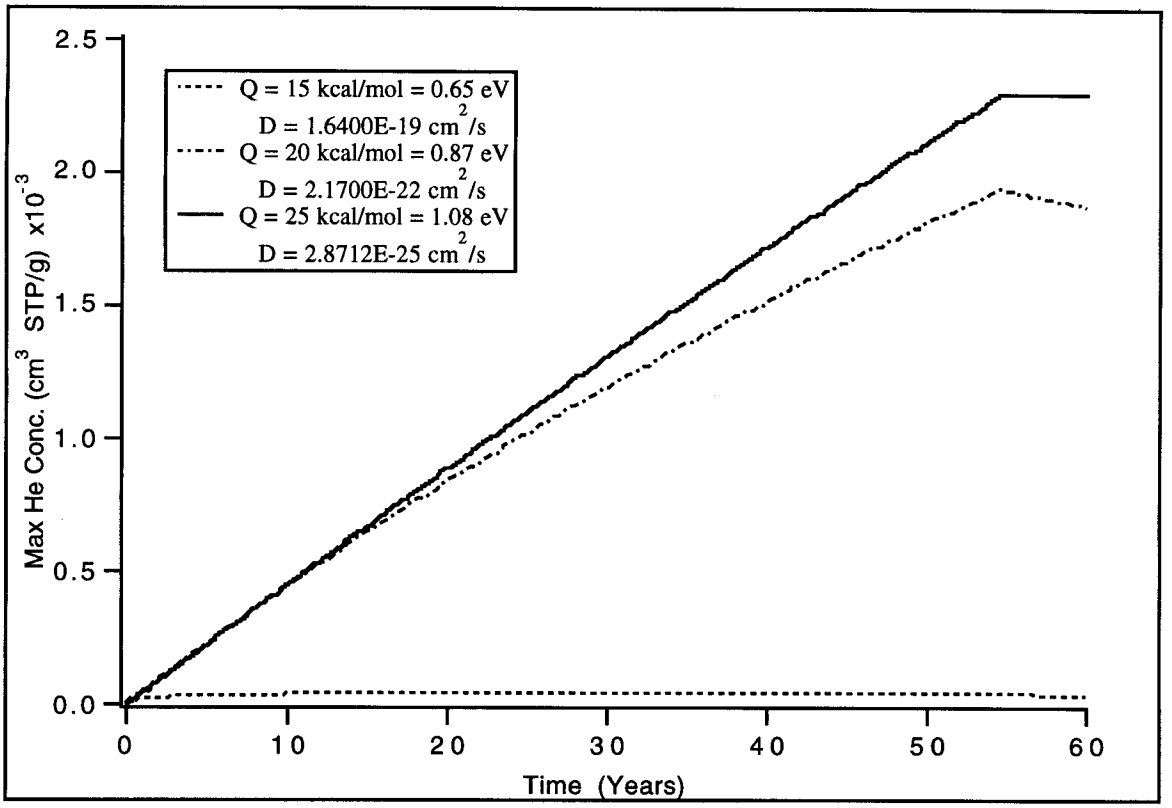

Figure 5-5. A plot of maximum He concentration in a single zone as a function of time in runs of LRD code for $D_0=7.08\times10^{-11}$ cm^2/s [Futagami et al., 1993] and three activation energies (Futagami, et. al. [1993] reported Q = 11 kcal/mol = 0.48 eV). Total time of each run was 60 years and the particle was gardened (i.e. buried so implantation is "turned off" and the temperature is determined by a linear approximation of the measured lunar temperature gradient) after about 54 years. The times were chosen for demonstration purposes.

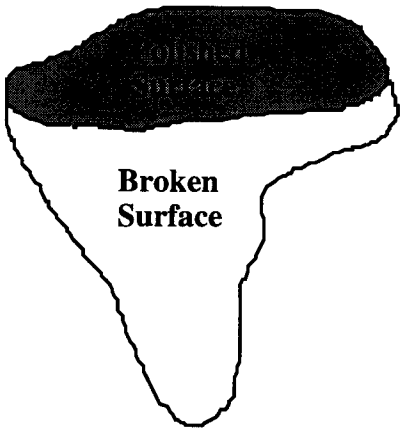

Figure 5-6. Schematic examples of particle shape after crushing. The polished surfaces are typically approximately 200 microns across.

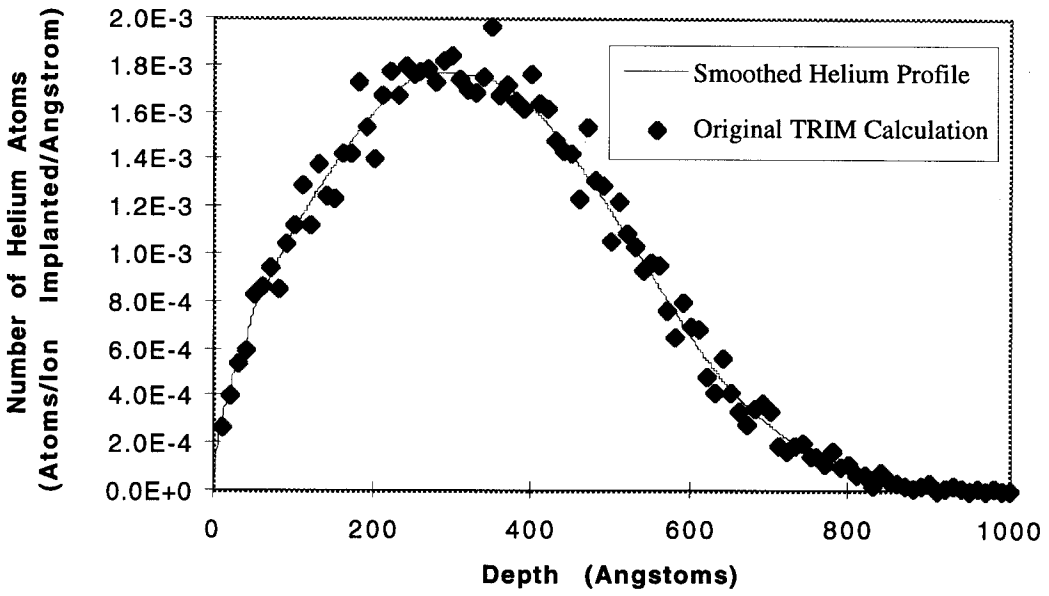

Figure 5-7. Depth profile of 4 keV ^4He in ilmenite ($FeTiO_3$). The original TRIM calculation [Zeigler, 1996] is shown as diamonds, and the solid line shows this data after 12 binomial smoothing passes using IGOR [WaveMetrics, 1993]. The first four points of the smoothed data were replaced by the original data in order to overcome discrepancies due to the smoothing process.

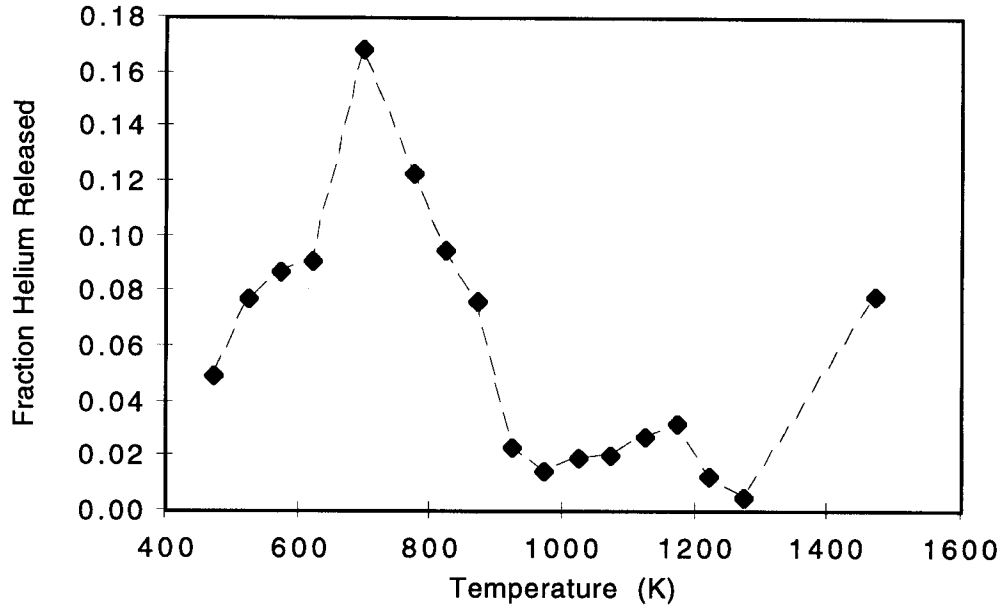

Figure 5-8. The input to the ANNEAL code is the measured fractional helium release as a function of temperature. This is an example of the He fractional release from the New York ilmenite implanted with 10^{16} helium atoms/cm^2 and annealed with 30 minute temperature increments of approximately 50°C. The dashed line is only included to aid the eye.

Chapter 6 Experimental Facilities and Techniques

6.1 Experimental Methods

Since computational methods have not always been effective in either directly observing lunar ^{3}He or identifying the trapping mechanisms for helium in lunar minerals, an experimental study was undertaken. The "roadmap" for this experimental program is shown in Figure 6-1. The first step in this research was the identification of a suitable terrestrial analog of lunar ilmenite [Harris-Kuhlman and Kulcinski, 1998]. Solar wind helium implantation was then simulated using Plasma Source Ion Implantation (PSII) at the University of Wisconsin - Madison [Conrad et al., 1990]. Next, the samples were subjected to isochronal and isothermal anneals and the gases evolved measured using a mass spectrometer [Frick et al., 1988]. The resulting data was used to calculate the diffusion coefficient and activation energy of helium within the ilmenite lattice using the three-dimensional diffusion code ANNEAL written for this thesis. Complimentary work to characterize the state of the samples was also done using positron annihilation spectroscopy (PAS) and transmission electron microscopy (TEM).

The following discussion will begin with the identification of a terrestrial ilmenite analogous to lunar ilmenite, including verification that the material behaves like lunar ilmenite under the simulated irradiation of solar wind helium. It will be shown that the release of helium by the implanted terrestrial ilmenite is quite similar to the helium release by the Apollo 11 samples [Pepin et al., 1970]. The experimental simulation of solar-wind helium and hydrogen incident on the lunar simulant will then be described in detail, followed by a brief description of the step-heating equipment used at the University of Minnesota for the annealing experiments. Finally, the results of the PAS study and TEM investigation will be reported, and the impact of these studies on the current work will be discussed.

6.2 Sample Selection

This study has focused on ilmenite ($FeTiO_3$) since lunar helium concentration has been empirically shown to be correlated with titanium content. Ilmenite is the most abundant oxide mineral in lunar rocks and accounts for most of the lunar titanium [Papike et al., 1991; Cameron, 1988]. Helium retentivity for lunar minerals ranges from the highest to the lowest in the following order: Fe-Ni > ilmenite > olivine-pyroxene > plagioclase [Wieler, 1995]. It has been postulated that either an amorphous coating or the resistance of ilmenite to radiation-induced damage is responsible for the relative enrichment of helium in high-Ti regoliths [Ducati et al., 1973]. It would be helpful if future studies would extend the current experimental method to olivine, pyroxene and plagioclase.

6.2.1 Lunar Ilmenite

Lunar ilmenite has been well studied [e.g. Haggerty et al., 1970; Agrell et al., 1970; Frondel et al., 1970; French et al., 1970; Lovering and Ware, 1970; Keil et al., 1970, McKay and Williams, 1979; Papike et al., 1991]. While it would have been preferable to perform this experimental work on lunar ilmenite returned by the Apollo missions [Schmitt, 1996], it is very difficult to obtain lunar samples from NASA without having demonstrated the experimental method [e.g. Dunstan, 1997]. Also, most of the single crystals of ilmenite that existed in the vesicles or vugs of some of the returned rocks have long since been removed for study [Taylor, 1996].

6.2.2 Synthetic Ilmenite

Pure synthetic ilmenite is difficult to grow [Lindsley, 1996]. This can be seen in the phase diagram (Figure 6-2) for the system Fe-Ti-O at 1200°C as a function of the Fe/Fe+Ti ratio and the oxygen partial pressure (P_{O2}) [Webster and Bright, 1961]. The field for which ilmenite is the only phase present is narrow and covers several orders of magnitude in P_{O2}. This diagram also demonstrates the possibility for non-stoichiometry of both ilmenite and

hematite. For instance, at $\log P_{O2}$ = -6 and 1200°C, ilmenite is present in the form $Fe_{1.2}Ti_{0.8}O_3$.

Professor Pandey at Texas A&M University (currently at the University of Alabama) has been able to grow single crystals of dimension 10 mm by 25 mm, much larger than previously possible [Lindsley, 1996]. He has been exploring the possibility of using ilmenite, a wide band gap semiconductor, for high temperature semiconductor substrates and space applications such as solar cells [Pandey et al., 1996]. Previous studies of synthetic ilmenite have shown exsolution of TiO_2 (phase unknown, but likely rutile) and free iron [Pandey et al., 1996]. This would indicate that the P_{O2} used was too low (Figure 6-2).

The chemical analysis of ilmenite is somewhat problematic because of its oxygen content and its solid solution with hematite. Oxygen is particularly difficult to quantify due to the high mass absorption coefficient for oxygen x-rays of many materials [Nash, 1992]. Oxide films and uneven carbon layers can wreak havoc with oxygen measurements [Goldstein et al., 1991]. The measurements are dependent on the chemical environment of the element being analyzed. This can be seen in Table 6-1 where the analysis of a pure iron standard using a calibration for iron from a hematite standard only yields about 89% by weight iron. Obviously pure iron is not an acceptable standard with which to analyze iron in oxides and vice versa. The differences in standards from the material being analyzed adds to the uncertainty of the measurements. Reliable measurements typically yield weight percentages of 100% ± 1%.

Reliable standards for ilmenite were not available at the time of this work, so the electron probe microanalyses performed for this thesis used a rutile (TiO_2) standard for Ti analysis and a hematite (Fe_2O_3) standard for Fe and O. To increase accuracy, the measurements for iron were taken by integrating over the iron K_α peak rather than taking the peak intensity. Additional standards included tephroite (Mn_2SiO_4) for Mn and Si, and chromite ($MgCr_2O_4$) for Mg and Cr. The presence of vanadium in the rutile standard was

also checked since the K_β x-ray of Ti and and the K_α x-ray of V have similar wavelengths. The weight percent of vanadium measured using EPMA in the rutile standard and pure titanium standard was 0.45 ± 0.02 and 0.30 ± 0.04 respectively. Therefore, vanadium is not considered in any of the analyses reported here.

Table 6-1. Electron microprobe analysis (weight percent) of as received synthetic ilmenite from Texas A&M (ave. of four points), inclusions in the synthetic ilmenite and the iron standard for comparison.

Element	Synthetic Bulk (Wt. %)	Synthetic Inclusions (Wt. %)	Iron Standard (Wt. %)
Mg	<< 0.01	0.01	<< 0.01
0	34.36	0.12	0.11
Al	<< 0.01	<< 0.01	<< 0.01
Si	0.07	0.07	0.02
Ti	47.51	0.73	0.01
Cr	0.03	0.01	<< 0.01
Mn	0.03	0.01	0.05
Fe	20.88	87.71	89.03
Total	102.88	88.65	89.22

A sample approximately 2 cm x 2 cm x 1 cm was received from Professor Pandey. The sample was seeded on a tungsten wire and grown from a melt in a nitrogen atmosphere [Pandey, 1997]. Preliminary backscattered images and electron probe microanalysis (EPMA) of the sample indicated that a relatively large amount of free iron had formed (Figure 6-3) indicating that the P_{O_2} during growth was too low. The analyses of the bulk material are

given in Table 6-1 through Table 6-3. It appears that the material is mainly pseudobrookite ($FeTi_2O_5$, orthorhombic phase) with iron inclusions (Figure 6-2).

Table 6-2. Electron microprobe analysis (atomic percent) of as received synthetic ilmenite from Texas A&M (ave. of four points).

Element	Synthetic Bulk Atomic Percent
Mg	0.01
0	61.06
Al	0.00
Si	0.07
Ti	28.20
Cr	.018
Mn	.016
Fe	10.63
Total	100.00

Annealing the sample at 1200°C for 8 hours in a reducing 1:1 $CO:CO_2$ atmosphere ($\log P_{O2} \approx -11$ or $\log[P_{CO}/P_{CO2}] \approx 0$) caused the free iron to dissolve back into the bulk. However, backscattered electron images taken during EPMA following the anneal showed that only about 30% of the sample became ilmenite while the remaining 70% had a composition between that of ilmenite ($FeTiO_3$) and ulvöspinel (Fe_2TiO_4) (Table 6-3 and Figure 6-4, upper left). Large voids also appeared which retained some of the silica polishing media (Figure 6-4, upper right). Since only one sample was available, the source was discarded. Sources for future work may include Los Alamos National Lab [Mitchell, 1996] and the State University of New York at Stony Brook [Lindsley, 1996].

Table 6-3. Elemental weight percent of several iron-titanium oxides compared to the weight percent analysis of the bulk synthetic ilmenite (ave. of four points) and the bulk synthetic ilmenite after annealing at 1200°C for 8 hours in 1:1 $CO:CO_2$.

Element	Fe_2TiO_4	$FeTiO_3$	$FeTi_2O_5$	Synthetic Bulk	Synthetic Bulk Annealed
Fe	49.95	36.80	24.11	20.88	34.47
Ti	21.42	31.57	41.36	47.51	30.02
O	28.62	31.63	34.53	34.36	36.80
Total	100.00	100.00	100.00	102.75	101.30

6.2.3 Polycrystalline Terrestrial Ilmenite

There are major differences between lunar ilmenite and terrestrial ilmenites. The main difference involves the fact that minerals on the Earth solidified in more oxygen-rich environments than did those on the Moon. Terrestrial minerals have also formed and preserved in the presence of water. Both of these differences resulted in mineral phases present in ilmenite on Earth that do not exist on the Moon. Terrestrial minerals in the crust formed in oxygen partial pressure (P_{O_2}) regions above the magnetite/wustite boundary (above about $\log P_{O_2} = -9$) while the lunar minerals formed in the region below the wustite/iron boundary (below about $\log P_{O_2} = -12$ at 1200°C) [Papike et al., 1991; Webster and Bright, 1961]. Consequently, the minerals hematite and magnetite are not found on the Moon.

The sample selection may not be as critical as one might think since modal analyses of the Apollo and Luna samples show relatively small percentages (0-20% by volume) of ilmenite [Papike et al., 1991]. Evidently, this small amount of ilmenite is responsible for the helium inventory and helium release characteristics of the Apollo 11 and Apollo 17 regoliths. It will be assumed that a terrestrial sample that is mainly ilmenite will display release behavior

similar to that of the lunar samples. This hypothesis is strengthened by the empirical correlation between helium and titanium [Cameron, 1988; Fegley and Swindle, 1993; Taylor, 1990]. Other phases presumably do not trap helium nearly as well and thus, will release their small helium inventory at lower temperatures than will ilmenite. Care has been taken to use samples with the highest proportions of ilmenite possible.

Natural polycrystalline ilmenites from Sierra Leone, Liberia, New York and Quebec have been considered in this study. The samples were examined using secondary electron microscopy (SEM), high-resolution transmission electron microscopy (HRTEM), energy dispersive x-ray analysis (EDX) and electron probe microanalysis (EPMA). These analyses have been complicated due to sub-micron diameter particles in some of the samples.

6.2.3.1 Ilmenite xenocrysts

Samples of natural ilmenite were obtained from Professor Haggerty of the University of Massachusetts. These ilmenite xenocrysts were formed in the mantle of the Earth, unfortunately at higher pressure than lunar ilmenites, but are known to be more reduced than most terrestrial ilmenites [Haggerty, 1996]. The samples were cross-sectioned, polished and analyzed using EPMA and the standards mentioned above.

The ilmenite in these samples is similar in bulk composition to the lunar regoliths from the Apollo 11 site (Table 6-4 and Figure 6-5). The EPMA measurements for these xenocrysts are only qualitative since a standard of magnesian ilmenite was not available at the time this work was done. The amount of Fe_2O_3 in the xenocrysts indicates that they are not as reduced as the lunar regolith or the lunar rocks. The xenocrysts all have amounts of $MgTiO_3$ (geikielite) similar to a geikielo-ilmenite fragment from lunar fines 10085. An even distribution of oriented precipitates have also been found in these xenocrysts (Figure 6-6). Quantitative analysis of these precipitates has proven difficult due to their small dimensions. Energy dispersive x-ray analysis of the precipitates shows elevated levels of chromium and aluminum.

6.2.3.2 Marcy anorthosite massif, Adirondack Mountains, New York

A granular ilmenite from Sanford Lake in the Adirondack Mountains was provided by Professor John W. Valley of the University of Wisconsin - Madison. This ilmenite probably formed under similar conditions as those in the crust of the Moon, although dissimilar to those formed in the lunar basalts that are the primary contributor to the regolith. This sample was polished and examined using EPMA. The composition of this ilmenite is very similar to that of most lunar ilmenites with a small amount of hematite present (Table 6-4 and Figure 6-5). This ilmenite also contains much less geikielite than the xenocrysts. This sample was useful in the current study since the small volume of the hematite lamellae and other inclusions (≈10%) will probably contribute little to the total evolved helium and/or will evolve helium at lower temperatures (Figure 6-7).

6.2.3.3 St. Urbain, Quebec, Canada

A sample of ilmenite from a group of anorthosite dikes and lenses in St. Urbain township of Quebec were provided by Professor Eugene N. Cameron of the University of Wisconsin - Madison. The sample was polished and examined using EPMA. This ilmenite is the most lamellae-rich sample of those examined (Figure 6-8). Note that the lamellae exist on different dimensional scales -- small hematite lamellae within the bulk ilmenite and small lamellae of ilmenite within the hematite lamellae. The oxide composition of the ilmenite in this sample is given in Table 6-4, and its mineral composition is shown Figure 6-5. The ilmenite in this sample appears to be somewhat more reduced than that of the previous samples since the amount of dissolved hematite is less than 4 percent as determined by EPMA. It also contains more geikielite than the Apollo 11 ilmenites.

Table 6-4. Compositions (weight percent) of ilmenite grains from Apollo 11 samples 10046 (average of first 6 points) [Lovering and Ware, 1970],10019 [Keil et al., 1970], 10020 and 10071 [Haggerty et al., 1970], 10085, 10045 (average of 6 points), and 10017 (average of 9 points) [Agrell et al., 1970], rock 10017 (Brown et al., 1970). These compositions are compared to those of ilmenite xenocrysts from Sierra Leone and Liberia and ilmenite from anorthite at Sanford Lake, New York and St. Urbain, Quebec analyzed with EPMA.

	Apollo 11 Samples										
Sample Number	10046-5	10019-22	10020-40	10071-28	10085-4-10	10045-35	10017-12	Liberia	Sierra Leone	New York	Quebec
TiO_2	53.13	51.8	53.9	52.8	56.3	53.65	53.95	50.53	50.12	49.14	51.06
SiO_2	0.08	N/A	N/A	N/A	N/A	0.08	N/A	0.09	0.02	0.33	0.02
Cr_2O_3	0.46	0.59	1.3	0.59	0.34	0.66	0.66	0.23	0.23	0.02	0.26
Al_2O_3	0.07	0.15	0.11	0.15	1.64	0.42	N/A	0.40	0.34	0.00	0.00
CaO	0.27	0.06	0.07	0.01	0.44	0.17	N/A	N/A	N/A	N/A	N/A
MnO	0.23	0.51	0.47	0.32	0.34	0.38	0.40	0.26	0.25	0.30	0.00
MgO	2.87	2.18	2.59	2.06	9.63	3.38	0.97	9.43	9.32	1.99	3.28
FeO	42.76	45.3	41.9	44.2	32.39	41.73	43.80	28.68	28.58	40.69	40.06
Fe_2O_3								8.11	9.77	8.03	3.48
Total Oxides	99.87	100.59	100.34	100.13	101.08	100.30	99.78	97.73	98.62	100.50	100.37

N/A = Not analyzed.

6.2.3.4 Ramifications of Using Terrestrial Ilmenites in this Research

A consequence of using natural terrestrial ilmenite for this study is the fact that these rocks always contain exsolved phases (Figures 6-6 through 6-8). These exsolution phases can be as small as several tens of nanometers in size (Figure 6-9 and Figure 6-10). These phases do not perfectly match the bulk and can provide fast diffusion paths along their grain boundaries. These inclusions can also undergo phase changes upon annealing, as well as having coefficients of thermal expansion that are different from the bulk material. Different rates of thermal expansion can stress the lattice such that additional planar defects can be generated and the diffusion characteristics can be changed.

Minerals on the Moon also solidified under very different oxygen fugacities from the same minerals on the Earth. This difference in oxygen fugacity results in different point defect structures for these materials (Chapter 3). The ilmenites from the Adirondacks cooled at approximately 1 - 5°C per million years resulting in a closure temperature in the range of 500 - 600°C (determined from oxygen diffusion data for magnetite [Giletti and Hess, 1988]). Lunar minerals cooled faster than terrestrial minerals with a closure temperature about 100 - 150°C above that of terrestrial minerals [Papike et al., 1991]. These closure temperatures allow the estimation of the concentration of point defects in these minerals (see Chapter 3 for a discussion of point defect thermodynamics). Assuming closure temperatures of 600°C and 750°C, the fractional concentration of vacancies in ilmenite are calculated to be about $1x10^{-5}$ and $7x10^{-5}$ for the terrestrial and lunar ilmenites, respectively.

6.2.4 Sample Criteria and Behavior

All of the samples contain exsolved phases of some kind. This cannot be avoided in natural samples. Ilmenite is only a small part of any lunar rock or sample of the regolith [Papike et al., 1991]. If the helium inventory is due to the small ilmenite component of the lunar regolith, then it must be assumed that the other minerals are either not trapping helium

or are losing it at lower temperatures during annealing. In either case, a "contaminated" terrestrial ilmenite appears to be a fairly close match to lunar ilmenite-rich regolith. The ilmenite from anorthite in New York was used in the first implantation experiment since these ilmenites most closely match the lunar ilmenites. The ilmenite from New York also contains the smallest amount of dissolved geikielite and exsolved hematite lamellae, thus decreasing the number of variable properties in this experiment.

6.2.4.1 Initial Implantation of Helium to Confirm Release Behavior

To determine how well the chosen terrestrial analog (discussed above) matches the behavior of lunar ilmenites under irradiation by solar-wind helium, plasma source ion implantation (PSII) was used to simulate the solar-wind. The samples were polished with 0.05 micron colloidal silica and mounted on a 6 inch (15.24 cm) silicon wafer to maintain normal ion incidence during PSII. After the PSII chamber was evacuated to a base pressure of about 10^{-6} torr, the samples were sputter-cleaned with 600 eV argon, and implanted with 4 keV ^{4}He to a dose of $1x10^{16}$ ions/cm^2 (details discussed in section 6-3). This dose was chosen to be below the amount of ^{4}He in grains of ilmenite from the mature lunar regolith sample 76501,44 [Ducati et al., 1973; Müller et al., 1976] in order to avoid saturation of the sample. The samples were then brought up to air before being put into the high-vacuum furnace/mass spectrometer system at the University of Minnesota [Frick et al., 1988]. These same procedures were used for the original Apollo samples. The implanted helium was released during a 30 minute isochronal anneal with steps of 50°C to correspond with the helium release data from the Apollo 11 [Pepin et al., 1970], and Apollo 17 samples [Frick et al., 1988].

6.2.4.2 Results Confirming Annealing Behavior Reminicent of Lunar Ilmenites

The helium release behavior of the implanted New York ilmenite is compared to the release from Apollo 11 rock 10069-21, regolith 10084-48, and two single grains of Apollo 17 ilmenite -- from sample 71501-38 (a sub-mature soil) and sample 79035-24 (a mature

breccia). The integrated release of helium from the implanted sample is quite similar to that of the Apollo samples (Figure 6-9).

Several observations can be made with respect to Figure 6-9. First, two slopes appear in the release from the simulant and are similar to the release of 10069-21, possibly indicating two different release mechanisms. The slopes of each of these curves change at about 590°C. Second, the slopes of these two curves are somewhat different from those of 71501-38 and 79035-24 below approximately 80% of total release. Finally, the release from the simulant begins at a lower temperature than for any of the lunar samples. This may be due to implantation rate effects. Longer implantation times are not expected to have much effect since the magnitude of the difference in exposure time is so great. This early release may also be a result of the "contamination" of the sample by hematite and/or other minerals.

It was concluded that PSII is capable of simulating the solar-wind implantation of volatile elements into minerals. The experiment also confirms that the release of helium by regoliths from high-titanium locations on the Moon is a function of their ilmenite content.

6.2.4.3 Final Selection

The selection of a terrestrial analog for lunar ilmenite was not a trivial exercise. It was complicated by the difficulty of the quanitative analysis of oxides by EPMA and the fact that the terrestrial ilmenites formed under very different conditions from those on the Moon. An ilmenite from the Marcy anorthosite massif in New York and an ilmenite from St. Urbain, Quebec were chosen to minimize the effects of dissolved geikielite and hematite. Isochronal annealing of an implanted sample of the New York ilmenite shows that two separate release mechanisms may be involved. Additional anneals with shorter time steps may illuminate the details of these mechanisms and will be useful for deconvolving the activation energy of the trapping mechanism(s). The co-implantation of hydrogen to simulate the effect of solar-wind hydrogen on the range of helium in ilmenite and the radiation-induced reduction of ilmenite will be discussed in the following chapter.

6.3 Simulation of Solar-Wind Implanted Helium and Hydrogen

Implantation of ^3He, ^4He and protons was done in the Plasma Source Ion Implantation (PSII) device operating at the University of Wisconsin - Madison [Conrad, 1988; Conrad et al., 1990; Malik et al., 1995]. This device is capable of implanting ions at solar-wind energies and higher using 4π geometry (Figure 6-12). Planar implantation has been used for several solar-wind implantation simulation studies [Lord, 1968; Ducati et al., 1973; Futagami et al., 1990; Futagami et al., 1993]. It is thought that the PSII method is more stable than beam-line techniques for the low energies and fluences considered in this thesis.

6.3.1 Sample Preparation

6.3.1.1 Mechanical Polishing

Samples of specular ilmenite (very large grain size) from New York and St. Urbain, Quebec were sliced into slabs about 2 cm x 3 cm x 1 mm thick with a diamond wafering blade, using water as a coolant. The wafers were then polished using standard metallographic techniques. Rough grinding was done with water on silicon carbide grinding papers: grits 60, 120, 240, 320, 400, 600, 800 and 1200. Diamond paste was used to polish the samples from 30 microns grain size down to 0.25 microns. The final mechanical polish was done with 0.05 micron colloidal silica. The samples were cleaned using detergent and water, ethanol and finally, a methanol rinse. The samples were mounted on a 6 inch (15.24 cm) low-resistivity silicon wafer (recycled from implantation studies using boron) using carbon tape to maintain electrical conductivity with the substrate. The samples were mounted away from both the center and the edge of the wafer in order to maintain as even an implantation as possible. After mounting the samples were again rinsed with ethanol to removed as much dust as possible.

6.3.1.2 Sputter-Cleaning with Argon

Since 0.05 micron silica leaves scratches 50 nm across with mechanical damage down to about 150 nm (as a rule of thumb), and the implantation depth of 4 keV ^{4}He in ilmenite is only about 33 nm, it was necessary to remove as much mechanical damage as possible to avoid its influence on the annealing experiments. Plasma source ion implantation (PSII) provided an easy way to sputter-clean the samples *in-situ* immediately before implantation. The parameters used for the sputter-cleaning runs in PSII are given in Table 6-5.

Table 6-5. PSII conditions used for the sputter-cleaning of samples performed in this thesis.

Parameter	Ar ($1x10^{16}$/cm^2)	Ar ($2x10^{17}$/cm^2)
Base Pressure	$3x10^{-6}$ torr	$5x10^{-6}$ torr
Voltage	0.6 kV	0.6 - 1 kV
Current per Pulse	14.55 μA	14 μA
Repetition Rate	350 Hz	350 Hz
Pulse Width	60 μsec	75 μsec
Total Filament Current	3.0 Amps	3.0 Amps
Time	15 min.	60 min.
Ar Pressure	4.2 - 4.3 mtorr	4.22 mtorr
Pumping	Cryo	Turbo

The electronic stopping code, TRIM, was used to estimate the dose required to remove the mechanical damage from the surfaces of the samples. The minimun energy for which PSII produces a stable argon plasma is around 600 eV [Fetherson, 1997]. Argon ions of this energy and normal incidence only penetrate ilmenite to a depth of about 3.5 nm (Figure 6-13). The sputtering yield for 600 eV Argon atoms at normal incidence was calculated to be

0.805 atoms/ion (see Chapter 5 for TRIM parameters for ilmenite). The removal of 150 nm of material would have required a dose of about 1.3×10^{18} Ar ions/cm^2. An initial dose of 1×10^{16} Ar ions/cm^2 was used due to concerns about blistering. It was estimated that this dose would remove about 0.76 nm. In later experiments, a sputter-cleaning dose of 2×10^{17} Ar ions/cm^2 was used to remove 15.6 nm of material based on positron annihilation spectroscopy (PAS) observations (see Section 6.3.1.3 for results and details). The samples were allowed to cool for 1 hour between sputter-cleaning and implantation to avoid diffusion due to heating. Heating due to implantation will be discussed in detail in Section 6.3.2.3

6.3.1.3 Positron Annihilation Spectroscopy

Positron annihilation spectroscopy (PAS) is uniquely sensitive to small concentrations of point defects -- vacancies, vacancy clusters and microcavities [Agullo-Lopez et al., 1988]. This analytical method, also known as age-momentum correlation spectroscopy, depends on the tendency of positrons to seek out open-volume defects where they exist until annihilated by electrons [Asoka-Kumar et al., 1994]. Positrons localized at these defects will have longer lifetimes and angular correlation of the 511 keV gamma-rays can be used to "finger print" defect structures.

Many good reviews have been written concerning PAS and its variations [Szeles and Lynn, 1995; Schultz, and Lynn, 1988; Lynn et al., 1991]. The reader is referred to the references for the details of PAS. Helium implantation into metals has also been investigated using slow, monoenergetic positron beams [Kogel and Triftshauser, 1983].

Several samples of the first ilmenite implanted with ^{4}He were analyzed using correlated PAS (coPAS) at Washington State University under the direction of Professor Kelvin G. Lynn. Correlated PAS requires two helium-cooled germanium gamma-ray detectors to record a single annihilation event. Both of the co-linear gamma-rays from an annihilation be detected for an event to be recorded.

Professor Lynn has constructed a variable positron source (50 eV to 30 keV) with a beam diameter of about 1 inch. The samples from this thesis were disks of ilmenite 3 mm in diameter (smaller than the beam diameter) so the gamma-ray yield from the samples was smaller than that used to calibrate the spectrometers. These samples were suspended from 0.13 mm tantulum wire in a chamber which was evacuated to a pressure of a few 10^{-6} torr. The sample assembly was attatched to a manipulator equipped with a micrometer. The samples were initially positioned with the micrometer, and finally positioning was accomplished by maximizing the gamma-ray signal measured by the detectors.

The results of the PAS investigation conducted are shown in Figure 6-14. The depth is calculated from the empirical relation [Schultz and Lynn, 1988]:

$$Depth = AE^n \qquad (6\text{-}1)$$

where A = 8.351 nm/keV, E is the positron energy, and n = 1.6 for positrons in most materials.

6.3.2 Plasma Source Ion Implantation

6.3.2.1 General Principles

Plasma source ion implantation (PSII) is a non-line of sight technique for the surface modification of materials [Conrad, 1988; Conrad et al., 1990]. The target -- in this case a silicon wafer with wafered samples lying on top -- is placed in a 1 m^3 chamber which is evacuated to a base pressure of about 10^{-6} torr. Gas of the species to be implanted is allowed to flow through the chamber at a pressure of several millitorr. A plasma is generated using tungsten filaments to ionize the gas by energetic primary electron impact. Other ways of generating a plasma for higher energy implantations are by radiofrequency (RF) or glow discharge methods.

A series of negative high voltage pulses are applied to the target (Figure 6-15), and the resulting electric field accelerates the ions in the plasma to high energies normal to the surface

of the target (Figure 6-12). In the case of a wafer, significant asymmetries can occur at the edges where the electric field is changing rapidly. Focusing of the ions at the center of the wafer can also occur [Fetherston, 1997]. Therefore, the samples of ilmenite are placed off-center and away from the edges to maintain a uniform implantation.

The time needed to implant a desired fluence is given by Equation 6-2:

$$time = \frac{Fluence * Area * e * (\gamma + 1)}{I_p * RR * N}. \qquad (6\text{-}2)$$

In Equation 6-2, "time" is the total time of the implantation (sec), fluence is the desired final dose (ions/cm^2), e is the charge on an electron (Coulombs per electron), γ is the secondary electron emission coefficient (SEEC) (electrons emitted per incident ion), I_p is the average current per "on-time" of the pulse (Amps), RR is the repetition rate (Hz) and N is the number of atoms per molecule of the precursor gas (i.e. N=1 for He, N=2 for H_2). The SEEC's used (Table 6-6) were taken from a study of electron emission from clean metal surfaces [Baragiola, 1979]. These values do not change drastically for other elements (± at most 0.2) at these energies and the choice of the value to use will not affect the calculation of time needed for the dose (a 30% error in γ only results in an error of 12% in Equation 6-2). The values of the SEEC were generalized to 0.25 for H and 0.5 for He in the current implantations.

6.3.2.2 Conditions

The general conditions under which the samples were implanted with ^{3}He and ^{4}He are listed in Table 6-7. Conditions for the hydrogen implantations are given in Table 6-8. During the implantation, the sample is best described as a flat plate since the samples have areas much smaller (~6 cm^2) than the silicon wafer (~180 cm^2) and the sample thickness (~1 mm) is much less than the wafer diameter (15.24 cm).

Table 6-6. Secondary electron emission coefficients for H and He on pure Cr [Baragiola, 1979]. These values of the SEEC were generalized to 0.25 for H and 0.5 for He in the current implantations.

Incident Ion	Energy (keV)	Electron yield per ion
H^+	1	0.280
H_2^+	1	0.240
$^3He^+$	3	0.420
$^4He^+$	4	0.485

Table 6-7. Typical PSII conditions used for the He implantations performed in this thesis.

Parameter	^3He ($1x10^{12}/cm^2$)	^4He ($1x10^{16}/cm^2$)
Base Pressure	$3x10^{-6}$ torr	$2x10^{-6}$ torr
Voltage	3 kV	4 kV
Secondary Electron Emission Coefficient	0.5	0.5
Current per Pulse	8 μA	7.5 μA
Repetition Rate	98 Hz	98 Hz
Pulse Width	120 μsec	125 μsec
Total Filament Current	0.2 Amps	0.1 Amps
Time	~50 pulses	9.5 min.
Gas Pressure	6 mtorr	5.0 mtorr

Table 6-8. PSII conditions used for the H implantations performed in this thesis.

Parameter	H_2 ($1x10^{14}$ H/cm^2)	H_2 ($5x10^{15}$H/cm^2)	H_2 ($1x10^{17}$H/cm^2)
Base Pressure	$5x10^{-6}$ torr	$5x10^{-6}$ torr	$5x10^{-6}$ torr
Voltage	2 kV	2 kV	2 kV
Secondary Electron Emission Coefficient	0.25	0.25	0.25
Current per Pulse	5.5 μA	6 μA	6 μA
Repetition Rate	1 Hz	100 Hz	100 Hz
Pulse Width	125 μsec	125 μsec	125 μsec
Total Filament Current	0.2 Amps	0.24 Amps	0.24 Amps
Time	5.5 min.	2.5 min.	54 min.
Gas Pressure	5.0 mtorr	5.0 mtorr	4.85 mtorr

6.3.2.3 Heating

The temperature of the ilmenite during plasma source ion implantation is of concern since heating will allow the implanted species to diffuse. Any diffusion due to heating will modify the depth profile, making the calculation of the depth profile using TRIM less acurate. Residual heat from sputter cleaning will have a similar effect. The surface temperature can be represented by Equation 6-3 where q_h'' is the applied surface heat flux, k is the heat conductivity and κ is the heat diffusivity [Blanchard, 1994].

$$T(0,t) = \frac{2q_n''}{k}\sqrt{\frac{\kappa t}{\pi}} \qquad (6\text{-}3)$$

Experimental data for these parameters is scarce and the values used are given in Table 6-9. Data for hematite (Fe_2O_3) and magnetite (Fe_3O_4) were substituted where data was unavailable for ilmenite.

The peak heat flux was calculated from the current on the sample during the pulse (Table 6-10). Average heat flux was calculated from the total current on the sample over the duration of the implantation (Table 6-10). As a worst-case senario, the heat flux lost due to radiation and conduction was ignored. The maximum peak heat flux for these implantations results in a surface temperature rise of 0.20 K for a 125 μsec pulse (from Equation 6-3). Using the thermal diffusivity of silicon instead of hematite (κ=0.01 cm^2/s) this temperature rise becomes 0.49 K over 125 μsec.

Table 6-9. Material properties used for the thermal analyses of PSII implantations in this thesis. Properties are for temperatures beween 300K and 400K.

Material	k (W/mK)	ρ (g/cm^3)	c_p (J/kgK)	κ (m^2/s)	Reference
$FeTiO_3$	-	4.79	741		Touloukian et al., 1973
Fe_2O_3	-	-	-	$1.75x10^{-7}$	Touloukian et al., 1973
Fe_3O_4	7	-	-		Robie et al., 1978

The target temperature can be calculated as a function of time using the lumped capacitance model developed by Blanchard [1994]. This model solves the equation,

$$mc_p \frac{dT}{dt} = A_h q_h'' - A_r q_r'' - \dot{Q}_c \qquad (6\text{-}4)$$

where m is the total mass of the base and targets, c_p is the mass-averaged heat capacity, A_h is the total heated area, q_h'' is the cycle -averaged heat flux applied to that area, A_r is the total radiating area, q_r'' is the radiation heat flux lost from that area and $\dot{Q}_c$ is the total heat lost to conduction. Several emissivities were considered -- 0.05, 0.10 and 0.25 for worst-case senarios, 0.4 for polished samples [Blanchard, 1994], and 0.77 for Fe_2O_3 at 373 K [Touloukian and DeWitt, 1972]. The results for the $2x10^{17}$ ions/cm^2 argon sputter-cleaning

run on ilmenite are shown in Figure 6-14. This run was considered because it has the highest average heat flux of all the implantations performed (Table 6-10).

Table 6-10. Average and peak heat fluxes for highest fluence PSII implantations done for this thesis.

Implanted Species	Energy (keV)	Fluence (ions/cm^2)	Ave. Heat Flux (W/m^2)	Peak Heat Flux (W/m^2)
Ar	0.6	$1x10^{16}$	10.68	397.45
	0.6	$2x10^{17}$	53.41	397.45
^{4}He	4.0	$1x10^{16}$	22.38	2192.81
H	1.0	$1x10^{17}$	49.45	1315.68

The composition of the target makes a difference in these calculations (Figure 6-17). If the target is assumed to be entirely ilmenite and the emissivity is assumed to be 0.1, the maximum temperature reached at the end of the sputter-cleaning is about 31°C and the wafer cools to about 20°C at the end of the cooling period. In the worst case, the target is assumed to be entirely Si (a silicon wafer with ilmenite impurities, ρ = 2.33 g/cm3) and emissivity is assumed to be ε = 0.1. These conditions result in a temperature of 75°C at the end of the sputter-cleaning (54 min.) with the sample cooling to about 34°C at the end of the cooling time. If the emissivity of Fe_2O_3 at 373 K is used (ε = 0.77), little difference is seen between the peak temperatures and the final temperatures of silicon and ilmenite. A silicon wafer reaches the equilibrium temperature more quickly than if the wafer was entirely ilmenite.

6.3.3 Post Implantation Handling

Immediately after implantation, the samples were brought up to air, and placed in a dessicator. They were stored in the desicator for various periods before annealing. Prior to analysis by step-wise heating, the samples were broken to make particles small enough to fit

into the furnaces at the University of Minnesota (Figure 6-18). These furnaces require that the samples be small so that the mass spectrometers are not overwhelmed with gas. Optical micrographs were taken of the polished surface areas of the individual grains produced by crushing so that the areas could be quantified using the computer progam NIH Image [National Institutes of Health, 1996].

6.4 Annealing

6.4.1 Common Techniques for Analyzing Rare Gases in Materials

6.4.1.1 Gas Ion Microprobe

In the 1970's, the Rare Gas Ion Probe (RGIP) was used extensively to obtain noble gas profiles in the outer layers of lunar samples. Warhaut et al. [1979] demonstrated that the RGIP could yield concentration profiles with 5 - 10 nm resolution. They also stated that it was difficult to establish relationships for elemental fractionations because less abundant isotopes fall below the detection limit of the RGIP. This detection limit is related to the fact that only $5x10^{-11}$ g samples of gas are extracted per second [Warhaut et al., 1979].

Müller, et al. [1976] were successful in measuring helium profiles in single grains of lunar ilmenite, plagioclase, glass and an iron spherule. The resolution of their measurements was approximately 100 Å, and the detection limit of ^{4}He was $2x10^{-12}$ cm^3 STP/g.

6.4.1.2 Closed System Stepwise Etching

Closed system stepped etching (CSSE) is a very refined technique developed by Benkert, et al. in Switzerland [Benkert et al., 1993; Signer et al., 1991]. This method avoids elemental or isotopic fractionation due to diffusion during the release of noble gases. This technique etches away the surface with hydrofluoric acid (HF) and then analyzes the gases evolved from the etchant as well as the residue. Although the etching time, temperature and state of the etchant were carefully recorded for each etching step, it remains impossible to reliably measure the volume -- and thus, the thickness -- of material etched in each step

[Wieler, 1995]. In practice, this method has not yielded reliable results due to the superposition of solar wind particles, solar energetic particles, solar flare particles and cosmogenic gases. Some particles etch faster than others and the results are most likely a combination of fractions from each of these groups from different particles.

6.4.1.3 Linear or Stepwise Heating with Mass Spectroscopy

Perhaps the most attractive of the methods used to analyze rare gases in minerals is linear or stepwise heating. However, these heating methods allow for the activation of diffusion mechanisms during the analysis, possibly increasing or decreasing the concentrations found at various depths, effectively "smearing" the results. Bubble formation and phase changes can overshadow the diffusion mechanisms. A further complication results from the temperature extremes on the Moon ranging from about 100 K at night to a maximum on the surface of 380 K during the day [Vaniman et al., 1991].

Most studies involving heating of the lunar samples begin with a sustained heat treatment of the samples at or above 373 K to remove any adsorbed water, etc. The samples appear to have been held at room temperature for an undetermined amount of time after their return from the Moon and dispersal to the research teams. It is unclear what temperatures the samples were exposed to upon reentry. Experiments that use heating methods fail to account for diffusion mechanisms that can take place below the highest temperature on the Moon (about 380 K). Complete understanding of the diffusion and trapping mechanisms of minerals on the lunar surface has not yet been achieved through these studies.

It is useful to look at the release of helium as a function of temperature, but this information is only one parameter. Information concerning the diffusivity can be only be obtained using data from an anneal with different time steps or a linear temperature ramp or in combination with an initial helium profile with respect to depth. Helium release data from several studies of lunar regolith is shown in Figure 6-19 and Figure 6-20 [Pepin, et.al., 1970;

Hohenberg et al., 1970; Srinivasan et al., 1972]. Note that about 50% of the helium in these studies is released by about 500°C and 100% of the helium is released at 1000°C.

6.4.2 Long Heating Time Furnace

One sample, 050997 (New York ilmenite, implanted with 4 keV ^{4}He, dose = $1x10^{16}$ $^4He/cm^2$), was annealed using 30 minute temperature steps of approximately 50°C each. The sample was analyzed [Becker, 1997] using the experimental set up described in detail by Frick et al., [1988] and Frick and Pepin [1981a, b]. The sample was wrapped in platinum foil for analysis and heated by an external resistance heater capable of at most 1200 - 1260°C. The system is evacuated to an equilibrium pressure of << $1x10^{-10}$ torr. A ZrTi bulk getter pump was used to initially "clean-up" the noble gases. Any heavier noble gases were frozen out on a metal frit. Further cleaning of the helium gas released was accomplished with ion getter pumps and noble gas separation on charcoal. Hydrogen was removed using a cold ZrTi alloy getter and N_2 was frozen out in another metal frit. The helium was then analyzed by a 6-inch double focusing Nier-type mass spectrometer with high mass resolution ($M/\Delta M$~800) [Frick et al., 1988]. The temperature of each step was measured using a thermocouple mounted on the quartz furnace.

Blank measurements were taken at 300°C, 600°C and 950°C. These measurements basically measure the amount of helium that diffuses into the quartz sample furnace from the outside atmosphere. These blank measurements are given in Table 6-11. All measurements and errors for this method were calculated using a spreadsheet of measurement and error analysis formulas developed by Dr. Becker [1997]. The average of the low temperature blanks was used for analysis of the measurements for temperatures below 600°C and the average of the blanks taken at 950°C was used for analysis of the remaining data points. The helium measurements for sample 050997 will be given in Chapter 7. Sample numbers in this thesis are of the form month/day/year of implantation. Subsamples are given numbers of the form 050997.1, etc.

6.4.3 Small Particle Furnace

All other samples for this thesis were analyzed [Schlutter, 1997 and 1998] using a pulse heating furnace developed for accurately measuring the noble gases released from interplanetary dust particles [Nier and Schlutter, 1993; Nier and Schlutter, 1992; Nier et al., 1990]. This furnace was used for its capability to analyze for both ^{3}He and ^{4}He. The main goal of this experimental setup is to reduce the mass of the furnace as much as possible and thus reduce the blank measurements since the amount of gas contained in these samples is very small [Nier and Schlutter, 1992].

Table 6-11. Blank measurements for the long duration heating furnace

Temperature	Blank (cm^3STP ^{4}He/g)	Error (%)
300°C	1.07×10^{-8}	± 8.53
600°C	9.59×10^{-9}	± 8.51
Average of low temp. blanks	1.07×10^{-8}	± 8.52
950°C	4.62×10^{-8}	± 10.00
950°C	1.37×10^{-8}	± 8.51
Average of blanks at 950°C	2.30×10^{-8}	± 9.26

The samples were wrapped in a tantulum foil which comprises the oven. The oven is then attached by spring tension to tungsten wires which are spot-welded to heavy nickel leads [Nier and Schlutter, 1992]. The oven material and tungsten springs are thorougly outgassed prior to use. However, these materials still release small amounts of gas during sample analysis. Blank runs are interspersed with the analysis runs. The gases are purified using liquid nitrogen-cooled charcoal traps and a hydrogen was gettered by a liquid nitrogen-cooled volume freshly coated with titanium. The mass spectrometer used is same one used in work

reported by Nier and Schlutter [1992, 1993] and is similar to the one described earlier by Nier and Schlutter [1985]. The sensitivity of the mass spectrometer in static operational mode is such that approximately $3x10^6$ atoms of He produces an ion current of one ion per second [Nier et al., 1990]. Ion counting is used with a background counting rate of less than 1 count per 200 seconds [Nier et al., 1990].

Heating in this apparatus is accomplished by resistive heating of the Ta foil furnace [Nier and Schlutter, 1990]. The nickle leads and tungsten springs are used to apply an electric current directly to the foil. Nier and Schlutter [1992] devised a circuit that multiplies the instantaneous current and voltage with this product determining the voltage needed to keep the power constant during a step. Temperatures above 770°C are typically measured using an optical pyrometer and lower temperatures were extrapolated using an empirical formula which assumes two modes of power loss: 1) conduction and 2) radiation [Nier and Schlutter, 1992]. Figure 6-21 shows the deviation of temperature from the equilbrium value (at long heating times) for 5 second and 30 second annealing times. These data were taken using a thermocouple attatched to one of the tungsten heating filaments [Schlutter, 1998].

A summary of the samples annealed in this apparatus are given in Table 6-12. The error analysis will be given in Chapter 7 along with the data with the results. The errors are assumed to be strictly due to counting statistics ($\sigma_x = \sqrt{N}$) [Bevington and Robinson, 1992; Schlutter, 1998].

6.4.4 Time Required to Reach Equilibrium Temperature

The question of whether or not the samples reach equilibrium with the oven in the heating times used is very relavant to the case of the small particle furnace. It is assumed that the sample annealed in the long heating time furnace reached equilibrium. The temperatures at depths of 300 Å and 1000 Å at annealing times of 5 and 30 seconds were calculated using Equation 6-5 for a semi-infinite solid [Carslaw and Jaeger, 1959].

$$T(t) = T_0 erfc\left(\frac{x}{2\sqrt{\kappa t}}\right) \qquad (6\text{-}5)$$

Table 6-12. Isochronal and isothermal anneals performed in the small particle furnace at the University of Minnesota.

Annealing Type	Time Steps (sec)	Sample Number
Isochronal	5	050997 (2 runs)
	30	050997
		040998
		041098
		041398
		041698
Calibration - No He impanted	30	123197
Isothermal (750°C)	2, 5, 10 and 30	050997

In Equation 6-5, t is the time, T_0 is the constant temperature at x=0, and κ is the thermal diffusivity in m^2/sec. The results are shown in Figure 6-22 with temperature given as the fraction of the surface temperature, T_0. The samples effectively reach equilibrium with their surroundings within the first second of heating to the depth that we are concerned with here (x < 500 Å). Of course this does not take into account the fact that diffusion inward will occur at high temperatures. At 1 μm the sample reaches 99.87% of the surface temperature in 1 sec., so the temperature gradient in the sample should not affect the results of the annealing experiments.

6.5 Transmission Electron Microscopy

The transmission electron microscope (TEM) has been extensively used to study defect clusters, voids and bubbles in metals [e. g. Rühle, 1969; Rühle, 1972; Eyre, 1973]. It is most useful for materials that have been heavily irradiated and have relatively large bubbles, voids or defects. The high resolution TEM complements the other methods used in this

research due to its ability to directly observe lattice disorder, and its ability to provide diffraction data concerning the structures of the samples.

Only a limited amount of transmission electron microscopy was performed for this thesis. High resolution TEM was performed on a sample of ilmenite implanted with ^{4}He using PSII on the CM 200 microscope at the University of Wisconsin [Barker, 1998]. Preliminary studies indicated the presence of a mostly amorphous layer about 25 nm thick (Figure 6-23). Lattice fringes are visible in the darker region of this micrograph indicating crystallinity. However, regions of this layer showed evidence of crystalline order (areas with interference fringes) indicating that this layer resembles the metamict state discussed in Chapter 3.

6.6 References

Agrell, S. O., J. H. Scoon, I. D. Muir, J. V. P. Long, J. D. C. McConnell and A. Peckett (1970) "Observations on the chemistry, mineralogy and petrology of some Apollo 11 lunar samples," *Proceedings of the Apollo 11 Lunar Science Conference*, **1**, pp. 93-128.

Agullo-Lopez, F., C. R. A. Catlow, and P. D. Townsend (1988) *Point Defects in Materials*, (London: Academic Press) pp. 327-329.

Asoka-Kumar, P., K. G. Lynn, and D. O. Welch (1994) "Characterization of Defects in Si and SiO_2-Si Using Positrons," *Journal of Applied Physics*, **76**(9), pp. 4935-4982.

Barker, W. (1998) Personal communication, University of Wisconsin - Madison.

Becker, R. H. (1997) Personal communication, University of Minnesota.

Benkert, J-P., H. Baur, P. Signer, and R. Wieler (1993) "He, Ne, and Ar From the Solar Wind and Solar Energetic Particles in Lunar Ilmenites and Pyroxenes," *Journal of Geophysical Research*, **98**(E7), pp. 13,147 - 13,162.

Bevington, P. R. and D. K. Robinson (1992) *Data Reduction and Error Analysis for the Physical Sciences*, Second Edition, (McGraw-Hill, Inc., New York) pp. 39-40.

Blanchard, J. P. [1994] "Target Temperature Prediction for Plasma Source Ion Implantation," *Journal of Vacuum Science and Technology*, **B12**(2), pp. 910-917.

Brown, G. M., C. H. Emeleus, J. G. Holland, R. Phillips (1970) "Mineralogical, chemical and petrological features of Apollo 11 rocks and their relationship to igneous processes," *Proceedings of the Apollo 11 Lunar Science Conference*, pp. 195-219.

Cameron, E. N. (1988) "Helium Mining on the Moon: Site Selection and Evaluation," *The Second Conference on Lunar Bases and Space Activities of the 21st Century*, (Houston, Texas: Lunar and Planetary Institute) pp. 89-97.

Carslaw, H. S. and J. C. Jaeger (1959) *Conduction of Heat in Solids* (Clarendon Press, Oxford) pp. 58-62.

Conrad, J. R., U. S. Patent No. 4,764,394, (August, 1988).

Conrad, J. R., R. A. Dodd, S. Han, M. Madapura, J. Scheuer, K. Sridharan and F. J. Worzala (1990) *Journal of Vacuum Science Technology A*, **8**, p. 3146.

Ducati, H., S. Kalbitzer, J. Kiko, T. Kirsten, and H. W. Müller (1973) "Rare Gas Diffusion Studies in Individual Lunar Soil Particles and in Artificially Implanted Glasses," *The Moon*, **8**, pp. 210-227.

Dunstan, J. E. (1997) "Free the Rocks," *Space News*, 7/23/98.

Eyre, B. L. (1973) "Transmission Electron Microscope Studies of Point Defect Clusters in FCC and BCC Metals," *Journal of Physics F: Metal Physics*, **3**, p. 422.

Fegley, B., Jr. and T. D. Swindle (1993) "Lunar Volatiles: Implications for Lunar Resource Utilization," *Resources of Near-Earth Space*, J. S. Lewis, M. S. Matthews, and M. L. Guerrieri, eds., (Tucson, Arizona: The University of Arizona Press) pp. 367-426.

Fetherston, P. (1997) Personal communication, University of Wisconsin - Madison.

French, B. M., L. S. Walter, and K. J. F. Heinrich (1970) "Quantitative Mineralogy of an Apollo 11 Lunar Sample," *Proceedings of the Apollo 11 Lunar Science Conference*, **1**, pp. 433-444.

Frick, U. and R. O. Pepin [1981a] "On the Distribution of Noble Gases in Allende: A Differential Oxidation Sudy," *Earth and Planetary Science Letters*, **56**, pp. 45-63.

Frick, U. and R. O. Pepin [1981b] "Microanalysis of Nitrogen Isotope abundances: Association of Nitrogen with Noble Gas Carriers in Allende," *Earth and Planetary Science Letters*, **56**, pp. 64-81.

Frick, U., R. H. Becker, and R. O. Pepin (1988) "Solar Wind Record in the Lunar Regolith: Nitrogen and Noble Gases," *Eighteenth Lunar and Planetary Science Conference*, G. Ryder, ed., (Cambridge: Cambridge University Press) pp. 87-120.

Frondel, C. C. Klein, Jr., J. Ito, and J. C. Drake (1970) "Mineralogical and Chemical Studies of Apollo 11 Lunar Fines and Selected Rocks," *Proceedings of the Apollo 11 Lunar Science Conference*, **1**, pp. 445-474.

Futagami, T., M. Ozima and Y. Nakamura (1990) "Helium Ion Implantation into Minerals," *Earth and Planetary Science Letters*, **101**, pp. 63-67.

Futagami, T., M. Ozima, S. Nagai, and Y. Aoki (1993) "Experiments on Thermal Release of Implanted Noble Gases in Lunar Soil Grains," *Geochimica et Cosmochimica Acta,* **57**, pp. 3177-3194.

Goldstein, J. J., S. K. Choi, F. J. J. van Loo, H. J. M. Heijligers, J. M. Dijkstra and G. F. Bastin (1991) "The Influence of Surface Oxygen Contamination of Bulk EPMA of Oxygen in Ternary Titanium-Oxygen-Compounds," Microbeam Analysis - 1991, D. G. Howitt, ed. (San Francisco Press) pp. 57-58.

Haggerty, S. E., F. R. Boyd, P. M. Bell, L. W. Finger and W. B. Bryan (1970) "Opaque minerals and olivine in lavas and breccias from Mare Tranquillitatis," *Proceedings of the Apollo 11 Lunar Science Conference*, **1**, pp. 513-538.

Haggerty, S. E. (1996) Personal communication, University of Massachusetts.

Harris-Kuhlman, K. R., and G. L. Kulcinski (1998) "Terrestrial Analogs for Lunar Ilmenite," *Proceedings of the Sixth International Conference on Engineering, Construction, and Operations in Space*, R. G. Galloway and S. Lokaj, eds., (American Society of Civil Engineers, Albuquerque, New Mexico, April 26-30) pp. 533-540.

Keil, K., T. E. Bunch and M. Prinz (1970) "Mineralogy and composition of Apollo 11 lunar samples," *Proceedings of the Apollo 11 Lunar Science Conference*, **1**, pp. 561-598.

Kogel, G. and W. Triftshauser (1983) "Helium Implantation in Metals Investigated by Monoenergetic Positrons," *Radiation Effects*, **78**, pp. 221-230.

Kulcinski, G. L, E. N. Cameron, J. F. Santarius, I. N. Sviatoslavsky, L. J. Wittenberg, and H. H. Schmitt (1988) "Fusion Energy from the Moon for the 21st Century," *The Second Conference on Lunar Bases and Space Activities of the 21st Century*, (Houston, Texas: Lunar and Planetary Institute) pp. 459-474.

Lindsley, D. H. (1996) Personal communication, State University of New York at Stony Brook.

Lord, H. C. (1968) "Hydrogen and Helium Ion Implantation into Olivine and Enstatite: Retention Coefficients, Saturation Concentrations, and Temperature-Release Profiles," *Journal of Geophysical Research*, **73**(16), pp. 5271-5280.

Lovering, J. F. and N. G. Ware (1970) "Electron probe microanalysis of minerals and glasses in Apollo 11 lunar samples," *Proceedings of the Apollo 11 Lunar Science Conference*, **1**, pp. 633-654.

Lynn, K. G., D. O. Welch, J. Throwe, and B. Nielsen (1991) "Interface Studies Using Variable Energy Positron Beams," *International Materials Review*, **36**(1), pp. 1-15.

Malik, S. M., D. E. Muller, K. Sridharan, R. P. Fetherston, N. Tran and J. R. Conrad (1995) "Distribution of Incident Ions and Retained Dose Analysis for a Wedge-shaped Target in Plasma Source Ion Implantation," *Journal of Applied Physics*, **77**(3), pp. 1-5.

Malik, S. M. (1998) Personal communication.

McKay, D. S. and R. J. Williams (1979) "A Geologic Assessment of Potential Lunar Ores," *Space Resources and Space Settlements*, J. Billingham et al., eds., pp. 243-256, NASA SP-428.

Mitchell, J. N. (1996) Personal communication, Los Alamos National Laboratory

Müller, H. W., J. Jordan, S. Kalbitzer, J. Kiko and T. Kirsten (1976) "Rare Gas Ion Probe Analysis of Helium Profiles in Individual Lunar Soil Particles," *Seventh Lunar Science Conference*, (Houston, Texas) pp. 937-951.

Nash, W. P. (1992) "Analysis of Oxygen with the Electron Microprobe: Applications to Hydrated Glass and Minerals," *American Mineralogist*, **77**, pp. 453-457.

National Institute of Health (1996) *NIH Image*, URL: http:// rsb.info.nih.gov/nih-image/

Nier, A. O, D. J. Schlutter and D. E. Brownlee (1990) "Helium and Neon Isotopes in Deep Pacific Ocean Sediments," *Geochimica et Cosmochimica Acta*, **54**, pp. 173-182.

Nier, A. O. and D. J. Schlutter (1985) "High-Performance Double-Focusing Mass Spectrometer," *Review of Scientific Instruments*, **56**, pp. 214-219.

Nier, A. O and D. J. Schlutter (1992) "Extraction of Helium from Individual Interplanetary Dust Particles by Step-Heating," *Meteoritics*, **27**, pp. 166-173.

Nier, A. O and D. J. Schlutter (1993) "Extraction of He and Ne from Individual Lunar Ilmentite Grains by Pulse Heating," *Meteoritics* (abstract), **28**, p. 412.

Pandey, R. K. (1997) Personal communication, Texas A&M University.

Pandey, R. K., S. Sunkara and J. Muthusami (1996) "Crystal Growth and Characterization of an Oxide Semiconductor (Ilmenite) for Novel Electronic Devices," *Space Technology and Applications International Forum*, AIP Conference Proceedings 316, (Albuquerque, NM).

Papike, J., L. Taylor and S. Simon (1991) "Lunar Minerals," *Lunar Sourcebook.*, G. Heiken, D. Vaniman and B. M. French, eds. (Cambridge, Cambridge University Press) pp. 121-182.

Pepin, R. O., L. E. Nyquist, D. Phinney, and D. C. Black (1970) "Rare Gases in Apollo 11 Lunar Material," *Proceedings of the Apollo 11 Lunar Science Conference*, **2**, pp. 1435-1454.

Robie, R. A., B. S. Hemingway and J. R. Fisher (1978) *Thermodynamic Properties of Minerals and Related Substances at 298.15 K and 1 Bar (10^5 Pascals) Pressure and at Higher Temperatures*, U.S. Geological Survey Bulletin 1452 (U.S. Government Printing Office, Washington, D.C.) p. 257.

Rühle, M. R. (1969) "Study of Small Defect Clusters in Irradiated Materials by Means of Transmission Electron Microscopy," *Symposium on Radiation Damage in Reactor Materials*, Vienna, Austria, International Atomic Energy Agency, ed., (International Atomic Energy Agency) pp. 113-158.

Rühle, M. R. (1972) "Transmission Electron Microscopy of Radiation-Induced Defects," *Radiation-Induced Voids in Metals*, Albany, New York, J. W. Corbett and L. C. Ianniello, eds., (U. S. Atomic Energy Commission) pp. 255-291.

Schlutter, D. J. (1997, 1998) Personal communication, University of Minnesota.

Schmitt, H. H. (1996) Personal communication, University of Wisconsin - Madison.

Schultz, P. J and K. G. Lynn (1988) "Interaction of Positron Beams With Solid Surfaces, Thin Films, and Interfaces," *Reviews of Modern Physics*, **60**(3), pp. 701-779.

Signer, P., H. Baur, and R. Wieler (1991) "Closed System Stepped Etching; An Alternative to Stepped Heating," *Alfred O. Nier Symposium on Inorganic Mass Spectrometry*, (Durango, Colorado) D. J. Rokop, ed., pp. 181-202.

Sunkara, S. S (1995) "Growth and Evaluation of Ilmenite Wide Bandgap Semiconductor for High Temperature Electronic Applications," Ph.D. Dissertation, (Texas A&M University, College Station, Texas) pp. 65-67.

Szeles, C. and K. G. Lynn (1995) "Positron-Annihilation Spectroscopy," Encyclopedia of Applied Physics, Vol. 14, (VCH Publishers, Inc.) pp. 1-26.

Taylor, L. A. (1990) "Hydrogen, Helium and other Solar-Wind Components in Lunar Soil: Abundances and Predictions," Proceedings of the 2rd International Conference on Engineering, Construction, and Operations in Space, Albuquerque, New Mexico, S. W. Johnson and J. P. Wetzel, eds., (American Society of Civil Engineers) pp. 68-77.

Taylor, L. A. (1996) Personal communication, University of Tennesee.

Touloukian, Y. S., R. W. Powell, C. Y. Ho and P. G. Klemens (1970) "Thermal Conductivity,"*Thermophysical Properties of Matter*, (IFI/Plenum, New York) **2**, p. 154.

Touloukian, Y. S., D. P. DeWitt (1972) "Thermal Diffusivity,"*Thermophysical Properties of Matter*, (IFI/Plenum, New York) **8**, pp. 279-282.

Touloukian, Y. S., R. W. Powell, C. Y. Ho and M. C. Nicolaou (1973) "Thermal Diffusivity,"*Thermophysical Properties of Matter*, (IFI/Plenum, New York) **10**, p. 391.

Vaniman, D., R. Reedy, G. Heiken, G. Olhoeft and W. Mendell (1991) "The Lunar Environment," *Lunar Sourcebook.*, G. Heiken, D. Vaniman and B. M. French, eds. (Cambridge, Cambridge University Press) pp. 27-60.

Warhaut, M., J. Kiko, and T. Kirsten (1979) "Microdistribution Patterns of Implanted Rare Gases in a Large Number of Individual Lunar Soil Particles," *Tenth Lunar and Planetary Science Conference*, Houston, Texas, Lunar and Planetary Institute, ed., (Pergamon Press) pp. 1531-1546.

Webster, A. H. and N. F. H. Bright (1961) "The System Iron-Titanium-Oxygen at 1200°C and Oxygen Partial Pressures Between 1 Atm. and 2 x 10^{-14} Atm.," *Journal of the American Ceramic Society*, **44** (3), p. 112.

Wieler, R. (1995) Personal communication, ETH, Zurich, Switzerland.

Wittenberg, L. J., J. F. Santarius, and G. L. Kulcinski (1996) "Lunar source of ^{3}He for commercial fusion power," *Fusion Technology*, **10** (2, pt 1), pp. 167-78.

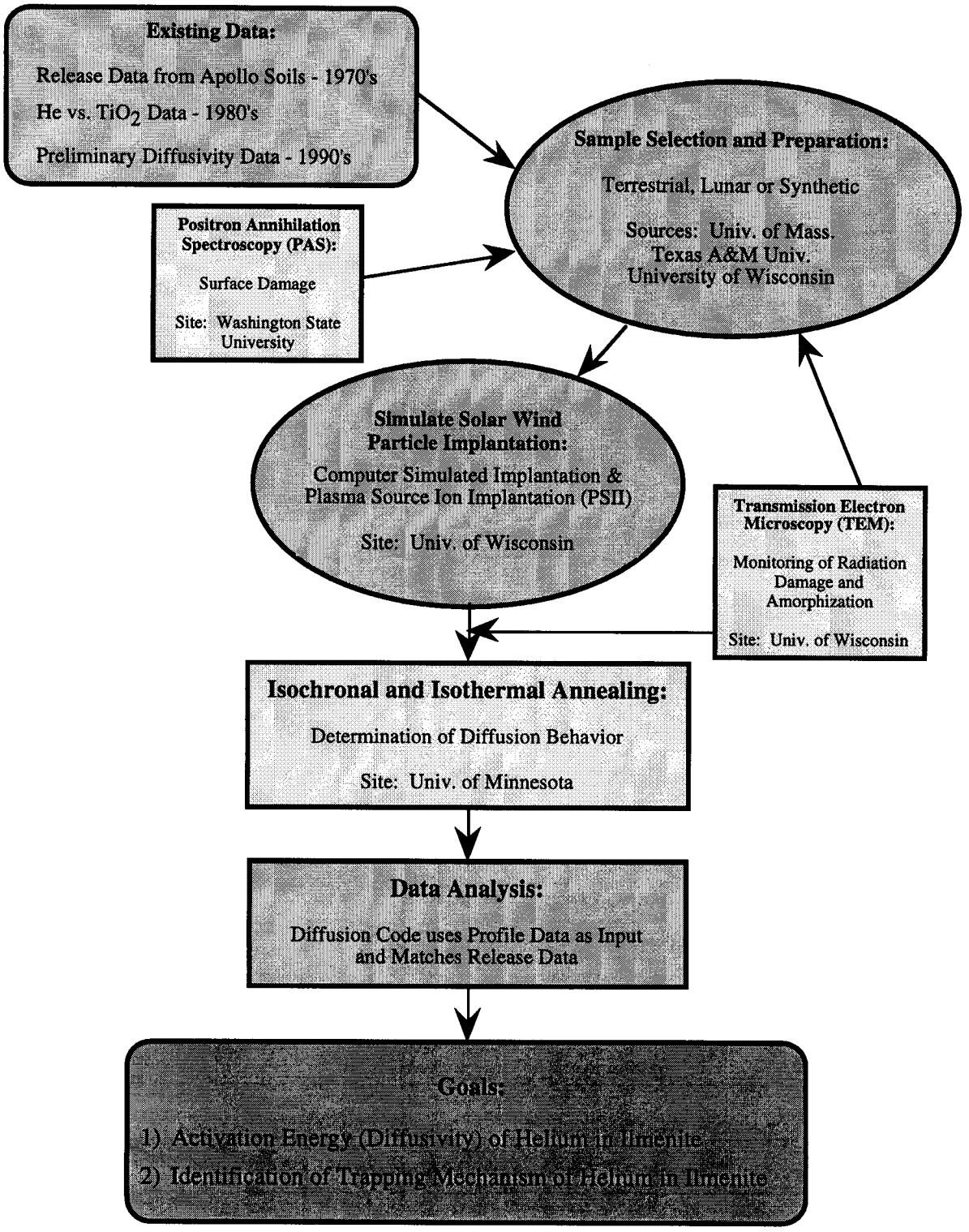

Figure 6-1. Flowchart of experimental research performed for this thesis.

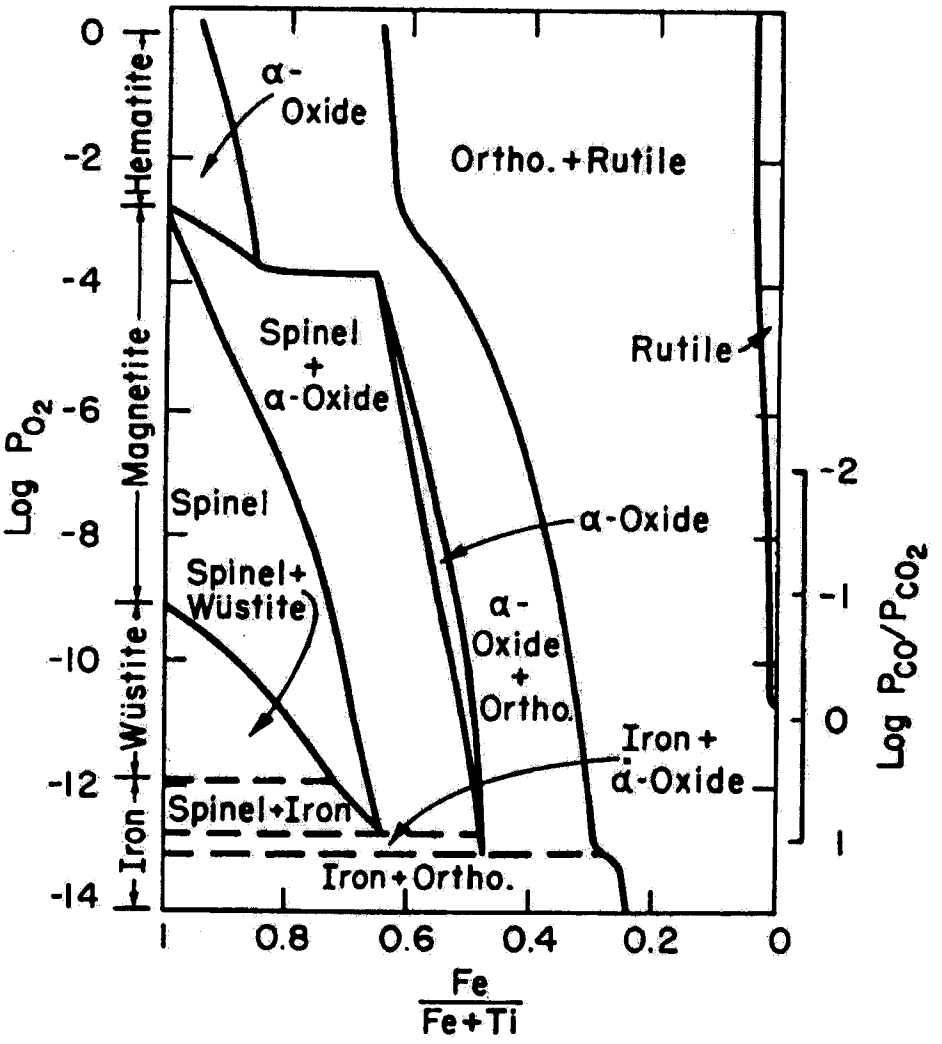

Figure 6-2. Phase diagram of the system Fe-Ti-O at 1200°C as a function of the Fe/Fe+Ti ratio and the oxygen partial pressure [After Webster and Bright, 1961]. Ilmenite is represented by the α-oxide in the region where ~0.3 < Fe/(Fe+Ti) < ~0.7.

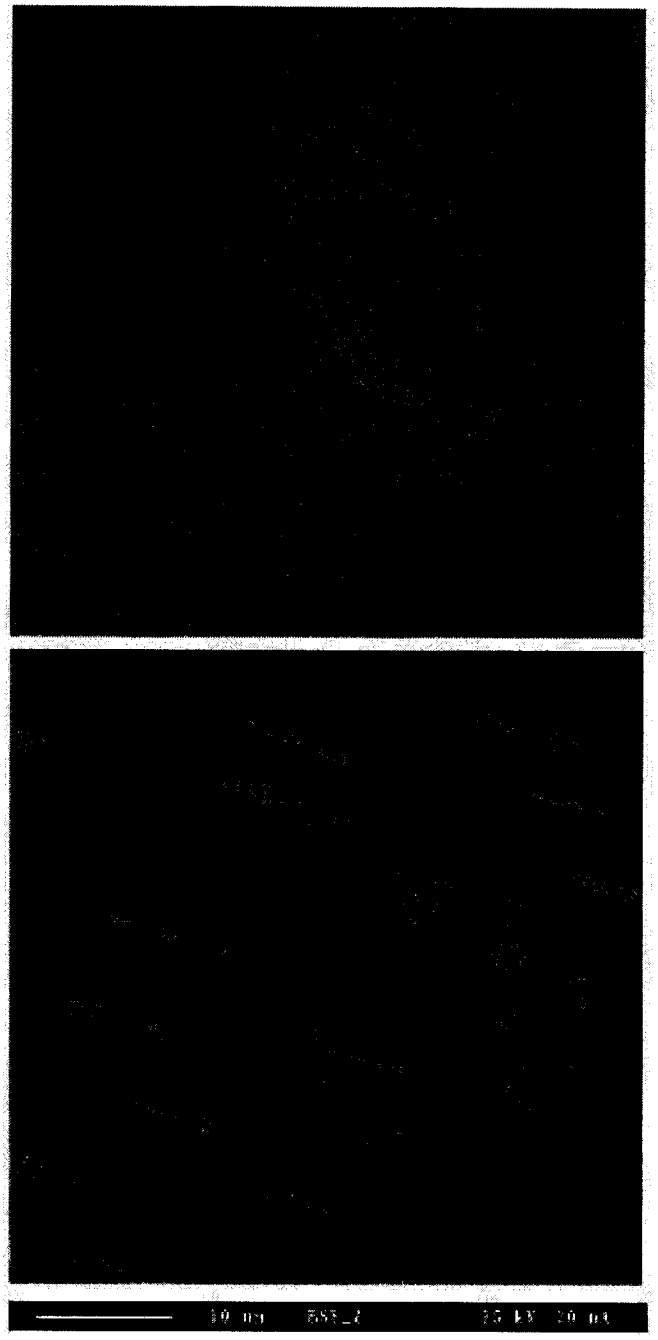

Figure 6-3. (a) Backscattered electron image and (b) iron elemental map of synthetic ilmenite as received. The dark areas in (a) indicate pure iron and the medium gray areas appear to be pseudobrookite ($FeTi_2O_5$). The lighter gray area appears to be rutile (TiO_2).

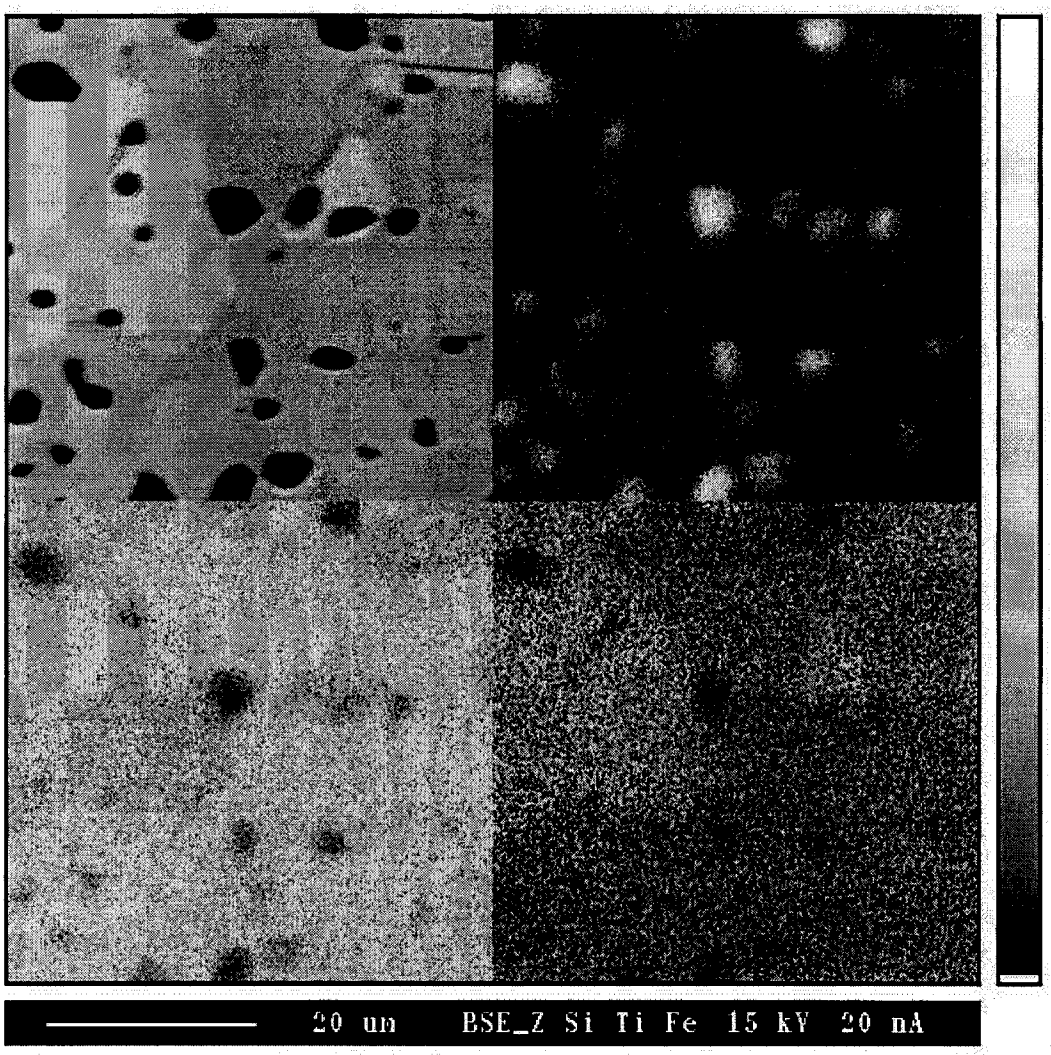

Figure 6-4. Backscattered electron image (upper left) and elemental maps of Si (upper right), Ti (lower left) and Fe (lower right) for synthetic ilmenite after annealing in 1:1 CO:CO_2 for 8 hours at 1200°C. The bright areas in the elemental maps indicate regions of higher concentration. Note that the black spots in the backscattered image correspond to the areas of high Si concentration (i.e. holes filled with silica from the polishing media).

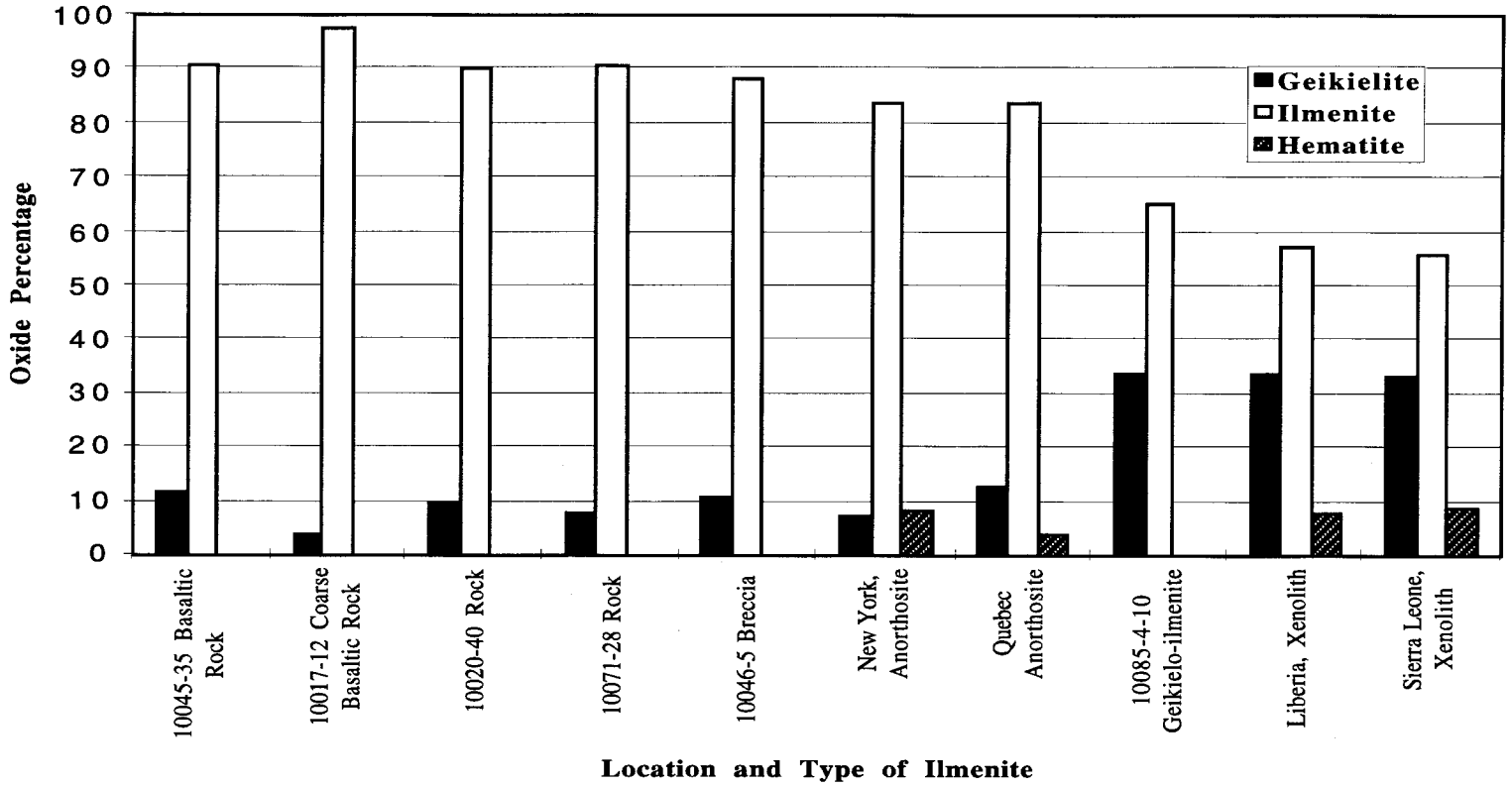

Figure 6-5. Mineral content of samples in Table 6-4. The terrestrial ilmenites from anorthosites are very similar to the Apollo 11 (Apollo 11 samples have the form 10XXX-XX) ilmenites except for the small amount of hematite present. The results for the terrestrial samples are qualitative only. The analyses are of the bulk ilmenite, not the hematite lamellae.

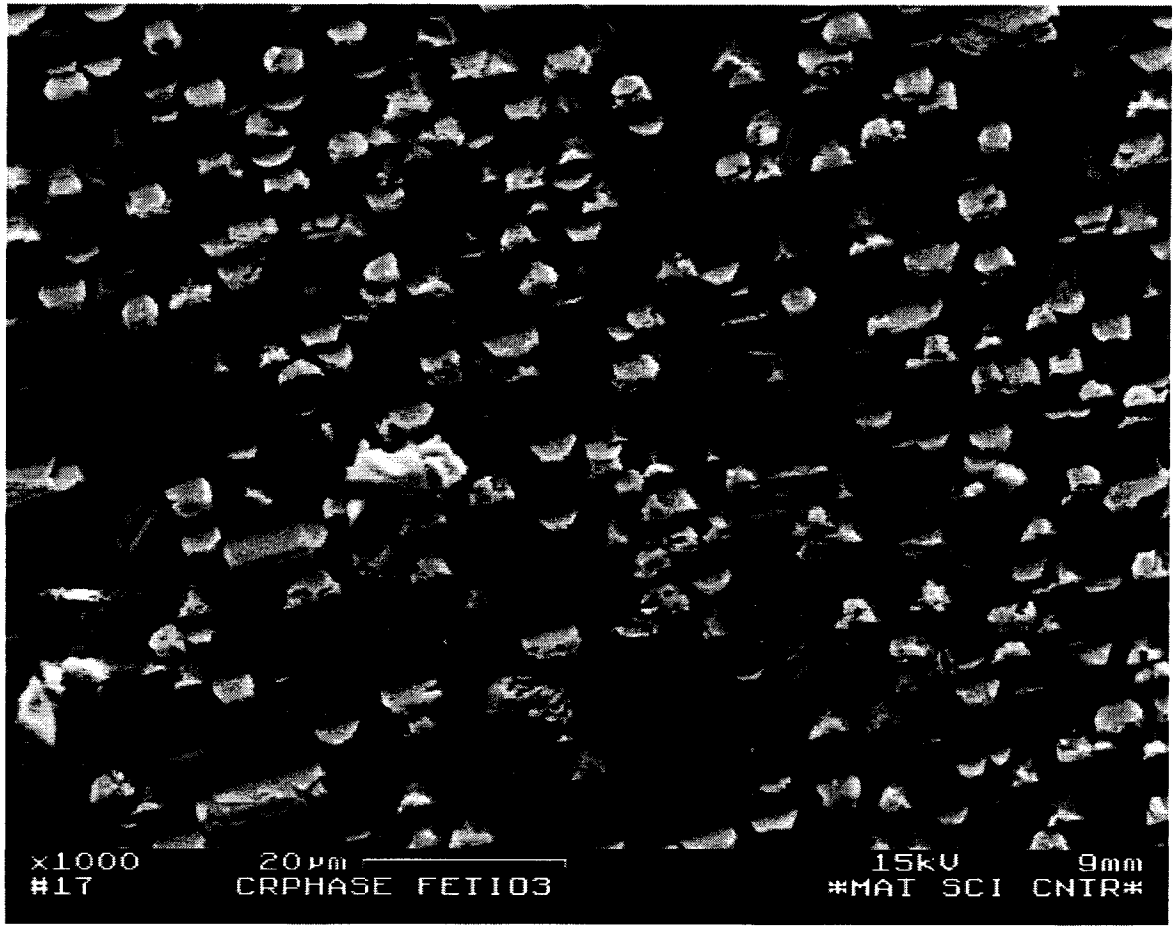

Figure 6-6. Secondary electron micrograph of polished section of ilmenite xenocryst from Sierra Leone etched in 25% HF for 5 min. (1000X). The precipitates appear to be Cr and Al-rich compared to the bulk.

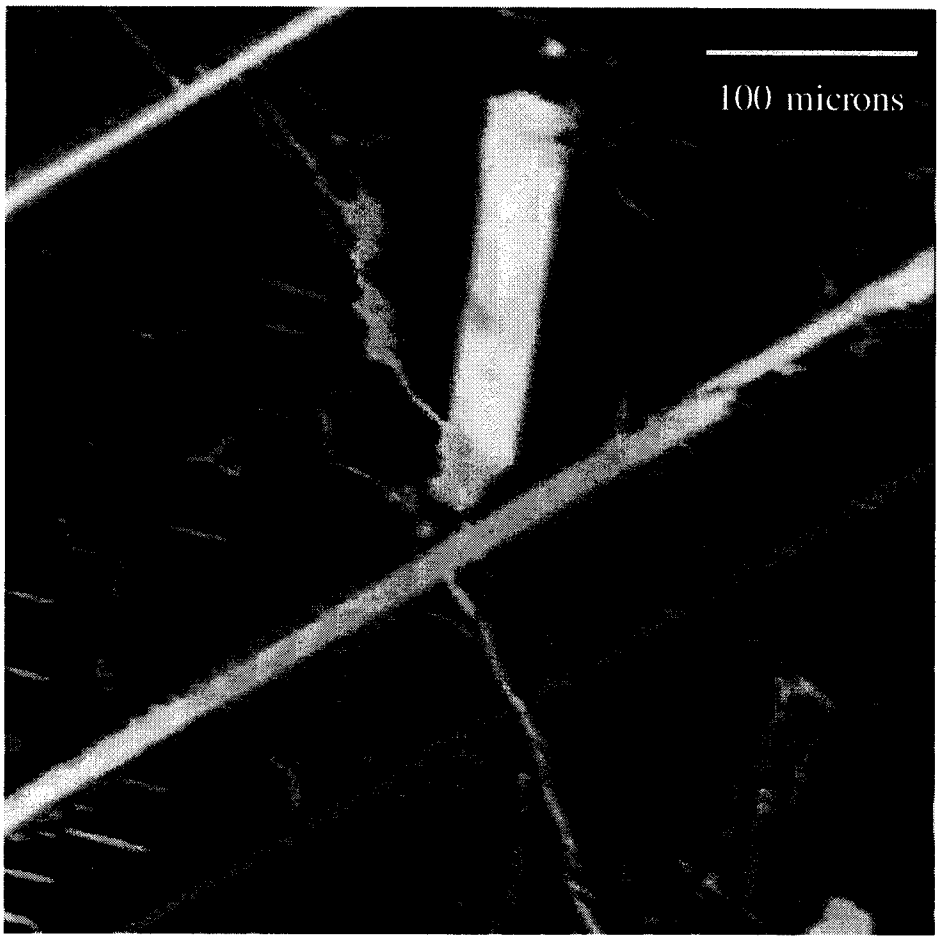

Figure 6-7. Backscattered electron image of ilmenite from the Marcy anorthosite massif, Sanford Lake, N.Y. The dark gray is ilmenite and the light gray lamellae are mainly hematite. Inclusions of mineral phases containing Na, Al, Si, S, Cu, As, Ca and K are also present.

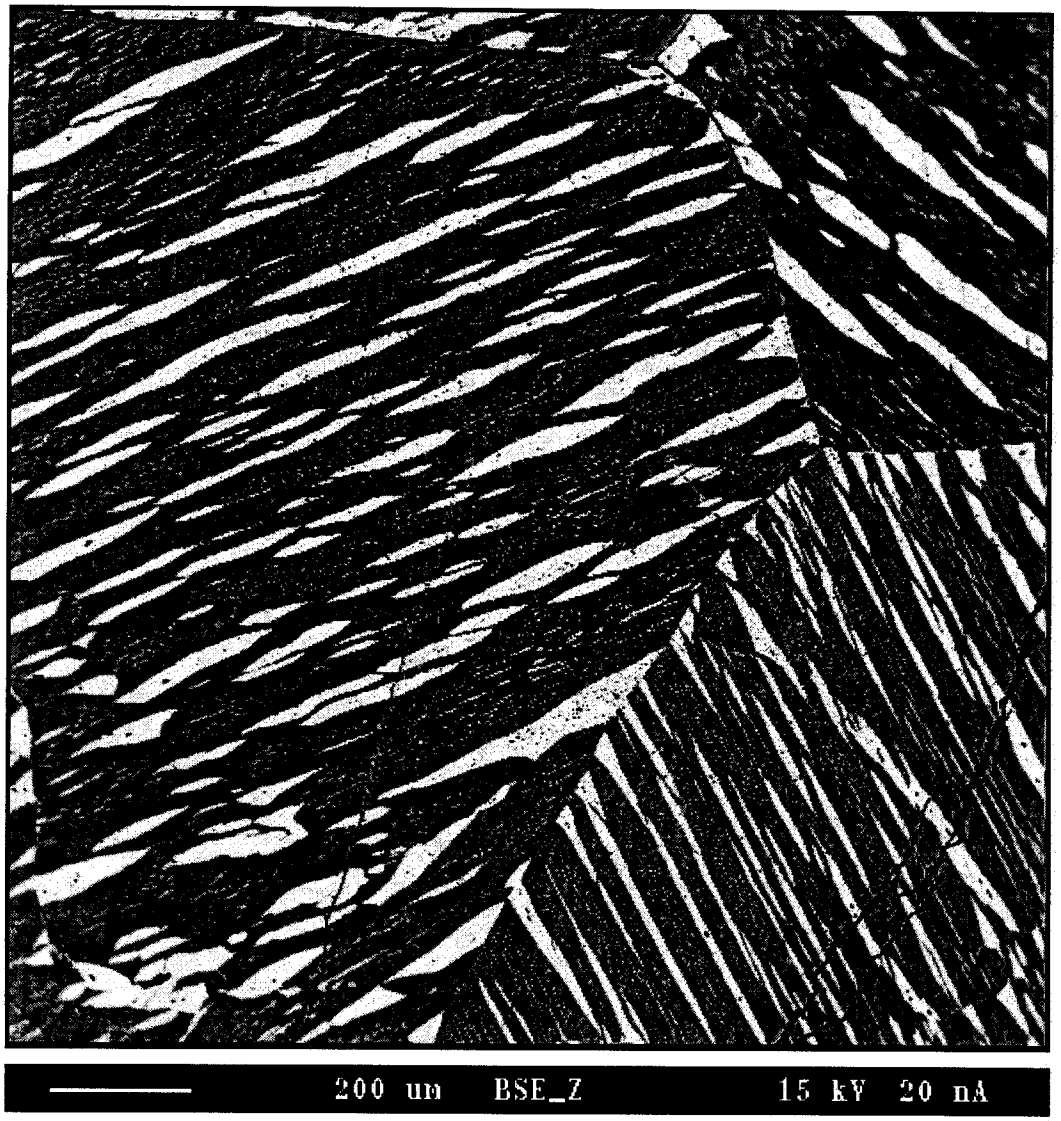

Figure 6-8. Backscattered electron image of a granular ilmenite from St. Urbain, Quebec. Medium gray areas are bulk ilmenite and white areas are hematite lamellae.

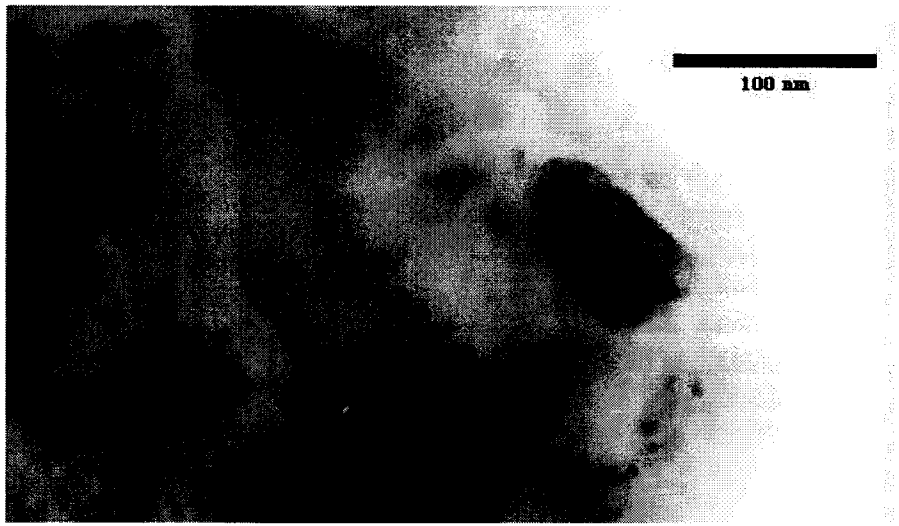

Figure 6-9. High resolution transmission electron micrograph of the ilmenite from Sanford Lake, New York. The particle on the right and slightly less than 100 nm in length was qualitatively identified as arsenopyrite using energy dispersive x-ray spectroscopy.

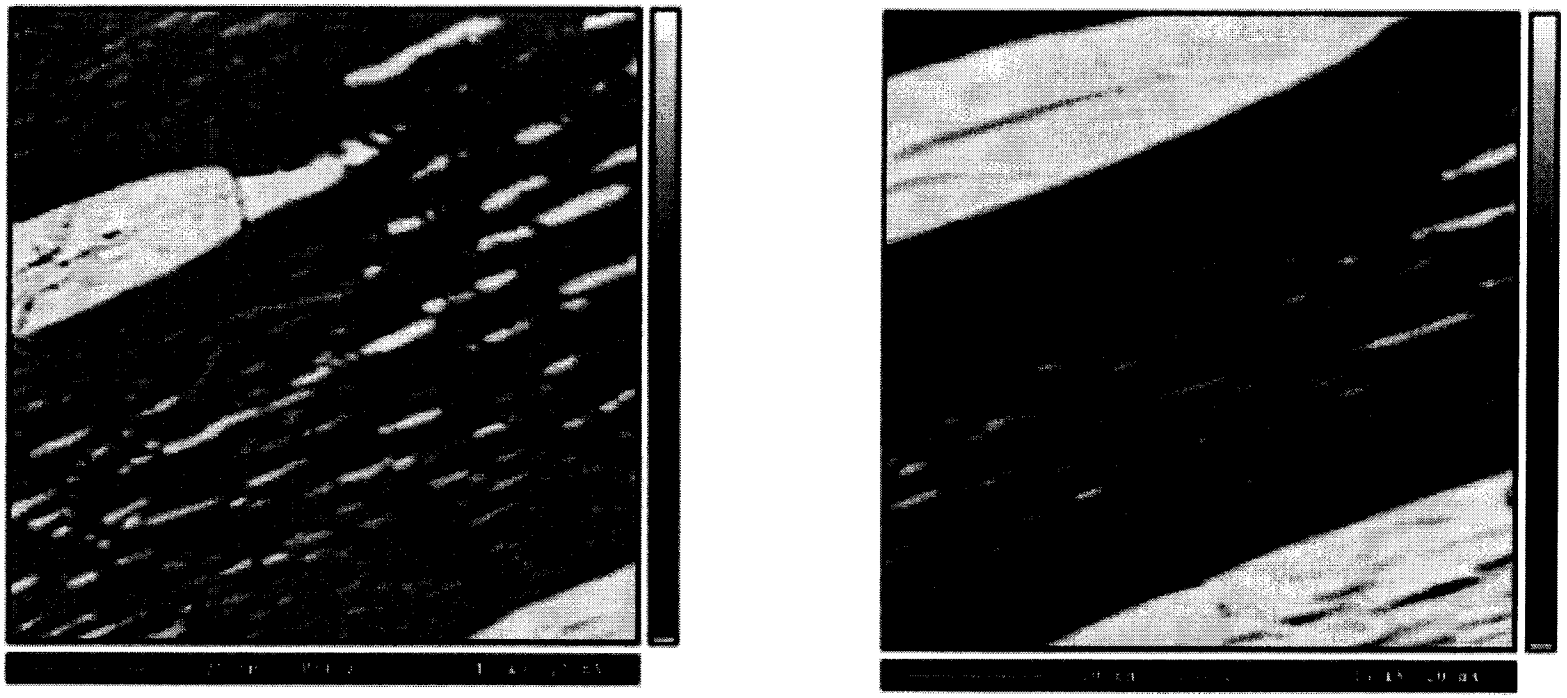

Figure 6-10. Backscattered electron micrographs of the ilmenite from St. Urbain, Quebec used in this thesis. Note the difference in scale between the two images. The dark gray bulk is ilmenite and the light gray is hematite.

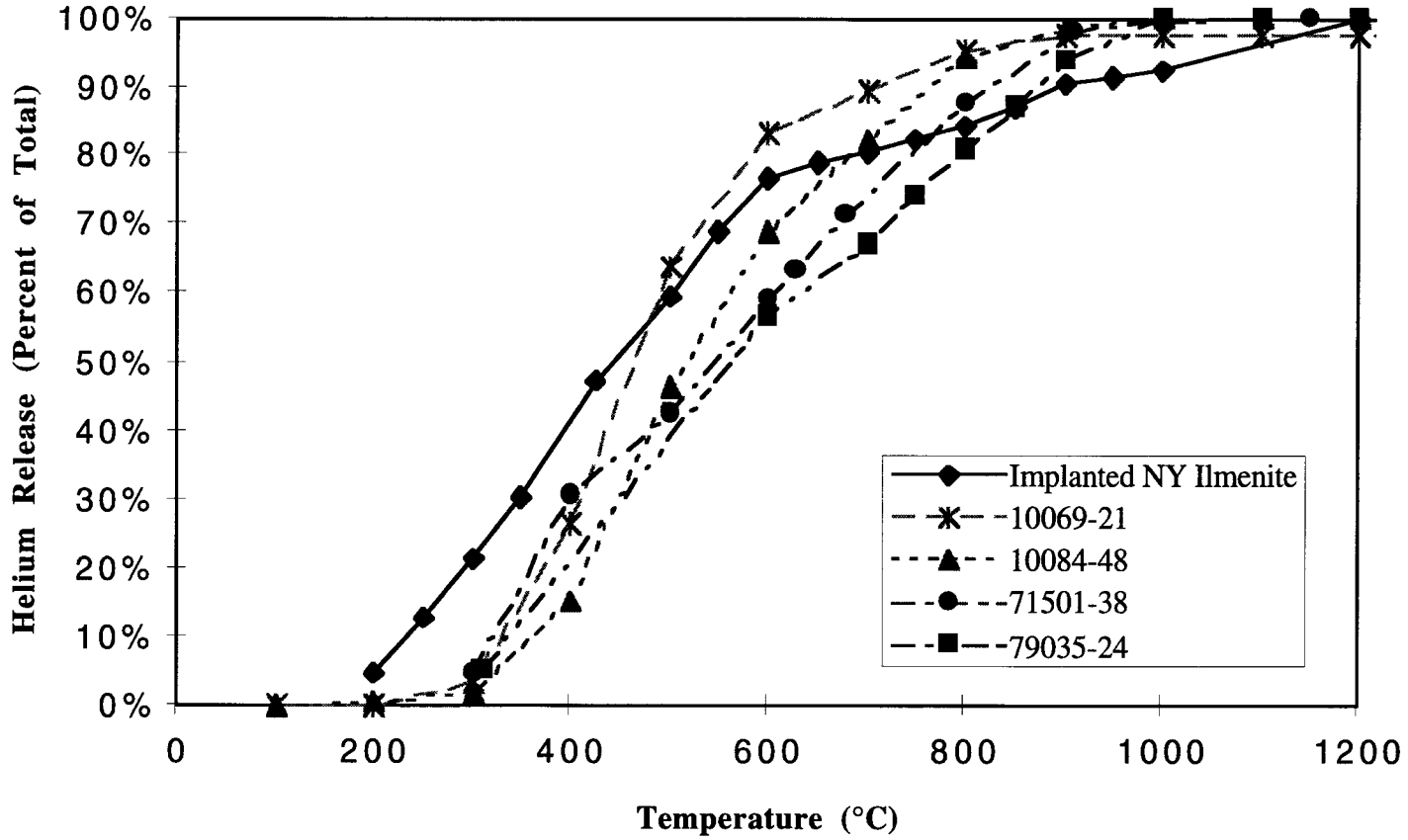

Figure 6-11. Release data of helium from the implanted New York ilmenite and samples of rocks and regolith from Apollo 11 (Pepin et al., 1970) and Apollo 17 (Frick et al., 1988). Annealing steps of 50°C and 30 minutes were used for the implanted terrestrial sample while steps of approximately 100°C and 1 hour were used for the Apollo samples.

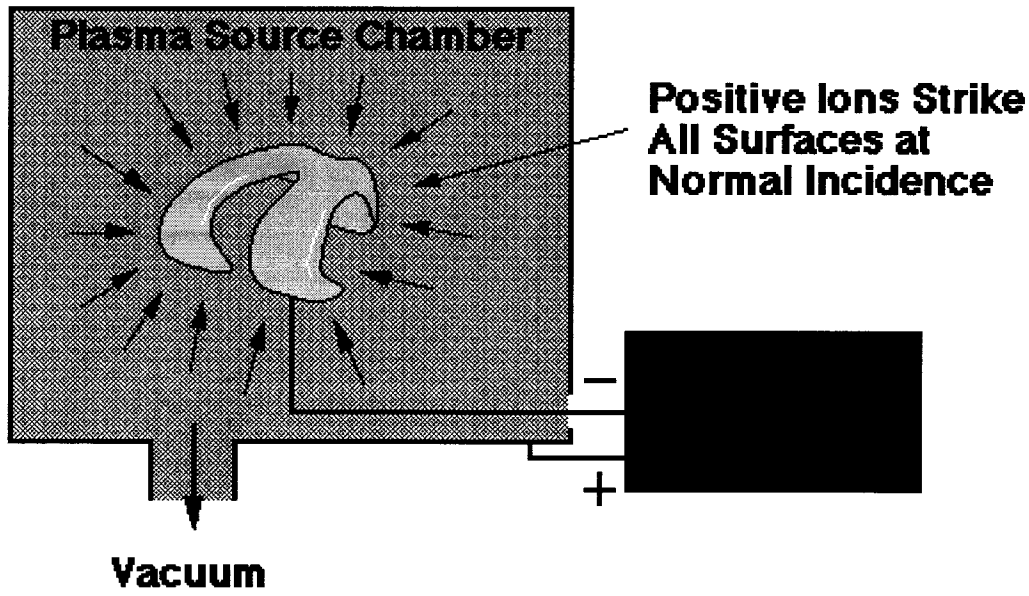

Figure 6-12. Schematic diagram of the Plasma Source Ion Implantation (PSII) process (here showing the implantation of an artificial knee component) [Malik, 1998].

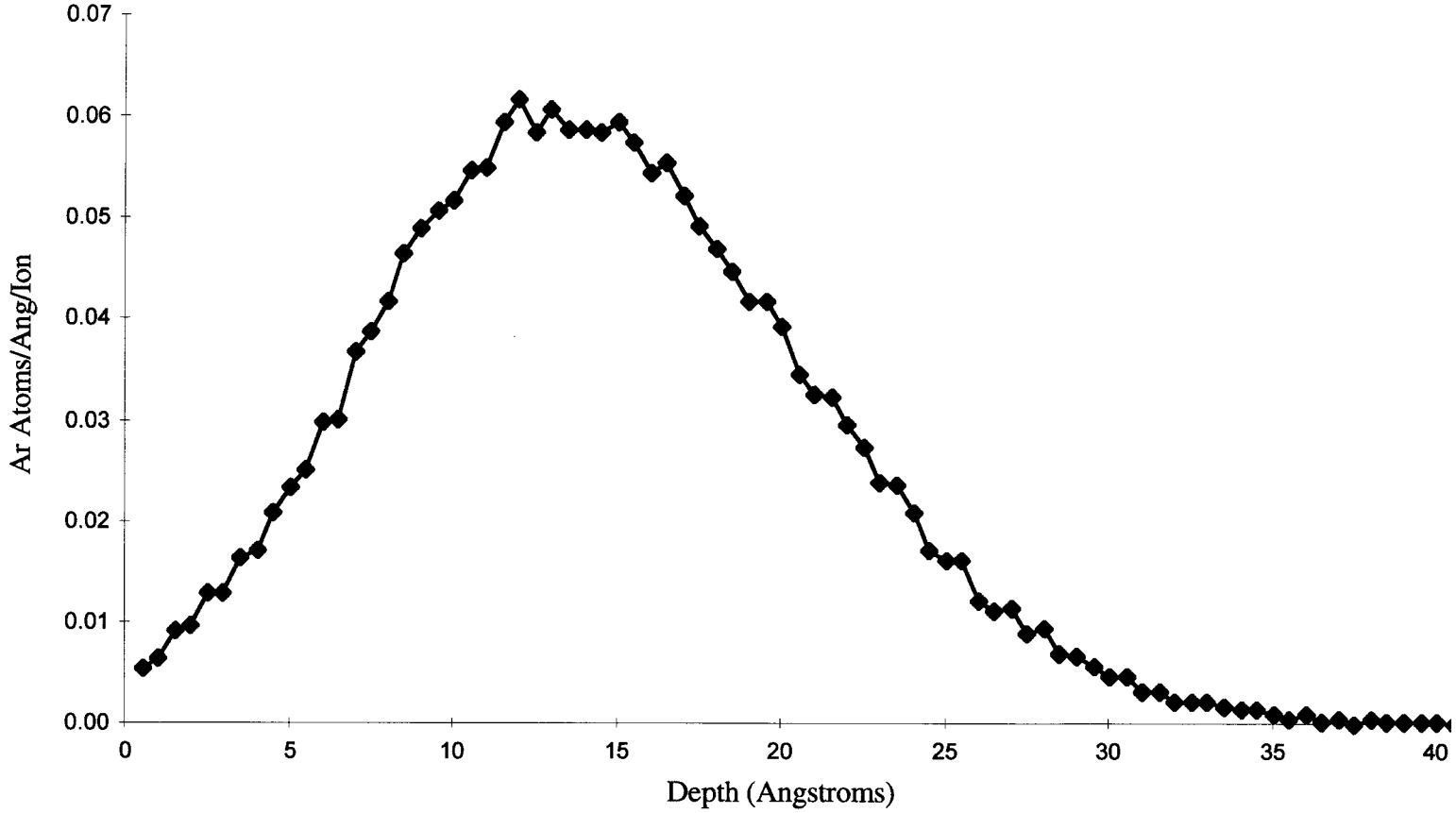

Figure 6-13. TRIM calculation of the depth profile resulting from sputter-cleaning of ilmenite using 0.6 keV Ar at normal incidence [Ziegler, 1996]. The sputter yield was calculated to be 0.805 atoms/ion.

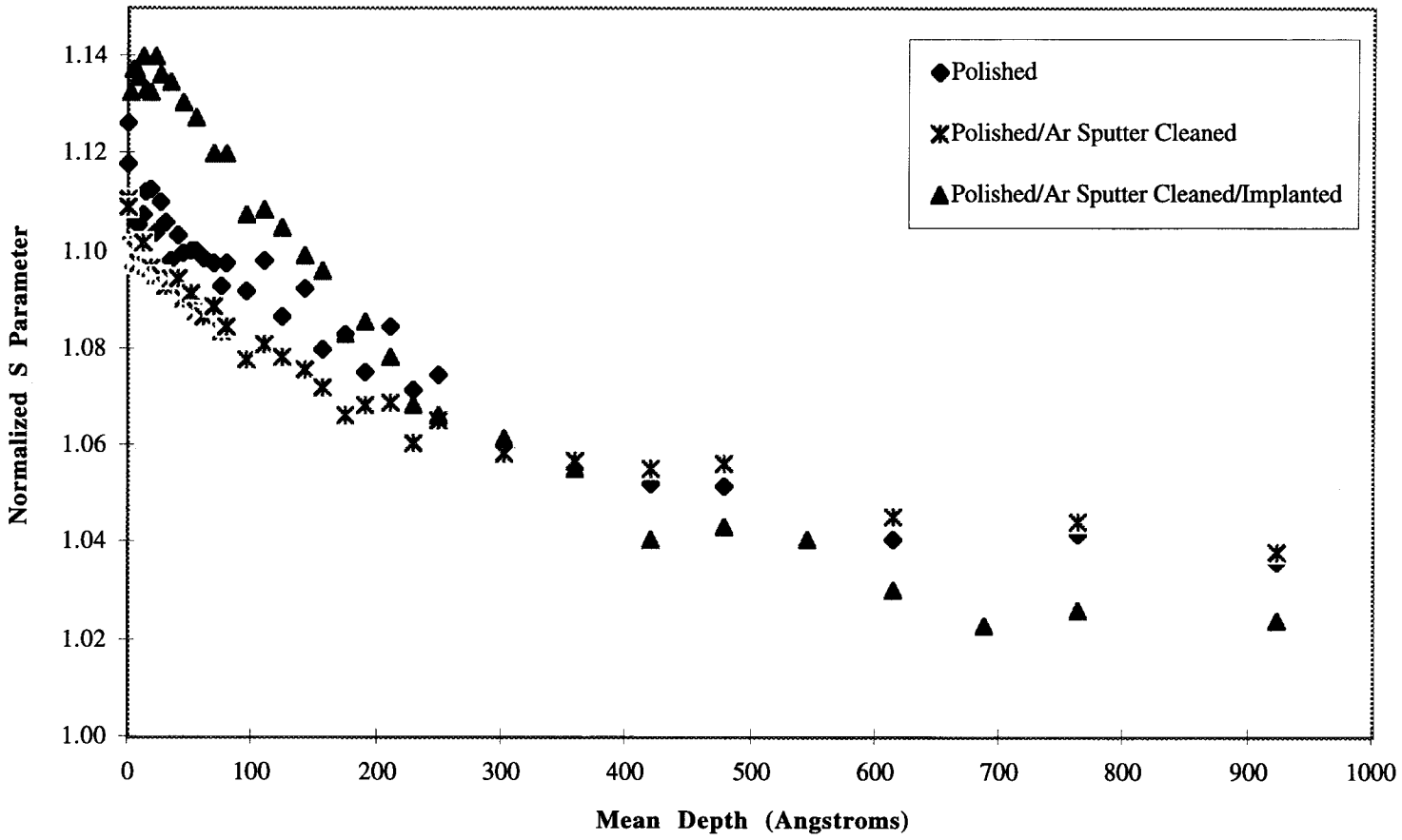

Figure 6-14. Results of coPAS study showing the reduction of surface damage by in-situ sputter-cleaning with 0.6 keV Ar $1x10^{16}$ ions/cm^2, and the affect of 4 keV ^{4}He $1x10^{16}$ ions/cm^2 implantation.

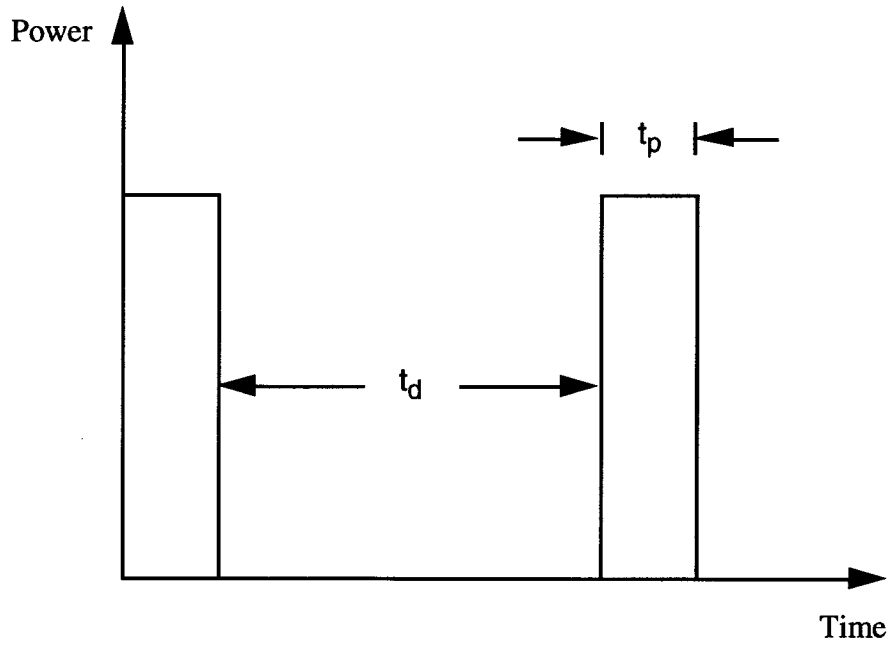

Figure 6-15 Schematic representation of a typical power trace for a Plasma Source Ion Implantation run. The figure is not drawn to scale. Typical pulse times (t_p) are tens of microseconds and "down" times (t_d) are typically tens of milliseconds.

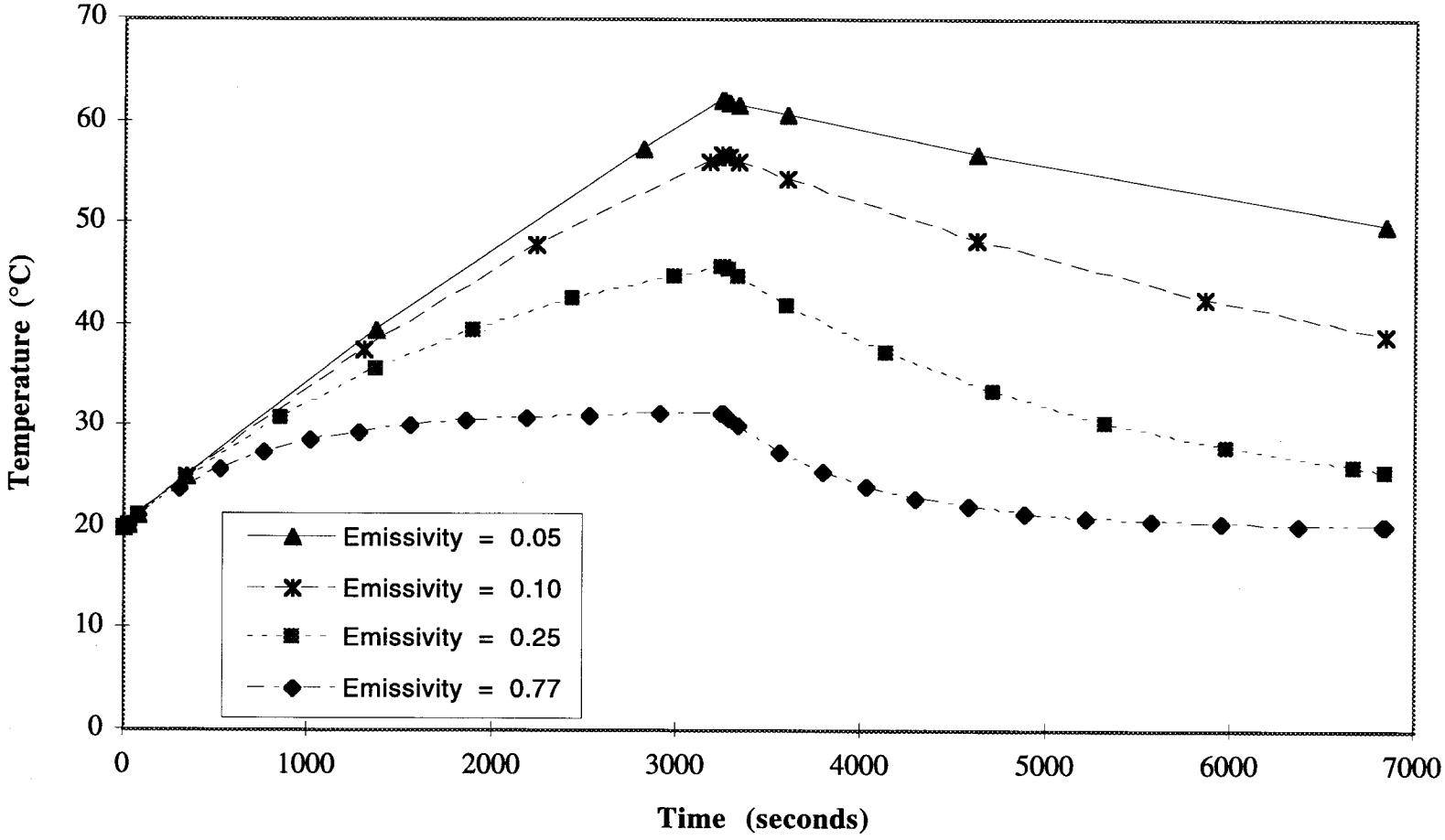

Figure 6-16. Predicted temperature of ilmenite wafer for 54 min. PSII Ar sputter-cleaning ($2x10^{17}$ Ar ions/cm^2) and 60 min. cooling time for various values of emissivity, ε. Calculations were performed using a lumped capacitance model. [Blanchard, 1994].

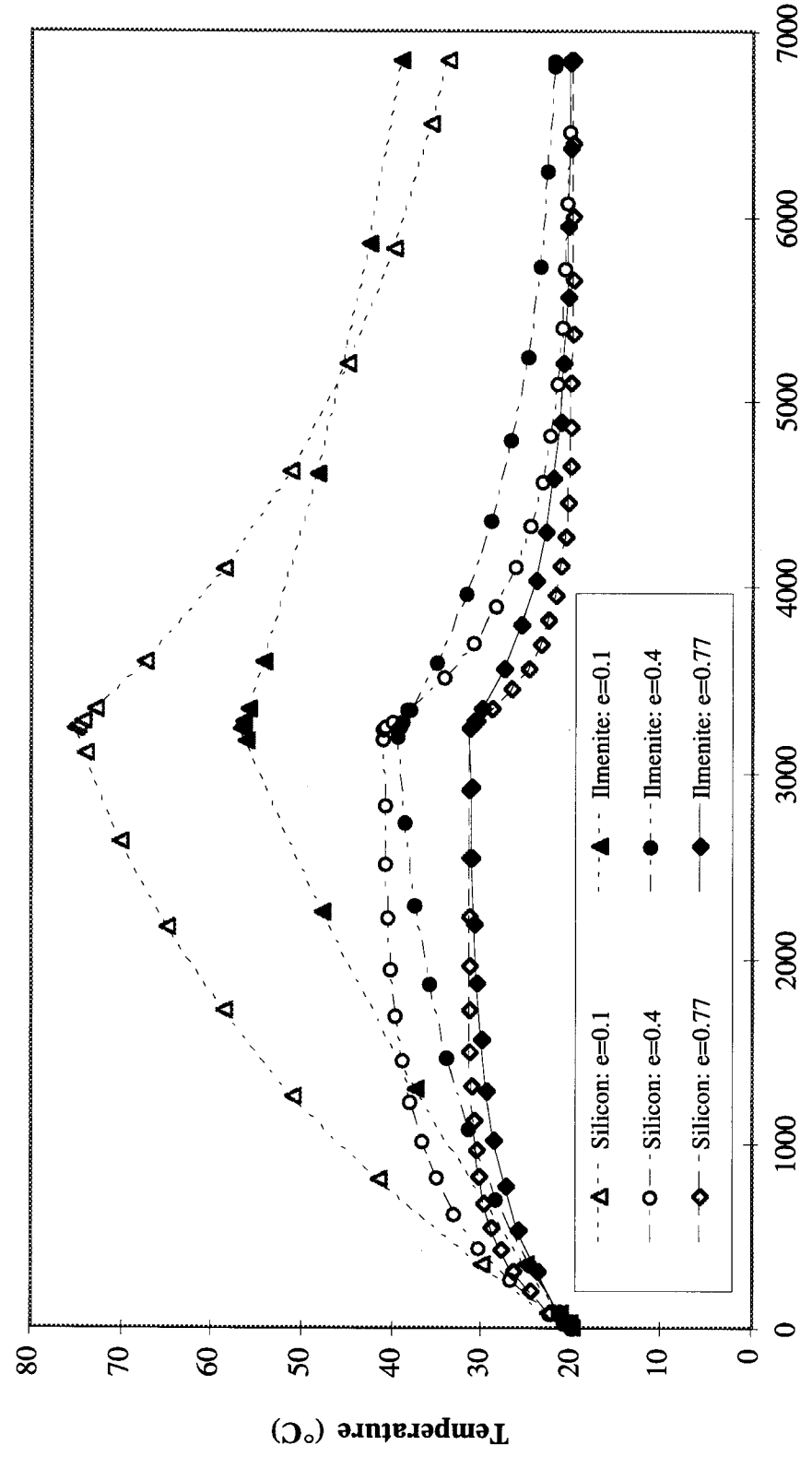

Figure 6-17. Predicted temperature of silicon and ilmenite wafers for 54 min. PSII Ar sputter-cleaning ($2x10^{17}$ Ar ions/cm^2) and 60 min. cooling time. Calculations were performed using a lumped capacitance model [Blanchard, 1994].

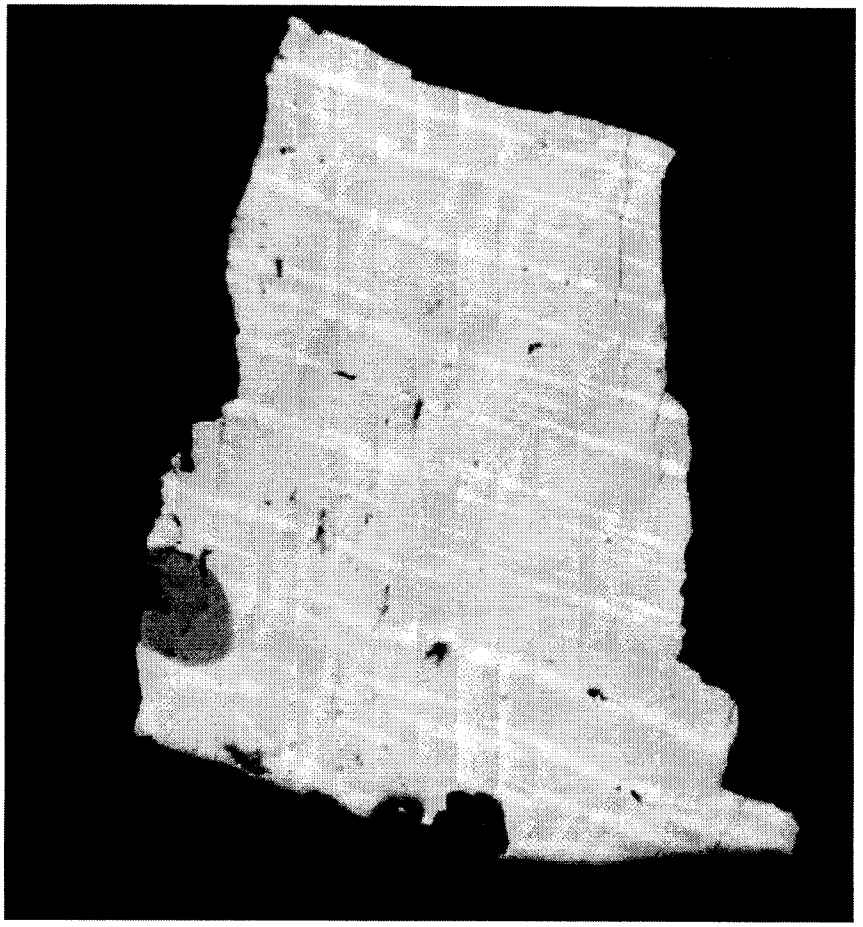

Figure 6-18. Optical micrograph of a crushed piece of sample 040998 (ilmenite from St. Urbain, Quebec. Note the polished surface showing lamellar hematite (light gray) crossing the ilmenite (darker bulk).

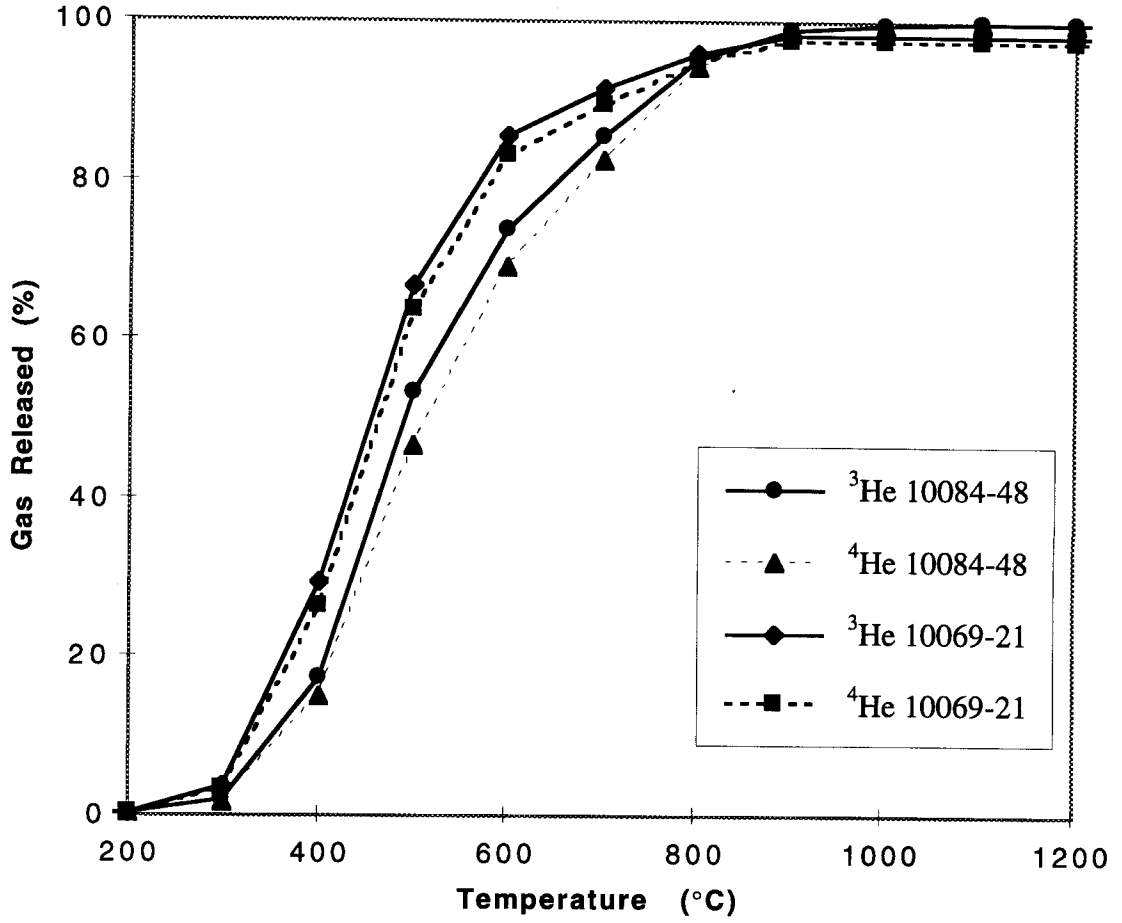

Figure 6-19. Helium release from Apollo 11 rock sample 10069 and regolith sample 10084 as a function of temperature during an isochronal anneal. Annealing temperature was increased 100 °C in time steps of 1 hour [Pepin, et al., 1970].

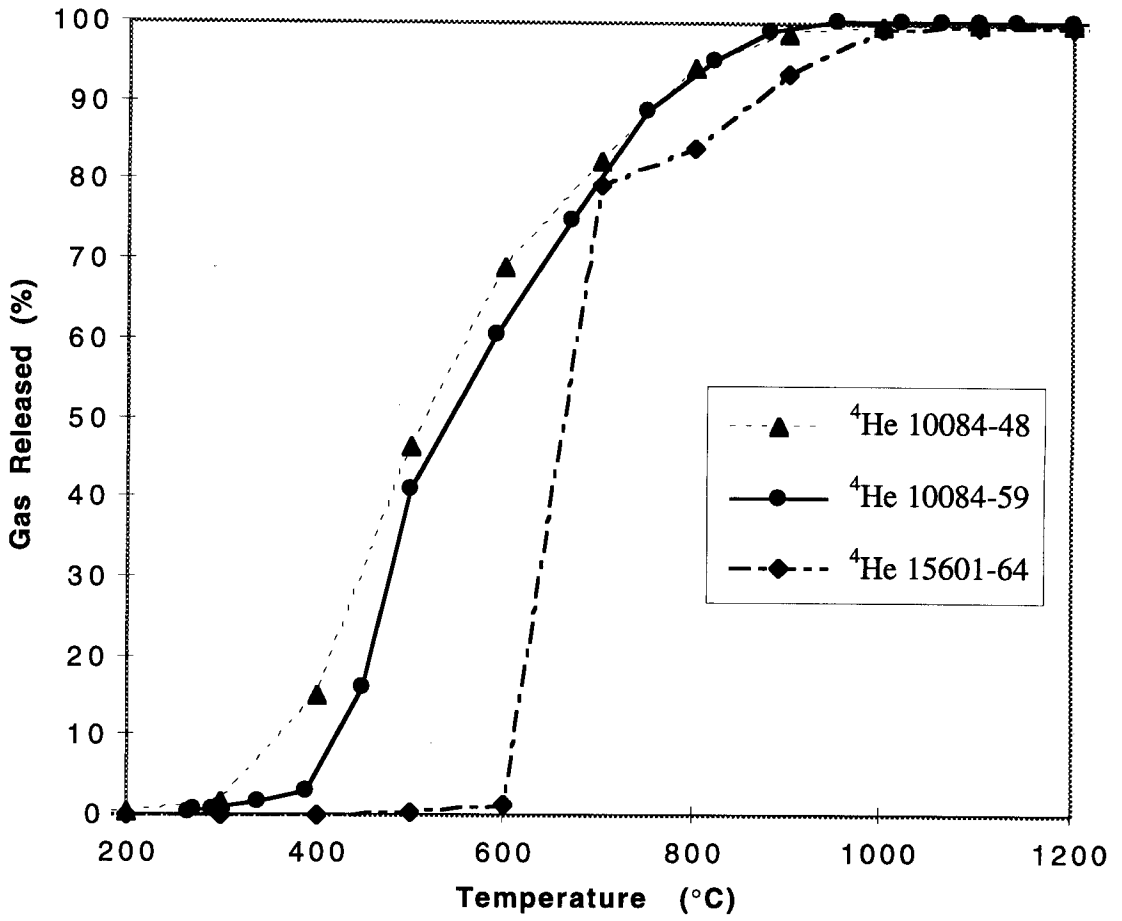

Figure 6-20. Results of three ^{4}He release data for Apollo 11 regolith sample 10084 and Apollo 15 fines sample 15601 as a function of temperature during isochronal anneals. The anneal of sample 10084-48 were done in 1 hour steps by Pepin, et al. [1970]. The anneal of 10084-59 was done in 1/2 hour steps by Hohenberg, et al. [1970]. The anneal of 15601-64 was done by Srinivasan, et al. [1972].

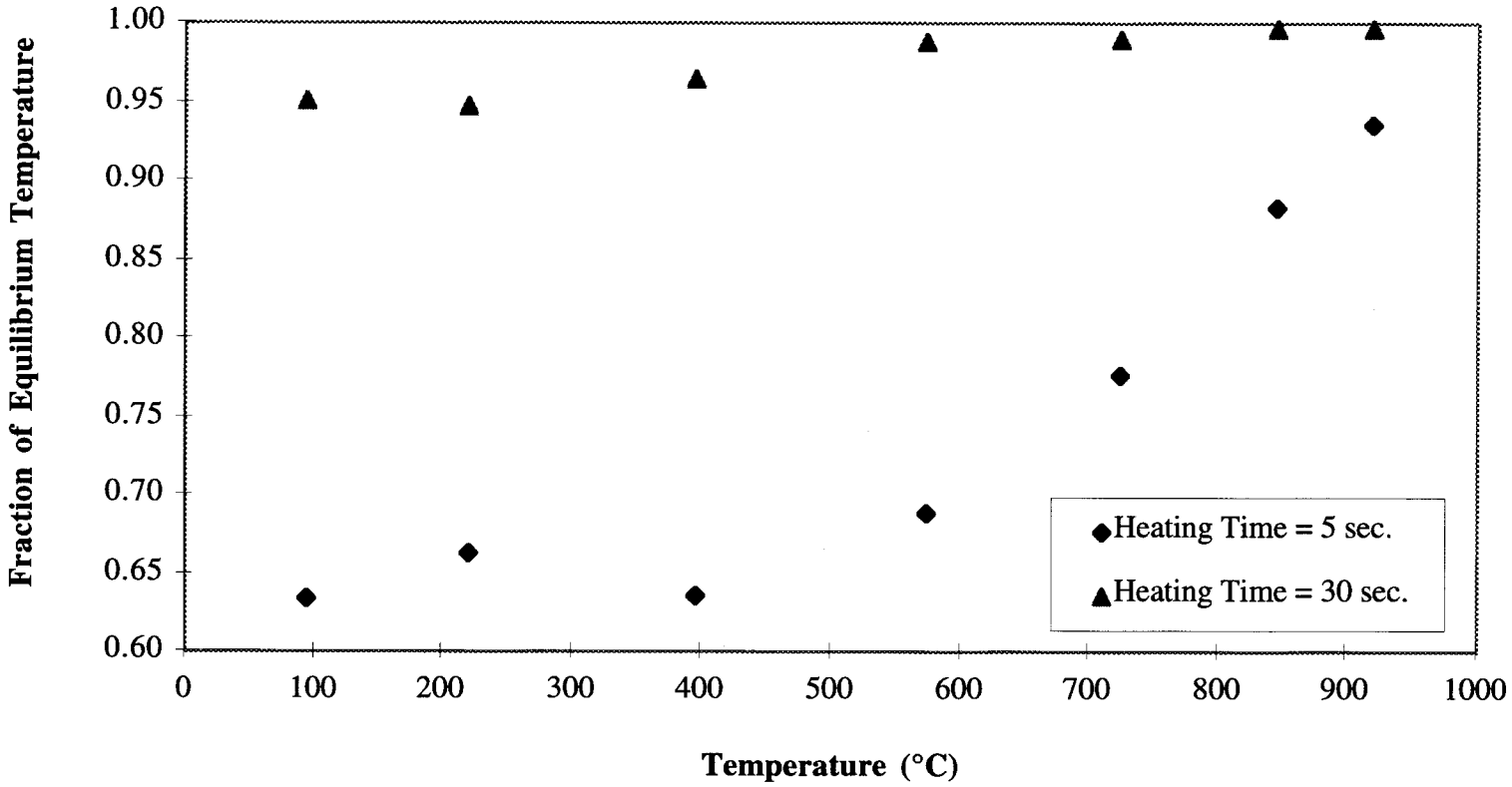

Figure 6-21. Percent of equilibrium temperature versus equilibrium temperature for 5 sec. and 30 sec. annealing times in resistively heated Ta furnaces in small particle furnace. Measurements taken by Schlutter [1998].

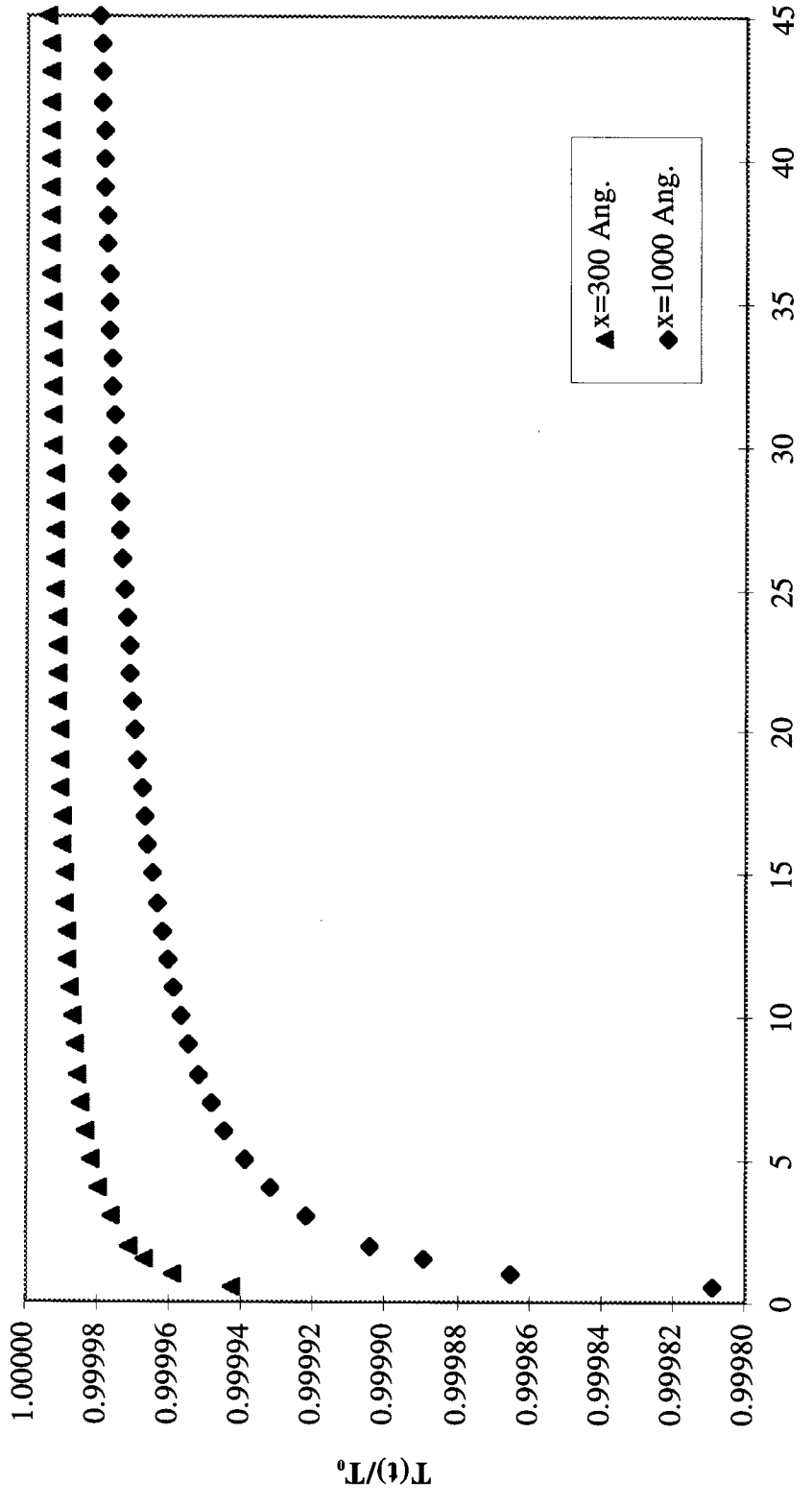

Figure 6-22. Predicted temperatures at 300 Å and 1000 Å as a function of annealing time.

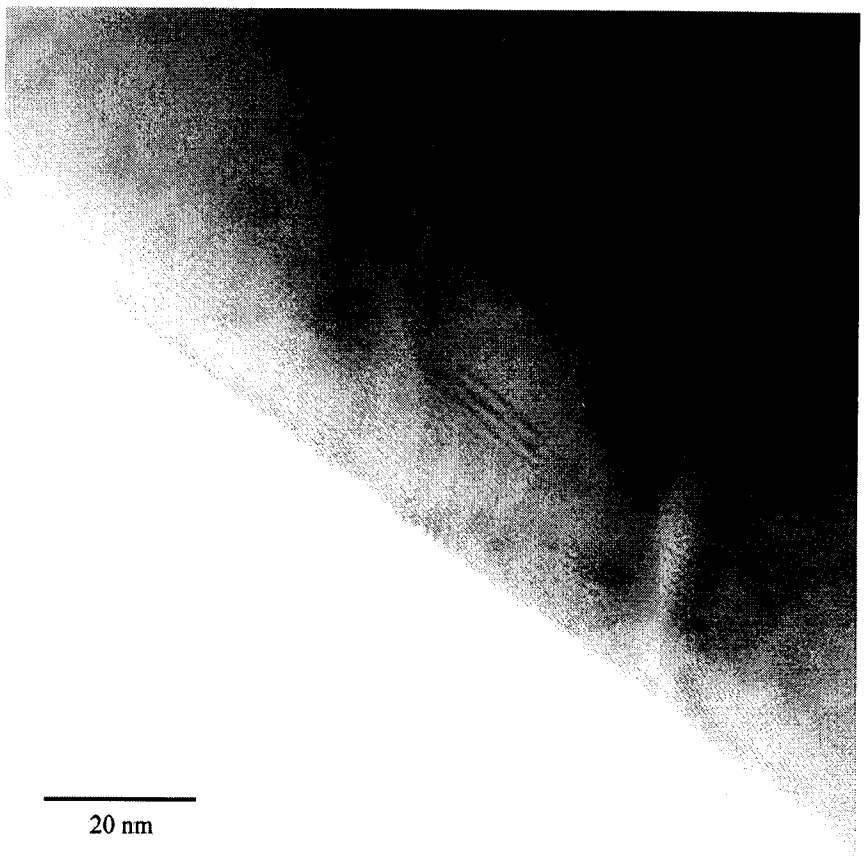

Figure 6-23. A high-resolution TEM image of the cross-section of the implanted surface of the New York ilmenite implanted with 4 keV ^{4}He $1x10^{16}$ ions/cm^{2}.

Chapter 7 Experimental Results

7.1 Error Analysis

In general, most of the error in the annealing runs is statistical in nature [Schlutter, 1998]. The exception is the annealing run done in the long time heating furnace (Chapter 6). The errors for this particular run will be discussed in Section 7.2.1.1 along with the data for this run.

A standard error analysis is applied to the number of counts recorded by the mass spectrometers [Bevington and Robinson, 1992]. A Poisson distribution is assumed and the error is given by the standard deviation,

$$\sigma_N = \sqrt{N}. \tag{7-1}$$

where σ_N is the standard deviation in the number of counts, N, at a temperature step. The measured number of counts must be converted to a fraction of the total counts needed for input to the ANNEAL code. Equation 7-3 describes the error propagation in this conversion.

$$\frac{\sigma_F^2}{F^2} = \left(\frac{\sigma_N^2}{N^2} + \frac{\sigma_{\Sigma N}^2}{(\Sigma N)^2} \right) \tag{7-3}$$

In Equation 7-3, F is the fractional release $\frac{N}{\Sigma N}$ and $\sigma_{\Sigma N}$ is the standard deviation in the total number of counts, ΣN. The second term on the right-hand side in Equation 7-3 is always much smaller than the first term since it is equal to $\sqrt{\Sigma N}/(\Sigma N)^3$. Thus, the second term will be ignored in the data that follow and

$$\sigma_F \approx \frac{\sigma_N}{\Sigma N} \approx \frac{F}{\sqrt{N}}. \tag{7-4}$$

7.2 Isochronal Annealing Results

The results of the annealing experiments are cataloged in this chapter along with other details concerning each run. Chapter 8 will present the results of applying the ANNEAL code to this data. The sensitivity of the mass spectrometer on the small particle furnace was 1.96×10^{-13} cm^3STP/count (5.25×10^6 atoms/count) [Schlutter, 1998]. The sensitivity of the mass spectrometer on the long time heating furnace was 3.01×10^{-13} cm^3STP/count (8.09×10^6 atoms/count) [Becker, 1997]. The amount released is given in terms of atoms/cm^2 for comparison to the implanted dose. This number is obtained by multiplying the total measured counts by the sensitivity of the spectrometer (in atoms/count) and dividing by the polished area of the sample.

7.2.1 Initial Samples Implanted with ^4He

7.2.1.1 Sample 050997.1

A piece of sample 050997 was annealed with time steps of 30 minutes in the long time annealing furnace (Chapter 6). The results are given in Tables 7-1 a and b and Figure 7-1. The main reason for this run was to compare a sample implanted with PSII to the data obtained on Apollo samples [e. g. Pepin, et. al. 1970]. The errors for this run were those determined for splitting of the gas volume and for the blanks. The errors were calculated using a spreadsheet calculation developed for this apparatus by Becker [1997]. The statistical error in Table 7-1b is two orders of magnitude smaller than the measured error and will be ignored.

7.2.1.2 Sample 050997.2

A piece of sample 050997 was annealed with time steps of 5 seconds in the small particle furnace (Chapter 6). The results are listed in Tables 7-2 a and b and Figure 7-2.

Table 7-1a. Summary of conditions for sample 050997.1

Annealing Time:	30 minutes
Date of Implant:	May 9, 1997
Date of Anneal:	August, 1997
PSII Treatment	
Ar:	$1x10^{16}$ ions/cm^2
^{4}He:	$1x10^{16}$ ions/cm^2

Table 7-1b. Results of annealing sample 050997.1

T (°C)	Total He Atoms Counted	Fractional Release	Measured Error (±)	Statistical Error (±) in Fractional Release
200	1.30E+05	4.96E-02	2.63E-03	4.13E-05
250	2.02E+05	7.73E-02	2.83E-03	3.31E-05
300	2.28E+05	8.72E-02	4.10E-03	3.12E-05
350	2.39E+05	9.11E-02	5.30E-03	3.05E-05
425	4.42E+05	1.69E-01	5.47E-03	2.24E-05
500	3.21E+05	1.22E-01	4.10E-03	2.63E-05
550	2.48E+05	9.46E-02	8.59E-03	2.99E-05
600*	2.01E+05	7.66E-02	3.42E-03	3.32E-05
650	6.10E+04	2.33E-02	1.40E-03	6.03E-05
700	3.76E+04	1.44E-02	1.02E-03	7.67E-05
750	4.99E+04	1.91E-02	1.13E-03	6.66E-05
800	5.45E+04	2.08E-02	2.89E-03	6.38E-05
850	7.05E+04	2.69E-02	2.30E-03	5.60E-05
900*	8.38E+04	3.20E-02	3.65E-03	5.14E-05
950	3.41E+04	1.30E-02	2.20E-03	8.06E-05
999	1.29E+04	4.92E-03	2.10E-03	1.31E-04
1200	2.04E+05	7.81E-02	2.32E-03	3.29E-05
Total	2.62E+06	1.00E+00	1.50E-03	9.20E-06

* Mechanical difficulties increased the measured errors by about 2%.

Table 7-2a. Summary of conditions for sample 050997.2

Annealing Time:	5 seconds
Date of Implant:	May 9, 1997
Date of Anneal:	July 1997
PSII Treatment	
Ar:	$1x10^{16}$ ions/cm^2
^{4}He:	$1x10^{16}$ ions/cm^2

7.2.1.3 Sample 050997.4

Another piece of sample 050997 was annealed several months later with time steps of 5 seconds in the small particle furnace. The results are listed in Tables 7-3 a and b and Table 7-3.

Table 7-3a. Summary of conditions for sample 050997.4

Annealing Time:	5 seconds
Date of Implant:	May 9, 1997
Date of Anneal:	December 10, 1997
PSII Treatment	
Ar:	$1x10^{16}$ ions/cm^2
^{4}He:	$1x10^{16}$ ions/cm^2

7.2.1.4 Sample 050997.3

A piece of sample 050997 was annealed with time steps of 30 seconds in the small particle furnace. The results are listed in Tables 7-4 a and b and Figure 7-4.

Table 7-4a. Summary of conditions for sample 050997.3

Annealing Time:	30 seconds
Date of Implant:	May 9, 1997
Date of Anneal:	December 17, 1997
PSII Treatment	
Ar:	$1x10^{16}$ ions/cm^2
^{4}He:	$1x10^{16}$ ions/cm^2

Table 7-2b. Results for sample 050997.2

Temp (°C)	Total Counts	Fractional Release	Statistical Error in Fractional Release (±)
25	0.00E+00	0.00E+00	0.00E+00
86	4.25E+02	2.90E-05	1.41E-06
176	1.55E+04	1.06E-03	8.49E-06
283	2.13E+05	1.46E-02	3.15E-05
396	1.04E+06	7.06E-02	6.94E-05
509	2.19E+06	1.49E-01	1.01E-04
616	7.36E+05	5.02E-02	5.85E-05
712	7.25E+05	4.94E-02	5.80E-05
796	1.56E+06	1.07E-01	8.53E-05
867	1.70E+05	1.16E-02	2.81E-05
925	1.59E+06	1.08E-01	8.59E-05
973	3.29E+06	2.24E-01	1.24E-04
1013	2.05E+06	1.40E-01	9.76E-05
1046	2.23E+04	1.52E-03	1.02E-05
1076	1.85E+04	1.26E-03	9.28E-06
1104	1.83E+04	1.24E-03	9.21E-06
1130	8.80E+04	6.00E-03	2.02E-05
1156	4.28E+05	2.92E-02	4.46E-05
1181	4.85E+05	3.31E-02	4.75E-05
1204	1.88E+04	1.28E-03	9.36E-06
1225	8.78E+03	5.98E-04	6.39E-06
1244	6.00E+03	4.09E-04	5.28E-06
1261	1.50E+03	1.02E-04	2.64E-06
1282	2.50E+03	1.70E-04	3.41E-06
1315	5.00E+02	3.41E-05	1.52E-06
Total	1.47E+07	1.00E+00	2.61E-04

Table 7-3b. Results for sample 050997.4

Temp (°C)	Total Counts	Fractional Release	Statistical Error in Fractional Release (±)
25	0.00E+00	0.00E+00	0.00E+00
116	5.00E+01	1.55E-06	2.20E-07
204	2.50E+03	7.77E-05	1.55E-06
288	5.15E+04	1.60E-03	7.05E-06
368	1.87E+05	5.81E-03	1.34E-05
444	3.92E+05	1.22E-02	1.95E-05
516	6.42E+05	1.99E-02	2.49E-05
583	9.32E+05	2.90E-02	3.00E-05
645	1.34E+06	4.16E-02	3.59E-05
703	2.01E+06	6.24E-02	4.40E-05
756	3.31E+06	1.03E-01	5.66E-05
805	4.46E+06	1.39E-01	6.56E-05
850	7.30E+06	2.27E-01	8.40E-05
891	6.46E+06	2.01E-01	7.90E-05
928	3.26E+06	1.01E-01	5.61E-05
961	8.86E+05	2.75E-02	2.92E-05
990	3.99E+05	1.24E-02	1.96E-05
1016	2.84E+05	8.84E-03	1.66E-05
1040	1.16E+05	3.60E-03	1.06E-05
1060	3.29E+04	1.02E-03	5.64E-06
1079	3.03E+04	9.41E-04	5.41E-06
1095	1.41E+04	4.38E-04	3.69E-06
1109	1.12E+04	3.49E-04	3.29E-06
1122	1.21E+04	3.74E-04	3.41E-06
1134	1.01E+04	3.14E-04	3.12E-06
1145	8.31E+03	2.58E-04	2.83E-06
1156	8.93E+03	2.77E-04	2.94E-06
1168	7.56E+03	2.35E-04	2.70E-06
1180	4.51E+03	1.40E-04	2.09E-06
1194	4.05E+03	1.26E-04	1.98E-06
1210	2.62E+03	8.13E-05	1.59E-06
Total	3.22E+07	1.00E+00	1.76E-04

Table 7-4b. Results for sample 050997.3

Temp (°C)	Total Counts	Fractional Release	Statistical Error in Fractional Release (±)
25	0.00E+00	0.00E+00	0.00E+00
159	3.92E+06	1.13E-02	5.68E-06
306	1.56E+07	4.48E-02	1.13E-05
439	3.23E+07	9.27E-02	1.63E-05
553	4.92E+07	1.41E-01	2.01E-05
648	5.48E+07	1.57E-01	2.12E-05
726	6.35E+07	1.82E-01	2.28E-05
790	4.79E+07	1.37E-01	1.98E-05
842	4.29E+07	1.23E-01	1.88E-05
885	2.81E+07	8.06E-02	1.52E-05
920	7.74E+06	2.22E-02	7.98E-06
950	1.80E+06	5.15E-03	3.84E-06
975	4.52E+05	1.30E-03	1.93E-06
996	1.34E+05	3.83E-04	1.05E-06
1014	7.17E+04	2.06E-04	7.68E-07
1030	5.10E+04	1.46E-04	6.48E-07
1042	4.92E+04	1.41E-04	6.36E-07
1049	3.60E+04	1.03E-04	5.44E-07
1052	2.28E+04	6.54E-05	4.33E-07
1065	2.10E+04	6.02E-05	4.16E-07
1080	1.95E+04	5.59E-05	4.01E-07
1093	1.23E+04	3.53E-05	3.18E-07
1105	1.08E+04	3.10E-05	2.98E-07
1115	6.00E+03	1.72E-05	2.22E-07
1125	3.75E+03	1.08E-05	1.76E-07
1135	3.00E+03	8.61E-06	1.57E-07
1145	2.70E+03	7.74E-06	1.49E-07
1154	1.50E+03	4.30E-06	1.11E-07
1164	1.50E+03	4.30E-06	1.11E-07
1174	1.05E+03	3.01E-06	9.29E-08
1183	1.50E+03	4.30E-06	1.11E-07
Total	3.49E+08	1.00E+00	5.36E-05

7.2.2 12XX97 Series Samples

7.2.2.1 Summary of 12XX97 Samples

A series of samples from St. Urbain, Quebec was implanted using PSII. The sputter-cleaning fluence was increased by a factor of 20 on the basis of the PAS analyses . The parameters used are summarized in Table 7-5. Unfortunately, samples 121997 and 123097 were implanted with a dose of ^{3}He that would have contaminated the background in the small particle furnace. Only sample 123197 (Ar sputter-cleaned only) was annealed to measure the native amount of ^{4}He in the Quebec samples.

Table 7-5. Summary of implantations for sample series 12XX97.

Sample	Ar (ions/cm^2)	H (ions/cm^2)	^{3}He (ions/cm^2)
121997	$2x10^{17}$	None	$1x10^{16}$
123097	$2x10^{17}$	$1x10^{17}$	$1x10^{16}$
123197	$2x10^{17}$	None	None

7.2.2.2 Sample 123197.1: Native Helium Measurement

A piece of sample 123197.1 was annealed with time steps of 30 seconds in the small particle furnace in order to determine the amount of helium naturally present in the sample. The conditions and results are tabulated in Tables 7-6 a and b and Figure 7-5.

Table 7-6a. Summary of conditions for 12XX97

Annealing Time:	30 seconds
Date of Implant:	December 31, 1997
Date of Anneal:	May 19, 1998
PSII Treatment	
Ar:	$2x10^{17}$ ions/cm^2
^{4}He:	None

Table 7-6b. Results for 30 second isochronal anneal of sample 123197.1 for calibration purposes.

Power (Watts)	Temperature (°C)	Total Counts	Fractional Release
0	22	300	9.12E-04
1	554	62700	1.91E-01
2	844	226200	6.87E-01
3	1003	4470	1.36E-02
4	1090	24780	7.53E-02
5	1150	N/A	N/A
6	1204	10590	3.22E-02
Total		329040	1.00E+00

N/A - The mass spectrometer recorded a negative number of counts. This fraction is thought to be neglible [Schlutter, 1998].

7.2.3 04XX98 Series Samples

The 04XX98 series of samples were sputter cleaned with $2x10^{17}$ Ar ions/cm^2 and included hydrogen preimplants of various fluences (Table 7-7). These samples were also implanted with ^{3}He -- $1x10^{13}$ ions/cm^2, except the last sample (041698) where the gas supply ran out and only a ^{3}He fluence of $2x10^{12}$ ions/cm^2 was achieved. This fluence of ^{3}He keeps the ^{4}He/^{3}He ratio about the same as this ratio in the solar wind. Keeping this ratio about the solar ratio prevented ^{3}He contamination of the small particle furnace. In all cases the order of implantation was 1) H (if any), 2) ^{4}He, $1x10^{16}$ ions/cm^2 and 3) ^{3}He, $1x10^{13}$ ions/cm^2. The purpose of this order is to create lunar-like conditions *before* the helium is implanted. The predicted depth profiles of these three implantations are shown in Figure 7-6. The average range and average straggling are given in Table 7-8. The error in the number of counts recorded by the mass spectrometer is statistical and will be omitted since they are much less than 1%. The errors only approach 1% in the analysis for ^{3}He, and only in the last few temperature steps of each run.

Table 7-7. Summary of hydrogen preimplants for the 04XX98 sample series.

Sample Number	Hydrogen Fluence
040998	$1x10^{14}$ ions/cm^2
041098	None
041398	$1x10^{17}$ ions/cm^2
041698	$5x10^{15}$ ions/cm^2

Table 7-8. Average range and average straggling calculation for species implanted in 04XX98 series. Calculations were done using TRIM [Ziegler, 1996] and 10,000 ions.

Species	Energy (keV)	Average Range (Å)	Average Straggling (Å)
H	1	147.14	76.46
^{3}He	3	261.06	138.02
^{4}He	4	333.29	173.81

7.2.3.1 Sample 040998.5

Subsample number 5 of sample 040998 was annealed with time steps of 30 seconds in the small particle furnace. The results are listed in Tables 7-9 a and b and Figure 7-7.

Table 7-9a. Summary of conditions for sample 040998.5

Annealing Time:	30 seconds
Date of Implant:	April 9, 1998
Date of Anneal:	May 11, 1998
PSII Treatment	
Ar:	$2x10^{17}$ ions/cm^2
H	$1x10^{14}$ ions/cm^2
^{3}He:	$1x10^{13}$ ions/cm^2
^{4}He:	$1x10^{16}$ ions/cm^2

Table 7-9b. Results for sample 040998.5

Temp (°C)	Total Counts ^{3}He	Fractional Release of ^{3}He	Total Counts ^{4}He	Fractional Release of ^{4}He
25	2065	3.05E-03	9450	7.37E-05
159	141145	2.09E-01	839100	6.55E-03
306	179891	2.66E-01	3834330	2.99E-02
439	97042	1.44E-01	12407070	9.68E-02
553	74658	1.10E-01	15316980	1.20E-01
648	14628	2.16E-02	4510200	3.52E-02
726	91887	1.36E-01	37577220	2.93E-01
790	37521	5.55E-02	26168850	2.04E-01
842	18611	2.75E-02	13691970	1.07E-01
885	8407	1.24E-02	6232620	4.86E-02
920	4526	6.70E-03	3500040	2.73E-02
950	3320	4.91E-03	2111940	1.65E-02
975	1138	1.68E-03	968700	7.56E-03
996	364	5.38E-04	316200	2.47E-03
1014	158	2.33E-04	128250	1.00E-03
1030	178	2.63E-04	162030	1.26E-03
1042	200	2.96E-04	205200	1.60E-03
1049	62	9.19E-05	85050	6.64E-04
1052	40	5.90E-05	39750	3.10E-04
1065	43	6.30E-05	23400	1.83E-04
1080	53	7.86E-05	16500	1.29E-04
Total	675933	1.00E+00	128144850	1.00E+00

7.2.3.2 Sample 041098.4

Subsample number 5 of sample 041098 was annealed with time steps of 30 seconds in the small particle furnace. The results are listed in Tables 7-10 a and b and Figure 7-8.

Table 7-10a. Summary of conditions for sample 041098.4

Annealing Time:	30 seconds
Date of Implant:	April 10, 1998
Date of Anneal:	May 12, 1998
PSII Treatment	
Ar:	$2x10^{17}$ ions/cm^2
H	none
^{3}He:	$1x10^{13}$ ions/cm^2
^{4}He:	$1x10^{16}$ ions/cm^2

Table 7-10b. Results for sample 041098.4

Temp (°C)	Total Counts ^{3}He	Fractional Release of ^{3}He	Total Counts ^{4}He	Fractional Release of ^{4}He
131	14035	1.48E-02	6270	4.44E-04
244	380183	4.01E-01	294480	2.08E-02
351	316392	3.34E-01	797178	5.64E-02
447	86732	9.15E-02	1009572	7.15E-02
532	35413	3.73E-02	1377627	9.75E-02
608	25098	2.65E-02	1757172	1.24E-01
676	29099	3.07E-02	2529561	1.79E-01
736	27296	2.88E-02	2546463	1.80E-01
788	14497	1.53E-02	1460187	1.03E-01
836	9552	1.01E-02	1048554	7.42E-02
879	4930	5.20E-03	598725	4.24E-02
918	2564	2.70E-03	332328	2.35E-02
953	1153	1.22E-03	158736	1.12E-02
985	601	6.33E-04	85842	6.08E-03
1015	267	2.81E-04	40464	2.86E-03
1079	177	1.86E-04	29190	2.07E-03
1132	93	9.84E-05	20661	1.46E-03
1178	68	7.12E-05	18957	1.34E-03
1215	30	3.16E-05	7584	5.37E-04
1248	26	2.78E-05	4716	3.34E-04
1275	15	1.58E-05	3948	2.79E-04
Total	948221	1.00E+00	14128215	1.00E+00

7.2.3.3 Sample 041398.5

Subsample number 5 of sample 041398 was annealed with time steps of 30 seconds in the small particle furnace. The results are listed in Tables 7-11 a and b and Figure 7-9.

Table 7-11a. Summary of conditions for sample 041398.5

Annealing Time:	30 seconds
Date of Implant:	April 13, 1998
Date of Anneal:	May 13, 1998
PSII Treatment	
Ar:	$2x10^{17}$ ions/cm^2
H	$1x10^{17}$ ions/cm^2
^{3}He:	$1x10^{13}$ ions/cm^2
^{4}He:	$1x10^{16}$ ions/cm^2

Table 7-11b. Results for sample 041398.5.

Temp (°C)	Total Counts ^{3}He	Fractional Release of ^{3}He	Total Counts ^{4}He	Fractional Release of ^{4}He
196	51085	1.29E-01	196290	3.78E-03
332	214484	5.40E-01	2541000	4.89E-02
445	50239	1.27E-01	4912830	9.46E-02
540	36446	9.18E-02	8046570	1.55E-01
622	24105	6.07E-02	11950680	2.30E-01
691	12767	3.22E-02	11409990	2.20E-01
752	3233	8.15E-03	4771830	9.19E-02
808	2898	7.30E-03	4811100	9.27E-02
856	724	1.82E-03	1398990	2.69E-02
899	388	9.77E-04	835200	1.61E-02
938	295	7.42E-04	647700	1.25E-02
973	119	3.00E-04	276450	5.33E-03
1006	28	7.03E-05	64260	1.24E-03
1035	14	3.55E-05	30720	5.92E-04
1063	11	2.72E-05	21000	4.05E-04
1300	24	6.05E-05	56610	1.09E-03
Total	396834	1.00E+00	51914610	1.00E+00

7.2.3.4 Sample 041698.5

Subsample number 5 of sample 041698 was annealed with time steps of 30 seconds in the small particle furnace. The results are listed in Tables 7-12 a and b and Figure 7-10.

Table 7-12a. Summary of conditions for sample 041698.5.

Annealing Time:	30 seconds
Date of Implant:	April 13, 1998
Date of Anneal:	May 13, 1998
PSII Treatment	
Ar:	$2x10^{17}$ ions/cm^2
H	$5x10^{15}$ ions/cm^2
^{3}He:	$2x10^{12}$ ions/cm^2
^{4}He:	$1x10^{16}$ ions/cm^2

Table 7-12b. Results for sample 041698.5.

Temp (°C)	Total Counts ^{3}He	Fractional Release of ^{3}He	Total Counts ^{4}He	Fractional Release of ^{4}He
314	16750	2.70E-01	13979760	1.52E-01
501	9919	1.60E-01	14672790	1.60E-01
630	11721	1.89E-01	15707970	1.71E-01
726	Sample Lost	Sample Lost	25661790	2.80E-01
799	14599	2.35E-01	14415810	1.57E-01
860	5907	9.52E-02	5404110	5.89E-02
908	1738	2.80E-02	1117200	1.22E-02
949	835	1.35E-02	459900	5.02E-03
985	313	5.04E-03	150000	1.64E-03
1016	97	1.57E-03	46290	5.05E-04
1043	48	7.74E-04	24750	2.70E-04
1067	38	6.19E-04	21150	2.31E-04
1089	35	5.71E-04	18000	1.96E-04
1109	37	5.95E-04	17940	1.96E-04
1126	3	4.84E-05	6240	6.80E-05
1227	8	1.31E-04	9090	9.91E-05
1299	8	1.31E-04	10200	1.11E-04
Total	62039	1.00E+00	91703700	1.00E+00

7.2.4 Isotopic Ratios of Released Helium

In this series of experiments, the release of ^3He was seen to occur at lower temperatures than expected from the release of ^3He from the Apollo samples (Figure 6-17). The ratio of $^4He/^3He$ for each of the 04XX98 series samples is shown in Figure 7-11. Note that the ratio of implanted $^4He/^3He$ was 1000 for each sample. A discussion of this data will be left to Chapter 9.

7.3 Isothermal Annealing Results

7.3.1 Sample 050997.4

A piece of sample 050997 was annealed with varying time steps of at 715°C seconds in the small particle furnace. Varying time intervals were used in the interest of keeping total time realistic. It was thought that the release would not change as fast at high temperatures due to the proportionality with time. However, the furnace did not reach equilibrium in the 2, 5, and 10 second steps as discussed in Chapter 6. An estimate of the percentage of equilibrium temperature reached for each time interval used is given in Table 7-13. This experiment essentially resulted in three different isothermal data sets instead of one. The results are listed in Tables 7-14 a and b and both the fractional release and cumulative fractional release are displayed in Figure 7-12.

Table 7-13. Estimates of percentage of equilibrium temperature reached in time intervals used for isothermal anneal of sample 050997.4 [Schlutter, 1998].

Time Interval (sec)	Percentage of Equilibrium Temperature
2	25
5	45
10	67
30	95
>45	100

Table 7-14a. Summary of conditions for sample 050997.4

Annealing Time:	30 seconds
Date of Implant:	May 9, 1997
Date of Anneal:	Feb 2, 1998
PSII Treatment	
Ar:	$1x10^{16}$ ions/cm^2
^{4}He:	$1x10^{16}$ ions/cm^2

The data in Figure 7-11 shows evidence of parabolic kinetics. When the isothermal data is plotted versus the square root of time, the linear relationship shown in Figure 7-12 is the result. This relationship is the unique signature of a diffusion-limited dynamic process.

7.4 Reproducibility of Results

Figure 7-14 shows that the release from sample 041098.4 begins at a slightly higher temperature, but the shapes of the two curves are approximately the same. Both curves also show the temperature of maximum release to be about 780°C. The small delay in He release from 041098.4 at low temperatures may be explained by the difference in the sputter-cleaning fluence. The comparison of these two samples demonstrates the reproducibility of this experiment.

7.5 References

Becker, R. H. (1997) Personal communication, University of Minnesota.

Bevington, P. R. and D. K. Robinson (1992) *Data Reduction and Error Analysis for the Physical Sciences*, Second Edition, (McGraw-Hill, Inc., New York), pp. 39-40.

Pepin, R. O., L. E. Nyquist, D. Phinney and D. C. Black (1970) "Rare Gases in Apollo 11 Lunar Material," *Proceedings of the Apollo 11 Lunar Science Conference*, **2**, pp. 1435-1454.

Schlutter, D. J. (1998) Personal communication, University of Minnesota.

Ziegler, J. P. (1996) *SRIM Instruction Manual: The Stopping and Range of Ions in Matter*, (Yorktown, New York: IBM - Research); based on Ziegler, J. P., J. P. Biersack and U. Littmark, *The Stopping and Range of Ions in Solids*, (New York: Pergamon Press, 1985).

Table 7-14b. Results for isothermal anneal of sample 050997.4. Equilibrium temperature was 715°C. The time intervals used were less than that needed for the furnace to reach equilibrium temperature (approx. 45 sec.). The temperatures given here reflect the data in Table 7-13. The last step was raised to 1000°C in order to remove all the ^{4}He from the sample.

Real Temp	Time Step (sec)	Total Counts	Fractional ^{4}He Release
179	2	48600	1.79E-02
322	5	154500	5.68E-02
322	5	2875	1.06E-03
322	5	1250	4.60E-04
322	5	850	3.13E-04
322	5	700	2.58E-04
322	5	610	2.24E-04
322	5	1250	4.60E-04
322	5	1060	3.90E-04
322	5	865	3.18E-04
479	10	392500	1.44E-01
479	10	30000	1.10E-02
479	10	13900	5.11E-03
479	10	10700	3.94E-03
479	10	8800	3.24E-03
479	10	7850	2.89E-03
479	10	6500	2.39E-03
479	10	5750	2.12E-03
479	10	5100	1.88E-03
479	10	3300	1.21E-03
679	30	810750	2.98E-01
679	30	360000	1.32E-01
679	30	102150	3.76E-02
679	30	51300	1.89E-02
679	30	35700	1.31E-02
679	30	22710	8.35E-03
679	30	21810	8.02E-03
1000	60	616800	2.27E-01
Total	417	616800	2.27E-01

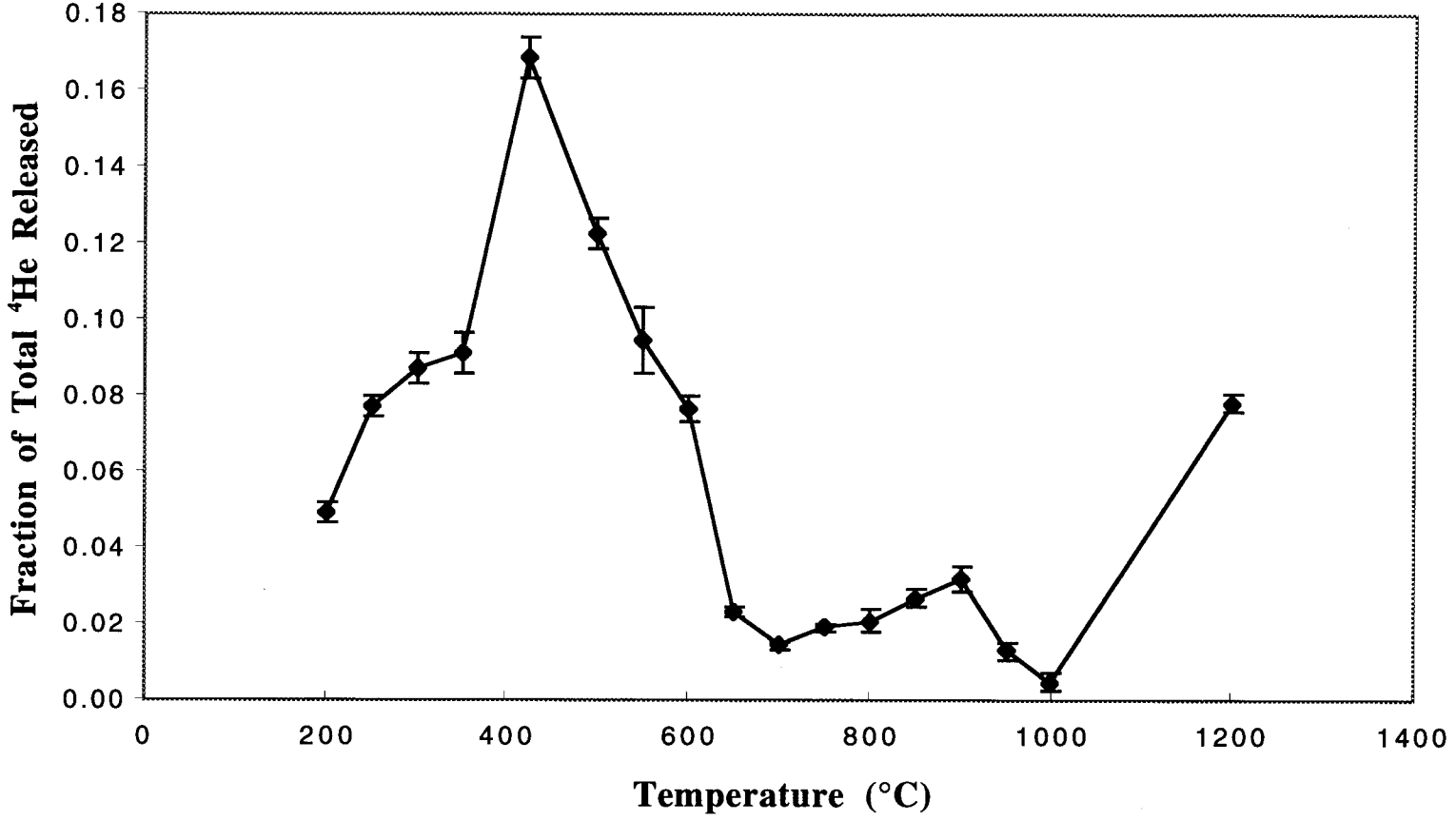

Figure 7-1. Fractional release of ^{4}He from sample 050997.1 during a 30 min. isochronal anneal. This data has been shown earlier in Figure 6-9 in the form of integrated release. The line is included to guide the eye.

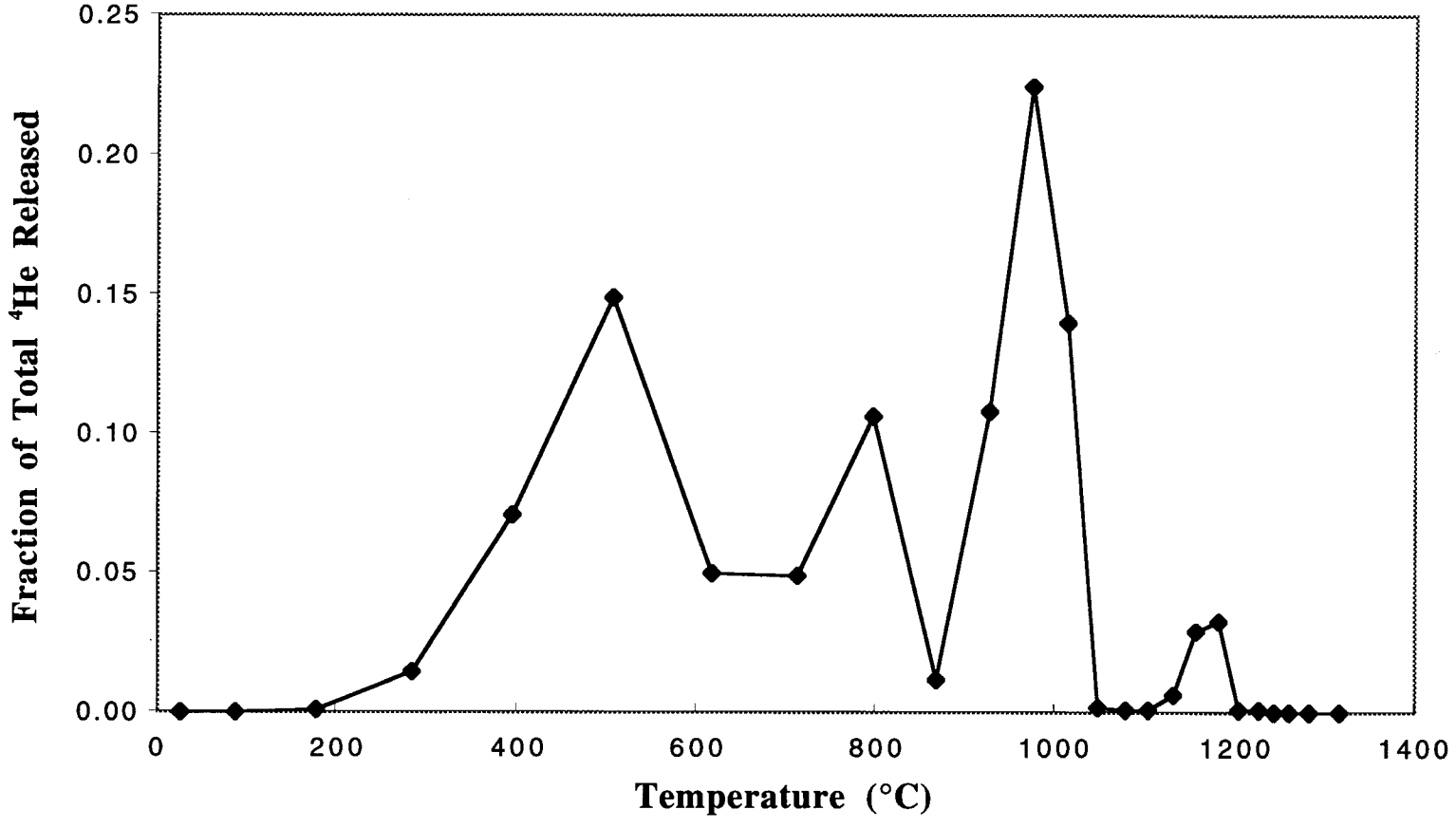

Figure 7-2. Fractional release of ^{4}He from sample 050997.2 during a 5 sec. isochronal anneal. The line is included to guide the eye. Errors are statistical and smaller than the size of the markers.

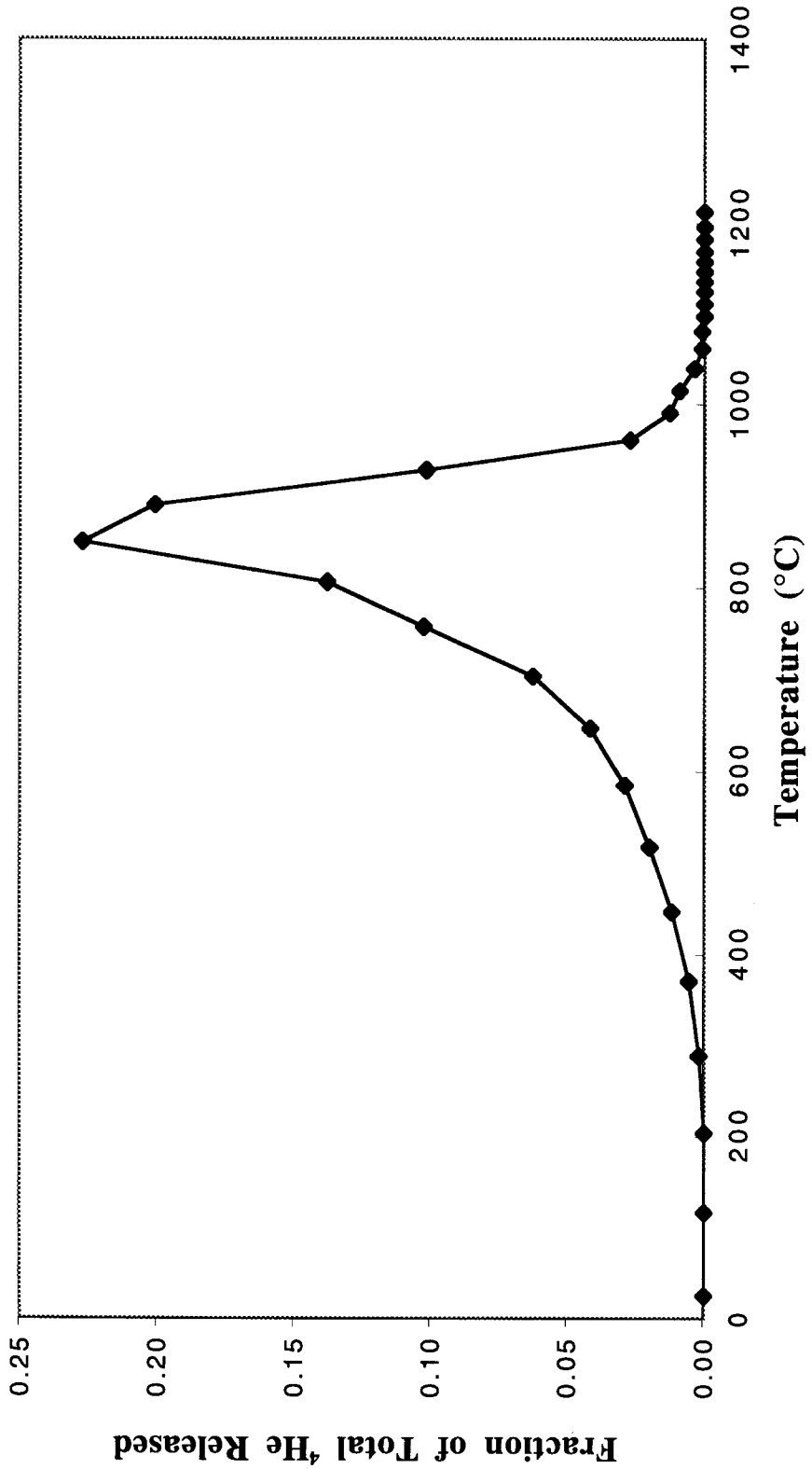

Figure 7-3. Fractional release of ^{4}He from sample 050997.3 during a 5 sec. isochronal anneal. The line is included to guide the eye. Errors are statistical and smaller than the size of the markers.

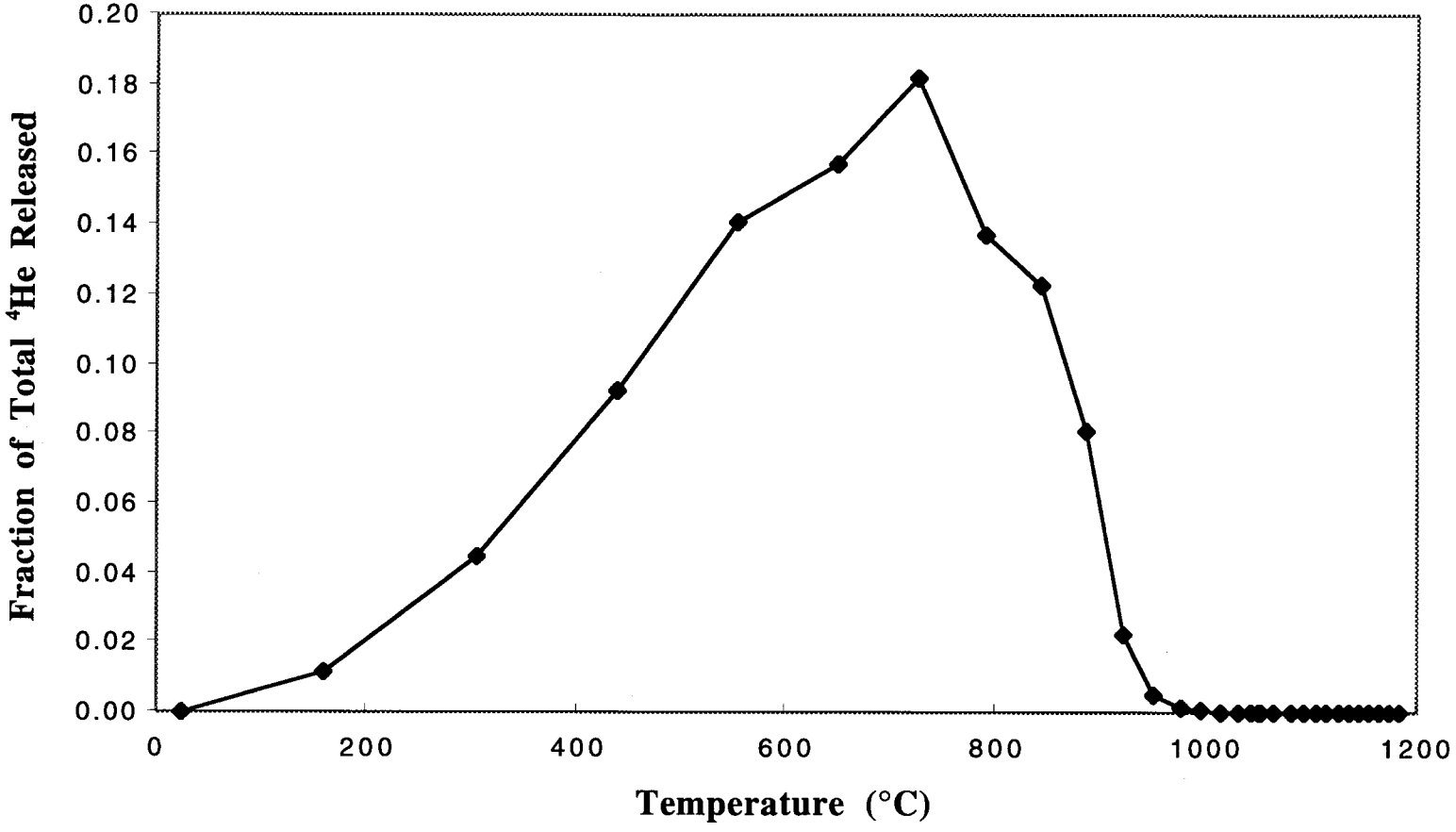

Figure 7-4. Fractional release of ^{4}He from sample 050997.4 during a 30 sec. isochronal anneal. The line is included to guide the eye. Errors are statistical and smaller than the size of the markers.

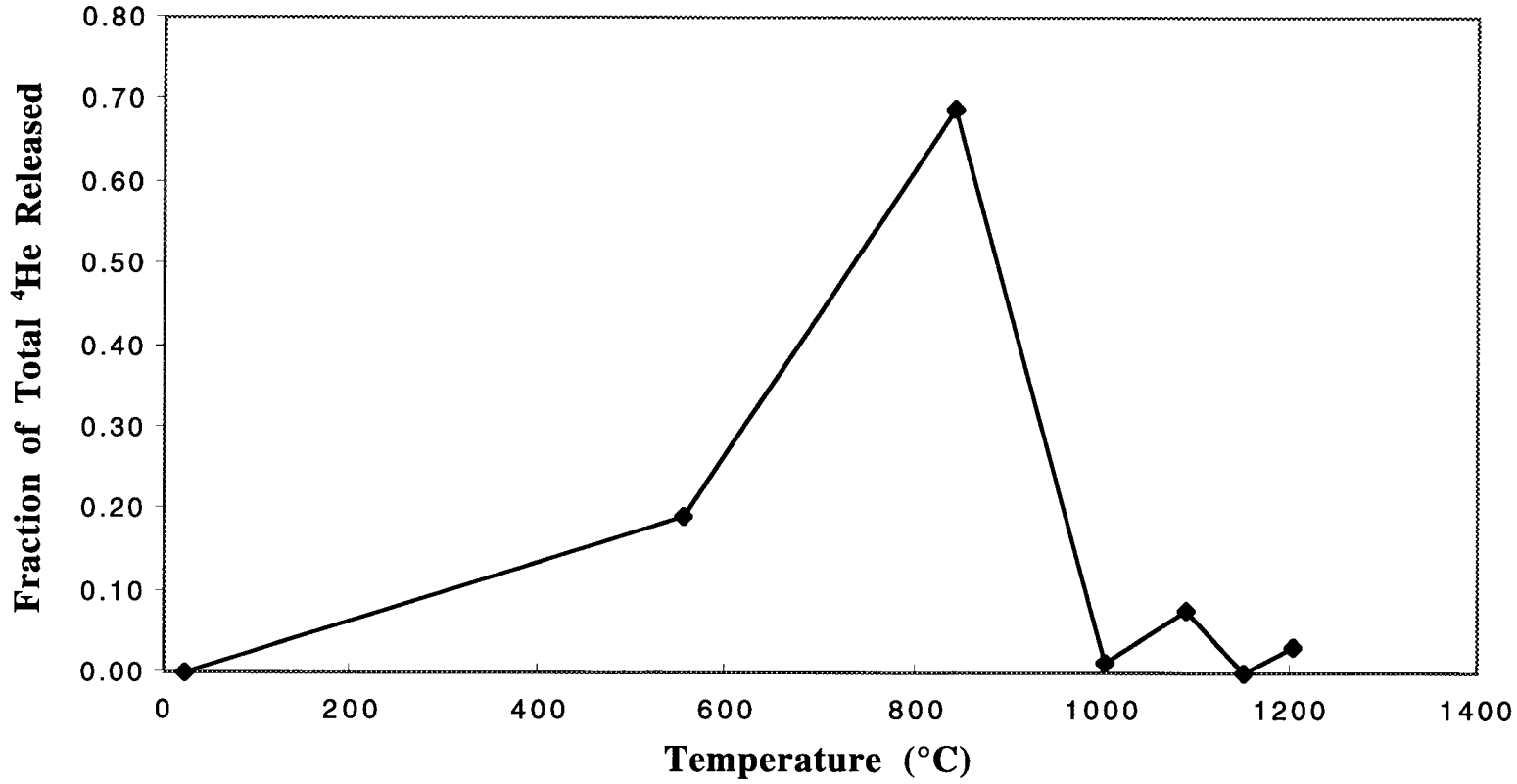

Figure 7-5. Fractional release of ^{4}He from sample 123197.1 during a 30 sec isochronal anneal. The ^{4}He released in this experiment is native to the sample. The line is included to guide the eye. Errors are smaller than the size of a marker.

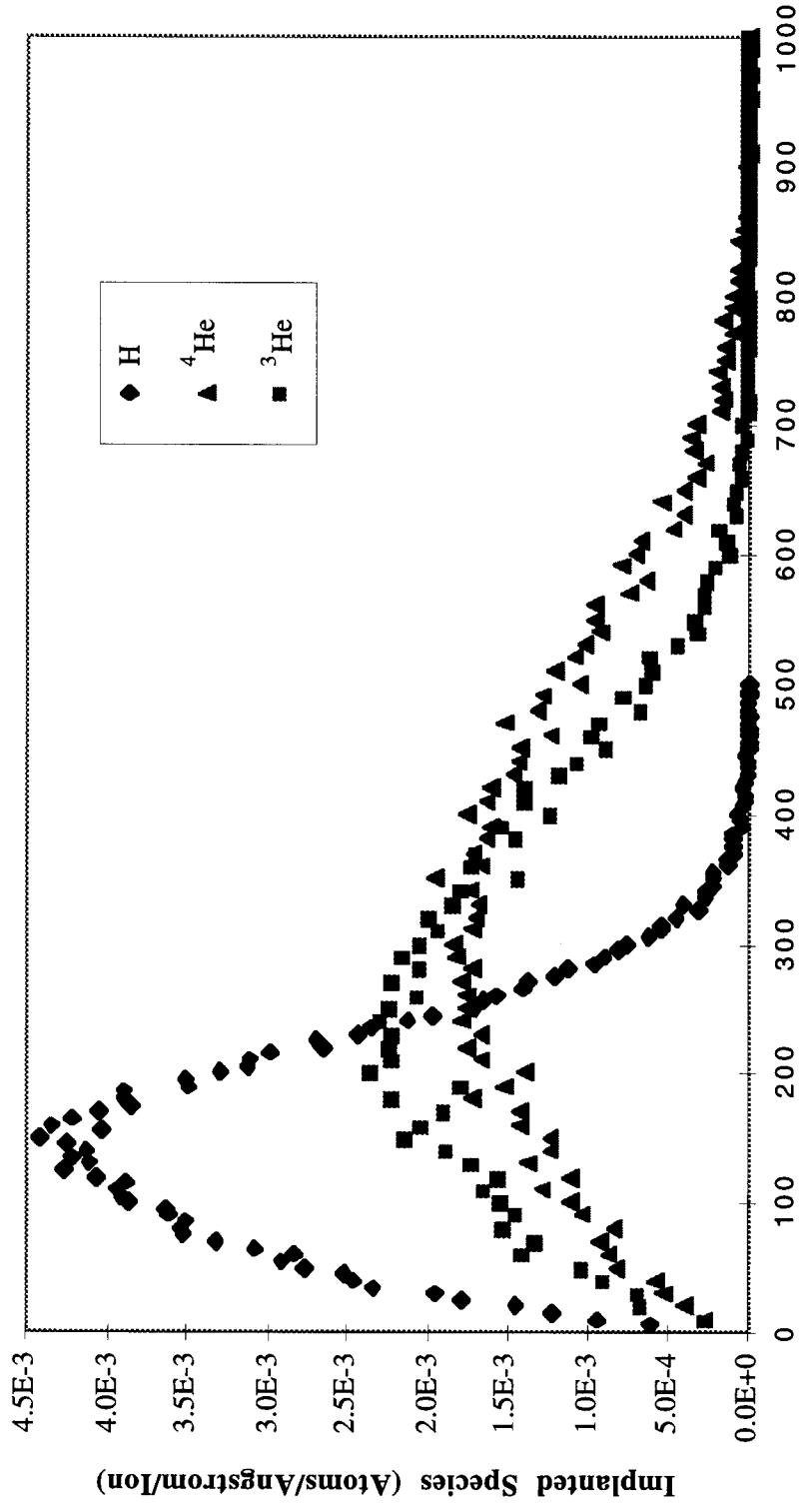

Figure 7-6. Predicted depth profiles of 1 keV H, 3 keV ^{3}He and 4 keV ^{4}He as calculated using TRIM [Ziegler, 1996].

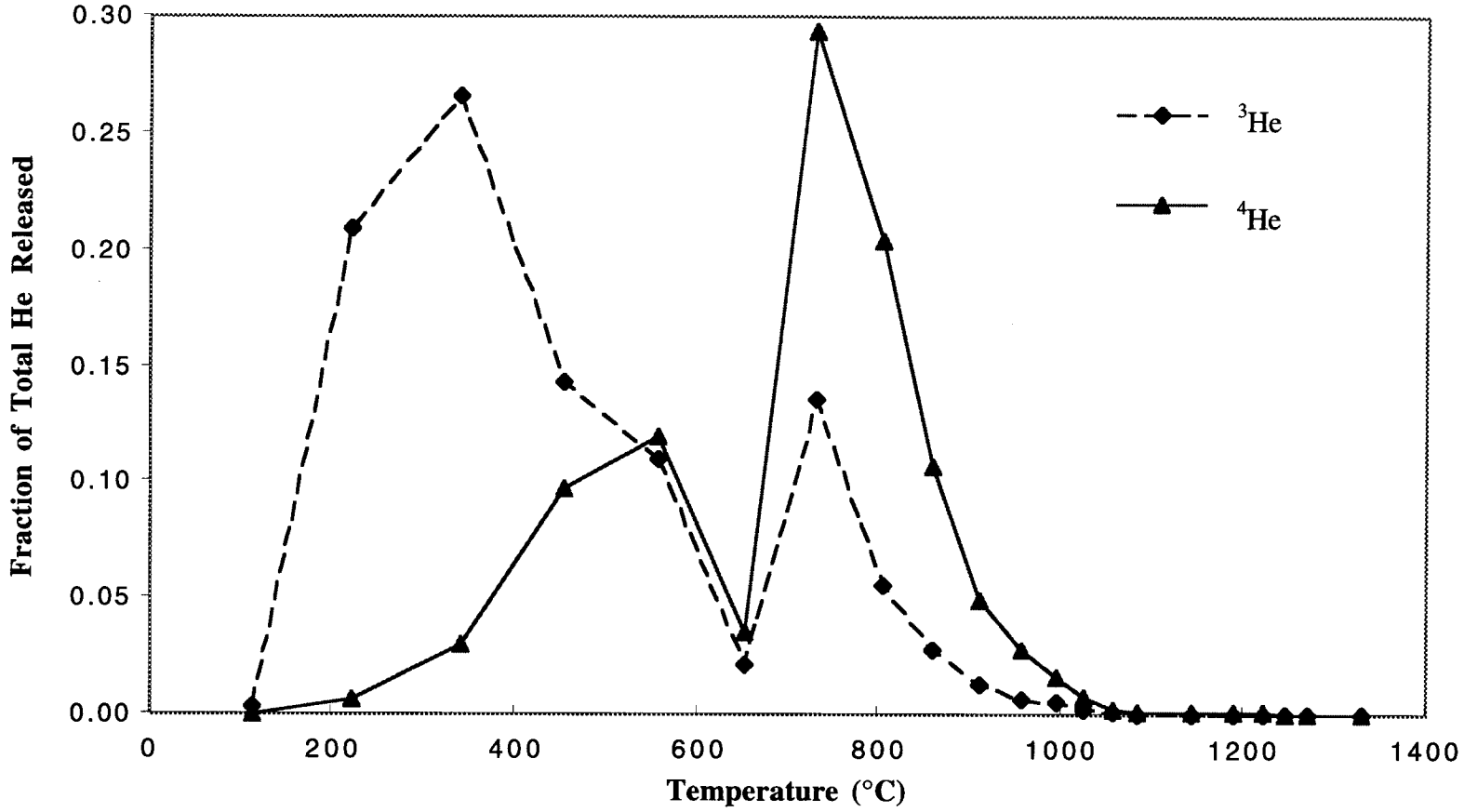

Figure 7-7. Fractional release of ^4He and ^3He from sample 040998.5 during a 30 sec. isochronal anneal. The lines are included to guide the eye. Errors are statistical and smaller than the size of the markers.

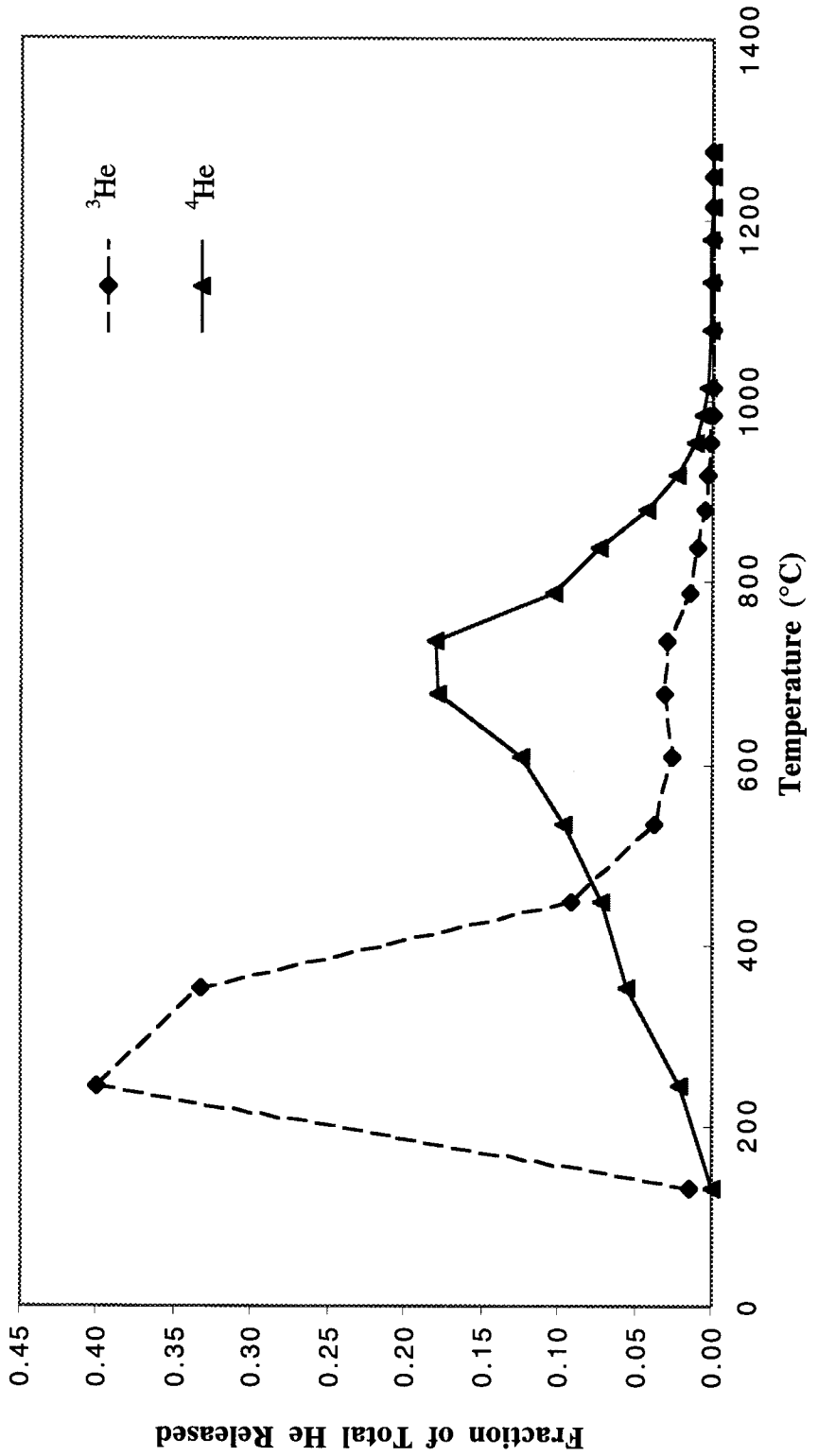

Figure 7-8. Fractional release of ^4He and ^3He from sample 041098.4 during a 30 sec. isochronal anneal. The lines are included to guide the eye. Errors are statistical and smaller than the size of the markers.

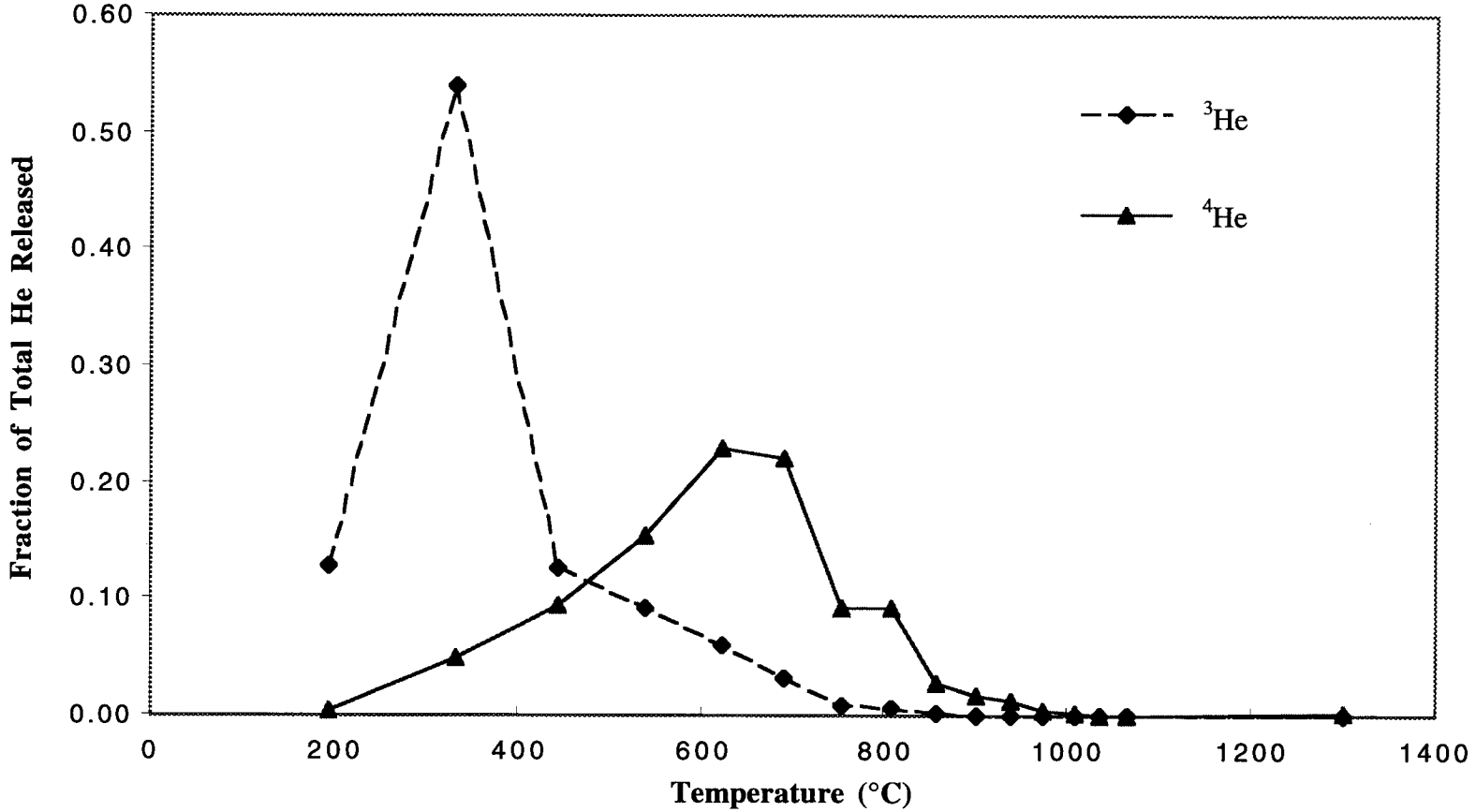

Figure 7-9. Fractional release of ^4He and ^3He from sample 041398.5 during a 30 sec. isochronal anneal. The lines are included to guide the eye. Errors are statistical and smaller than the size of the markers.

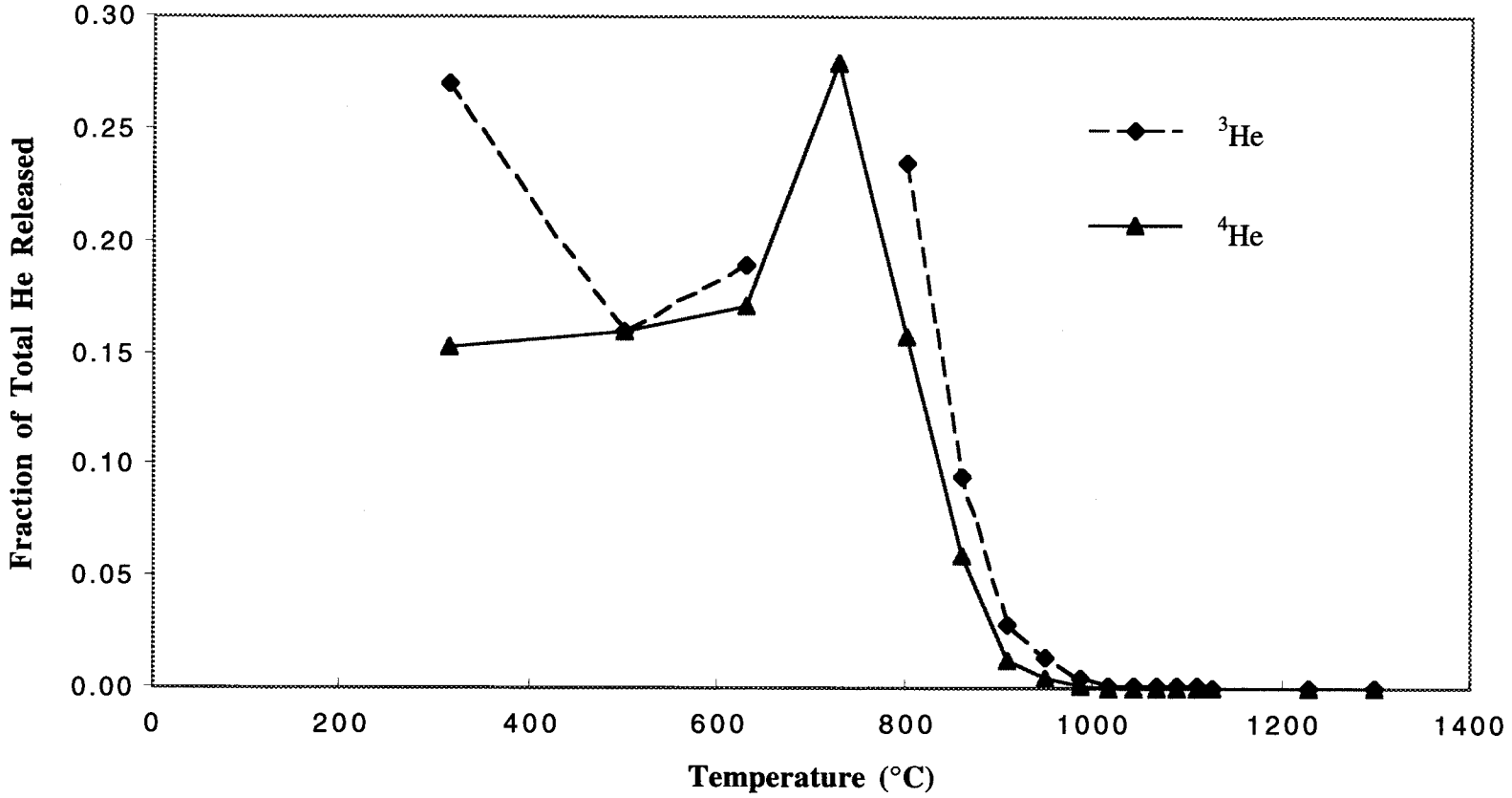

Figure 7-10. Fractional release of ^4He and ^3He from sample 041698.5 during a 30 sec. isochronal anneal. The lines are included to guide the eye. Errors are statistical and smaller than the size of the markers. The fraction of ^4He at 726°C was lost due to mechanical difficulty.

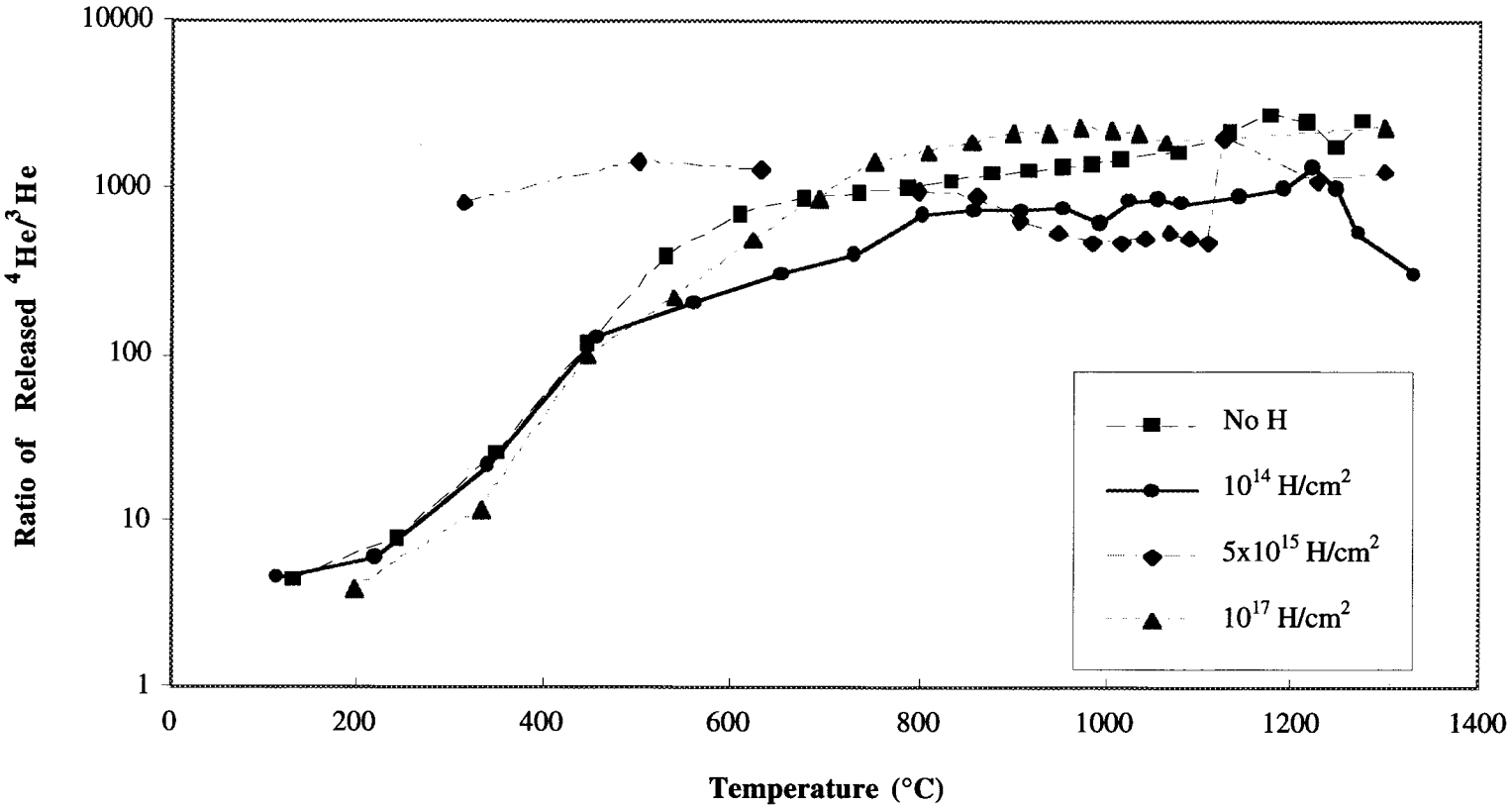

Figure 7-11. Ratio of released ^4He to released ^3He from the 04XX98 series of samples during 30 sec. isochronal anneals. Note that the implanted ratio $^4He/^3He$ was 1000. The lines are included to guide the eye. The fraction of ^4He from sample 041698.5 at 726°C was lost due to mechanical difficulty.

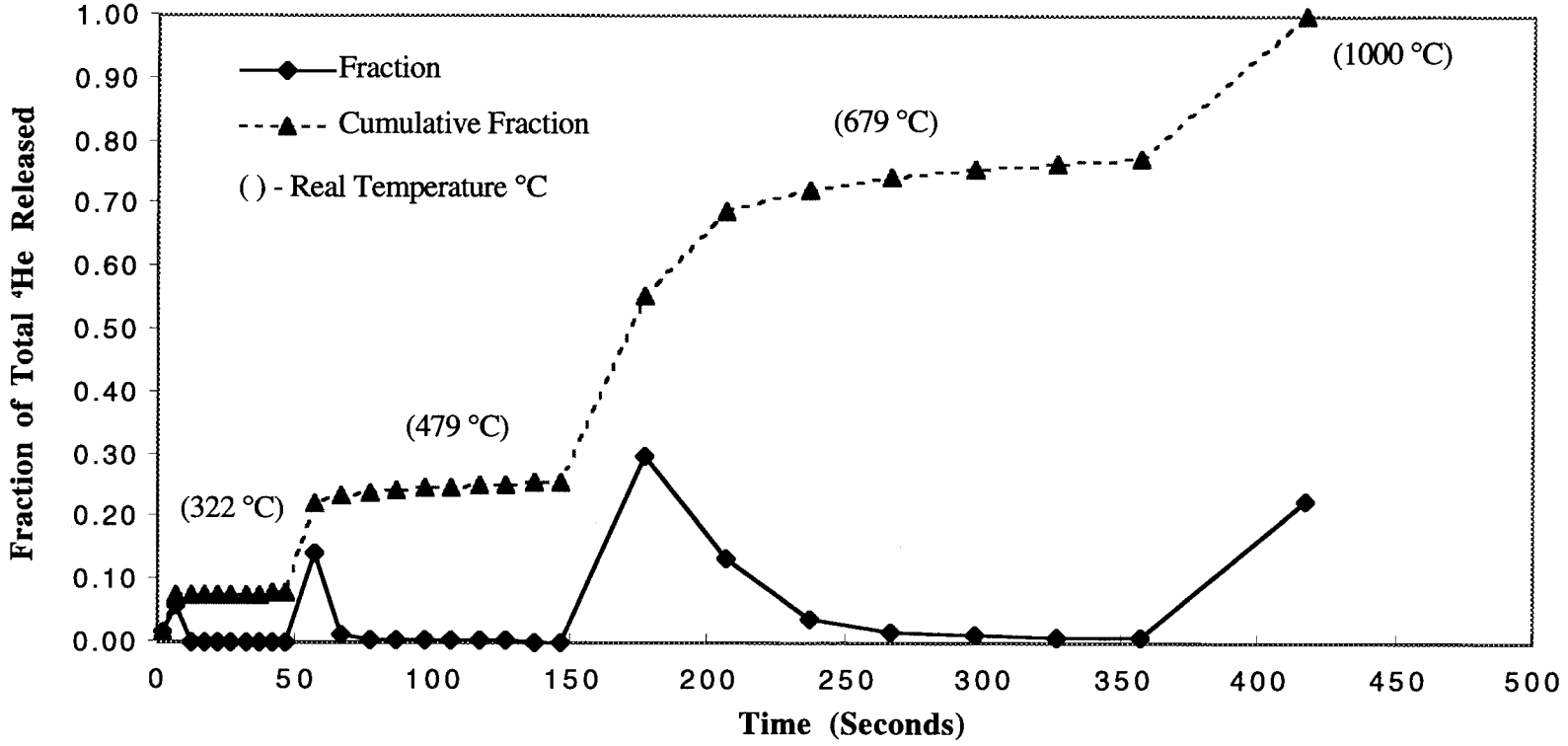

Figure 7-12. Fractional release of ^4He from sample 050997.6 during an "isothermal" anneal. Note the sharp increase in release after each change in time interval. The is a result of the longer heating interval and the time needed for the Ta furnace to come to equilibrium (approximately 60 sec.). The lines are included to guide the eye. Errors are statistical and smaller than the size of the markers.

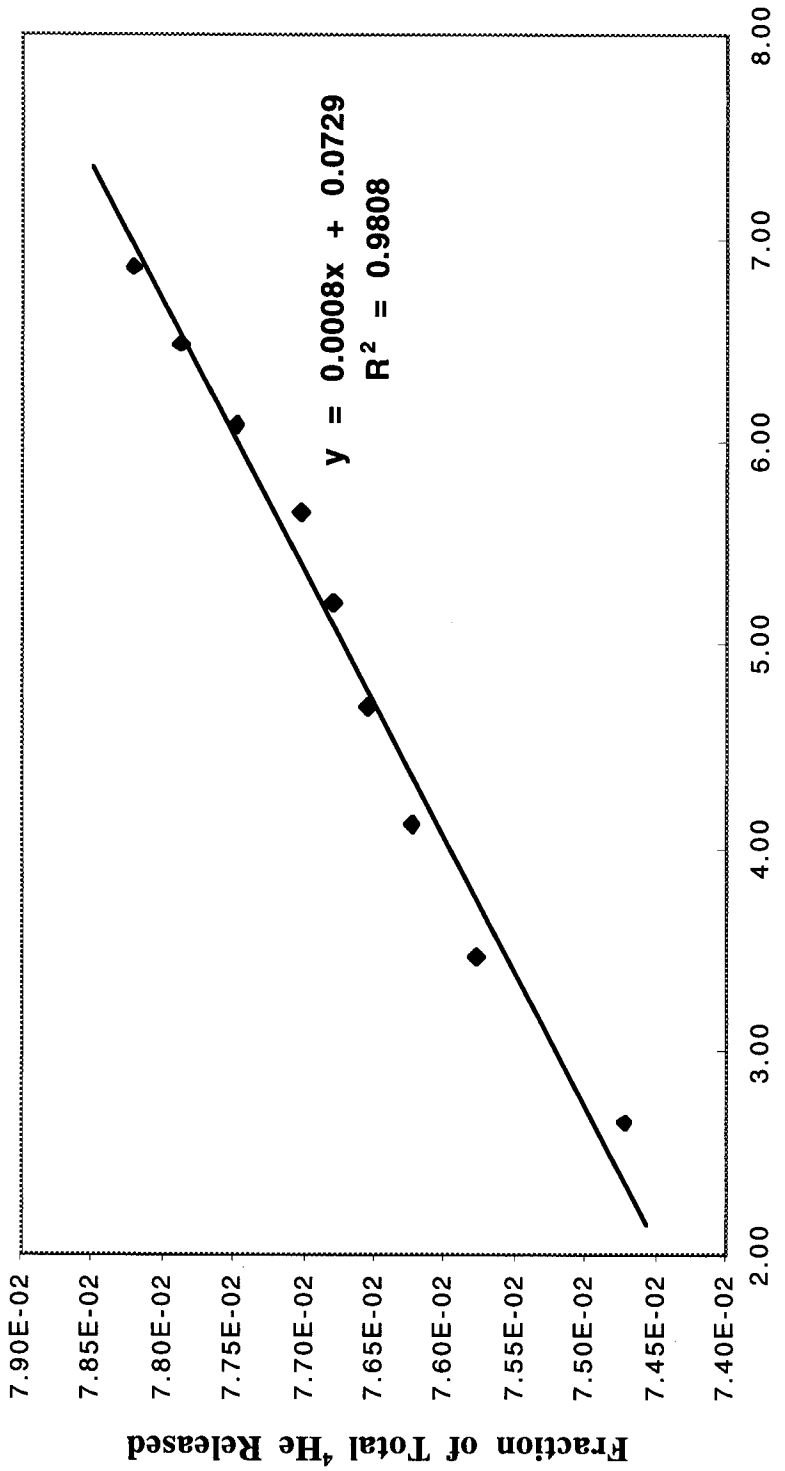

Figure 7-13. Release of ^4He vs. square root of time for isothermal annealing of sample 050997.6. The parabolic dependence of ^4He release on time is the unique signature of a diffusion limited dynamic process.

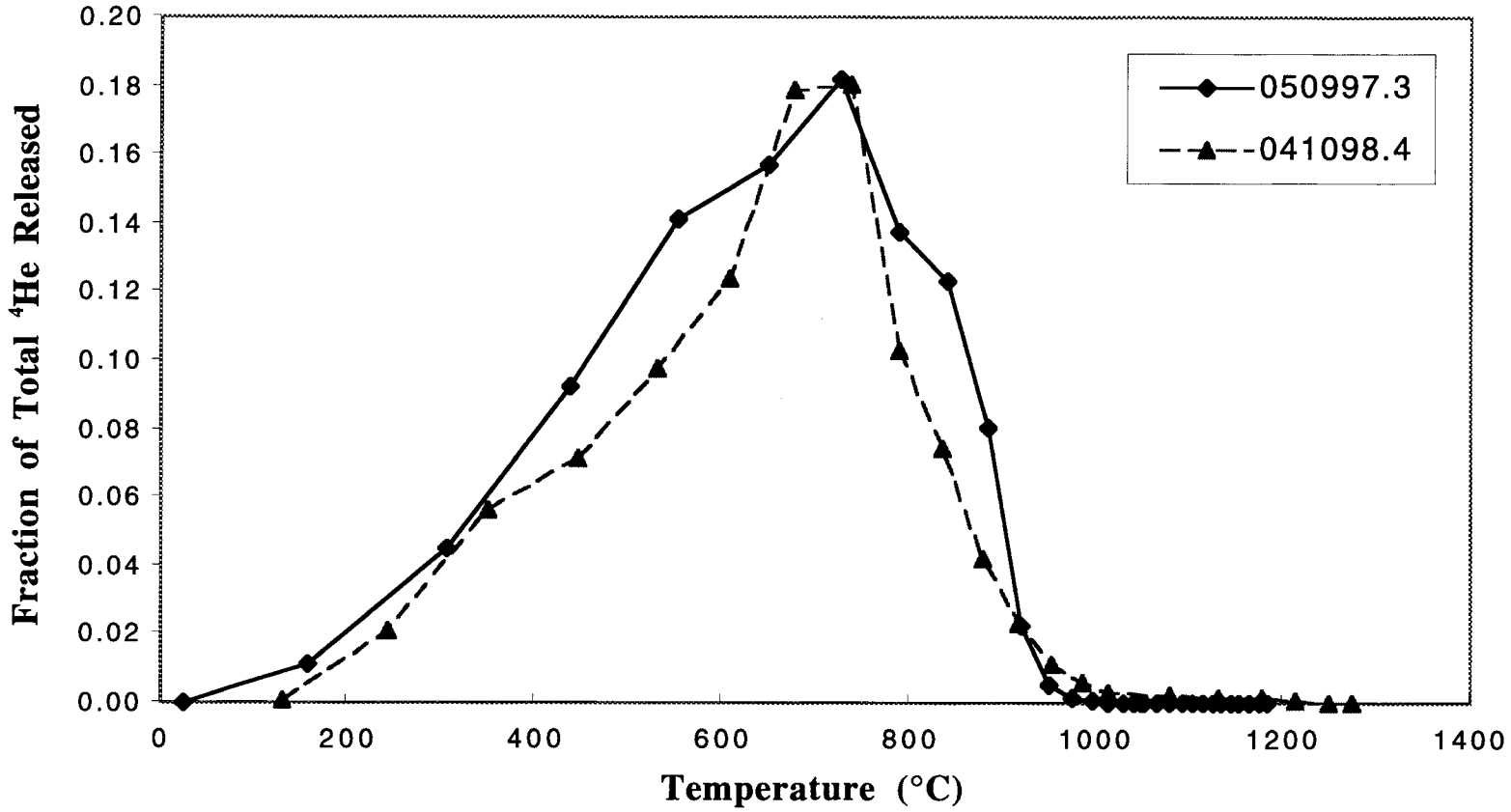

Figure 7-14. Fractional release of ^{4}He from sample 050997.3 (New York Ilmenite) and 041698.5 (Quebec Ilmenite) during a 30 second isochronal anneal. The lines are included to guide the eye. Errors are statistical and smaller than the size of the markers.

Chapter 8 Application of the ANNEAL Code to the Data

8.1 Error Analysis

In this section, the errors generated by the ANNEAL code will be discussed. These errors are generated by propagation of the measured error, the mesh size (Δx), and the assumption of the monoenergetic He profile calculated by TRIM. In most cases the data generated by ANNEAL does not represent the entire fractional release of a sample. This is mainly due to the computational time needed to run the code and have it remain stable (Chapter 5).

8.1.1 Propagation of Measured Error

The propagation of measured error was calculated by generating random numbers within the measured error from Chapter 7. A random number was generated between -1 and 1, and was multiplied by the measured error to generate a uniform distribution about the measured value [Hart, 1982]. The new error was used to calculate a new number of counts, which in turn was used to recalculate the fractional release, normalized to 1. The results of this procedure for the release from sample 050997.1 is shown in Figure 8-1.

8.1.2 Error Introduced by Choice of Spatial Grid Size

The error introduced by the choice of grid size, Δx, is shown in Figure 8-2. The data for sample 041398.5 was analyzed using the ANNEAL code and grid sizes of 1, 5, 10, 20 50 and 100 Å. The error used is two standard deviations of the data for each temperature. Only one data point was calculated for 1 Å and three data points were calculated for 5 Å due to the amount of computational time needed.

The error appears to be greatest at the lowest temperature and for Δx=100 Å. However, the data given in this chapter is primarily run with Δx=100 Å to increase accuracy at high temperatures where the diffusion out the opposite side of the artificially thin

computational space can become significant for smaller Δx. The result of the ANNEAL calculation for ^4He from sample 041398.5 with the calculated error is given in Figure 8-3.

8.1.3 Error Introduced by Assumption of TRIM Profile

A fundamental assumption in this thesis is that the implantations were monoenergetic and that the depth profile of the implanted species is accurately modeled using TRIM. In reality, the implantations vary during tuning of the parameters and the voltage pulse is not a perfect square wave. The voltage pulse used for ^4He typically varied by 0.2 kV resulting in an implantation energy of 4 ± 0.2 keV. It was also assumed that no He^{++} was produced in the plasma. The error generated by the assumption of a monoenergetic implantation error can then be modeled using TRIM calculations at various energies. Profiles were calculated for 3.8 keV and 4.2 keV and used in ANNEAL with the release data from sample 050997.1. The result of the ANNEAL calculation for 4.0 keV is shown in Figure 8-4 with the error generated from these two runs. The error ranges between 7% and 12% and is the largest of the three types of error considered here. Since the other errors are at most 1%, they are ignored.

8.2 Curve Fitting

The data resulting from ANNEAL are fitted to an Arrhenius equation,

$$D = D_0 \exp\left[-\frac{E_a}{k_b T}\right], \qquad (8\text{-}1)$$

with temperature where D_0 is the diffusion constant, n is the defect concentration, E_a is the activation energy of the defect, k_b is the Boltzmann constant and T is the temperature. The fitting is done with Microsoft Excel 5.0 [Microsoft, 1998]. Excel uses a transformed regression model to generate the R^2 value which is a measure of the quality of the fit. $R^2=1$ is a perfect fit. The R^2 value is calculated using Equation 8-2 where Y is a data point, n is the number of data points and i is the ith data point.

$$R^2 = 1 - \frac{\Sigma\left(Y_i - \overline{Y}_i\right)^2}{\left(\Sigma Y_i^2\right) - \frac{\left(\Sigma Y_i\right)^2}{n}} \qquad (8\text{-}2)$$

8.3 Annealing Results

The results of applying the ANNEAL code to the data from annealing experiments on samples 041098.4 and 041398.5 are given in this section. These samples were chosen because they represent the extremes of no hydrogen implantation and $1x10^{17}$ H/cm^2 preimplantation, respectively.

8.3.1 Isochronal Anneals

8.3.1.1 Sample 050997.1

The result of applying the ANNEAL code to the ^{4}He release data of sample 050997.1 is shown in Figure 8-5. The dip in the curve at approximately 675 °C is likely a phase change due to the long heating times (30 minutes) and high vacuum (i.e. very low P_{O2}) [Muan, and Osborn, 1965]. Three regions of diffusion are identified and are summarized in Table 8-1.

Table 8-1. Summary of diffusion characteristics of ^{4}He release from sample 050997.1.

Temperature Range (°C)	Diffusion Coefficient (cm^2/s)	Activation Energy (eV)
200-350	$1x10^{-13}$	0.26
350-675	$1x10^{-11}$	0.54
700-900	$4x10^{-08}$	1.38

8.3.1.2 Sample 041098.4

The result of applying the ANNEAL code to the ^{4}He and ^{3}He release data of sample 041098.4 is shown in Figure 8-6. Two regions of diffusion are identified in the release of both ^{4}He and ^{3}He. The diffusion characteristics are summarized in Table 8-2. Note the lack

of a dip in the data. The short heating times (30 seconds) likely prevent any phase change from occurring.

Table 8-2. Summary of diffusion characteristics of ^4He and ^3He release from sample 041098.4.

	^4He		^3He	
Temperature Range (°C)	Diffusion Coefficient (cm^2/s)	Activation Energy (eV)	Diffusion Coefficient (cm^2/s)	Activation Energy (eV)
130-675	$5x10^{-11}$	0.49	$3x10^{-09}$	0.49
675-1000	$7.2x10^{-02}$	2.24		

8.3.1.3 Sample 041398.5

The result of applying the ANNEAL code to the ^4He and ^3He release data of sample 041398.5 is shown in Figure 8-7. Two regions of diffusion are identified in the release of both ^4He and ^3He. However, in this case, not enough data was analyzed to make a good fit of the ^3He data in the higher temperature range. The fit of ^3He in this range was done with two points simply to show that the activation energy is increasing. The diffusion characteristics are summarized in Table 8-3. Again, note the lack of a dip in the data.

Table 8-3. Summary of diffusion characteristics of ^4He and ^3He release from sample 041398.5.

	^4He		^3He	
Temperature Range (°C)	Diffusion Coefficient (cm^2/s)	Activation Energy (eV)	Diffusion Coefficient (cm^2/s)	Activation Energy (eV)
200-675	$8x10^{-11}$	0.50	$9x10^{-09}$	0.55
675-750	$3x10^{-05}$	1.47	$4x10^{-05}$	1.19

8.4 References

Hart, G. C. (1982) *Uncertainty Analysis, Loads, and Safety in Structural Engineering*, (Prentice-Hall, Inc. Englewood Cliffs, New Jersey), 224 pp.

Microsoft (1993) *Excel User's Guide* (Microsoft Corporation), p. 353.

Muan, A. and E. F. Osborn (1965) *Phase Equilibria Among Oxides in Steelmaking*, (Addison-Wesley Publishing Company, Inc., Reading, Mass.).

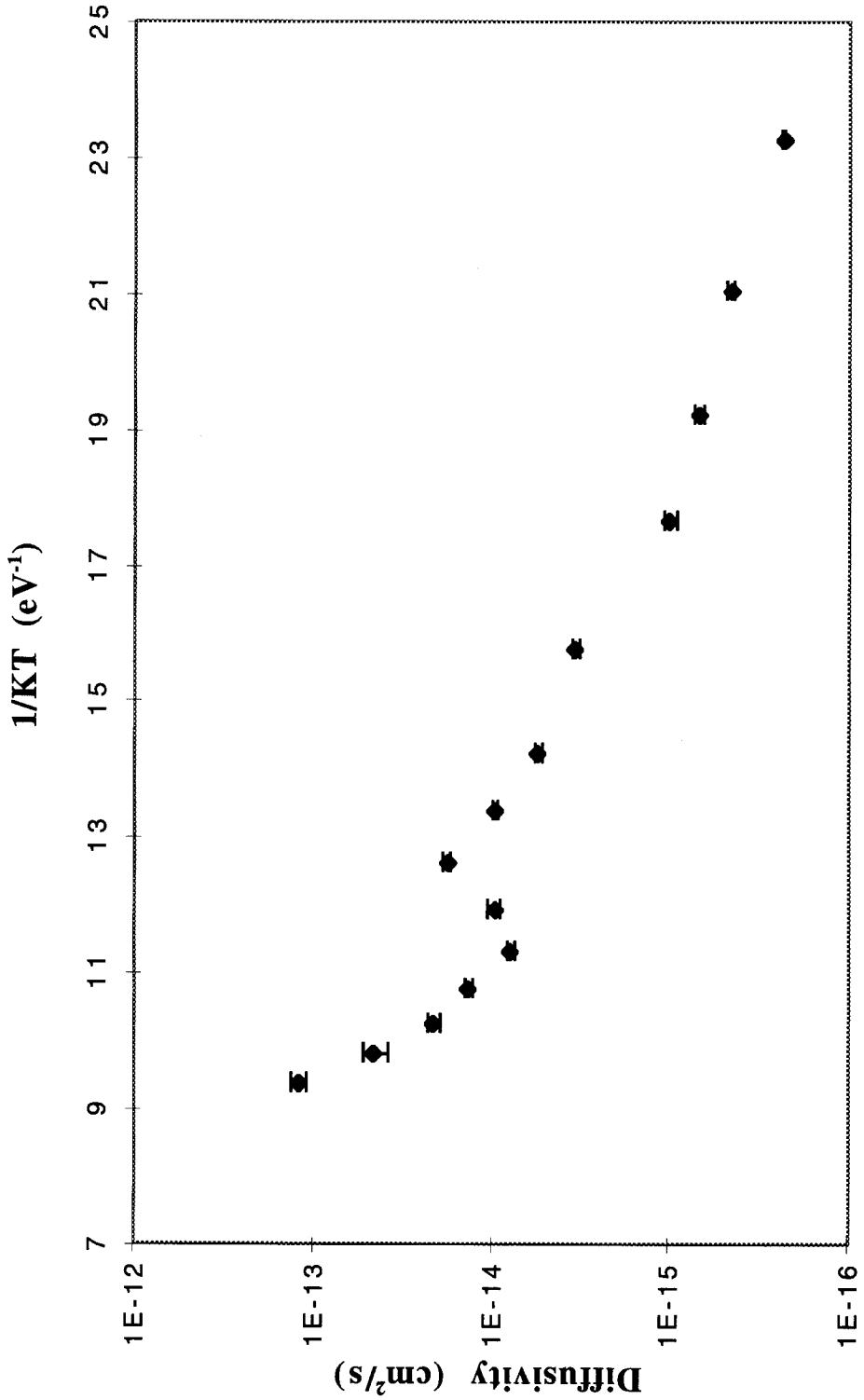

Figure 8-1. Propagation of measured error for the 30 minute annealing of sample 050997.1.

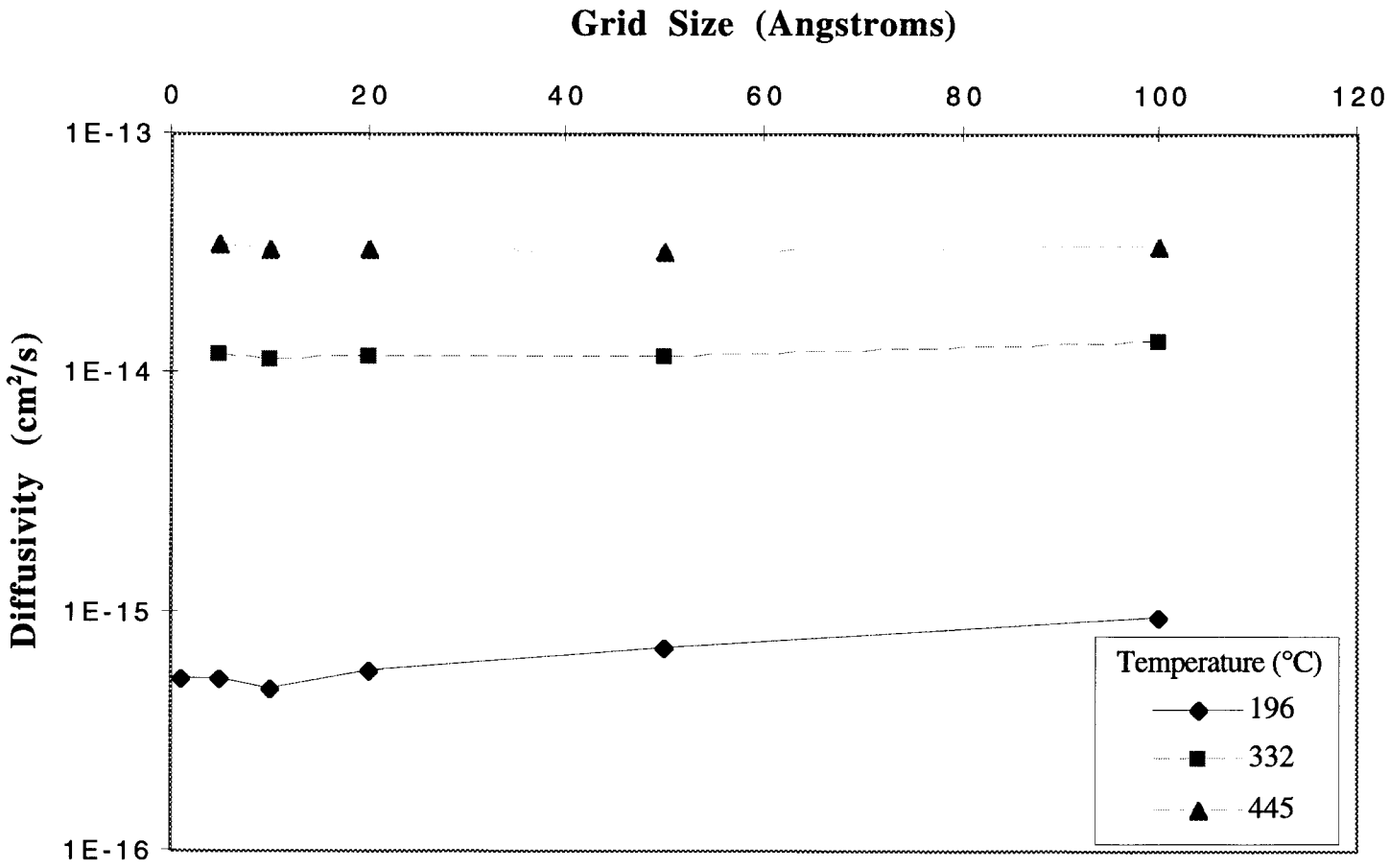

Figure 8-2. Error due to choice of grid size (Δx). Error shown was calculated using the data from sample 041398.5 for ^4He. The lines are included the aid the eye.

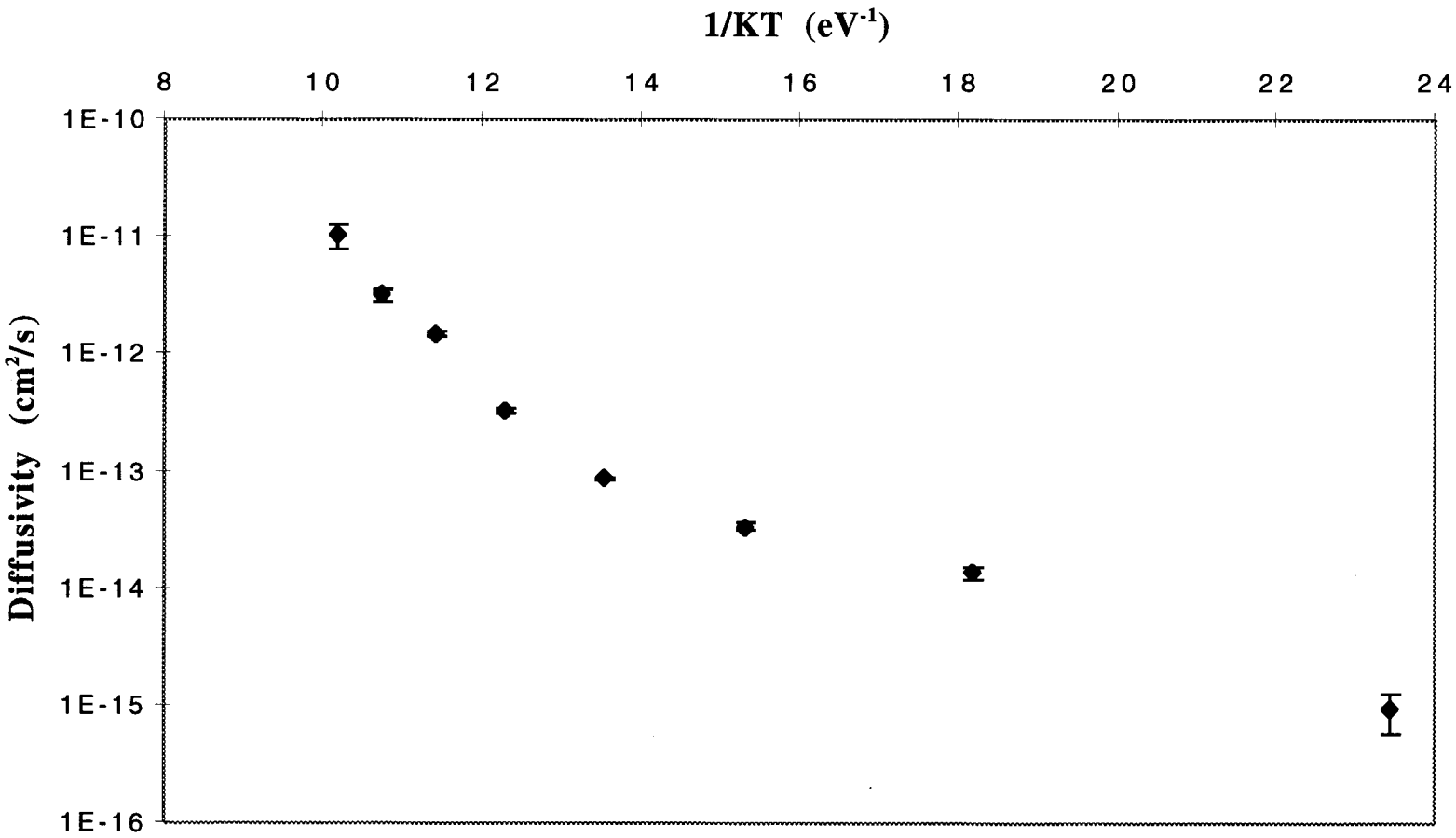

Figure 8-3. ANNEAL results for sample 041398.5 for ^{4}He showing magnitude of error due to choice of grid size = 100 Å.

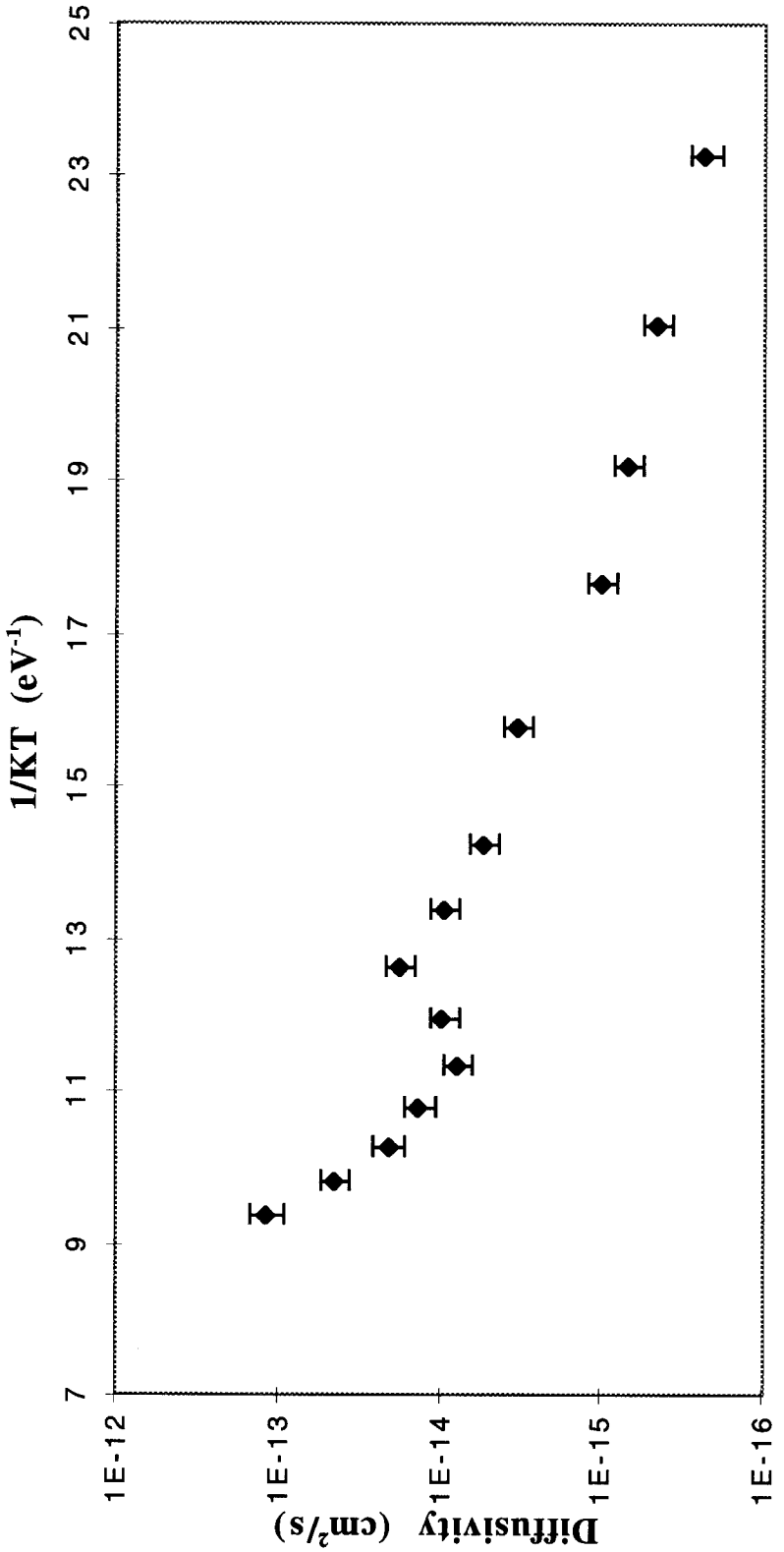

Figure 8-4. Error introduced by assuming that implantation is monoenergetic and calculated by TRIM. The error represents two standard deviations between TRIM runs of 4 ± 0.2 keV.

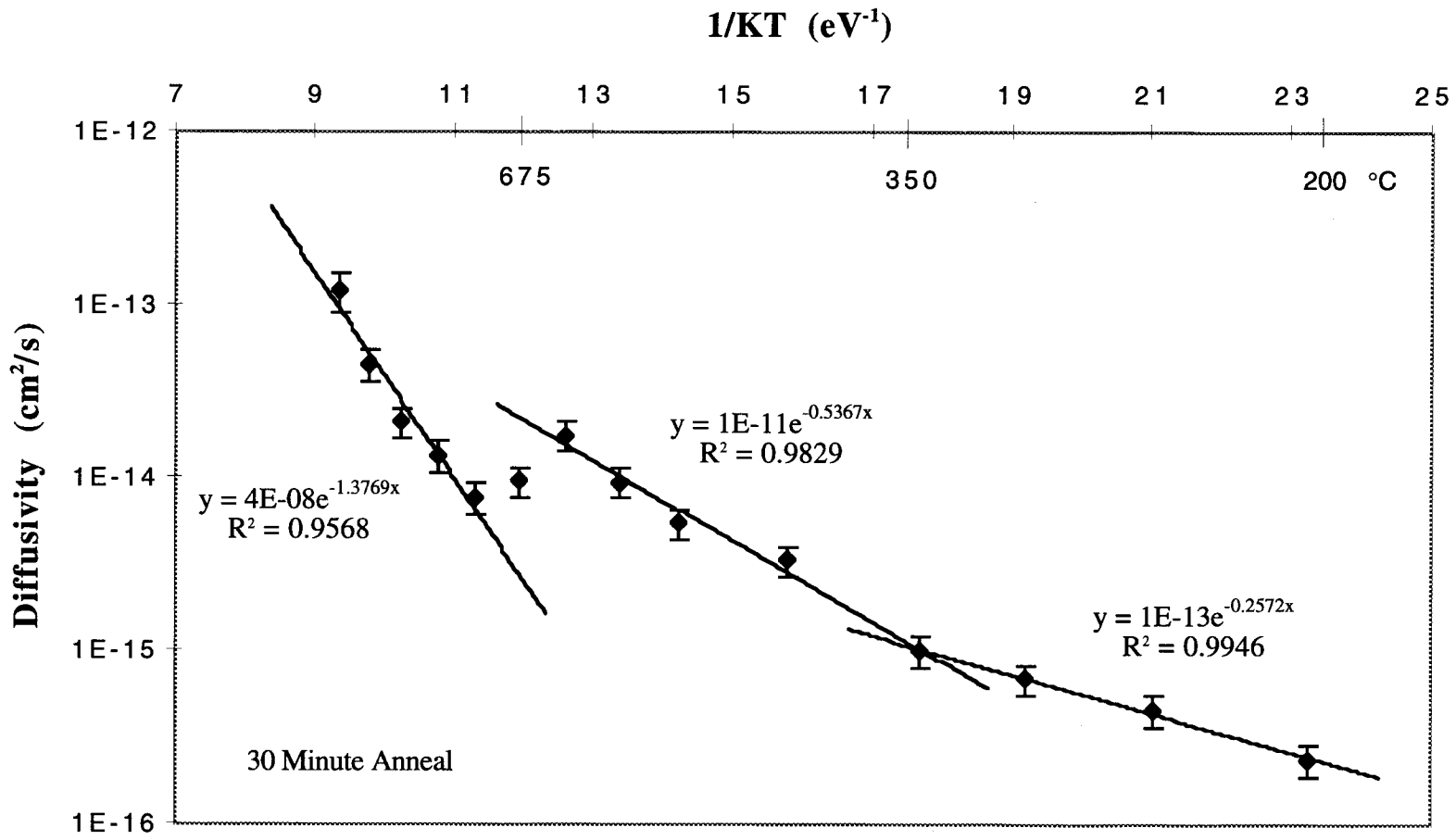

Figure 8-5. Results of applying the ANNEAL code to the ^4He release data from sample 050997.1. This sample was implanted with $1x10^{16}$ $^4He/cm^2$. The error is that due to the assumption of a monoenergetic implantation.

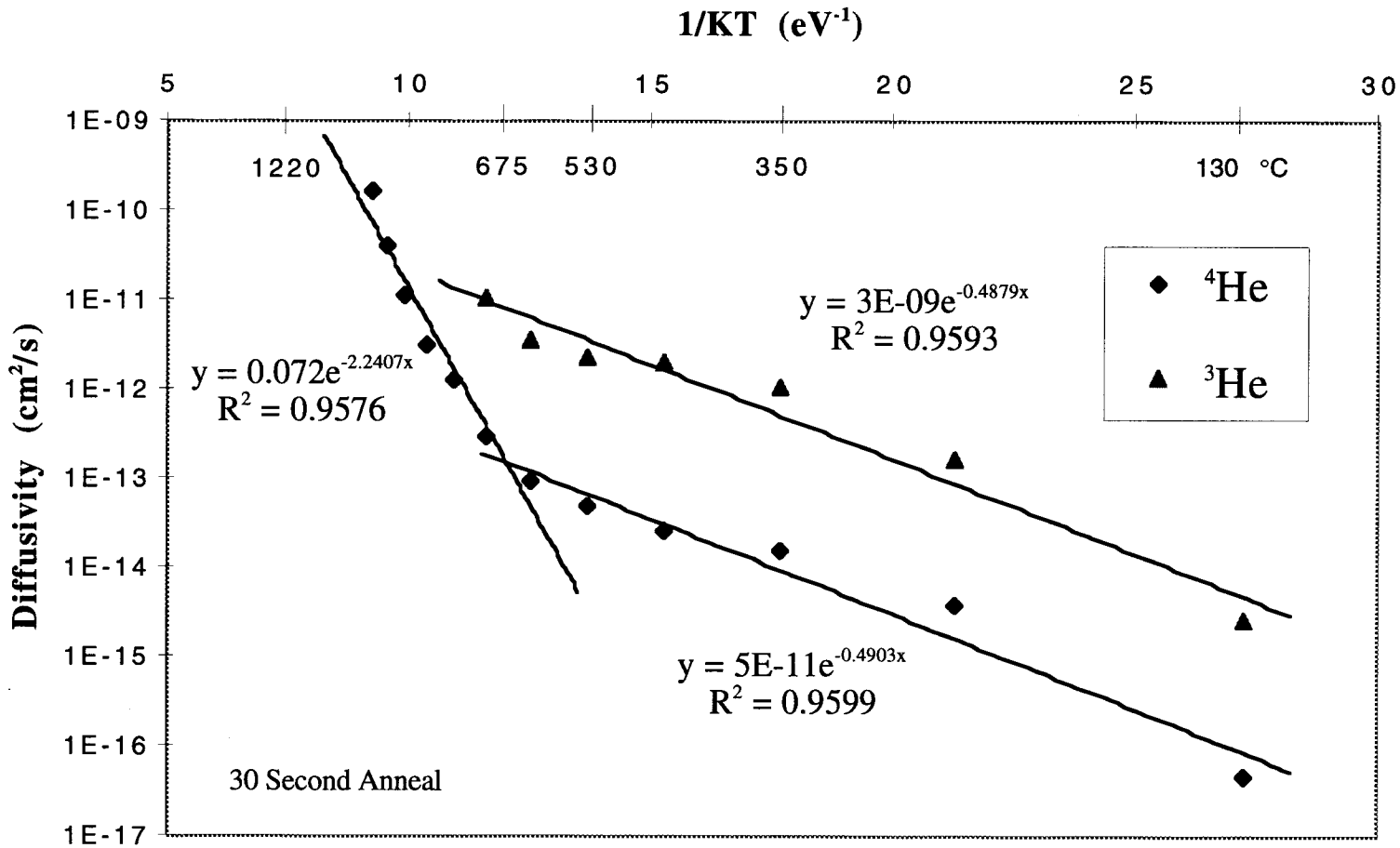

Figure 8-6. Results of applying the ANNEAL code to the ^4He and ^3He release data from sample 041098.4. This sample had no hydrogen preimplantation and was implanted with ^4He to $1x10^{16}$ ions/cm^2 and ^3He to $1x10^{13}$ ions/cm^2.

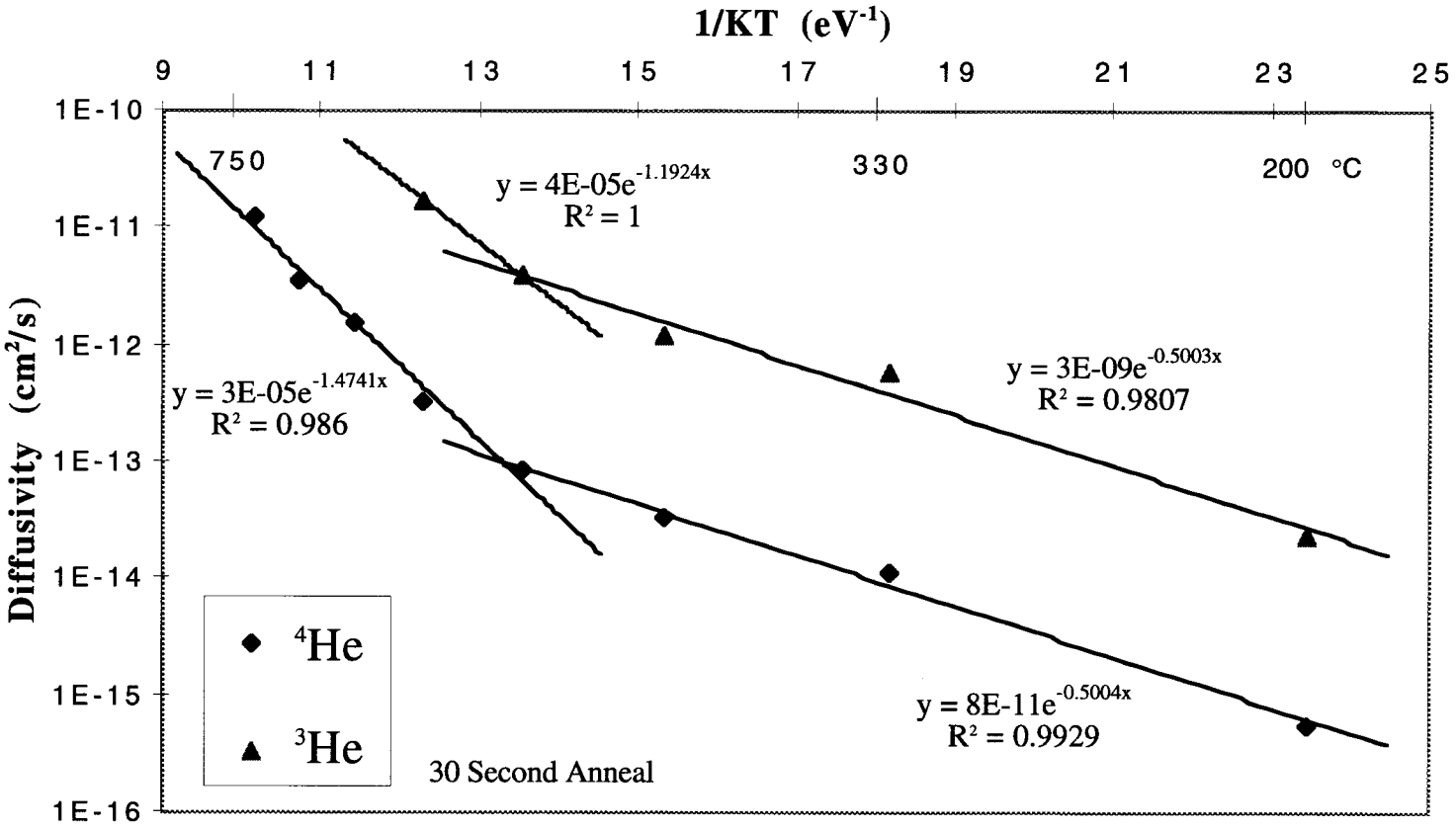

Figure 8-7. Results of applying the ANNEAL code to the ^4He and ^3He release data from sample 041398.4. This sample was implanted with H to $1x10^{17}$ ions/cm^2, ^4He to $1x10^{16}$ ions/cm^2, and ^3He to $1x10^{13}$ ions/cm^2.

Chapter 9 Discussion

The interpretation of the experimental results presented in Chapters 7 and 8, requires an understanding of several properties of ionic crystalline solids. The "free" space available between atoms in the structure, the mobility of the constituent ions within that structure, the number and type of point, line and plane defects present, and the solubility of helium all play a role in determining the trapping mechanism of helium in ilmenite. Several major observations emerge from the experiments documented in this thesis regarding possible trapping and diffusion mechanisms:

- Helium release from implanted terrestrial ilmenites is diffusion-limited as opposed to reaction rate-limited.
- Helium diffusion in terrestrial ilmenite implanted with ^4He and ^3He is characterized by four distinct activation energies, $E_1 = 0.26$ eV, $E_2 \cong 0.5$ eV, $E_3 \cong 1.4$ eV and $E_4 > 2.2$ eV.
- In the temperature range studied here, the diffusivity of helium implanted in ilmenite is much greater than the self-diffusivities observed for anions and cations in rhombohedral oxides or other iron oxides.
- The diffusivity of ^3He in terrestrial ilmenite implanted with ^4He and ^3He is greater than the diffusivity of ^4He.
- Moderate fluences ($<1x10^{15}$ cm^{-2}) of hydrogen preimplantation retard ^3He diffusion in terrestrial ilmenite implanted with ^4He and ^3He. High fluence H preimplantation (10^{17} cm^{-2}) has virtually no effect on ^3He diffusion.

These observations lead to the following model for diffusion of solar-wind helium implanted into ilmenite. Additional observations will be discussed later in this chapter in the context of this model.

9.1 A Model for the Diffusion of Helium Implanted into Ilmenite

Parabolic kinetics is the unique signature of a diffusion-limited dynamic process [Crank, 1956; Carslaw and Jaeger, 1959]. The release of implanted helium from ilmenite during isochronal annealing is linear with respect to the square root of time (Figure 7-13). Therefore, the release of the implanted helium is limited by diffusion mechanisms.

The results of the ANNEAL code applied to the fractional release of the implanted helium indicate four activation energies: $E_1 = 0.26$ eV, $E_2 \cong 0.5$ eV, $E_3 \cong 1.4$ eV and $E_4 > 2.2$ eV (the results from Chapter 8 are summarized in Tables 9-1 and 9-2). It is clear from the analyses in Chapter 8 that the diffusivity of the implanted helium is several orders of magnitude greater than the self-diffusivities of component ions observed for other rhombohedral oxides or other iron oxides (Chapter 3). Therefore, the helium is diffusing through a quasi-stationary structure, i.e. ionic diffusion processes and related point defect relaxations are negligible.

Table 9-1. Summary of diffusion characteristics for ^{4}He in simulated lunar ilmenite calculated using the ANNEAL code (Chapter 8).

Sample	Temperature Range (°C)	Diffusion Constant, D_0 (cm^2/s)	Activation Energy (eV)
050997.1 (no H)	200-350	$1x10^{-13}$	0.26
	350-675	$1x10^{-11}$	0.54
	700-900	$4x10^{-08}$	1.38
041098.4 (no H)	130-675	$5x10^{-11}$	0.49
	675-1000	$7x10^{-02}$	2.24
041398.5 ($1x10^{17}$ H/cm^2)	200-675	$8x10^{-11}$	0.50
	675-750	$3x10^{-05}$	1.47

Table 9-2. Summary of diffusion characteristics for ^3He in simulated lunar ilmenite calculated using the ANNEAL code (Chapter 8).

Sample	Temperature Range (°C)	Diffusion Constant, D_0 (cm^2/s)	Activation Energy (eV)
041098.4 (no H)	130 - 675	$3x10^{-09}$	0.49
041398.5 ($1x10^{17}$ H/cm^2)	200 - 675	$9x10^{-09}$	0.55
	675 - 750	$4x10^{-05}$	1.19

The implantation of He and H (as well as Ar during sputtering cleaning, Chapter 6) has modified the surface of the ilmenite to a depth of approximately 50 nm (Figure 7-6). In addition to raising the ilmenite to a higher energy state by the introduction of He and H, the crystalline structure of the ilmenite is partially destroyed by the irradiation. A schematic of the "layered" material created is shown in Figure 9-1. The activation energy, $E_1 = 0.26$ eV, could be explained by radiation damage caused by the Ar sputter-cleaning which damages the upper 5 nm of the surface (Region A in Figure 9-1). The activation energy, $E_2 \cong 0.5$ eV, might be explained by radiation damage caused by the implantation of ^4He or the numerous exsolution lamellae shown to exist in terrestrial ilmenites (Chapter 6) (Region B in Figure 9-1). The activation energy, $E_2 \cong 1.4$ eV, could correspond to the binding energy for helium trapping in oxygen vacancies as calculated by Welch, et al. [1976] and observed by Allen [1991] for α-Al_2O_3 (Chapter 3). Finally, the activation energy, $E_3 > 2.2$ eV, may be an indication of helium trapping in constitutional vacancies (naturally vacant octahedral sites) in the corundum-like structure of ilmenite, also calculated by Welch, et al. [1976] and observed by Allen [1991] for α-Al_2O_3 (Chapter 3). These latter two mechanisms are likely to be high energy states for He and are likely obtained only by the energetic implantation of He into the crystalline structure. Once the sample is heated enough to overcome the binding energy of He

to either type of trap, the He appears to diffuse to the surface and escape. The various influences on He diffusion in this model are discussed in more detail below.

9.1.1 Solubility of He in Minerals

In order to be able to discuss diffusion of ^{4}He in ilmenite, one must first have an idea of the amount of helium that is naturally soluble in the lattice. While solubility data for helium in ilmenite has not been found, an estimate can be made using data for magnetite and basaltic glass. The solubility limit of helium in magnetite has been measured to be 6.1×10^{16} atoms/g or 23 ppm at 723°C [Lancet and Anders, 1973]. The solubility of He in obsidian and basaltic glass is approximately the same, about 14 ppm, at about 300°C and 1 atmosphere [Jambon and Shelby, 1980]. Calculations using TRIM indicate that the maximum concentration of implanted ^{4}He is about 4.2×10^{20} atoms/g for an implantation of 1×10^{16} ions/cm^2. Thus, the solubility limit is about four orders of magnitude lower than peak implantation concentration. The profile of implanted helium provides the driving force for diffusion because of the local supersaturation of helium caused by the implantation.

9.1.2 Lattice Disorder and Radiation Damage

The diffusion constant, D_0, is a convolution of the distance between equilibrium positions of the diffusing species and an entropy term which is given in Equation 9-1 [Jost, 1960].

$$D = D_0 \exp\left(\frac{\Delta H}{RT}\right) = a^2\left(\frac{kT}{h}\right)\exp\left(\frac{\Delta S}{R}\right)\exp\left(\frac{\Delta H}{RT}\right), \qquad (9\text{-}1)$$

In Equation 9-1, a is the distance between equilibrium positions (effective jump distance), k is Boltzmann's constant, T is the temperature in Kelvin, h is Planck's constant, R is the gas constant, ΔS is the change in entropy and ΔH is the effective activation energy between the activated and normal states [Jost, 1960]. For diffusion in a crystalline solid, the entropy term is typically the order of unity. However, since the helium is being placed in the lattice by

irradiation, it is instructive to estimate the magnitude of the energy of disorder, $T\Delta S$, for each of the temperature regimes observed (Table 9-3). In this estimation, the effective jump distance has been assumed to be 0.5 nm, the lattice parameter in the a-direction in ilmenite (Chapter 3). This energy of disorder can then be compared to the energy of fusion for ilmenite, ΔH = 0.94 eV (91 kJ/mol).

Table 9-3 reveals that the energy of disorder for the temperature range 130 - 675°C is considerably larger than the activation energy measured for helium diffusion and approaches the enthalpy of fusion for ilmenite. The entropy term is negative as opposed to the positive activation energy. The large negative entropy term suggests that the highly damaged lattice is relaxing to a more ordered, lower energy state as the sample is heated. This entropy contribution also suggests that the ilmenite has been at least partially amorphized by the irradiation. The metamict state discussed in Chapter 3 may be a good approximation of the state attained by the implantation. This layer may contain very small regions of crystalline order among basically amorphous material. These tiny crystalline domains may exhibit behavior similar to that seen in Ar dating studies of systems with multiple diffusion domains (MDD's) [Lovera et al., 1989]. This phenomenon could be explored using the current sample set with much smaller temperature steps at low temperatures. It should be noted that dating studies assume uniform distribution of the noble gas within the material and the models derived typically do not apply to irradiation damaged material.

Amorphization is further corroborated here since the diffusion of helium in this temperature range with an activation energies of 0.26 eV and 0.5 eV is similar to the diffusion of helium in glass (Chapter 3). At higher temperatures, the activation energy becomes significantly larger than the entropy term, indicating that most of the energy of disorder has been released. Finally, the entropy term becomes positive and very small. At this point, the entropy term becomes negligible and the effective jump distance for diffusion is approximately 0.5 nm (the lattice parameter in the a-direction; Chapter 3).

Table 9-3. Entropy contribution to the diffusion constant calculated from the data of Chapter 8 and Equation 9-1.

Possible Diffusion/ Trapping Mechanism	Temperature Range (°C)	Experimentally Measured Activation Energy (eV)	Diffusion Constant, D_0 (cm^2/s)	Energy of Disorder, $T\Delta S$ (eV)
Radiation Damage Planar Defects	130-300	0.26	$1x10^{-13}$	-0.90 (130°C)
Radiation Damage or Planar Defects	130-675	0.49	$5x10^{-11}$	-0.69 (130°C)
Oxygen Vacancies	675-750	1.47	$3x10^{-05}$	-0.62 (700°C)
Constitutional Vacancies	750-1000	2.24	$7x10^{-02}$	0.006 (1000°C)

Another possible explanation for the activation energies, E_1 and E_2, and the corresponding diffusion constants is the detrapping from high concentrations of planar defects associated with the exsolved phases within the terrestrial ilmenite. The helium could also be interacting with the stresses around those planar defects induced by thermal expansion and phase changes as the temperature increases. Further work is required using high resolution TEM to justify this explanation since it was not possible to quantify the spatial defect concentrations in the current study. The methods of Lovera et al. [1989] may be again be applicable since there may be more than one type of defect, but on a different spatial scale than discussed earlier.

9.1.3 Point Defect Concentrations in Ilmenite

The point defect thermodynamics for hematite developed by Dieckmann [1993] can be used as a model for ilmenite. If a closure temperature (the temperature at which the material

"closes" to diffusion of the constituent species) of 600°C is assumed for terrestrial ilmenite and 750°C for lunar ilmenite (see discussion in Chapter 6), the oxygen vacancy concentrations are found to be 13 ppm and 66 ppm, respectively. This concentration of oxygen vacancies is smaller than the local implanted ^{4}He concentration, but provides a uniform concentration of traps as the helium is implanted further into the undamaged lattice. Additional evidence that helium is bound to oxygen vacancies in ilmenite is provided by the observations of Dieckmann [1996] that oxygen vacancies in hematite are capable of storing He. These vacancies are naturally present in the undamaged lattice and may provide the trapping mechanism for helium implanted beyond the "amorphous" layer.

9.1.4 Traps for Helium in Implanted Ilmenite

The calculations by Welch, et al. [1976] and the experimental observations of Allen [1991] and Allen and Zinkle [1993] for He in α-Al_2O_3 can also provide some guidance in identifying the trapping mechanisms above. It must be kept in mind that the bonding in α-Al_2O_3 and in $FeTiO_3$ will be quite different despite the fact that they have the same crystal structure. Welch, et al. [1976] calculated that the energy difference between a He atom in an oxygen vacancy and a He atom in an interstitial site in α-Al_2O_3 is 1.7 eV. An analogous situation in ilmenite could be indicated by the measured activation energy, $E_2 \cong 1.4$ eV. A separate calculation by Welch et al. [1976] for He in an intrinsically vacant octahedral site relative to a perfect crystal resulted in an energy difference of 2.7 eV. In the current study, this trapping mechanism may be associated with the increase in activation energy measured at higher temperatures, $E_3 > 2.2$ eV. The lower population in these high energy traps may be related to the energy barrier required for He to get into these traps in the first place. Computational molecular simulations would be very useful in characterizing the energies of He in the myriad positions it could occupy in the ilmenite lattice.

9.1.5 Concentrations Calculated by TRIM

The number of oxygen vacancies caused by the 4 keV ^{4}He irradiation to $1x10^{16}$ ions/cm^2 can be estimated using TRIM. It has been established that oxygen vacancies are larger than helium atoms while the cation vacancies are smaller than helium atoms in ilmenite (Chapter 3). The results for oxygen vacancies are shown in terms of number per lattice atom in Figure 9-2 along with the concentrations of ^{4}He and ^{3}He atoms in terms of number per lattice atom ($9.5x10^{22}$ atoms/cm^3 for $FeTiO_3$). The calculation of the vacancy concentrations has been reduced by a factor of 10 based on the observations of Biersack [1987] which indicate that the residual number of point defects is about an order of magnitude less than that calculated by TRIM. The peak number of vacancies also occurs closer to the surface, at about 17 nm, whereas the peak ^{4}He concentration occurs at 33 nm from the surface. Since the ^{4}He must diffuse through this region of a large concentration of oxygen vacancies before escaping from the solid, this calculation supports the observation of trapping in oxygen vacancies with E_3 = 1.4 eV (and demonstrated by Allen [1991]).

The ratio of the diffusivities of ^{3}He and ^{4}He, D_{3He}/D_{4He}, for sample 041098.4 in the temperature range 130-675°C is about 60. This anomalous diffusion of ^{3}He is much greater than expected for the isotope effect,

$$\frac{D_{^3He}}{D_{^4He}} \approx \left(\frac{m_{^4He}}{m_{^3He}}\right)^{-1/2} = 1.15, \qquad (9\text{-}2)$$

where m is the mass of the isotope [Jambon and Shelby, 1980]. The only explanation for the increased diffusivity of ^{3}He is that since it is implanted last, the helium and/or hydrogen have saturated the available traps. The majority of the implanted ^{3}He must also diffuse out through the damaged lattice with activation energy E_2 = 0.5 eV since the ^{3}He is exposed to few traps. The fraction of ^{3}He implanted into the relatively undamaged portion of the lattice (Region C in

Figure 9-1) may be responsible for the appearance of a higher activation energy at higher temperatures (Figures 8-6 and 8-7). Figures 9-3 through 9-6 illustrate the concentrations of the various implanted species and the oxygen vacancies produced. The calculations displayed in these figures were performed using TRIM. The results for oxygen vacancy concentrations have again been reduced by a factor of 10 to reflect observations that the residual number of point defects is about an order of magnitude less than the number calculated by TRIM [Biersack, 1987]. Figure 9-3 represents the implantation of ^{4}He for sample 050997 and ^{4}He and ^{3}He for 041098. The ^{4}He may saturate the O vacancies produced. The vacancies are not available to trap the ^{3}He except in this part of the amorphous region and in the relatively undamaged bulk. Therefore, the activation energy, $E_2 \cong 0.5$ eV, is observed for the ^{3}He diffusing through the amorphous region.

The indication of rising activation energy above 675°C (Table 9-2) is likely due to the tail of the ^{3}He (or ^{4}He) distribution deeply implanted into the crystalline bulk. A similar situation exists for sample 040998 (Figure 9-4). The retardation of the release of ^{3}He from this sample (040998) relative to sample 041098 may be a result of additional vacancies produced by the implantation of hydrogen ($1x10^{14}$ cm^{-2}). The decrease in diffusivity of ^{3}He may also be due to the implantation of hydrogen that subsequently reacts with oxygen, creating a small energy barrier for ^{3}He diffusion. The hydrogen may also react with the constituent atoms, forming new traps or making it possible for oxygen vacancies to be available to trap the ^{3}He. The implantation profile for sample 041698 are shown in Figure 9-5. The effect of retarding ^{3}He release increases as the fluence of implanted H increases to $5x10^{15}$ cm^{-2} (Figure 9-7). This delay in ^{3}He release may again be the result of H reacting with the constituent atoms, forming new traps or leaving oxygen vacancies available to the ^{3}He. Finally, a fluence of hydrogen approaching the solar wind ratio compared with the implanted helium fluences results in a release profile similar to the case with no hydrogen implantation (Figure 9-6). Figure 9-6 illustrates the fact that the number of oxygen vacancies

produced by the implantation of H has approached the number of oxygen vacancies produced by the ^{4}He implantation to a depth of about 10 nm. The lack of a difference between no H implantation and the implantation of H to $1x10^{17}$ cm^{-2} may be a result of H simply saturating all of the oxygen vacancies produced. In this case, the only oxygen vacancies remaining will be in the relatively undamaged region below about 50 nm. With no traps available to the ^{3}He implanted last, the activation energy, E_2, will again be observed.

9.1.6 Effects of Hydrogen Preimplantation

None of the studies in the literature have explored the effect of hydrogen on the diffusion of solar-wind implanted He isotopes. Since protons make up the majority of the solar-wind and are very reactive, it seems possible that they could control the diffusion of He in lunar minerals by modifying existing traps. Lord [1968] suggested that the implanted H could bond to oxygen atoms in the lattice. The implantation of 1 keV H also creates additional damage in the lattice (Figure 7-6) which could generate traps for He. This is seen in the current experiment by the difference in total counts of evolved ^{4}He measured in samples 041098.4 (no H implantation) and 041398.5 (H implanted to $1x10^{17}$ cm^{-2}). Assuming that the surface area of the two samples are approximately the same, the fact that sample 041398.5 retains about 3.7 times more ^{4}He than sample 041098.4 could be indicative of the higher trap density caused by the H implantation. Conversely, sample 041098.4 retained 2.5 times more ^{3}He than did 041398.5. This observation supports the theory that the anomalously high diffusivity of ^{3}He is due to the order of implantation in this experiment. The low ^{3}He retentivity of 041398.5 may be due to the occupation of the available traps by the high doses of H and ^{4}He implanted prior to the ^{3}He implantation.

9.1.6.1 Release of ^{4}He with Hydrogen Preimplantation

The fractional release of ^{4}He for the 04XX98 series of samples is shown in Figure 9-8. The release is fairly consistent with varying fluences of preimplanted H and no systematic

correlations with H are apparent. The release of ^{4}He begins at approximately the same temperature, and the shapes of the curves are similar. A similar spread in ^{4}He release can be seen in the Apollo samples (Figure 9-9, Figure 3-9 and Figure 3-10).

The 4 keV ^{4}He generates a large number of vacancies at its mean range, about 33 nm, which could be responsible for the ^{4}He trapping and release with a characteristic activation energy of 1.38 - 1.47 eV. The activation energy for ^{4}He with no H preimplantation was measured as 2.24 eV and increases at higher temperature. This release may be due to constitutional vacancies (naturally vacant octahedral sites which account for 1/3 of all cation sites). The data supports a combination of both types of traps since the diffusivity shows a smooth increase in activation energy from 1.38 to 2.24 eV.

9.1.6.2 Release of ^{3}He with Hydrogen Preimplantation

The fractional release of ^{3}He for the 04XX98 series of samples is shown in Figure 9-7. The release is seen to change dramatically with varying fluences of preimplanted H (Figure 7-11). The release of ^{3}He occurs very early in the case of no H preimplantation relative to the ^{4}He release of all these samples. As the fluence of H is increased, the ^{3}He release occurs at progressively higher temperatures. However, the behavior of the sample implanted with solar wind ratios of H, ^{3}He and ^{4}He returns to the release behavior of the sample with no hydrogen implanted. Sample 041698.5 with hydrogen implanted to $5x10^{15}$ cm^{-2} exhibits release of ^{3}He and ^{4}He similar to the Apollo regoliths (Figure 9-9). In this sample, the diffusivities of ^{3}He and ^{4}He are basically related by the isotope effect. Very few data points were taken at low temperatures and the temperature of the first data point is quite high compared to the other samples. The ratio of the ^{4}He/^{3}He released approaches the ratio of the implanted gases as the temperature increases (Figure 7-11). This behavior may well be an artifact of the order in which the species were implanted as discussed above and should be investigated further.

9.2 Other Observations

Several other observations can be made concerning the data presented in Chapters 7 and 8 based on the model for helium diffusion and trapping discussed above.

- Helium implanted terrestrial ilmenite exhibits release behavior similar to that of the lunar regolith during 30 minute isochronal annealing.
- Annealing ilmenite implanted with H, ^{4}He, and ^{3}He results in a diffusivity of 8.9×10^{-24} cm^2/s at 400 K, which is in reasonable agreement with the upper bound of 2.9×10^{-25} cm^2/s determined with the Lunar Regolith Dynamics (LRD) code (Chapter 5).
- Helium appears to diffuse at room temperature over a period of time into a single type of trap in implanted ilmenite.

9.2.1 Comparison with ^{4}He Release from Lunar Regoliths and Rocks

A piece of sample 050997 was annealed in the long time furnace using 30 minute time steps as discussed in Chapter 6. The ^{4}He release from sample 050997.1 is compared in Figure 9-9 to the ^{4}He release from four lunar specimens: Apollo 11 rock 10069-21, regolith 10084-48, and two single grains of Apollo 17 ilmenite (from 71501-38, a sub-mature soil, and 79035-24, a mature breccia) [Pepin et al., 1970; Frick et al., 1988]. The integrated release of helium from the implanted sample is shown to be quite similar to that of the Apollo samples (Figure 9-9).

Two distinct slopes are evident in the simulant and are similar to the release of 10069-21, two separate release mechanisms. The slopes of each of these curves both change at about 590°C. The low temperature slope of the curve for the simulant is somewhat less than the slope of the Apollo 11 samples shown, but quite similar to the slopes of ilmenite samples 71501-38 and 79035-24 below approximately 80% of total release. The can be explained by

the fact that the regolith and rock samples from Apollo 11 contain many different minerals while the Apollo 17 sample are single grains of ilmenite.

The ^{4}He release from the simulant begins at lower temperature than for any of the lunar samples. This early release may be due to the 15 minute implantation time for sample 050997.1 (high flux) versus exposure times of the order of 10^9 years for the lunar samples (very low flux). Longer implantation times (within reason) would not be expected to have much effect since the magnitude of the difference in exposure time is so great. This early release may also be a result of the "contamination" of the sample by hematite and/or other minerals which release He as lower temperatures than ilmenite. Another explanation may involve the co-implantation of solar-flare hydrogen which would generate additional radiation damage, possibly increasing the range and trapping of the implanted helium.

9.2.2 Helium Diffusion in Minerals for U+Th/He Dating

The closest experimental comparison to the activation energies calculated in this thesis is the value measured by Boschmann-Käthler [1986] for hematite. Volume diffusion studies of the native He in bulk hematite yielded a range of activation energies from 1.20 to 1.32 eV, slightly lower than the values measured here for the temperature range 675-1000°C. The diffusivity of He in hematite at 673°C was measured to be approximately $3x10^{-22}$ cm^2/s, much lower than the diffusivities measured in the current experiment for temperatures between 130 and 675°C, but roughly the same as the diffusivity in the temperature range 675 - 1000°C extrapolated to 675°C. Since the hematite in the previous study was not damaged by irradiation, this is another piece of evidence supporting the theory that the release with characteristic activation energy, E_2, is due to amorphization of the lattice.

9.2.3 Implantation of Helium in Terrestrial Ilmenite

Futagami, et. al. [1993] performed an experiment similar to the one designed for this thesis, but they used 20 keV ^{4}He rather than the 4 keV ^{4}He and 3 keV ^{3}He characteristic of

the solar-wind. In earlier work, Futagami, et. al. [1990] used 3.6 keV ^{4}He on ilmenite, olivine, magnetite and rutile, but activation energies were not reported. They concluded that the activation energies for the release of ^{4}He from implanted ilmenite and olivine were 0.48 eV and 1.34 eV, respectively. This is counterintuitive to the higher retention of helium by high-Ti regoliths observed by Cameron [1988]. The activation energy obtained for the release of He from ilmenite, 0.48 eV, is consistent with the low temperature behavior seen in the current research and is likely due to surface amorphization mentioned earlier. The activation energy for olivine, 1.34 eV, is relatively low compared to other studies of native He diffusion in olivine which have obtained a value of 5.21 eV [Hart, 1984]. The activation energy for He release from olivine measured by Futagami et. al. [1993] is somewhat higher than the activation energy of about 1.09 eV obtained by Trull, et. al. [1991] for cosmogenic ^{3}He in olivine. It is likely that the high activation energy measured by Hart [1984] is due to a small population of high-energy traps which have retained their He over a geologic time period while the He in lower energy traps diffused out.

9.2.4 Comparison with result of LRD Calculation

The simulation of lunar regolith dynamics (LRD) with helium diffusion was discussed in Chapter 5. The results of this simulation established an upper boundary for helium diffusion in the lunar regolith based on the solar wind flux measured by Pioneer 10 and a ^{4}He profile measured in a lunar ilmenite grain using the Rare Gas Ion Probe (RGIP) [Müller et al., 1976]. Based on an activation energy of 1.08 eV and $D_0 = 7.1 \times 10^{-11}$ cm^2/s, the diffusivity of ^{4}He in the lunar regolith is required to be less than 3×10^{-25} cm^2/s at the maximum lunar temperature of about 400 K (Chapter 5) to explain the Apollo results. The results of the annealing experiments described in this thesis (activation energy of 1.47 eV and $D_0 = 3 \times 10^{-5}$ cm^2/s for the case of near solar wind ratios of H, ^{3}He and ^{4}He in sample 041398.5) would predict a diffusivity of about 9×10^{-24} cm^2/s at 400 K. This reasonably close agreement

would indicate that He trapped in oxygen vacancies in ilmenite is the mechanism responsible for the helium evolution seen in the high-titanium regoliths. This agreement would also predict that He incident on the lunar poles will be even more strongly trapped in ilmenite in the regolith due to the extremely low temperatures (~100 K).

9.2.5 Possible Room Temperature Annealing of Radiation Damage

Two samples of 050997 were annealed with 5 second time steps in the small particle furnace. The cumulative ^{4}He release from these samples is shown in Figure 9-10. The difference between the release curves has three possible explanations. First, the difference may be an instrumental or procedural artifact. An instrumental error is thought to be unlikely because the small particle furnace was designed specifically to avoid these problems [Nier and Schlutter, 1992]. A second possible explanation is the possibility of inclusions of other mineral phases in the sample. These inclusions could lie beneath the surface and not be visible to optical microscopy. One could then explain the low-temperature ^{4}He release from 050997.2 as coming from grain boundaries or less retentive phases. Conversely, the high temperature release of ^{4}He may be due to a more retentive phase. A third way to explain the difference between the curves could be connected to the length of time between implantation and annealing. Sample 050997.2 was annealed about 2 months after implantation while sample 050997.4 was annealed about 7 months after implantation. The samples were stored in a desiccator immediately following implantation, but no vacuum was drawn. It may be possible that the lattice is slowly relaxing from a complex damaged state to a state where all of the helium is located in a single trap. Further experiments are needed to determine which of these three possibilities is occurring.

9.2.6 Equation for the Annealing of Defects

When Equation 3-6 is applied to the ^{4}He release from the 5 sec anneal of sample 050997.3 (Figure 7-3), an activation energy of 1.53 eV is the result. This is the only set of

data in this thesis to which this equation can be applied because it is the only data set that behaves like a first order chemical reaction with only one diffusion mechanism present. The parameters used to obtain the activation energy for this data set were $P_m = 0.359P_0$ (35.9% of the He was released after T_m), $(dP/dT)_m = -4.78x10^{-3}$ P_0/K, at T_m = 850°C. This activation energy is consistent with the observations for 30 second anneals between 675 and 1000°C discussed earlier, and provides additional evidence for helium diffusion via oxygen vacancies in ilmenite.

9.3 References

Allen, W. R. (1991) "Lattice Location of Ion Implanted ^{3}He in Sapphire," *Nuclear Instruments and Methods in Physics Research*, **B61**, pp. 325-336.

Biersack, J. P. (1987) in *Ion Beam Modification of Insulators*, Vol. 2, eds. P. Mazzoldi and G. W. Arnold (Elsevier, Amsterdam), p. 38.

Boschmann-Kathler, W. (1986) "Uran und Helium in Erzmineraliwn und die Frage ihrer Datierbarkeit," PhD Thesis, (Heidelberger Geowiss. Abh., Heidelberg).

Cameron, E. N.(1988) "Helium Mining on the Moon: Site Selection and Evaluation." *The Second Conference on Lunar Bases and Space Activities of the 21st Century*, (Houston, Texas: Lunar and Planetary Institute), pp. 89-97.

Dieckmann, R. (1993) "Point Defects and Transport in Haematite ($F_e2O_{3-\varepsilon}$)," *Philosophical Magazine, A* **68**(4), pp. 725-745.

Dieckmann, R. (1996) Personal communication.

Frick, U., R. H. Becker, and R. O. Pepin (1988) "Solar Wind Record in the Lunar Regolith: Nitrogen and Noble Gases." *Eighteenth Lunar and Planetary Science Conference*, G. Ryder, ed., (Cambridge: Cambridge University Press), pp. 87-120.

Futagami, T., M. Ozima, Y. Nakamura (1990) "Helium Ion Implantation into Minerals" *Earth and Planetary Science Letters,* **101**, pp. 63-67.

Futagami, T., M. Ozima, S. Nagai, and Y. Aoki (1993) "Experiments on Thermal Release of Implanted Noble Gases in Lunar Soil Grains." *Geochimica et Cosmochimica Acta*, **57**, pp. 3177-3194.

Hart, S. R. (1984) "He Diffusion in Olivine." *Earth and Planetary Science Letters*, **70**, pp. 297-302.

Jambon, A. and J. E. Shelby (1980) "Helium Diffusion and Solubility in Obsidians and Basaltic Glass in the Range 200-300°C," *Earth and Planetary Science Letters*, **51**, pp. 206-214.

Jost, W. (1952) *Diffusion in Solids, Liquids, Gases* (Academic Press Inc., New York) p.137.

Lancet, M. S. and E. Anders (1973) "Solubilities of Noble Gases in Magnetite: Implications for Planetary Gases in Meteorites," *Geochimica et Cosmochimica Acta*, **37**, pp. 1371-1388.

Lovera, O. M., F. M. Richter and T. M. Harrison (1989) "The $^{40}Ar/^{39}Ar$ Thermochronometry for Slowly Cooled Samples Having A Distribution of Diffusion Domain Sizes," *Journal of Geophysical Research*, **94**(B12) pp. 17,917-17,935.

Müller, H. W., J. Jordan, S. Kalbitzer, J. Kiko and T. Kirsten (1976) "Rare Gas Ion Probe Analysis of Helium Profiles in Individual Lunar Soil Particles," *Seventh Lunar Science Conference*, (Houston, Texas), pp. 937-951.

Nier, A. O and D. J. Schlutter (1992) "Extraction of Helium from Individual Interplanetary Dust Particles by Step-Heating," *Meteoritics*, **27**, pp. 166-173.

Pepin, R. O., L. E. Nyquist, D. Phinney, and D. C. Black (1970) "Rare Gases in Apollo 11 Lunar Material," *Proceedings of the Apollo 11 Lunar Science Conference*, **2**, pp. 1435-1454.

Trull, T. W., M. D. Kurz, and W. J. Jenkins (1991) "Diffusion of Cosmogenic ^3He in Olivine and Quartz: Implications for Surface Exposure Dating." *Earth and Planetary Science Letters* **103**, pp. 241-256.

Welch, D. O., O. Lazareth, G. J. Dienes and R. D. Hatcher (1976) "Theory of Helium Migration and Trapping in α-Al_2O_3" *Radiation Effects*, **28**, pp. 195-198.

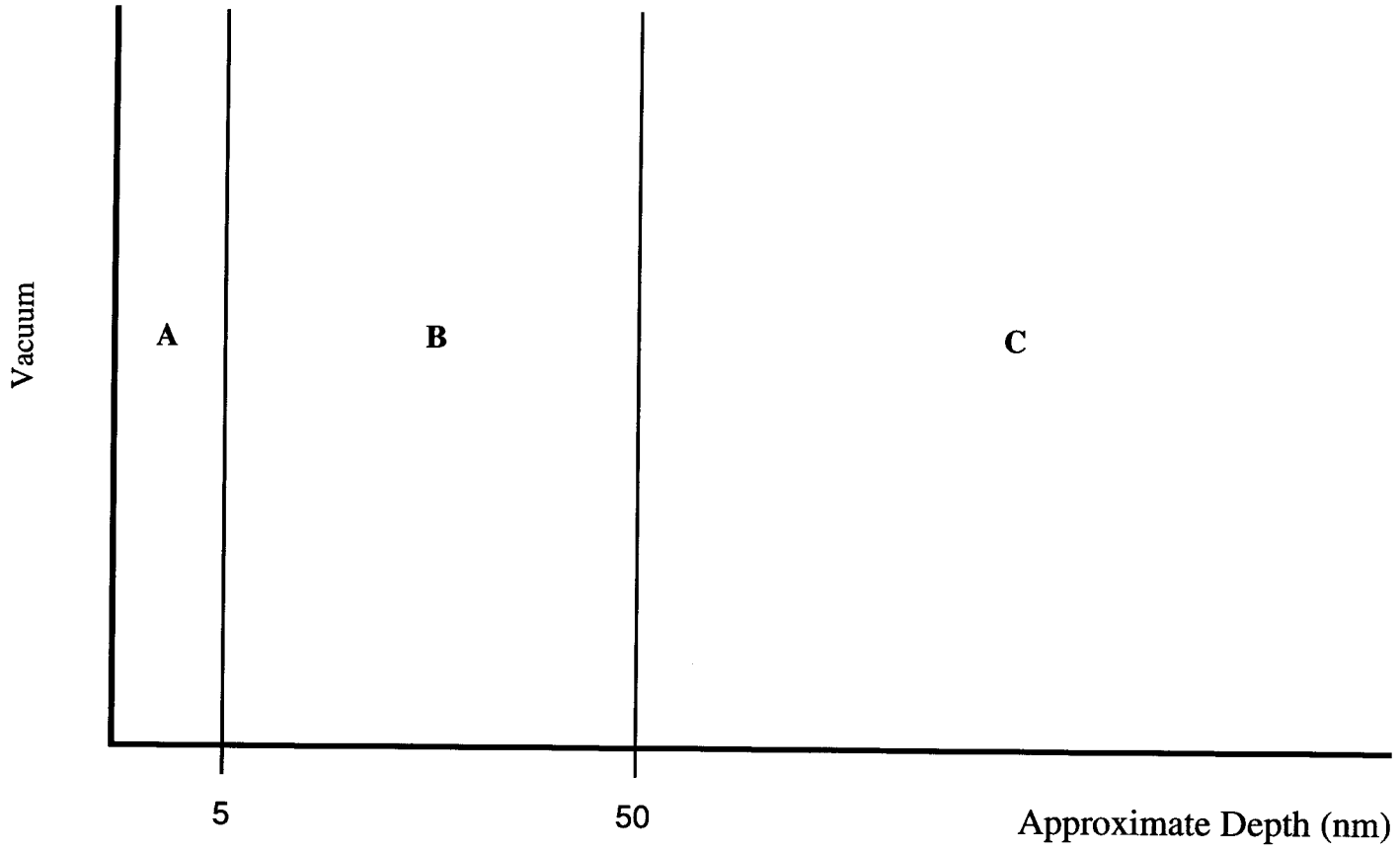

Figure 9-1. Schematic of damaged regions of ilmenite sputter-cleaned with Ar and implanted with H and He. Region A represents the region damaged by Ar sputter-cleaning. Region B is the area damaged by the ^{4}He (and H) implantation. Region C is relatively undamaged ilmenite.

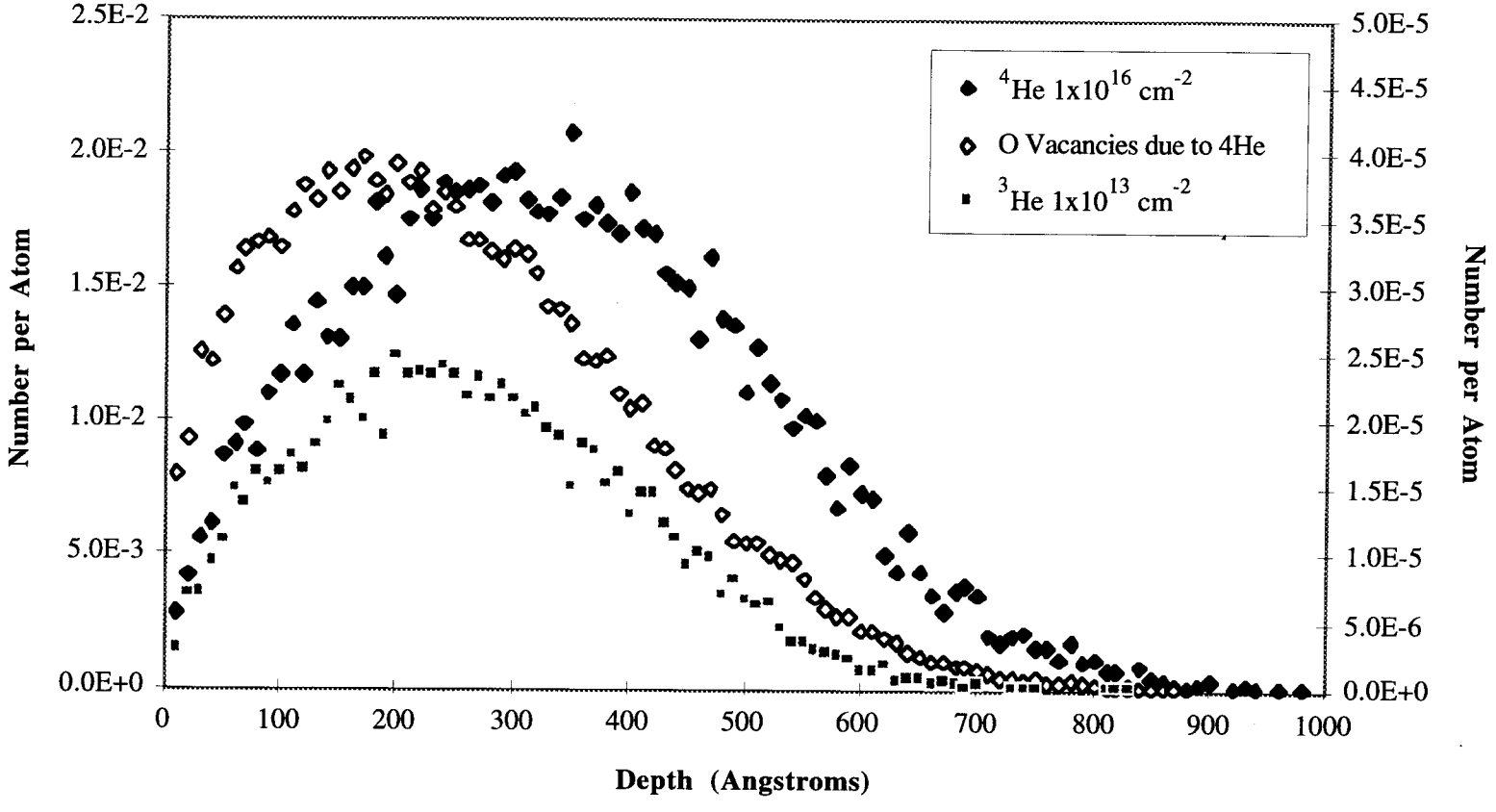

Figure 9-2. Calculations of the number of oxygen vacancies and helium atoms per lattice atom performed using TRIM, ^4He implanted to $1x10^{16}$ ions/cm^2 and ^3He implanted to $1x10^{13}$ ions/cm^2 (Sample 041098). Note the difference in scale for the ^3He concentrations. The number of oxygen vacancies reflects the observations of Biersack [1987] that the residual number of point defects is about an order of magnitude less than that calculated by TRIM.

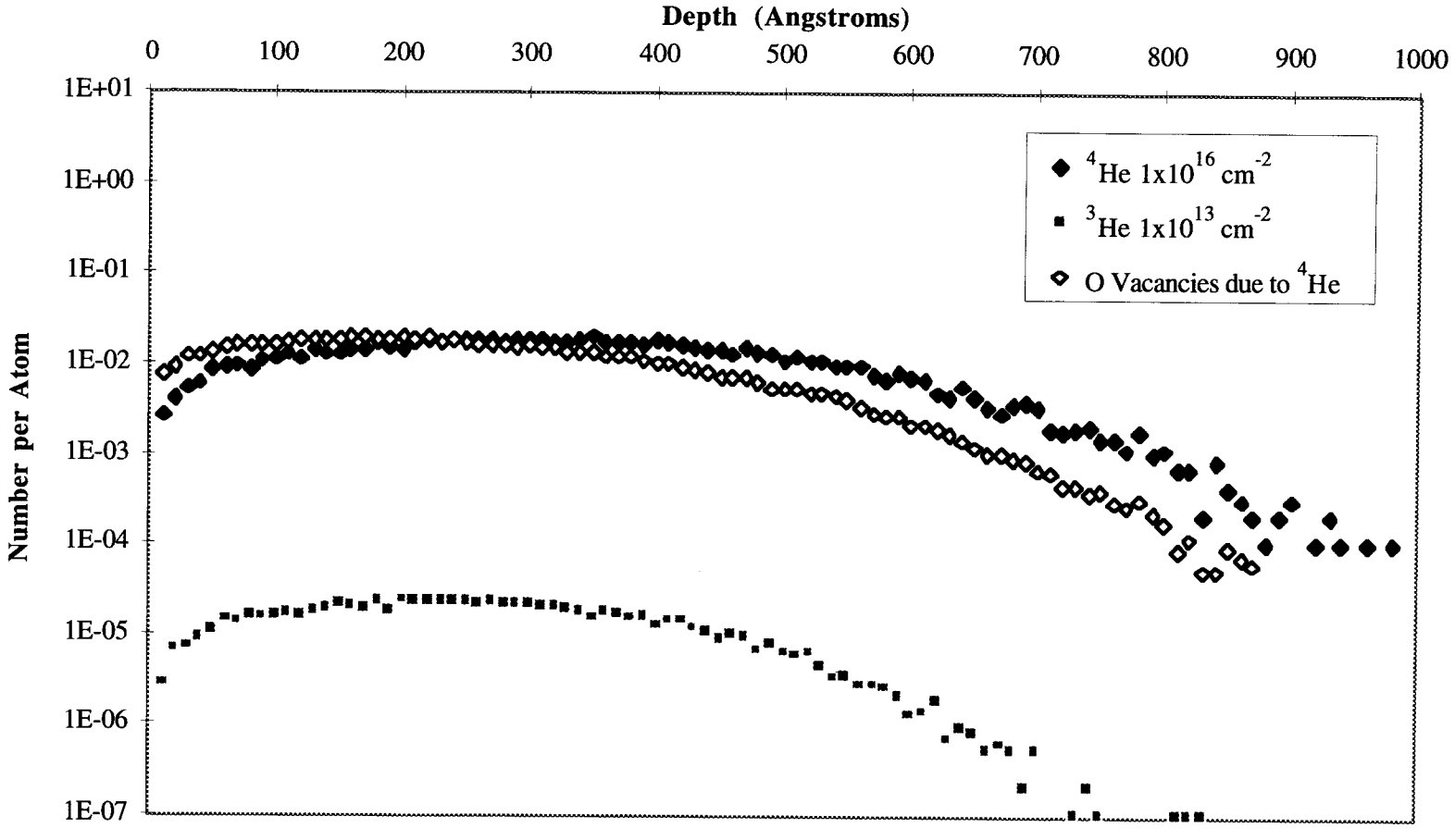

Figure 9-3. Calculations of the number of oxygen vacancies produced and helium atoms deposited per lattice atom. These calculations were performed using TRIM and the implantation fluences shown. This data also shown in Figure 9-3 and models the implantation for samples 050997 and 041098.

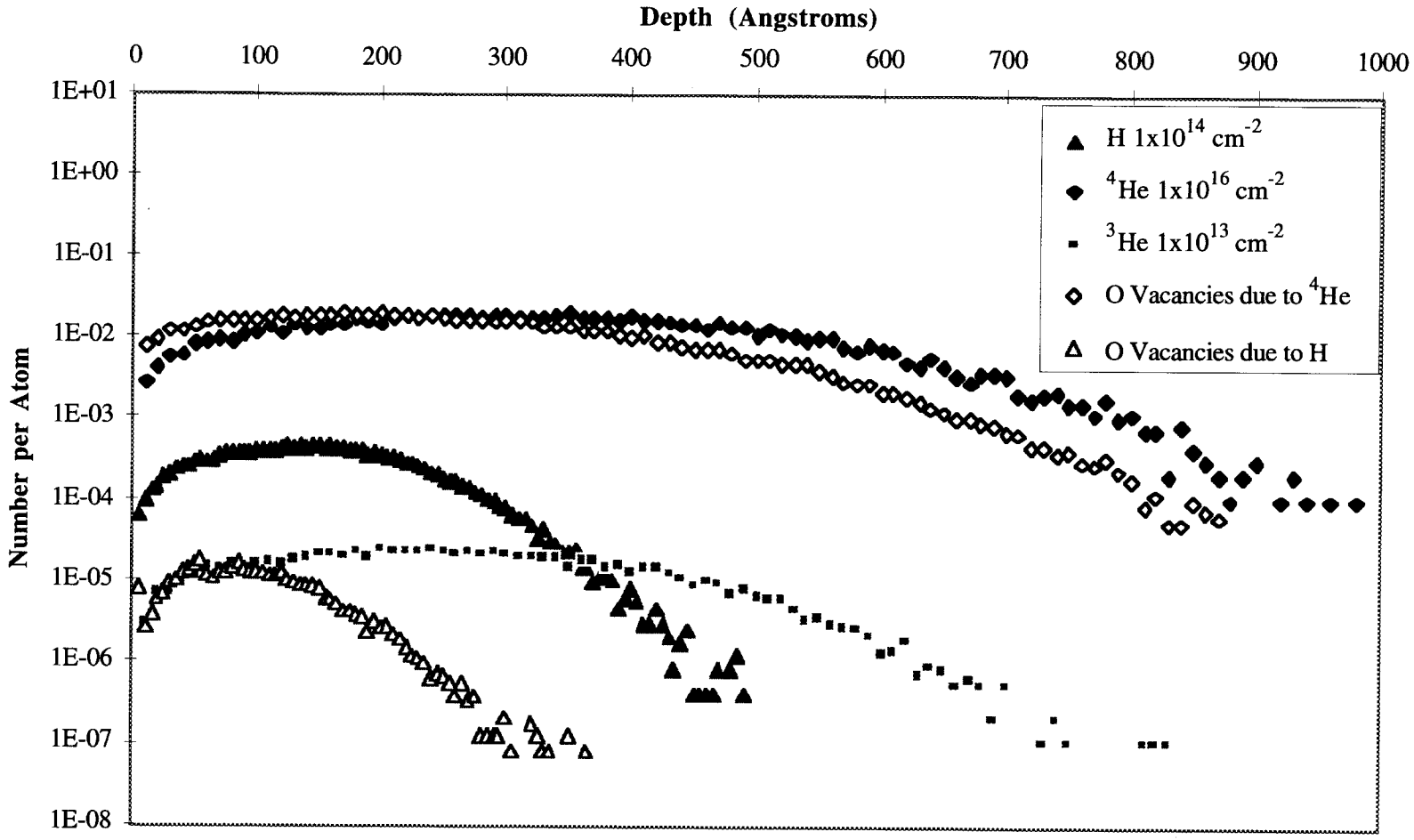

Figure 9-4. Calculations of the number of oxygen vacancies produced and helium atoms deposited per lattice atom. These calculations were performed using TRIM and the implantation fluences shown for sample 040998.

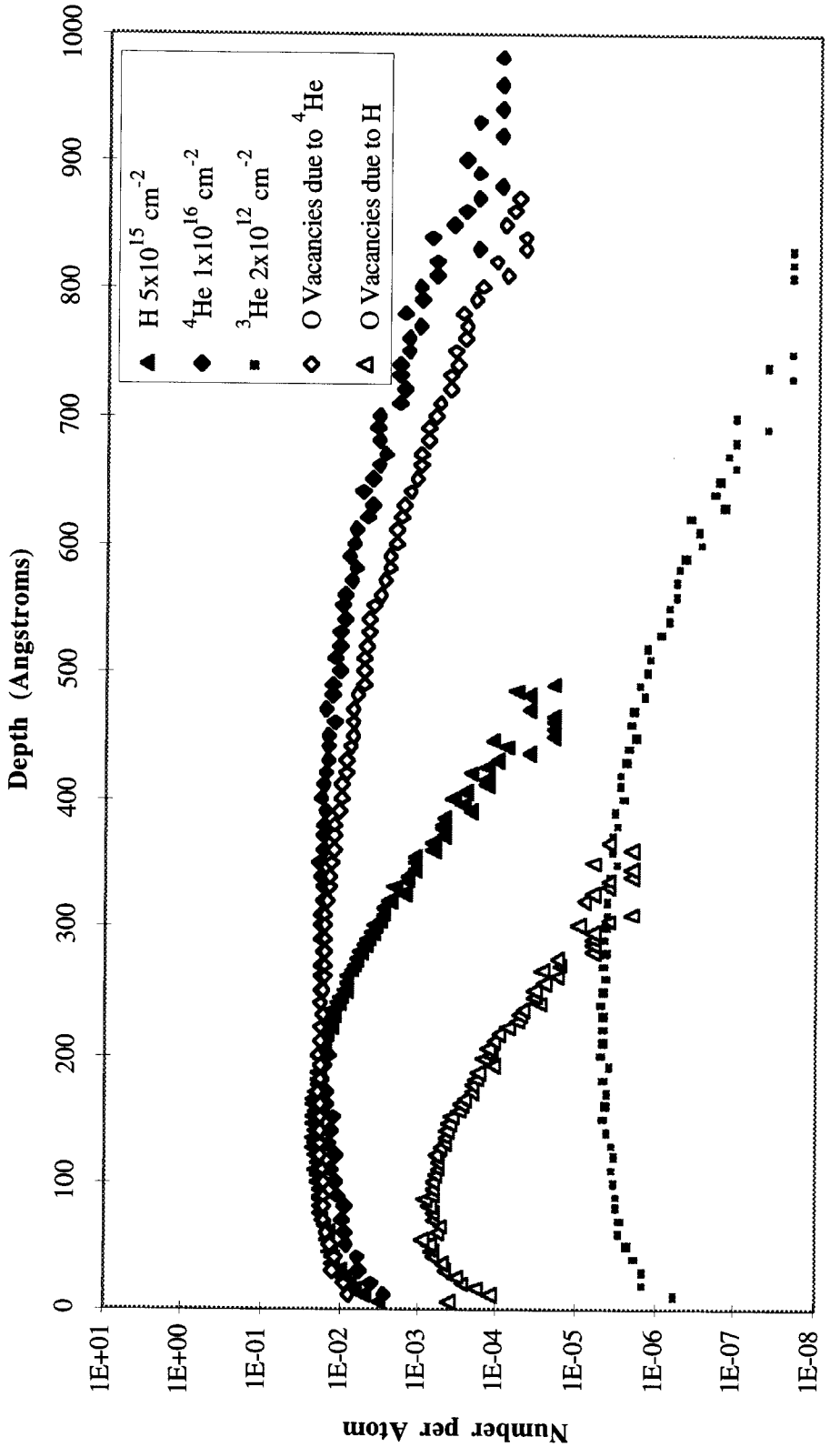

Figure 9-5. Calculations of the number of oxygen vacancies produced and helium atoms deposited per lattice atom. These calculations were performed using TRIM and the implantation fluences shown for sample 041698.

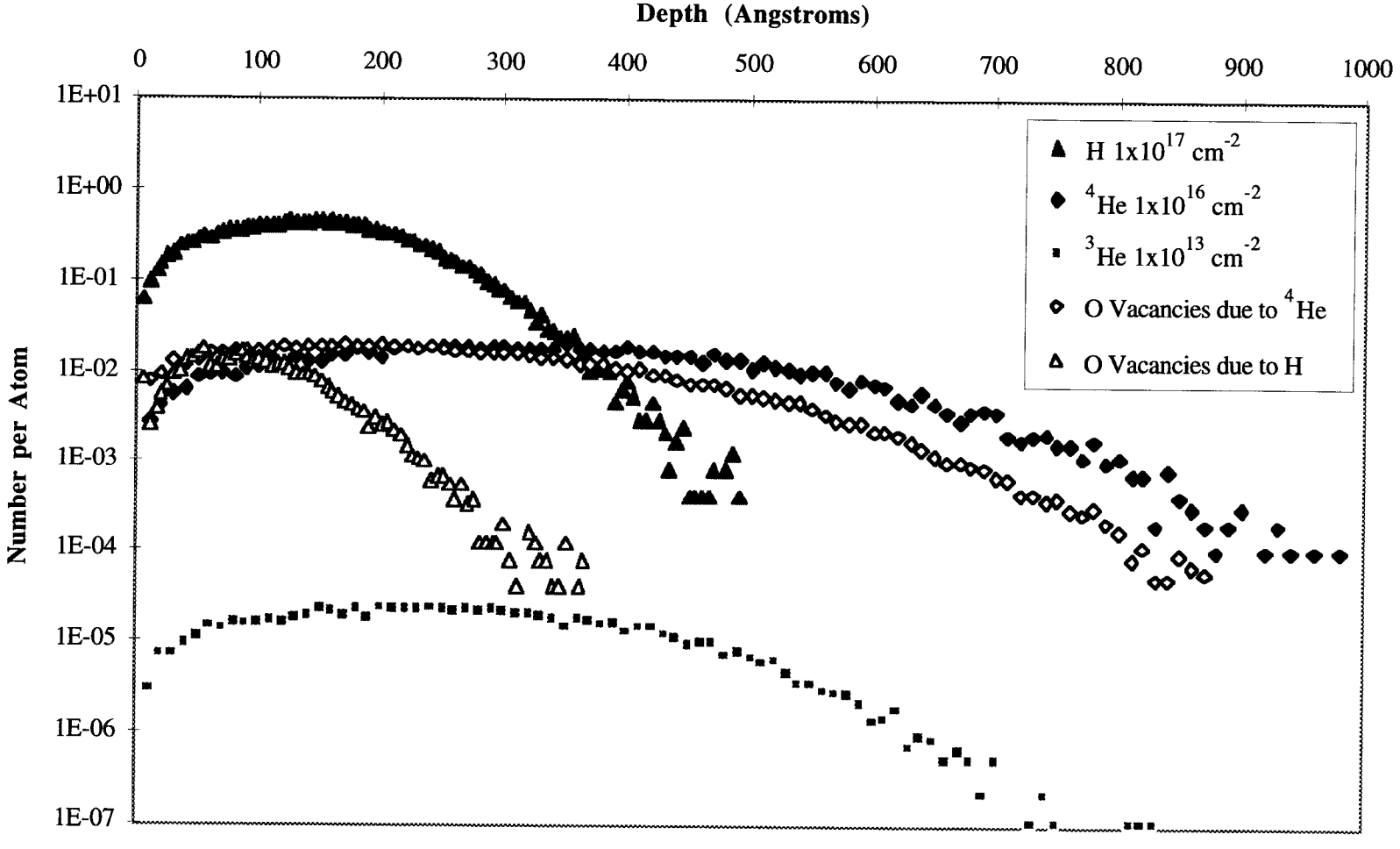

Figure 9-6. Calculations of the number of oxygen vacancies produced and helium atoms deposited per lattice atom. These calculations were performed using TRIM and the implantation fluences shown for sample 041398.

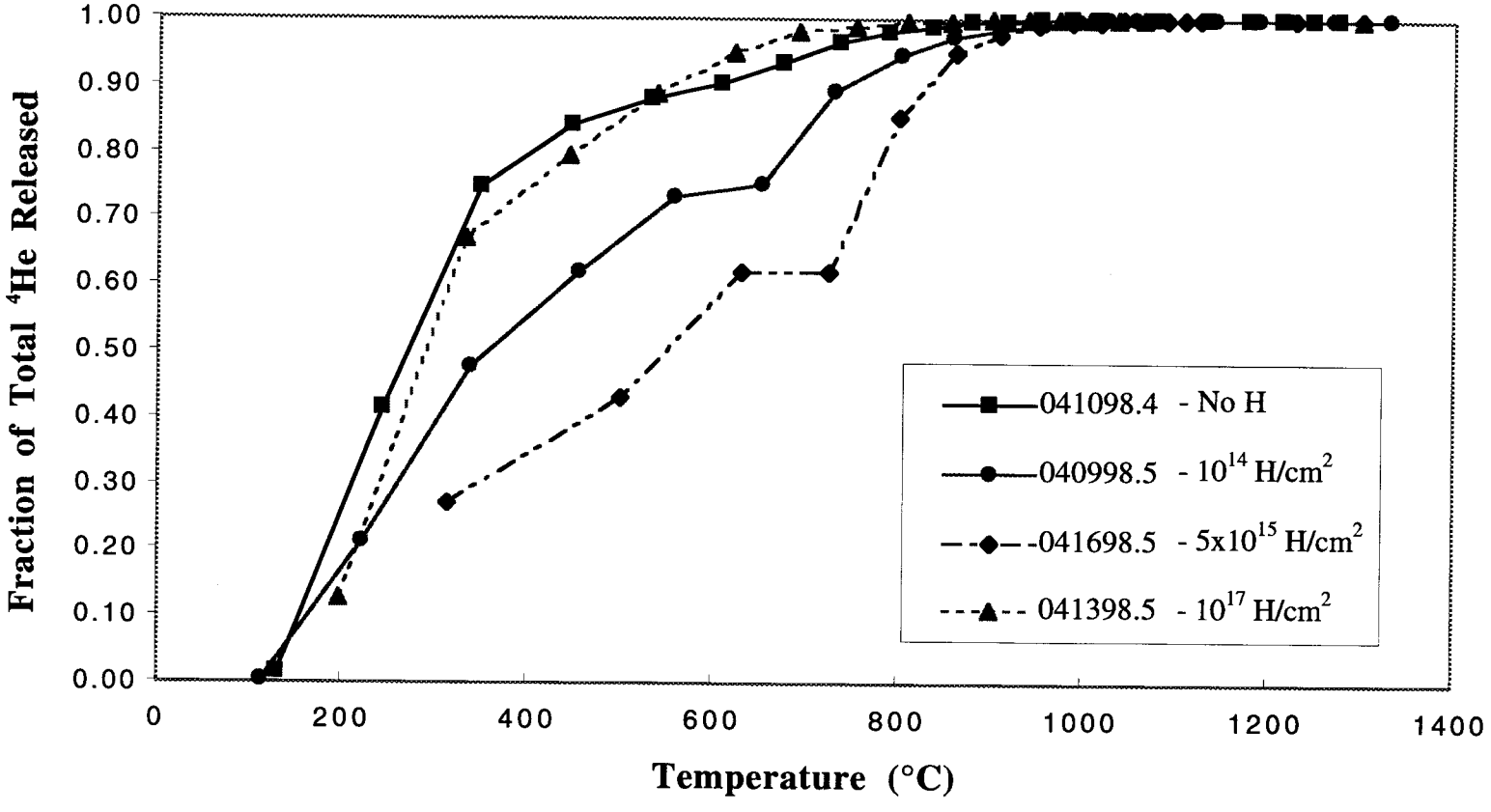

Figure 9-7. Cumulative fractional release of ^{3}He from the 04XX98 series of samples. The hydrogen initially retards ^{3}He evolution but the highest H fluence has virtually no effect on ^{3}He release. The lines are included to guide the eye.

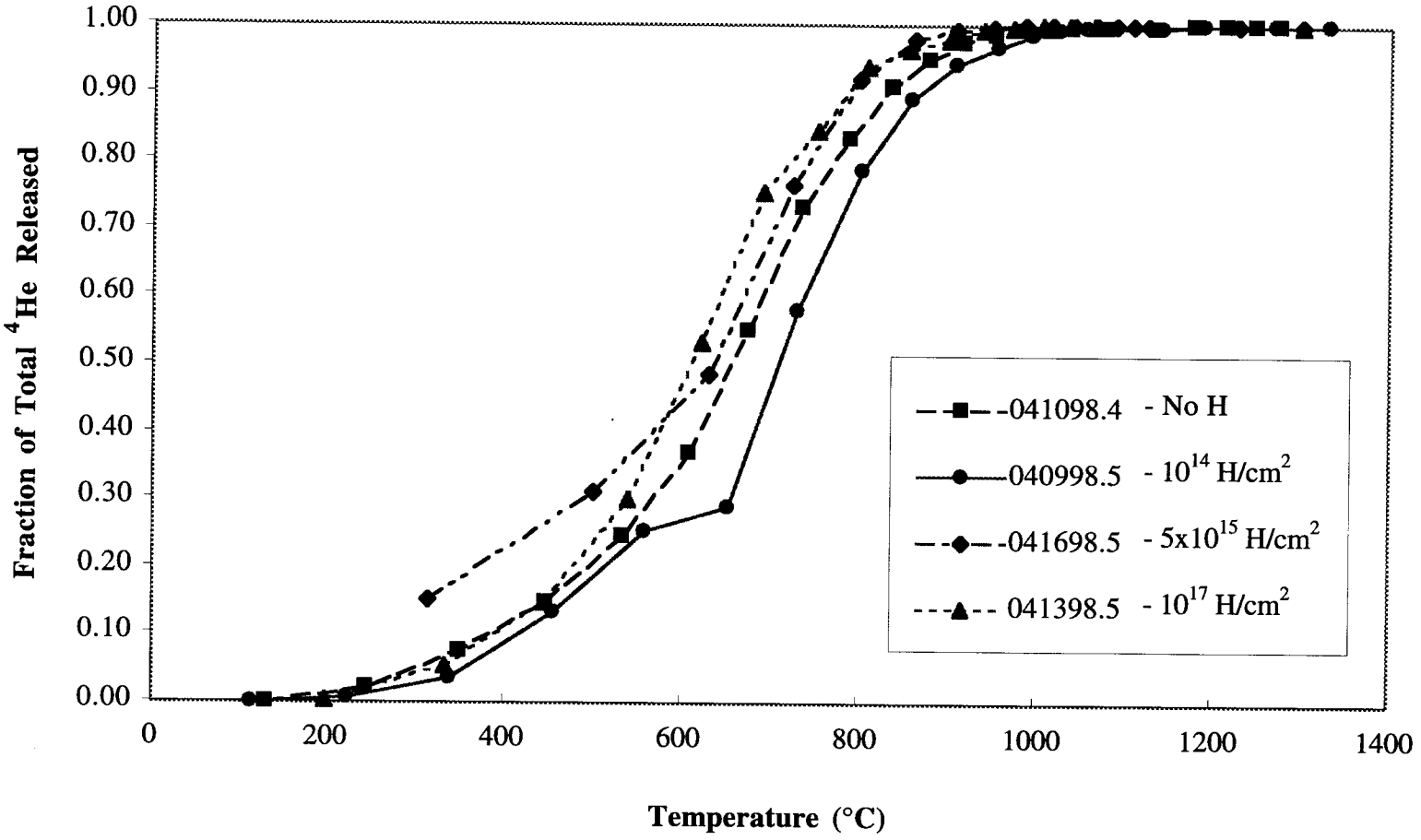

Figure 9-8. Cumulative fractional release of ^{4}He from the 04XX98 series of samples. Increasing H fluence has virtually no influence on the release of ^{4}He. The lines are included to guide the eye.

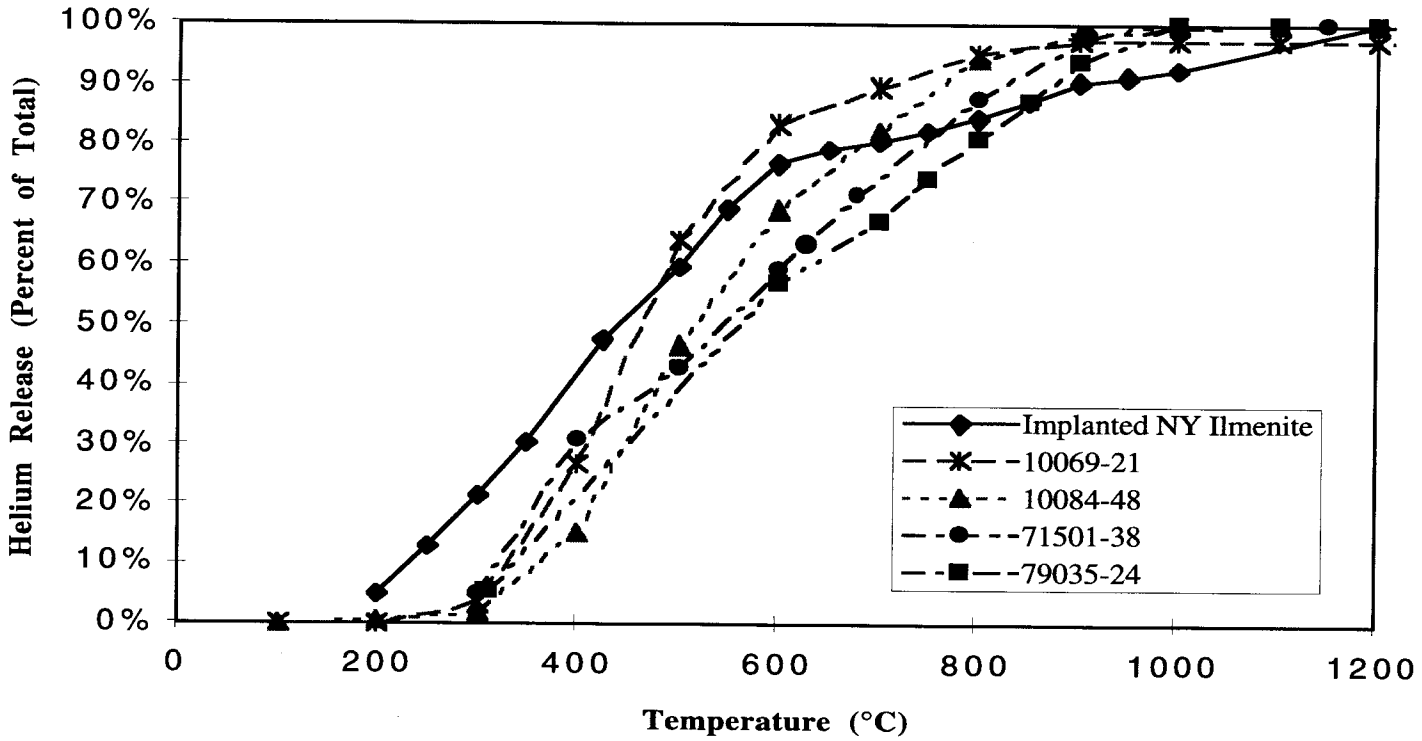

Figure 9-9. Release data of ^4He from sample 050997.1 and samples of rock and regolith from Apollo 11 [Pepin et al., 1970] and single grains of ilmenite from Apollo 17 [Frick et al., 1988]. Annealing steps of 50°C and 30 minutes were used for the sample 050997.1 while steps of approximately 100°C and 1 hour were used for the Apollo samples. The lines are included to guide the eye.

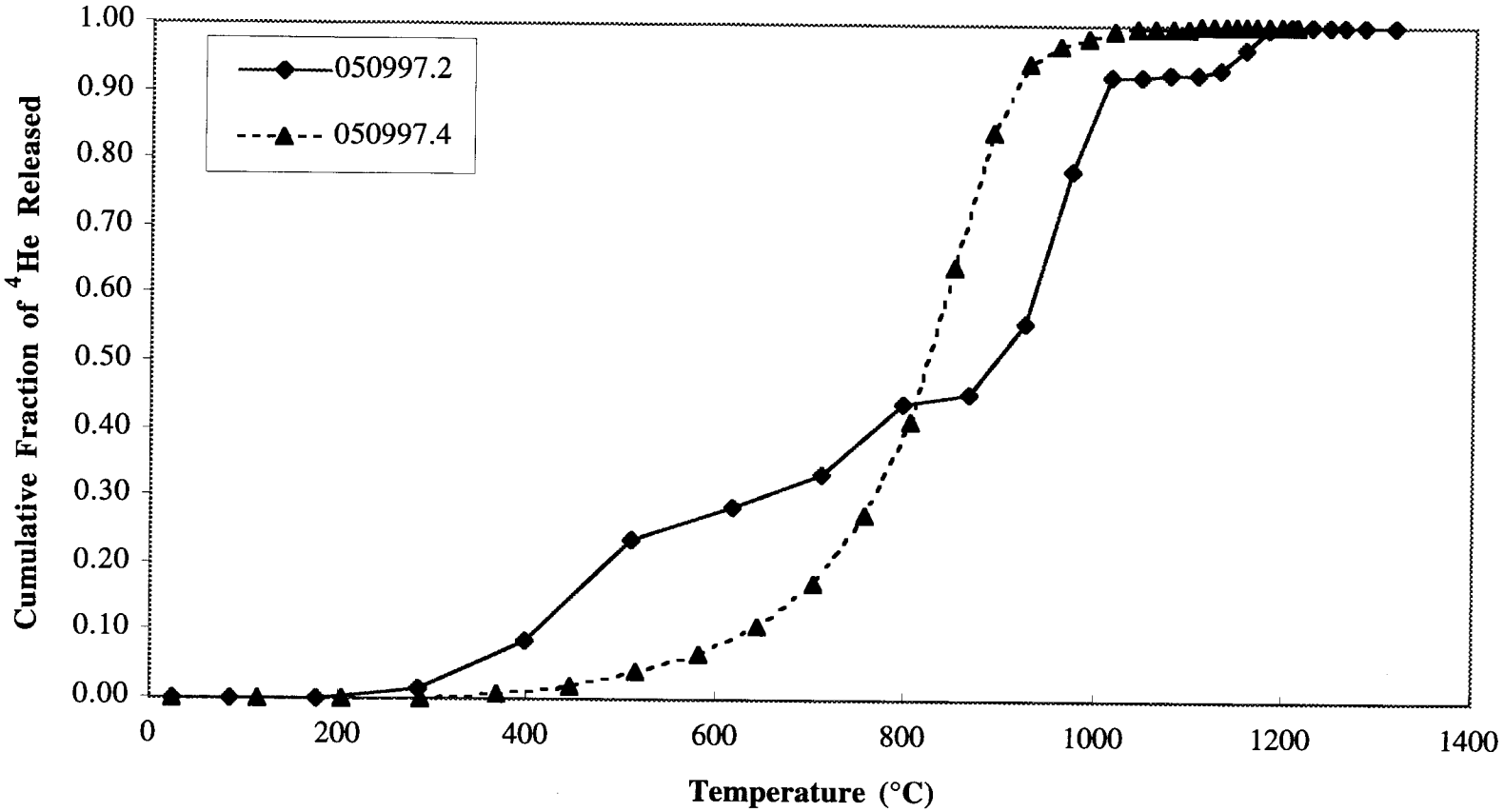

Figure 9-10. Cumulative fractional release of ^{4}He from samples 050997.2 and 050997.4 during 5 sec. isochronal anneals. Sample 050997.2 was annealed 2 months after implantation, and sample 050997.4 was annealed 7 months after implantation. The lines are included to guide the eye.

Chapter 10 Conclusions

Several major observations emerge regarding possible trapping and diffusion mechanisms:

- Helium release from implanted terrestrial ilmenites is diffusion limited as opposed to reaction rate-limited.
- Helium diffusion in terrestrial ilmenite implanted with ^4He and ^3He is characterized by four distinct activation energies, $E_1 = 0.26$ eV, $E_2 \cong 0.5$ eV, $E_3 \cong 1.4$ eV and $E_4 > 2.2$ eV.
- In the temperature range studied here, the diffusivity of helium implanted in ilmenite is much greater than the self-diffusivities observed for anions and cations in rhombohedral oxides or other iron oxides.
- The diffusivity of ^3He in terrestrial ilmenite implanted with ^4He and ^3He is greater than the diffusivity of ^4He.

These observations lead to a model for diffusion of solar-wind helium implanted into ilmenite. Additional observations can be made from the results of the experiment described in this thesis and explained using the diffusion and trapping model discussed in Chapter 9:

- Helium implanted terrestrial ilmenite exhibits release behavior similar to that of the lunar regolith during 30 minute isochronal annealing.
- Moderate fluences ($<1x10^{15}$ cm^{-2}) of hydrogen preimplantation retard ^3He diffusion in terrestrial ilmenite implanted with ^4He and ^3He. High fluence H preimplantation (10^{17} cm^{-2}) has virtually no effect on ^3He diffusion.
- Annealing ilmenite implanted with H, ^4He, and ^3He results in a diffusivity of $9x10^{-24}$ cm^2/s at 400 K, which is in reasonable agreement with the upper bound of $3x10^{-25}$ cm^2/s determined with the Lunar Regolith Dynamics (LRD) code.

- Helium appears to diffuse at room temperature over a period of time into a single type of trap in implanted ilmenite.

10.1 Helium Diffusion in Implanted Ilmenite is Diffusion Limited

It has been established that the diffusion of He in implanted ilmenite is limited by diffusion processes. The release of He follows a parabolic relationship with time during isochronal annealing. Since the release is diffusion controlled, a model of the diffusion/ trapping mechanisms responsible for the release of He during isochronal annealing has been developed.

10.2 Activation Energies

Helium diffusion in terrestrial ilmenite implanted with ^4He and ^3He at solar wind energies (~1 keV/nucleon) exhibits diffusivity with four activation energies, $E_1 = 0.26$ eV (150 °C < T < 300°C), $E_2 \cong 0.5$ eV (150 °C < T < 675°C), $E_3 \cong 1.4$ eV (675 °C < T < 900°C) and $E_4 > 2.2$ eV (900°C < T) These energies were determined by measuring the fraction of helium released during isochronal anneals of several samples of terrestrial ilmenite implanted with ^4He and ^3He using Plasma Source Ion Implantation (PSII). A $^4He/^3He$ ratio of about 1000 was used in all implantations involving ^3He. The solar wind ratio of ^4He to ^3He is approximately 2000. These activation energies are characteristic of the individual mechanisms by which He is trapped or diffuses in the irradiation damaged ilmenite. It has been shown that the low temperature activation energy ($E_2 = 0.5$ eV) is typical of He diffusion in glasses and other amorphous materials. This similarity suggests that an amorphous layer or layers caused by radiation damage may be responsible for the low temperature release of He from lunar ilmenites. The higher temperature activation energy (1.4 eV) is characteristic of the detrapping of helium from oxygen vacancies. The data also suggests that a fourth mechanism may exist in these samples. The activation energy is seen to increase continuously to above 2.2 eV with no hydrogen preimplantation. This observation

indicates that constitutional vacancies (intrinsically vacant octahedral sites) may trap some of the helium.

10.3 Simulation of Lunar He Evolution

It has been demonstrated that the ^{4}He evolution from terrestrial ilmenite during 30 minute isochronal annealing is quite similar to the evolution of ^{4}He from the Apollo regoliths (Chapters 6 and 7). This indicates that the ilmenite in the lunar regoliths (15-20% by volume in the Apollo 11 and 17 regoliths) is responsible for the ^{4}He retention behavior. The cumulative fraction of ^{4}He released from the implanted terrestrial sample shows diffusion behavior that is likely related to a phase change in accompanying hematite lamellae. The activation energies obtained from this sample are consistent with the values measured in samples annealed for 30 seconds.

10.4 Diffusivity of ^{4}He versus ^{3}He in Implanted Ilmenite

The isochronal annealing of ilmenite implanted with ^{4}He and ^{3}He (in that order) results in a considerably higher diffusivity for ^{3}He than for ^{4}He. This behavior is very different from the lunar samples where the release curves are very nearly the same (Chapter 7). The reason for this behavior is not immediately obvious. The isotope effect indicates that the ratio of the diffusivities should be inversely proportional to the ratio of the square-root of their masses (Chapter 3), a factor of 1.15. Instead, the diffusivities differ by several orders of magnitude. This may be explained by the order in which the helium isotopes are implanted. If the implanted ^{4}He and/or H saturates the available trapping sites, the ^{3}He will not have access to these sites and will diffuse out through the amorphous layer with an activation energy of 0.5 eV.

10.5 Effect of Hydrogen Preimplantation

The preimplantation of 1 keV H was seen to affect the release of ^{3}He, but not ^{4}He, in these experiments. Several fluences of H were used: $1x10^{14}$ ions/cm^2, $5x10^{15}$ ions/cm^2 and $1x10^{17}$ ions/cm^2. The highest fluence corresponds to the ratio between H and ^{4}He in the solar wind. Moderate fluences of H appear to retard the evolution of ^{3}He during 30 second isochronal anneals while the cases of no H and the solar wind ratio of H behave similarly with the ^{3}He escaping at relatively low temperatures. Again, this can be explained by the order in which the various species were implanted. The implanted species do two things in the lattice: 1) produce radiation damage and 2) occupy traps. If lower fluences of H produce enough traps, but the available traps are not saturated, there will traps available for the subsequently implanted ^{3}He. The highest fluence of H may saturate these traps, leaving no traps available for the ^{3}He. The ^{3}He would then diffuse out as if there were no traps due to the hydrogen implantation.

10.6 Experimental versus Computational Results

The upper bound to the diffusivity of $3x10^{-25}$ cm^2/s was calculated using the Lunar Regolith Dynamics (LRD) code written for this thesis. The annealing experiment on sample 041398.5 (implanted with H to 10^{17} ions/cm^2, ^{4}He to 10^{16} ions/cm^2 and ^{3}He to 10^{13} ions/cm^2) was analyzed using the ANNEAL code. This experiment yielded a value for diffusivity due to oxygen vacancies of approximately $9x10^{-24}$ cm^2/s. This reasonable agreement indicates that solar-wind He trapped in oxygen vacancies in ilmenite is responsible for the He release patterns seen in the lunar regoliths.

10.7 Room Temperature Diffusivity of He in Implanted Ilmenite

Evidence is found for the annealing (or relaxation) of the damaged lattice at room-temperature in two 5 second isochronal anneals of terrestrial ilmenite implanted with ^{4}He. The two samples were annealed about 5 months apart. The later sample exhibited ^{4}He release

indicative of a single trapping mechanism (Chapter 7). The earlier sample showed higher release at low temperature and lower release at high temperature. This can be explained if ^4He in the lattice has diffused over time into a single trap with a characteristic activation energy. This activation energy was calculated to be 1.4 eV, consistent with helium trapped in oxygen vacancies as discussed earlier.

Chapter 11 Recommendations

The following are suggestions for further research:

- It would be useful to apply the experimental procedure described in this thesis to olivine, pyroxene, plagioclase and lunar-like glass to determine the activation energies and diffusion coefficients for He diffusion in these minerals.
- Additional TEM work is needed to more thoroughly understand the radiation damage to the surfaces of solar-wind exposed materials. A greater understanding of the number and type of defects would be useful. The presence of very small-scale crystalline domains (the metamict state) could also be explored using TEM.
- It would be useful to anneal more samples from each run to increase the number of data points at lower temperatures. This data would be useful for studying possible multiple diffusion domains.
- It would be quite useful to find a way to measure the amount of OH^- formed in the ilmenite lattice due to the implantation of H. The implantation of olivine with subsequent analysis using infrared (IR) spectroscopy would be a good first step in determining OH^- content. Olivine is easily analyzed with IR spectroscopy because it is not opaque. Ilmenite is opaque, so another method must be used.
- An experiment using the samples prepared for this thesis could be used for an energy-filtered TEM (EFTEM) study of He diffusion. The EFTEM would allow the direct observation of the growth of He bubbles as a function of temperature. The information gained through this method would be useful in refining mining techniques.
- The He profiles could be accurately measured using nuclear activation analysis or Rutherford backscattering experiments.

Appendix A Lunar Regolith Dynamics Code

```
      PROGRAM Diffuse
c
c     Version1.2
c     Kim R. Kuhlman
c     August 12, 1996
c
c
c     Driver for Routines TRIDAG,
c     Declarations
c
      INTEGER ZMAX,TMAX,KMAX,i,j,l,k,out,wrfreq,FREQ
      REAL DTIME,TIMEYR,WRCYCLE,LOWC,Na,JOULE,AE,pi,Dalpha
      PARAMETER(ZMAX=2500, TMAX=1e6, KMAX=2501, DTIME=3.6e04)
      PARAMETER(FREQ=10,TIMEYR = 6.0e-1,WRCYCLE = 1.1,LOWC=1.0e-99)
      PARAMETER(Na=6.0221e23,JOULE=1.6022e-19,AE=15)
      PARAMETER(Dalpha=1.0e-5,pi = 3.14159265)
      REAL sputter,time,month,nbottom,thick,nthick
      REAL z(ZMAX),dz(ZMAX),n(ZMAX),alpha,kb,alen
      REAL dt,swfhe(ZMAX),an(ZMAX),bn(ZMAX),cn(ZMAX),week,nloc(TMAX)
      REAL a(ZMAX),b(ZMAX),c(ZMAX),nend(ZMAX),ntime(TMAX+3),ntop,nmax
      REAL agd(ZMAX),bgd(ZMAX),cgd(ZMAX),agn(ZMAX),bgn(ZMAX),cgn(ZMAX)
      REAL dzi,TD,TN,rho,R,sig,diff0
      REAL TGD,TGN,daygrad,nightgrad,q,ntotal,year1
      INTEGER zstep,tstep,zzone,distend,end
      REAL distin(ZMAX),timeout
c
      COMMON /const/ zzone,kb,q,diff0,sig,dt,alpha,dz
c
c     Solves a Parabolic Partial Differential Equation
c     One-D Problem
c
c     Single Cubic Particle of Lunar Regolith on Surface
c
      OPEN(UNIT=4,FILE='dist.in',STATUS='old')
c
c     Average Particle Diameter = 67.5 microns (LSB p. 321)
c     (or for ilmenite, alen = 100-150 microns (Frick,et.al.18th LPSC)
c     alen in (cm)
      alen = 1.0e-4
c     Read in dx from "dist.in"
      read(4,'(t12,f8.4)') dx
      dx = dx/1.0e8
c     dx is in Angstroms; must change to cm
      write(*,*) "dX = ",dx
      read(4,*)
      read(4,*)
      read(4,*)
c     Number of spatial steps = length/dx plus two phantom zones
      zstep = (alen*1.0e8/dx) + 2
```

```
      dzi = dx
      zzone = zstep-1
      zzone = ZMAX
      write(*,*) "zzone = ",zzone
c     Fill z, dz and distin arrays
      z(1) = -dzi
      dz(1) = dzi
      distin(1) = 0.0
      do 10 i = 2,zzone
         read(4,'(1x,e10.4,6x,e12.4)',end=8) z(i), distin(i)
c          write(*,'(1x,e10.4,6x,e10.4)') z(i), distin(i)
        dz(i) = dzi
c       distin(i) is in cm3/g/year; must conver to cm3/g/sec
        distin(i) = distin(i)/(3600*24*365)
c       z(i) is in angstroms; must convert to cm
          z(i) = z(i)/1.0e8
          end = i
c        write(*,*)"z(i) = ",z(i)," i = ",i," distin(i) = ",distin(i)
c          write(*,*) "dz(i) = ",dz(i)," i  = ",i
10    CONTINUE
8     distend = end
      do 11 j = distend+1, zzone
        z(j) = z(j-1) + dzi
          distin(j) = 0.0
          dz(j) = dzi
c         write(*,*)"z(j) = ",z(j)," j = ",j," distin(j) = ",distin(j)
11    CONTINUE
c
c     Set Surface Temperature (in Kelvin)
c     Day:
      TD = 380.
c     Night:
      TN = 100.
c
c     FOR DIFFUSION - Fick's Law
c     Diffusion Constant (from Hart,"Diffusion of He in Olivine")
c     diff0 = 2.2e8
c     From Futagami, 1993
      diff0 = 7.08e-11
c     Boltzman's Constant (J/(mole*K))
      kb = 1.38e-23*6.022e23
c
c     Adjust time step to maintain program stability
      write(*,*) 'diff0 = ', diff0
      dt = Dalpha*(dx*dx)/(diff0*exp(-(4.186*1.0e3*AE)/(kb*TD)))
c
c     Set Time Steps :  dt in seconds
      dt = DTIME
      tstep = TIMEYR*(3600*24*365)/dt
      if (tstep.gt.TMAX) then
        write(*,*) "TSTEP > TMAX; PROGRAM EXITED"
        goto 999
```

```
      endif
      write(*,*) "Tstep = ",tstep
c
c     Set Write Frequency for Output File
      wrfreq = tstep/FREQ
c
c     Set Gardening Cycle Time (Dependent on depth)
c     Number of times on the surface during time = year
      year = TIMEYR*(365*24*3600)
c     year = TIMEYR*(3600*24*365)
      write(*,'(1x,a,5x,f14.4)')"Year = ",year/(3600*24*365)
c     For Project, to show decay after gardening; time of saturation
      year1 = year
c     WRCYCLE = division of total time when gardening occurs.
c     Years on the Surface in each gardening cycle
      cycle = year/WRCYCLE
      write(*,*) "Cycle = ",cycle/(3600*24*365)
c     Lunar Month in seconds
      month = 24.*3600.*28.
c     Depth of Gardening (in cm) for single particle
      depth = 0.1
c
c     Set Subsurface Temperatures using gradient from Langseth and Keihm
c     Temperature gradient to 80 cm (in K/cm) (estimate from L. and K.)
c     Day and Night Gradients are unequal due to changing thermal
c     conductivity of lunar regolith.
      daygrad = 1.35
      TGD = TD - daygrad*depth
      nightgrad = 1.875
      TGN = TN + nightgrad*depth
c
c     Set dt to iterate through one gardening cycle
c     dt = year/TMAX
c     dt = 60.*10000.
c
c     LUNAR MATERIAL PROPERTIES
c     Density
c     Mean for Moon = 3.34g/cm3, LSB, p. 28 (changes with depth)
c     For Ilmenite, rho=4.7-4.8g/cm3, Frick, et.al. 18th LPSC
      rho = 3.34
      rho = 4.7
c
c     Activation Energy (J/mole)
c     q = 120 kcal/mol (from Hart,"Diffusion of He in Olivine")
c     q = 25.2 kcal/mol (from Trull, et. al., p.248, he4 in quartz)
c     1 cal = 4.186 J
c     q = 4.186*25.2e3
c     From Futagami, 1993
c     q = 4.186*11.0e3
      q = 4.186*1.0e3*AE
c     Sputtering Rate (cm/s) equals 0.02544 Angstroms/year from TRIM
c       Calculations and Compliation
```

```
      sputter = 2.5e-10/(365*24*3600)
c     sputter = 0.0
c
c     Solar Wind Flux (atoms/(cm2*s))
c     swf = 3.e8
c     Fraction of Solar Wind that is Helium 4
c     he4 = 1./22.
c     Solar Wind Flux of Helium
c     swfhe = swf*he4
c
      OPEN (UNIT=7,FILE='OUTPUT.2',STATUS='NEW')
c
c     Fill Vectors for TRIDAG
      call fill(a,b,c,TD)
      call fill(an,bn,cn,TN)
      call fill(agd,bgd,cgd,TGD)
      call fill(agn,bgn,cgn,TGN)
c
      do 12 i=1,zzone
        n(i) = 0.0
12    continue
c
c     Initial Loading Vector
      do 13 j=1,zzone
        nend(j)=distin(j)*dt
          swfhe(j) = distin(j)
13    continue
c
      week = 0.0
      time = 0.0
      out=0
c
c     Iterate on Concentration vs. Time
      do 15 i=1,tstep
c
        week = week + dt
        time = time + dt
c         write(*,*) "Iteration Number ", i
        do 86 k=2,zzone-1
c       n(k)=nend(k)
c         /Diffusion Only/
        n(k)=nend(k)+swfhe(k)*dt
c         write(*,*) "n(k) = ",n(k)," k = ",k
86      continue
c
c     While time<cycle, particle is on surface - Sputtering
c     write(*,*) "Sputtering Started, Particle on Surface"
        if (time.lt.cycle) then
c           write(*,*) "TIME = ",time," CYCLE = ",cycle
c!!         if (week.lt.month/2.) then
c           Day Side Conditions
c           write(*,*) 'Day Side'
```

```
            call TRIDAG(a,b,c,n,nend,zzone)
c           write(*,*) "TRIDAG Called"
            do 929 k = 1,zzone
              swfhe(k) = distin(k)
929           CONTINUE
c!!            thick = sputter*dt
            thick = sputter*dt/2
              nthick = nend(2)*thick/dz(1)
c       write(*,*) "nend(1) = ", nend(1)," time = ",time/(3600*24*365)
              nend(1) = nend(1) + nthick
              do 88 l = 2, zzone-1
                   nthick = nend(l)*thick/dz(l)
                   nend(l)=nend(l)+nthick-nend(l+1)*sputter*dt/dz(l+1)
88            continue
              dz(zzone-1) = dz(zzone-1) - thick
              z(zzone) = z(zzone) - thick
              z(zzone+1) = z(zzone) - thick
c           Merge last two real zones and rename phantom zone when dz of
c                 last physical zone gets smaller than one angstrom
              if (dz(zzone-1).le.1.e-8) then
                   n(zzone-2) = n(zzone-1) + n(zzone-2)
                   z(zzone-1) = z(zzone)
                   dz(zzone-2) = z(zzone) - z(zzone-2)
                   n(zzone-1) = n(zzone)
                   z(zzone) = z(zzone+1)
                   dz(zzone-1) = dz(zzone)
                   zzone = zzone-1
c                  write(*,*) 'zzone = ',zzone
              endif
            call fill(a,b,c,TD)
c!!       else if (week.le.month) then
c           write(*,*) "WEEK = ",week," MONTH = ",month
c           Night Side Conditions
c            write(*,*) 'Night Side'
c!
c!          call TRIDAG(an,bn,cn,n,nend,zzone)
c!          do 900 k = 1,zzone
c!             swfhe(k) = 0.0
c!900          CONTINUE
c!
c!!       else if (week.gt.month) then
c           write(*,*) 'One Lunar Day on  surface'
c!!         week = 0.0
c!!       endif
c       Under Surface Conditions
c     While time>cycle, particle is under surface - no sputter,s.wind
       else if (time.lt.year) then
c           write(*,*) "TIME<YEAR"
c!!        if (week.lt.month/2.) then
c           Day Side Conditions
c           write(*,*) 'Day Side; Garden'
            call TRIDAG(agd,bgd,cgd,n,nend,zzone)
```

```
          do 909 k = 1,zzone
            swfhe(k) = 0.0
909         CONTINUE
c!!       else if (week.le.month) then
c           Night Side Conditions
c           write(*,*) 'Night Side; Garden'
c!
c!          call TRIDAG(agn,bgn,cgn,n,nend,zzone)
c!          do 919 k = 1,zzone
c!              swfhe(k) = 0.0
c!919         CONTINUE
c!
c!!       else if (week.gt.month) then
c           write(*,*) 'One Lunar Day under surface'
c!!         week = 0.0
c!!       endif
          else if (time.ge.year) then
             cycle = cycle + year1
             year = year + year1
      endif
c
      ntop = nend(1)+ntop
      nbottom = nend(zzone) + nbottom
        nmax = 0.0
      do 50 j = 1,zzone-1
          if (nmax.le.n(j)) then
            nmax = n(j)
            nloc(i) = j
            ntime(i) = nmax
        endif
50      continue
c
c     Write to OUTPUT File
        if (out.lt.wrfreq) then
          out=out+1
      else if (out.eq.wrfreq) then
        write(7,*)
c       wrfreq = wrfreq*2
c       write(*,*) "wrfreq = ", wrfreq
          timeout = i*dt/(3600*24*365)
          write(7,'(1x,a,t9,e16.5,t26,i10)') "Time = ", timeout,i
          write(7,'(1x,a,t16,a)') "n(k)","z(k)"
       do 21 k=1,ZMAX/100
c
c       Convert z in cm to z in microns
         if (n(k).lt.LOWC) then
             write(7,'(1x,e15.5,5x,e15.5)')  0.0,z(k)*1.0e4
         else
             write(7,'(1x,e15.5,5x,e15.5)') n(k),z(k)*1.0e4
         endif
21       continue
c
```

```
          do 122 l=(ZMAX/100) + 1,zzone
          if (n(l).lt.LOWC) then
              write(7,'(1x,e15.5,5x,e15.5)')  0.0,z(l)*1.0e4
          else
              write(7,'(1x,e15.5,5x,e15.5)') n(l),z(l)*1.0e4
          endif
122       continue
c
c        write(7,*)
        out=0
      endif
c     Zero out first and last zones
      n(1) = 0.0
      n(zzone+1) = 0.0
c     write(*,*) "ntime(1) = ",ntime(1)
15   Continue
c
c    write(*,'(1x,a,5x,e14.5)') "NTIME = ",ntime(1)
c
c
c    Write Concentration vs. Z
c
     write(*,'(1x,a,t26,a,t40,a)') 'n (cm3 He/gram reg.)','nend','z'
    write(7,'(1x,a)') "Concentration vs. Z"
    write(7,'(1x,a,t9,e16.7)') "Time = ",time/(3600*24*365)
c   write(7,*)
    write(7,'(1x,a,t18,a)') "n(k)","z(k)"
   do 30 k=1,ZMAX/100
c     Convert z in cm to z in microns
      if (n(k).lt.LOWC) then
          write(7,'(1x,e15.5,5x,e15.5)')  0.0,z(k)*1.0e4
      else
          write(7,'(1x,e15.5,5x,e15.5)') n(k),z(k)*1.0e4
      endif
30   continue
c
   do 31 l=(ZMAX/100 + 1),zzone
      if (n(l).lt.LOWC) then
          write(7,'(1x,e15.5,5x,e15.5)')  0.0,z(l)*1.0e4
      else
          write(7,'(1x,e15.5,5x,e15.5)') n(l),z(l)*1.0e4
      endif
31   continue
c
c    Write Concentration vs. Time
c
    write(*,*)
    write(7,*)
     write(7,'(1x,t5,a,t30,a)') 't (years)','n'
    write(*,*) "TSTEP = ",tstep
    do 40 i=1,tstep,100
    write(7,'(1x,e16.8,t20,e16.7)') i*dt/(3600*24*365),ntime(i)
```

```
c     write(*,'(1x,e14.8,5x,i4)') ntime(i),nloc(i)
c     write(*,'(1x,e14.8,t20,e14.8)') i*dt/(3600*24*365),ntime(i)
40    continue
c     do 42 i=10001,tstep,100
c     write(7,'(1x,e16.8,t20,e16.8)') i*dt/(3600*24*365),ntime(i)
c     write(*,'(1x,e14.8,t20,e14.8)') i*dt/(3600*24*365),ntime(i)
c42   continue
      write(*,*)
c
c     Write Run Parameters
c
      write(*,'(1x,a)') 'Run Parameters'
      write(*,*)
      write(*,'(1x,a,2x,i15)') 'Time Steps = ',tstep

      write(*,'(1x,a,2x,f14.5,2x,a)')'Total Time = ',
     *     dt*tstep/(3600*24*365),"years"
      write(*,*) 'Surface Time = ',cycle/(3600*24*365),
     *           ' years'
      write(*,*)
      write(*,'(1x,a)') "Gardening Parameters"
      write(*,*)
      write(*,'(1x,a,2x,f9.5,2x,a)') "Garden Depth = ",depth,"cm"
      write(*,'(1x,a,1x,f9.5,2x,a)') "Surface Day Temp. = ",TD,"K"
      write(*,'(1x,a,1x,f9.5,2x,a)') "Surface Night Temp. = ",TN,"K"
      write(*,'(1x,a,1x,f9.5,2x,a)') "Gardened Day Temp. = ",TGD,"K"
      write(*,'(1x,a,1x,f9.5,2x,a)') "Gardened Night Temp. = ",TGN,"K"
      write(*,*)
998   write(*,'(1x,a)') 'TRIDAG Parameters'
      write(*,*)
      write(*,'(1x,a,2x,f20.5,2x,a)') 'dt = ',dt,' sec'
      write(*,'(1x,a,2x,f20.5,2x,a)') 'dt = ',dt/(3600),'hours'
      write(*,'(1x,a,2x,f20.5,2x,a)') 'dt = ',dt/(3600*24*365),'years'
c
      write(*,'(1x,a,2x,e15.5)') 'alpha = ',alpha
      write(*,'(1x,a,2x,e15.5)') 'D = ',diff0*exp(-q/(kb*TD))
      write(*,'(1x,a,2x,e15.5)') 'diff0 = ',diff0
      write(*,'(1x,a,2x,e15.5)')'D*alpha = ',diff0*exp(-q/(kb*TD))*alpha
      write(*,'(1x,a,e15.5,a)')'Act. Energy = ',q/(Na*JOULE),' eV'
      write(*,'(1x,a,e15.5,a)')'Act. Energy = ',q/4186,' kcal/mole'
c
      write(*,'(1x,a,2x,e15.5,2x,a)')'dz =',dzi*1.e4,' microns'
      write(*,*)
c
c     Write Release Results
c
      write(*,'(1x,a)') "Release Results"
      write(*,*)
      write(*,'(1x,a,2x,e15.5)') 'He released, top = ',ntop
      write(*,'(1x,a,2x,e15.5)') 'He released, bottom = ',nbottom
      ntotal = 0.0
      do 43 l=1,zzone-1
```

```
          ntotal = ntotal + dz(l)*n(l)
 43    continue
       ntotal = ntotal + ntop + nbottom
        write(*,'(1x,a,2x,e15.5,a)') 'ntotal = ',ntotal,' cm3/g released'
       write(*,*)
c
       CLOSE(UNIT=7)
 999   END
c
c
       SUBROUTINE tridag(a,b,c,r,u,n)
       INTEGER n,NMAX
       REAL a(n),b(n),c(n),r(n),u(n)
       PARAMETER (NMAX=2500)
       INTEGER j
       REAL bet,gam(NMAX)
       if(b(1).eq.0.)pause 'tridag: rewrite equations'
       bet=b(1)
       u(1)=r(1)/bet
       do 71 j=2,n
c          write(*,*)"TRIDAG  a(j)= ",a(j)," b(j)= ",b(j)," r(j)= ",r(j),
c     *       " j= ",j
        gam(j)=c(j-1)/bet
        bet=b(j)-a(j)*gam(j)
        if(bet.eq.0.)pause 'tridag failed'
        u(j)=(r(j)-a(j)*u(j-1))/bet
 71    continue
       do 75 j=n-1,1,-1
        u(j)=u(j)-gam(j+1)*u(j+1)
 75    continue
       return
       end
c
c
       SUBROUTINE fill(a,b,c,T)
       INTEGER NMAX, zzone
       PARAMETER (NMAX=2500)
       REAL a(NMAX),b(NMAX),c(NMAX),T,alpha,q,dz(NMAX),kb,dt
       COMMON /const/ zzone,kb,q,diff0,sig,dt,alpha,dz
c
c      Fill Vectors for TRIDAG
c      Use Differential Boundary Condition
c      Zone 1 and zzone have 0.0 coefficients since n=0.0
c      Set minimum diffusion coefficient
c!     diffmin = -1.0e-99
       alpha = dt/(dz(1)*dz(1))
       b(1) = 1.0 + 2.*alpha*diff0*exp(-q/(kb*T))
       c(1) = -alpha*diff0*exp(-q/(kb*T))
c!     if (c(1).gt.diffmin) then
c!        c(1) = diffmin
c!     endif
       a(1) = -alpha*diff0*exp(-q/(kb*T))
```

```
c!    if (a(1).gt.diffmin) then
c!       a(1) = diffmin
c!    endif
c     write(*,*) "a = ",a(1)," b = ",b(1),"c = ",c(1)
c
c     write(*,*)"zzone (fill) = ",zzone
      do 20 i=2,zzone
c
c     Calculate Coefficient of Diffusion Term
c
       alpha = dt/(dz(i)*dz(i))
c     write(*,*) "Alpha = ",alpha,"dt = ",dt,"dz(1) = ",dz(i)," i = ",i
c      c corresponds to i+1
       c(i) = -alpha*diff0*exp(-q/(kb*T))
c!     if (c(i).gt.diffmin) then
c!          c(i) = diffmin
c!       endif
c      b corresponds to i
       b(i) = 1.0 + 2.*alpha*diff0*exp(-q/(kb*T))
c      a corresponds to i-1
       a(i) = -alpha*diff0*exp(-q/(kb*T))
c!     if (a(i).gt.diffmin) then
c!          a(i) = diffmin
c!       endif
c     write(*,*) "FILL a = ",a(i)," b = ",b(i),"c = ",c(i), " i = ",i
20    continue
c
      return
      end
```

Appendix B ANNEAL Code

```
      PROGRAM  Anneal3D
c
c     Version2.0
c     Kim R. Kuhlman
c     August 31, 1998
c     Derived from Diffuse (1996)
c
c
c     Driver for Routines TRIDAG
c     Declarations
c
      INTEGER ZMAX,TMAX,KMAX,XMAX,f,i,j,l,k,out,wrfreq,LIM,MAX,p,m
      PARAMETER(ZMAX=2012,XMAX=22,TMAX=30000, KMAX=1001, MAX=50)
      REAL pi,vol,time,sum,runningsum,TIMESEC,initial,dx,sum2
      PARAMETER(pi = 3.14159265,LIM=10)
      REAL nstart(XMAX,XMAX,ZMAX),narray(XMAX,XMAX,ZMAX),x(XMAX)
      REAL nend(XMAX,XMAX,ZMAX),distin(ZMAX),sumnend,nin(ZMAX)
      REAL z(ZMAX),dz,alpha,kb,alen,xlen,nloc(TMAX),dose
      REAL a(ZMAX),b(ZMAX),c(ZMAX),ntime(TMAX+3),nmax(KMAX)
      REAL a1(ZMAX),b1(ZMAX),c1(ZMAX),alpha1,dvol,relcheck
      REAL dzi,R,sig,dt1,dt(MAX),nsides(MAX),zsum(ZMAX)
      REAL ntotal(MAX),Dirr(MAX),Dcalc(MAX),noiter(MAX)
      REAL ntop(MAX),nbottom(MAX),release(MAX),length(MAX)
      INTEGER xzone,zzone,distend,end,energy,notempsteps,T(MAX),mark
      REAL timeout,fac,nfinal(MAX)
c     data.in header information
      REAL helium3,helium4,hydrogen,argon,area,rho,slope(MAX)
      REAL toler,Dguess(MAX),compare,releasebottom,releasetop
      REAL releasecalc(MAX),Dfinal(MAX)
      INTEGER tstep
      PARAMETER(toler=0.99999)
      CHARACTER distfile*10,resultsfile*12,outputfile*15
      CHARACTER mineral*12,sample*10,rundate*9,species*4,junk*25
c
      COMMON /const/ zzone,kb,Dguess,sig,dt1,f
c
c     Solves a Parabolic Partial Differential Equation - One-D Problem
c
c     Simulates Annealing of PSII Implanted Wafers
c
c     Read Input Deck of Needed Files for the Simulation
c     contains filenames of implantation profile and annealing protocol/results
      OPEN(UNIT=2,FILE='input.deck',STATUS='old')
      read(2,*)
      read(2,'(10a)') distfile
      read(2,*)
      read(2,'(10a)') resultsfile
      read(2,*)
      read(2,'(10a)') outputfile
```

```
      CLOSE(UNIT=2)
c
c
c     SET TEMPERATURES AND TIME STEP USING EXPERIMENTAL INPUT DECK
c
      OPEN(UNIT=3,FILE=resultsfile,STATUS='old')
c
c     Read in header information
c
        read(3,'(a,t29,a)') junk, rundate
        read(3,'(a,t29,e11.4)') junk, alen
        read(3,'(a,t28,f6.1)') junk, TIMESEC
        read(3,'(a,t31,f8.3)') junk, dt1
c       dt is read in microsec -> convert to sec
        dt1 = dt1*1.0e-6
        read(3,'(a,t30,i6)') junk, wrfreq
        read(3,'(a,t29,a)') junk, sample
        read(3,'(a,t29,a)') junk, mineral
        read(3,'(a,t29,f6.3)') junk, rho
        read(3,'(a)') junk
c       helium3 and helium4 are dose respectively in ions/cm2
        read(3,'(a,t29,e11.4)') junk, helium3
        read(3,'(a,t29,e11.4)') junk, helium4
        read(3,'(a,t29,e11.4)') junk, hydrogen
        read(3,'(a,t29,e11.4)') junk, argon
        read(3,'(a,t29,f6.3)') junk, area
        read(3,'(a,t30,a)') junk, species
        read(3,'(a,t30,i4)') junk, energy
        read(3,'(a,t30,i3)') junk, notempsteps
        read(3,'(a)') junk
        read(3,'(a)') junk
        DO 26 i=1,notempsteps
         read(3,4) T(i),release(i),Dirr(i),dt(i),length(i)
4          format (i4,2x,f8.6,2x,e8.2,3x,f8.0,2x,e6.1)
c        Convert D from cm2/s to microns2/s
           Dirr(i) = Dirr(i)*1.0e+8
           write(*,*) "Dirr(i) = ",Dirr(i)
         write(*,3) T(i),release(i),Dirr(i)*1.0e-8,dt(i),length(i)
3          format (i4,2x,f8.6,2x,e8.2,3x,f10.0,2x,e6.1)
         dt(i) = dt(i)*1.0e-6
26       CONTINUE
        CLOSE(UNIT=3)
c
c        write(*,'(f4.1)') TIMESEC
c        write(*,'(e9.4)') alen
c        write(*,'(e9.3)') dt1
c        write(*,'(i6)') wrfreq
c        write(*,'(a)') sample
c        write(*,'(a)') mineral
c        write(*,'(f6.3)') rho
c       helium3 and helium4 are doses ions/cm2
          dose = 1.0e+16
```

```
      write(*,'(e9.4)') helium3
      write(*,'(e9.4)') helium4
c      write(*,'(e9.4)') hydrogen
c      write(*,'(e9.4)') argon
c      write(11,'(f6.3)') area
c      write(11,'(a)') species
c      write(11,'(i4)') energy
c      write(11,'(i3)') notempsteps
c     write(11,*)
c
c     DO 27 i=1,notempsteps
c      write(11,6) T(i),release(i),Dirr(i),dt(i)
c6       format (i4,2x,f8.6,2x,e8.2,3x,f8.4)
c27    CONTINUE
c
c
c   Read in file containing implantation profile
    OPEN(UNIT=4,FILE=distfile,STATUS='old')
c
c   INPUT DECK
c
c   Slab Thickness = 1000 microns -> alen is in cm
c   Read in dz from profile file
    read(4,'(t8,f4.0)') dz
c   dz is in Angstroms => microns
    dz = dz/1.0e+4
c   Convert alen from cm to microns
    alen = alen
    write(*,'(a,e9.2,a,e9.2)') "dZ = ",dz," alen = ",alen
    read(4,*)
    read(4,*)
    read(4,*)
c
c   SET UP GRID
c
c   Volume of phantom zones
c   dz must be in units of cm, currently in Ang.
    out = 0
c   Number of spatial steps in x or y = length/dx plus two phantom zones
c   dx and xlen used to be in cm
c   dx is in microns => 10 microns fixed for computational space) = dy
    dx = 1.0e-3*1.0e+4/2.
c   xlen in microns (fixed at 100 micron for x and y dimensions)
    xlen = 1.0e-2*1.0e+4
    xzone = xlen/dx + 2
    write(*,'(a,e9.2,a,e9.2)') "dX = ",dx," xlen = ",xlen
c   Number of spatial steps = length/dz plus two phantom zones
    zzone = (alen/dz) + 2
    dzi = dz
    write(*,*) "zzone = ",zzone, " xzone = ",xzone
c   Fill z, dz and distin arrays
    z(1) = -dz/2.
```

```
      distin(1) = 0.0
      distin(zzone) = 0.0
      sum = 0.0
      initial = 0.0
      dvol = dx*dx*dz
      write(*,*) "dvol = ",dvol," cm Cubed"
c     read in inital distribution in z direction only
      do 10 i = 2,zzone-1
         read(4,'(f4.0,4x,e10.4)',end=8) z(i), distin(i)
c        concentration = distin*dose(ions/cm2) => units => atoms/cm2Ang
c        Also convert to atoms/microns3 => divide by 1e+4 microns/cm
           distin(i) = distin(i)*dose/1.0e+4
         z(i) = z(i)/1.0e+4
           end = i
10    CONTINUE
c
8     distend = end
c
c     Fill zones beyond distribution calculation with zeros
      do 11 j = distend+1, zzone
        z(j) = z(j-1) + dz
           distin(j) = 0.0
11    CONTINUE
c
      CLOSE(UNIT=4)
c
c     Fill initial 3-D array of concentration values (xzone=yzone, dx=dy)
c     First fill sides of prism with zeroes
      do 210 j = 1,xzone
c       Top and Bottom (z-planes)
        do 211 i = 1,xzone
          narray(i,j,1) = 0.0
          narray(i,j,zzone) = 0.0
211     CONTINUE
c       Sides (xz and yz planes)
c       do 213 k = 1,zzone
c          narray(1,j,k) = 0.0
c          narray(xzone,j,k) = 0.0
c          narray(j,1,k) = 0.0
c          narray(j,xzone,k) = 0.0
c213     CONTINUE
210   CONTINUE
c
c     Now fill interior of prism
      initial = 0.0
      do 5 i = 2,xzone-1
        do 105 j = 2,xzone-1
          do 205 k = 2,zzone-1
c           extend z dist throughout xy plane
            narray(i,j,k) = distin(k)
            nstart(i,j,k) = narray(i,j,k)
            initial = initial + narray(i,j,k)*dvol
```

```
            if (i.eq.xzone/2) then
                  if (j.eq.xzone/2) then
                    if (k.lt.20) then
                    write(*,*) narray(i,j,k)
                    endif
              endif
            endif
205         CONTINUE
c          pause 'end of yz plane'
105       CONTINUE
5     CONTINUE
      write(*,*) "Initial After Filling = ",initial
      relcheck = 0.0
      mark = 0
c
c     WRITE OUTPUT FILE
c
c     OPEN(UNIT=7,FILE=outputfile,STATUS='OLD')
      OPEN(UNIT=19,FILE='Diff.out',STATUS='OLD')
c
      write(19,'(1x,a,t10,a,t23,a,t37,a)') "T (K)","Dirr (cm2/s)",
     *   "Dcalc (cm2/s)","Release_Calc"
c
c     Iterate on Concentration vs. Time using Dirr(j) as first guess
c     Make two guesses then use linear interpolation to find "root"
c
c     Outside Loop -> Controls Loop Through Temperature Step Protocol
c     Loops around j
c
      DO 1 j=1,notempsteps
      write(*,*)
      write(*,*) "Step ",j ," of TempSteps = ",notempsteps
      relcheck = relcheck + release(j)
      write(*,*) "Total release to this point = ",relcheck
c     set up new grid if length has changed
c     initialize all side of rect. prism
      sum = 0.0
c     if length has changed for temperature step, must write new distribution
      if(j.gt.1) then
        if(length(j).gt.length(j-1)) then
          fac = length(j)/length(j-1)
          write(*,*) "CALLING DEPTH"," Factor = ",fac
c         narray is expanded array, nstart is final dist. from last T
      call depth(length(j),dz,zzone,z,nstart,narray,sum,fac,dx,xzone)
          dvol = dx*dx*dz
            write(*,*) "DVOL = ",dvol
c       if we don't call depth, nstart=narray so continue to f loop
        endif
      endif
c
c     Third Loop -> Changes Dguess until release calc. matches release meas.
c     Loops around f
```

```
      f=0
c     1st Guess => Irregular Model or last guess for last j
      if(j.eq.1) then
        Dguess(1) = Dirr(j)
      else
        Dguess(1) = Dfinal(j-1)
        dt(j) = dt(j-1)
      endif
c
126   f=f+1
      ntop(f)=0.0
      nbottom(f)=0.0
      nsides(f)=0.0
      time = 0.0
c
c     Move narray into nstart to restart calculation using new D
c     narray is dist at the beginning of Temp. step!!
      do 420 l=1,xzone
        do 430, m=1,xzone
          do 440 k=1,zzone
            nstart(l,m,k)=narray(l,m,k)
440       CONTINUE
430     CONTINUE
420   CONTINUE
c
c     Fill Vectors for TRIDAG
c     Must fill two separate set of vectors since dx=dy.ne.dz
c     generate alpha based on Dguess for this iteration
c
      tstep=TIMESEC/dt(j)+1
      alpha  = Dguess(f)*dt(j)/(dx*dx)
      alpha1 = Dguess(f)*dt(j)/(dz*dz)
c     write(*,*) "Alpha1 = ", alpha1
c     if new tstep is too large, call expand to increase dx while maintaining
c     the length of the distribution (modification of 'depth')
      if(j.eq.10) then
      if(f.eq.1) then
c       first call to expand when total release > 50.0%
c     if(mark.eq.0) then
c      if(relcheck.gt.0.500) then
          write(*,*) "EXPAND CALLED!!!"
        fac = 10
c      call expand(length(j),dz,zzone,z,nstart,narray,sum,fac,dx,xzone)
        alpha1 = Dguess(f)*dt(j)/(dz*dz)
          dvol = dx*dx*dz
          mark = mark + 1
c      else if(relcheck.gt.0.4) then
c       fac = 10
c      call expand(length(j),dz,zzone,z,nstart,narray,sum,fac,dx,xzone)
c       alpha1 = Dguess(f)*dt(j)/(dz*dz)
c         dvol = dx*dx*dz
c      else if(relcheck.gt.0.2) then
```

```
c       fac = 10
c      call expand(length(j),dz,zzone,z,nstart,narray,sum,fac,dx,xzone)
c       alpha1 = Dguess(f)*dt(j)/(dz*dz)
c       dvol = dx*dx*dz
c      else if(relcheck.gt.0.07) then
c       fac = 10
c      call expand(length(j),dz,zzone,z,nstart,narray,sum,fac,dx,xzone)
c       alpha1 = Dguess(f)*dt(j)/(dz*dz)
c       dvol = dx*dx*dz
c      endif
c      endif
      endif
      endif
c
      if(alpha1.gt.0.10) then
      if(zzone.gt.50) then
       if(tstep.lt.100000) then
        dt(j) = dt(j)/2
        dt(j) = 0.1*(dz*dz)/Dguess(f)
           tstep1=tstep
        tstep = TIMESEC/dt(j) + 1
           if(tstep.eq.tstep1) then
             dt(j) = dt(j)/2
             tstep = TIMESEC/dt(j) + 1
        endif
        alpha  = Dguess(f)*dt(j)/(dx*dx)
        alpha1 = Dguess(f)*dt(j)/(dz*dz)
        write(*,*) "Alpha1 New = ", alpha1
c      Call EXPAND if time steps exceed a certain number
c      Need to adjust this so it only happens once
       else
c       pause "tsteps exceeded 1000"
           fac = 2
      call expand(length(j),dz,zzone,z,nstart,narray,sum,fac,dx,xzone)
           alpha1 = Dguess(f)*dt(j)/(dz*dz)
        dvol = dx*dx*dz
       endif
      else
        write(*,*) "zzone less than 50"
        goto 426
      endif
      endif
c
      write(*,*)
c     convert Dguess back to cm2/s
       write(*,*) "Dguess(",f,") = ",Dguess(f)*1.0e-8
      write(*,*) "Alpha = ", alpha," Call Fill T = ",T(j)
      write(*,*) "Alpha1 = ", alpha1," Time Steps= ",tstep
      write(*,*) "dt(j) = ",dt(j)," DZ = ",dz
c
      call fill(a,b,c,T(j),alpha)
      call fill(a1,b1,c1,T(j),alpha1)
```

```
c
c    Second Loop -> Controls Iteration on Single Temp and Dguess
c    Loops around i
c
     sum=0.0
c
c    loop through z and send one value of x, whole range of y to TRIDAG so
c    that we give successive lines to the subroutine
c
     write(*,*) "ZZONE = ",zzone
     write(15,*)
     write(15,*) "J = ",j,"  f = ",f
     do 12 i=1,zzone
c    Original array is maintained in narray
c    Must retain last distribution for initial dist of new temperature
c    This is done at line 533 or so => nend->nstart
c
c    New 3-D array of concentration (assumes no loss during crushing)
c      loop through y (j -> temperature step index)
       zsum(i) = 0.0
       do 112 l=1,xzone
c        loop through x
         do 212 k=1,xzone
           nend(k,l,i)=nstart(k,l,i)
           zsum(i) = zsum(i) + nstart(k,l,i)*dvol
           sum=sum+nstart(k,l,i)*dvol
212      continue
112    continue
       if(i.lt.101) then
       write(15,*) "ZSUM = ",zsum(i),i
       endif
12   continue
c
     write(*,*)
c    write(*,*) "Dguess(",f,") = ",Dguess(f)
     write(*,*) "Sum = ",sum," Initial = ",initial
     write(*,*) "DT = ",dt(j)
     write(*,*) "DZ = ", dz
     write(*,*) "DX = ", dx
     write(*,*) "TIME STEP = ", tstep
     runningsum=0.0
c
c    START TIME ITERATIONS
     do 15 i=1,tstep
c
c    move nend() into nstart.  nend will be overwritten on each iteration
     time = time + dt(j)
c      ADI Method for 3 space variables [Douglas, 1962]
c      Ending matrix becomes begining matrix for this time step
c      Iterate across X-Direction
c      Y first
       do 260 m=1,xzone
```

```
c       Then Z
        do 261 k=1,zzone
c         Then X
          sumnend = 0.0
          sum2 = 0.0
          do 262 l=1,xzone
           n=0.0
           sumnend = 0.0
c          fill inital vector in x direction for TRIDAG
c          This nstart => Eqn.1 for x direction
           n = nstart(l,m,k)*(1-3.*alpha-2.*alpha1)
           sumnend = nstart(l+1,m,k)+nstart(l-1,m,k)
           sumnend = sumnend + 2.*(nstart(l,m+1,k)+nstart(l,m-1,k))
           n = n+(alpha/2.)*sumnend
           n = n+alpha1*(nstart(l,m,k+1)+nstart(l,m,k-1))
           nin(l) = n
262         CONTINUE
c          pause 'first equation'
            call TRIDAG(a,b,c,nin,nfinal,xzone)
          do 263 l=1,xzone
c           put finished line into nend
            nend(l,m,k) = nfinal(l)
            sum2 = sum2+nend(l,m,k)
263         CONTINUE
261       CONTINUE
260     CONTINUE
c
c       pause 'Second Step Reached'
        sum2 = 0.0
c       Must set up new nstart matrix using Equ. 2 for y direction
c       Iterate across Y-Direction
c       X first
        do 270 l=1,xzone
c         Then Z
          do 271 k=1,zzone
c           Then Y
            do 272 m=1,xzone
             n=0.0
c            fill inital vector in y direction for TRIDAG
c            This nin => Eqn.2 for y direction
             n = alpha*nstart(l,m,k)+nend(l,m,k)
             n = n - (alpha/2.)*(nstart(l,m+1,k)+nstart(l,m-1,k))
            nin(m)=n
c       write(*,*) "NIN=",nin(m)," ne=",nend(l,m,k),"ns=",nstart(l,m,k)
272           CONTINUE
c           pause 'second equation'
             call TRIDAG(a,b,c,nin,nfinal,xzone)
            do 273 m=1,xzone
c             put finished line into nend
              nend(l,m,k) = nfinal(m)
c              write(*,*) "NEND = ",nend(l,m,k),l,m,k
              sum2 = sum2+nend(l,m,k)
```

```
273         CONTINUE
c          pause 'first equation after TRIDAG'
271        CONTINUE
270     CONTINUE
c       write(*,'(a,e15.6)') "Sum2 = ",Sum2," Second Step"
c
c      write(*,*) "Third Step Reached"
c      Must set up new nin array using Equ. 3 for z direction
c      Iterate across Z-Direction Last
c      X first
       sum = 0.0
       sum2 = 0.0
       do 290 m=1,xzone
c        Then Y
         do 291 l=1,xzone
c          Then Z
           do 292 k=1,zzone
            n=0.0
c           fill inital vector in y direction for TRIDAG
c           This nin => Eqn.2 for y direction
            n = alpha1*nstart(l,m,k)+nend(l,m,k)
            n = n - (alpha1/2.)*(nstart(l,m,k+1)+nstart(l,m,k-1))
            nin(k) = n
292          CONTINUE
c           pause 'Third Equation'
             call TRIDAG(a1,b1,c1,nin,nfinal,zzone)
           do 293 k=1,zzone
c            put finished line into nend
             nend(l,m,k) = nfinal(k)
             sum = sum + nend(l,m,k)
293          CONTINUE
291        CONTINUE
290     CONTINUE
c
c      Save release from sides of prism and replace with zeroes
c      ntop(f), etc. are initialized at beginning where f=f+1
         sum = 0.0
c        write(*,*) "Initial = ",initial," dvol = ",dvol
       do 310 l = 1,xzone
c       Top and Bottom (z-planes)
        do 311 p = 1,xzone
           sum = nend(p,l,1)*dvol + sum
          ntop(f) = nend(p,l,1)*dvol/initial + ntop(f)
           nend(p,l,1) = 0.0
          nbottom(f) = nend(p,l,zzone)*dvol/initial + nbottom(f)
           nend(p,l,zzone) = 0.0
311     CONTINUE
c       Sides (xz and yz planes)
        do 313 k = 1,zzone
     nsides(f)=(nend(1,l,k)+nend(xzone,l,k))*dvol/initial+nsides(f)
          nend(1,l,k) = 0.0
          nend(xzone,l,k) = 0.0
```

```
      nsides(f)=(nend(l,1,k)+nend(l,xzone,k))*dvol/initial+nsides(f)
           nend(l,1,k) = 0.0
           nend(l,xzone,k) = 0.0
313      CONTINUE
310    CONTINUE
c        write(*,*) "Sum for top = ", sum
c        write(16,601) "ntop=",ntop(f)," nsides=",nsides(f)," nbottom=",
c     *  nbottom(f)
c601       format(a,e12.5,a,e12.5,a,e12.5)
           nmax(f) = 0.0
         runningsum=0.0
         if (nbottom(f).lt.0.0) then
           nbottom(f) = 0.0
         endif
c
c      Move nend into nstart for beginning of next time step
c
      do 520 l=1,xzone
        do 530, m=1,xzone
          do 540 k=1,zzone
            nstart(l,m,k)=nend(l,m,k)
540       CONTINUE
530     CONTINUE
520   CONTINUE
c
15    CONTINUE
c
c     Check to see if release matches
      releasecalc(f) = ntop(f)+nbottom(f)+nsides(f)
      if(releasecalc(f).gt.release(j)) then
        compare=(release(j)/releasecalc(f))
c        write(*,*) "Compare for gt = ",compare
      else if(releasecalc(f).lt.release(j)) then
        compare=(releasecalc(f)/release(j))
c        write(*,*) "Compare for Lt = ",compare
      endif
c
      ntotal(f) = 0.0
c
      write(*,*) "Alpha first = ", alpha
      write(*,*) "Ntop = ",ntop(f)," Nbottom = ",nbottom(f)
      write(*,*) "Nsides = ",nsides(f)
      write(*,*) "Rel_calc",releasecalc(f),"  Release Meas.",release(j)
c     write(*,*) releasecalc(f)," ",release(j)," ",Dguess(f)," ",f
      write(*,*) "compare = ",compare," tol = ",toler
c
cc    write(*,*)
c
c     Calculate 2nd Dguess f=2
      if(f.eq.1) then
        if(compare.gt.toler) then
          goto 326
```

```
      endif
      if(releasecalc(f).lt.release(j)) then
c       write(*,*) "Before: Dguess(f) ",Dguess(f)
          Dguess(f+1)=Dguess(f)*2
c       write(*,*) "Dguess(",f+1,") = ",Dguess(f+1)
        goto 126
      else if(releasecalc(f).gt.release(j)) then
          Dguess(f+1)=Dguess(f)/2
c       write(*,*) "Dguess(",f+1,") = ",Dguess(f+1)
        goto 126
      endif
    endif
c
c   Calculate Next Dguess
c
    if(f.ge.2) then
      if(compare.lt.toler) then
          releasetop = Dguess(f-1)-Dguess(f)
       releasebottom = (releasecalc(f-1)-releasecalc(f))
          if(releasebottom.eq.0.0) then
            releasebottom = 1.0e-10
          endif
       slope(f)=(releasetop/releasebottom)
    Dguess(f+1)=slope(f)*(release(j)-releasecalc(f-1)) + Dguess(f-1)
    if (Dguess(f+1).lt.0.0) then
        Dguess(f+1) = -Dguess(f+1)
    endif
c       write(*,*) "F = ",f
c       write(*,*) "Slope(f) = ",slope(f)
       goto 126
      endif
    endif
c
326  Dfinal(j) = Dguess(f)
    write(*,*) "DFINAL = ",Dfinal(j)*1.0e-8
c
c     Write to OUTPUT File
     write(17,*) "z      n"
     write(17,*)
       write(*,*) "DVOL = ", dvol
     sum2 = 0.0
     do 443 k = 1,zzone
         zsum(k) = 0.0
       do 441 m = 1, xzone
         do 442 l = 1, xzone
           zsum(k) = zsum(k) + nend(l,m,k)*dvol
           sum2 = zsum(k)+sum2
442    CONTINUE
441    CONTINUE
      write(17,'(e12.5,6x,e12.5)') z(k),zsum(k)
443    CONTINUE
       write(*,*) "SUM2= ",sum2
```

```
c
      sum = 0.0
      do 320 l=1,xzone
        do 330, m=1,xzone
          do 340 k=1,zzone
c           dist. here is dist. to start next Temp. step
            nstart(l,m,k)=nend(l,m,k)
              narray(l,m,k)=nend(l,m,k)
            sum = sum+nstart(l,m,k)*dvol
c           write(17,*) k*dz,narray(l,m,k)
340       CONTINUE
330     CONTINUE
320   CONTINUE
      write(*,*) "Sum at End of f = ",sum
      write(*,*) "Fraction Left = ", sum/initial
c
      do 53 k=1,f
       write(19,'(1x,i4,2x,e12.4,2x,e12.4,2x,e12.4)') T(j),
     * Dirr(j)*1.0e-8,Dguess(k),releasecalc(k)
       write(18,'(1x,i4,2x,e12.4,2x,e12.4,2x,e12.4)') T(j),
     * Dirr(j)*1.0e-8,Dguess(k),releasecalc(k)
53    continue
c
1     CONTINUE
c
c     Write Results of Temperature Step to file
426       write(19,190) "DZ = ",dz, "microns, sample = ",sample
190   format (a,e12.4,a,a)
      do 54 k=1,j
      Dfinal(k) = Dfinal(k)*1.0e-8
      Dirr(k) = Dirr(k)*1.0e-8
       write(19,'(1x,i4,5x,e15.5,5x,e15.5)') T(k),Dirr(k),Dfinal(k)
       write(18,'(1x,i4,5x,e15.5,5x,e15.5)') T(k),Dirr(k),Dfinal(k)
54    continue
c
      CLOSE(UNIT=19)
c
c     write(7,*) "D(",j,") = ", Dfinal(j)
      write(*,*) "D(",j,") = ", Dfinal(j)*1.0e-8
c
999   END
c
c
      SUBROUTINE tridag(a,b,c,r,u,n)
      INTEGER n,ZMAX,XMAX
      REAL a(n),b(n),c(n),r(n),u(n)
      PARAMETER (ZMAX=2012,XMAX=22)
      INTEGER j
      REAL bet,gam(ZMAX)
c     write(*,*) "TRIDAG Entered"
      if(b(1).eq.0.)pause 'tridag: rewrite equations'
      bet=b(1)
```

```
      u(1)=r(1)/bet
      do 71 j=2,n
c           write(*,*)"TRIDAG  a(j)= ",a(j)," b(j)= ",b(j)," r(j)= ",r(j),
c     *       " j= ",j
       gam(j)=c(j-1)/bet
       bet=b(j)-a(j)*gam(j)
c       write(*,*) "c(j-1)=",c(j-1)," bet=",bet,"  gam(j)=", gam(j)
       if(bet.eq.0.)pause 'tridag failed'
       u(j)=(r(j)-a(j)*u(j-1))/bet
c        write(*,*) "n = ",r(j)," u = ",u(j)
71     continue
c      write(*,*) "Loop 71 complete"
      do 75 j=n-1,1,-1
       u(j)=u(j)-gam(j+1)*u(j+1)
75     continue
      return
      end
c
c
      SUBROUTINE fill(a,b,c,Temp,alpha)
      INTEGER ZMAX,zzone,Temp
      PARAMETER (ZMAX=2012, MAX=50)
      REAL a(ZMAX),b(ZMAX),c(ZMAX),alpha,q,kb,dt1,diffmin
      COMMON /const/ zzone,kb,Dguess(MAX),sig,dt1,f
c
c     Fill Vectors for TRIDAG using Crank-Nicholson Hybrid Method
c     Use Differential Boundary Condition
c     Zone 1 and xzone have 0.0 coefficients since n=0.0
c     Change back to zzone after debugging
c     Set minimum diffusion coefficient
      diffmin = -1.0e-20
      a(1) = -alpha/2.
      b(1) = (1.0+alpha)
      c(1) = -alpha/2.
c      write(*,*) "a = ",a(1)," b = ",b(1),"c = ",c(1)," zZONE = ",zzone
c
      do 20 i=2,zzone
c
c     Calculate Coefficient of Diffusion Term
c
c      write(*,*) "Alpha = ",alpha,"dt = ",dt," i = ",i
c       a corresponds to i-1
       a(i) = -alpha/2.
c       b corresponds to i
       b(i) = (1.0+alpha)
c       c corresponds to i+1
       c(i) = -alpha/2.
c      write(*,*) "FILL a = ",a(i)," b = ",b(i),"c = ",c(i), " i = ",i
20     continue
c
      return
      end
```

```
c
c
      SUBROUTINE depth(alen,dz,zzone,z,nstart,narray,sum,fac,dx,xzone)
      INTEGER ZMAX,zzone,MAX,bz,index,XMAX,k,xzone
      PARAMETER (ZMAX=2012,XMAX=22,MAX=50)
      REAL z(ZMAX),alen,dz,j,sum,newzone,dist,fac,sum2,dx
      REAL narray(XMAX,XMAX,ZMAX),nstart(XMAX,XMAX,ZMAX)
c     SET UP GRID
c
c     Number of spatial steps = length/dz plus two phantom zones
c     Expand dz by fac of 10 -> alpha*0.001
      k=0
      sum2=0
      bz = zzone-2
      newzone = fac
      dz=dz*fac
      dvol = dz*dx*dx
      write(*,*) "Alen = ",alen," dz = ",dz
      zzone = (alen/dz) + 2
      write(*,*) "ALEN/DZ = ",alen/dz," ZZONE = ",zzone
      write(*,*) "bz = ",bz," zzone = ",zzone
c
c     Calculate new z array
      DO 201 k = 1,zzone
        z(k) = (k-3./2.)*dz
c       write(*,*) z(k)
201   CONTINUE
c
c     Now run through all x and y for points 2 to zzones-1; i and j do this
c     k loops through all of new zzones and l through 10 zones to be summed
      sum2=0.0
      do 200 i=1,xzone
        do 300 m=1,xzone
c     iterate from (e.g. fac = 10) 2 to 100 for index while covering all
c     1000 of the previous depth's zones.
      DO 100 k = 2,zzone/fac+1
c       since taking an average of the concentration over the zones
c       combined, the z point must be in the middle of this zone
        dist = 0.0
        do 101 l = 2,fac+1
c         Run from 2 to 11, etc. since (1) is phantom zone
          index = (k-2)*fac + l
          dist = dist + narray(i,m,index)
          sum2 = sum2 + narray(i,m,index)*dvol
101     continue
c       concentration is in form of atoms/angstroms3, so divide by dx
c       initial is originially divided by dx
        nstart(i,m,k) = dist/fac
c         narray(i,m,k) = dist/fac
        sum = sum + nstart(i,m,k)*dvol
100   CONTINUE
        nstart(i,m,1) = 0.0
```

```
c       narray(i,m,1) = 0.0
c     Must fill remainder of array (past previous depth) with zeroes
      do 11 k = zzone/fac+2, zzone
        nstart(i,m,k) = 0.0
c       narray(i,m,k) = 0.0
11    CONTINUE
300     CONTINUE
200   CONTINUE
c
c     Need to copy nstart into narray
      do 320 k=1,zzone
        do 330 m = 1,xzone
          do 340 l = 1, xzone
            narray(l,m,k) = nstart(l,m,k)
340       CONTINUE
330     CONTINUE
320   CONTINUE
      end
c
c
      SUBROUTINE expand(alen,dz,zzone,z,nstart,narray,sum,fac,dx,xzone)
      INTEGER ZMAX,zzone,MAX,bz,index,XMAX,k,xzone
      PARAMETER (ZMAX=2012,XMAX=22,MAX=50)
      REAL z(ZMAX),alen,dz,j,sum,newzone,dist,fac,sum2,dx
      REAL narray(XMAX,XMAX,ZMAX),nstart(XMAX,XMAX,ZMAX)
c     SET UP GRID
c
c     Number of spatial steps = length/dz plus two phantom zones
c     Expand dz by fac of 10 -> alpha*0.001
c     Debugging**************************************************
      sum = 0.0
      dvol = dx*dx*dz
      write(*,*) "Beginning of Expand"
      do 320 k=1,zzone
        sum2 = 0.0
        do 330 m = 1,xzone
          do 340 l = 1, xzone
            sum2 = sum2 + nstart(l,m,k)*dvol
340       CONTINUE
330     CONTINUE
        sum = sum + sum2
        if(k.lt.20) then
          write(*,'(e10.2,5x,e10.2)') z(k),   sum2
        endif
320   CONTINUE
      write(*,'(a,e12.4)') "Sum at Beginning of Expand = ", sum
c     End of Debugging**************************************
      k=0
      sum2=0
      bz = zzone - 2
      newzone = fac
      write(*,*) "Alen = ",alen," dz = ",dz, "Before"
```

```
      dz=dz*fac
      dvol = dx*dx*dz
      write(*,*) "Alen = ",alen," dz = ",dz
      zzone = (alen/dz) + 2
      write(*,*) "ALEN/DZ = ",alen/dz," ZZONE = ",zzone
c     if((zzone-2).lt.alen/dz) then
c       zzone = (alen/dz) + 3
c     endif
      write(*,*) "zzone = ",zzone
c
c     Calculate new z array
c       since taking an average of the concentration over the zones
c       combined, the z point must be in the middle of this zone
      DO 201 k = 1,zzone+1
        z(k) = (k-3./2.)*dz
c       write(*,*) z(k)
201   CONTINUE
c
c     Now run through all x and y for points 2 to zzones-1; i and j do this
c     k loops through all of new zzones and l through 10 zones to be summed
      sum2=0.0
      do 200 i=1,xzone
        do 300 m=1,xzone
      DO 100 k = 2,zzone
        dist = 0.0
        do 101 l = 2,fac+1
c         Run from 2 to 11, etc. since (1) is phantom zone
          index = (k-2)*fac + l
          dist = dist + narray(i,m,index)
101     continue
        sum2 = sum2 + narray(i,m,index)*dvol
c       concentration is in form of atoms/angstroms, so divide by dx
c       initial is originially divided by dx
        nstart(i,m,k) = dist/fac
        narray(i,m,k) = dist/fac
100   CONTINUE
        nstart(i,m,1) = 0.0
        narray(i,m,1) = 0.0
        nstart(i,m,zzone) = 0.0
        narray(i,m,zzone) = 0.0
300     CONTINUE
200   CONTINUE
      write(*,'(a,e12.4)') "Sum2 after expansion = ", sum2
      write(17,*) "zexp","   nexp"
      sum = 0.0
      do 900 k=1,zzone
        sum2 = 0.0
        do 902 i=1,xzone
          do 904 m=1,xzone
            sum2 = sum2 + nstart(i,m,k)*dvol
904       CONTINUE
902     Continue
```

```
      sum = sum +sum2
      write(17,*) z(k),   sum2
         if(k.lt.20) then
          write(*,'(e12.4,5x,e12.5)') z(k),  nstart(5,5,k)*dvol
      endif
900   CONTINUE
     write(*,'(a,e12.5)') "SUM = ",sum
    end
```